DEPARTMENT OF ELECTRONIC & ELECTRICAL ENGINEERING

University of Strathclyde Engineering

DIELECTRIC BARRIER DISCHARGES FOR OZONE GENERATION

A thesis presented in fulfilment of the requirement for the degree of

Doctor of Philosophy

Guangming Huang, B.Eng(Honours)

2016

Department of Electronic and Electrical Engineering

University of Strathclyde

Glasgow, UK

Declaration of Authenticity and Author's Rights

‘This thesis is the result of the author’s original research. It has been composed by the author and has not been previously submitted for examination which has led to the award of a degree.’

Signed:

Date:

ACKNOWLEDGEMENTS

I would firstly like to thank Dr. Tao Wang for his continuous supervision, guidance and encouragement throughout the course of this study. His rigorous research attitude and strong commitments to excellence in research have set a good example for me and inspired me to pursue the extraordinary in my future career.

I would also like to express my gratitude to Prof. Scott MacGregor for the opportunity, support and the encouragement. Many thanks to Dr. Igor Timoshkin for his invaluable technical input provided throughout the study. Many thanks to Dr. Mark Wilson and Dr. Michelle MacLean for their continuous help whatever in the research or in life. In particular, I would like to express my gratitude to Dr. Mark Wilson for his advice and corrections on my academic papers and thesis throughout the study.

Thanks to all the guys in the High-Voltage Mechanical Workshop: Sean Doak, Andy Carlin, Frank May, and David Griffin for all their help with designing and machining reactors and other experimental equipment over the course of this study. Thanks to Mrs. Maureen Cooper for all her assistance, particularly in ordering experiment equipment and organising conference trips.

Thanks to all my colleagues in the HVT Research Group and also to my friends for providing technical discussions in the study and bringing fun to my life over the years. In particular, I would like to thank Dr. Xiao Hu, Dr. Liang Ji and Dr. Yuxian Tao for all their help at the beginning of my PhD study. In addition, many thanks to Athanasios Mermigkas for his assistances on thesis submission.

I would also like to thank my family for their deep love and continuous support in my life. Lastly, I would like to thank my girlfriend for all her support and understanding.

ABSTRACT

Non-thermal plasma discharges, particularly dielectric barrier discharges (DBDs), are the most common method of ozone generation. The aim of this research was to optimize the micro-discharges in DBDs, to improve ozone generation efficiency. The electrical characteristics of DBDs were researched, and the effects of the physical and electrical parameters of DBDs on ozone generation were investigated. Four DBD based ozone reactors, including plate configuration and cylindrical configuration, were designed and developed. Three major energization modes, including transient (40 ms) AC power supply, continuous AC power supply and pulsed power supply, were used for the investigation of ozone generation performance.

Under transient AC energisation in oxygen, it was found that the ozone generation efficiency at 2 bar absolute was 217 g/kWh, increased by 31% compared with that at 1 bar absolute. The ozone generation efficiency was found to increase with decreasing *E/N* in the range from 126 Td to 185 Td. Under continuous AC energisation, the ozone concentration was found to increase as the gas flow rate decreased (from 1 L/min to 0.4 L/min) or applied voltage was increased (from 3.5 kV to 6 kV). Under optimized conditions, the highest ozone concentration obtained was 271 g/Nm^3, which is promising in comparison with previously-published data. The ozone generation efficiency was found to reduce as the ozone concentration increased above 30 g/Nm^3. Furthermore, it was found that the AC energization frequency had no obvious effect on the behaviour of micro-discharges, or on the ozone generation efficiency. Pulsed DBDs for ozone generation was found to be less efficient than continuous AC energisation, for the conditions investigated herein.

This research has achieved the desired combination of high ozone generation efficiency at high ozone concentration (>150 g/Nm^3), based on DBDs. The curve of ozone generation efficiency versus ozone concentration achieved shows more efficient performance than that in the literature: at the typical industrial ozone concentration of 150 g/Nm^3 for waste water treatment, the ozone generation efficiency in this work was ~8.2 kWh/kg, ~20% higher than that in the literature.

Contents

List of Abbreviations

AC	Alternating current
AOX	Adsorbable organic halides
BPA	Bisphenol A
CT	Current transformer
DC	Direct current
DBD	Dielectric barrier discharge
DBDs	Dielectric barrier discharges
$deNO_x$	Reduction of oxides of nitrogen (NO and NO_2)
EDC	Endocrine-disrupting compound
FWHM	Full width at half maximum
FCT	Fast current transformer
ns	Nanosecond
OD	Outer diameter
OSHA	Occupational Safety and Health Act
PD	Power density
PDM	Power density modulation
PWM	Power width modulation
PMT	Photomultiplier
PVC	Polyvinyl chloride
PTFE	Polytetrafluoroethylene
pps	Pulses per second
UV	Ultraviolet
µM	Micro-molar

List of Symbols

σ	Collision cross-section
λ	Mean free path
z	Collision frequency
N	Number density of gas molecules
N_1	Number of molecules
n	Number of moles
w	Reaction rate
k	Reaction rate coefficient
$\Delta_f H°$	Standard molar enthalpy of formation of chemical species
ΔH	Enthalpy change
e	Charge of an electron
E	Electric field
E/N	Reduced electric field
ΔE_e	Energy obtained by an electron in the electric field per cm of path
ΔE_t	Energy obtained by charged particles in the electric field per cm of path
k_r	Portion of energy carried by electrons
η	Ozone generation efficiency
C_1	Number of ozone molecules formed per one oxygen atom
v_d	Drift velocity of electrons
x_{10}	Ratio between oxygen atoms and oxygen molecules
α	Ionization coefficient
β	Attachment coefficient
V_a	Applied voltage across the DBD reactor
V_b	Discharge gap breakdown voltage

V_{max}	Maximum applied voltage
V_{min}	Minimum applied voltage required to sustain the discharge
V_d	Voltage across the dielectric barrier
V_g	Voltage across the discharge gap
V_m	Voltage across the measurement capacitor C_m
V_{ig}	Ignition voltage
V_p	Peak voltage
p	Absolute gas pressure
d	Gap length
ε	Electron energy
T_e	Electron temperature
k_B	Boltzmann constant
C_m	Capacitance of the measurement capacitor
P	Discharge power
T	Period of applied voltage
I_t	Current measured in the external circuit
I_f	Filamentary current in the discharge gap
Q	Charge through DBD reactor
ΔQ	Charge transfer during half voltage cycle
$\Delta Q'$	Charge required for a voltage reversal across the gap from V_b to -V_b
Q_g''	The charge in the high voltage electrode provided by AC source
Q_d''	The charge in the ground electrode provided by AC source
Q_g'	The charge in the high voltage electrode induced by accumulated charge
Q_d'	The charge in the ground electrode induced by accumulated charge
Q_{ac}	The charge accumulated on the dielectric surface

C_g	Gap capacitance
C_d	Dielectric barrier capacitance
C_t	Total capacitance of the DBD reactor
f	Energization frequency of AC power
R	Universal gas constant
n_1	Number of moles of oxygen input per minute
$n_1^{'}$	Number of moles of oxygen input per second
m	Mass of oxygen input per minute
$m^{'}$	Mass of oxygen input per second
c	Ozone concentration with the unit of g/Nm^3
n_2	Number of moles of ozone
r	Oxygen gas volume flow rate
V_{mixture}	Molar volume of the mixture gas (ozone and oxygen)
n_{mixture}	Number of moles of the mixture gas (ozone and oxygen) per cubic meter
n_3	Number of moles of oxygen in the output mixture gas
x	Weight concentration of ozone in the mixture gas
$x^{'}$	Volume concentration of ozone in the mixture gas
m_1	Weight of the ozone generated per hour
m_0	Weight of the ozone generated per second
m_t	Weight of the ozone generated over 200 voltage cycles
W_t	Discharge energy over 200 voltage cycles
W_0	Micro-discharge energy
d_g	Gap length
n_0	Number of discharges per cycle
I_p	Amplitude of the filamentary current

t_d	Duration of the filamentary current pulse
Q_c	Transferred charge associated with a filament
N_e	Electron density
v_d	Electron drift velocity
F_c	Cross-section of the micro-discharge channel
ε_r	Relative permittivity
ε_0	Permittivity of free space
l	Length of ozone reactor
t_s	Statistical time lag
t_f	Formative time of gas breakdown
g/Nm^3	Gram per cubic meter at 0ºC and 1 atm
L/min	Litre per minute
J/L	Joule per litre

1 INTRODUCTION

1.1 Overview

This research project is focused on the optimization of the ozone generation using dielectric barrier discharges (DBDs). The electrical behaviours of DBDs and the corresponding ozone generation performance under different experimental conditions, including different discharge gap lengths, gas pressures, gas flow rates, reactor geometries and energization modes (AC continuous power and impulse power supplies), were investigated and compared. The maximum ozone concentration achieved in this work was 278 g/Nm^3 and the maximum ozone generation efficiency was 217 g/kWh. These concentration and efficiency values are promising compared with the data from literature. However, the maximum values of the ozone concentration and the ozone generation efficiency cannot be obtained simultaneously according to the achieved results in the work. The optimum ozone generation efficiency in this work (based on an oxygen-fed cylindrical DBD reactor with a narrow gap length of 0.3 mm, driven by a high-frequency (kHz) AC power supply) is 20% higher than the ozone generation efficiency of a conventional ozone generator in the literature, at the same ozone concentration [1]. This research contributes a large amount of experimental data on a wide range of ozone concentrations from 4 g/Nm^3 to 278 g/Nm^3, which can provide a good reference on the design of a high concentration industrial DBD-based ozone generator.

1.2 Research Motivation

Historically, ozone has been identified as a strong and environmentally-friendly oxidant and disinfectant for more than one hundred years. The powerful oxidization and disinfection effects of ozone have found a wide range of applications in industry, including water treatment, food processing, pulp bleaching and odour control. Ozone generation based on the dielectric barrier discharges was started by Siemens in 1857 [2]. A DBD is a non-thermal plasma discharge, generated by placing at least one dielectric layer between two metal electrodes and applying AC or pulsed voltages. This type of discharge can generate a large amount of energetic electrons without heating up the gas temperature, which has a great benefit in the synthesis of temperature sensitive chemistry such as ozone. Until now, the DBD is still the most widely used method for ozone generation in industry. However,

compared with the theoretical ozone generation efficiency of 1197.6 g/kWh [3], commercial ozone generators based on DBDs are still not efficient. In commercial systems, at the concentration of 150 g/Nm^3, the ozone generation efficiency is less than 100 g/kWh [4-6]. Considering the conversion efficiency, only about 12% of the input energy is utilized for ozone synthesis, while the remainder is wasted as heat produced in the discharge gap. Therefore, with the increasing demand for ozone in the water treatment nowadays, there is a growing worldwide interest in the improvement of the ozone concentration and generation efficiency. DBDs for ozone generation have been investigated by many researchers in the past 40 years [7-12], but the electrical behaviours of DBDs still cannot be quantitatively described, which can be attributed to the difficulty in the study of micro-discharges with a very short lifetime (of the order of ns) happening randomly in the discharge gap. From the literature, it is well known that ozone generation based on DBDs is strongly dependent on the properties of these micro-discharges. Therefore, it is the interest of this research to investigate the electrical behaviours of the micro-discharges and the ozone generation performance based on different physical and electrical conditions, in order to increase the ozone generation efficiency.

1.3 Research Objectives

The aim of this research is to optimize the ozone generation performance of a DBD-based, oxygen-fed, ozone generator with a narrow discharge gap (<1 mm). This involves the establishment of an electrical model of the DBDs, and optimization of the ozone concentration and generation efficiency, based on optimum conditions for DBDs. To achieve this aim, the work is divided into the following objectives:

- Theoretically analyse the chemical and physical kinetics of ozone generation and identify the parameters that affect the ozone generation efficiency.
- Experimentally investigate the electrical characteristics of the DBDs which involve the accurate measurement of the impulsive discharge current in the external circuit and derive the filamentary current in the discharge gap based on an electrical model of the DBD.
- Investigate the properties of the impulsive micro-discharge and the ozone generation efficiency by using a transient AC voltage.
- Investigate the ozone concentrations versus different specific energies under different experimental conditions.

- Investigate ozone concentration and generation efficiency by using a continuous AC power supply operating at different frequencies and derive the optimum conditions for achieving the highest ozone concentration and the highest ozone generation efficiency.
- Investigate the ozone generation under a pulsed power supply with a rise time of the order of nanoseconds.

1.4 Thesis Outline

This thesis is focused on DBDs for ozone generation, in an attempt to increase the ozone generation efficiency. The thesis is divided into eight chapters and the contents of the subsequent chapters are presented in the following:

Chapter 2 provides a general background and literature review on the research topic. First of all, the properties of ozone, applications of ozone and the ozone safety limits are reviewed, which provides background knowledge of ozone. Furthermore, the chemical and physical kinetics of ozone generation are analysed, with focus on the energy transfer during the ozone generation process. This part provided a firm understanding of the ozone generation mechanism in gas discharges. Moreover, the fundamental gas discharge theory is reviewed, followed by a review of industrial ozone generation technology, including DBDs and pulsed corona discharges. The important characteristics of DBDs are comprehensively reviewed, which informed the basis of the experimental work in the following chapters.

Chapter 3 details the experimental equipment and systems that were utilised throughout the course of this project, including gas handling systems, power supplies, and discharge diagnostics (electrical and optical). The common methods used for all the experimental work are introduced in this chapter, such as the ozone concentration and generation efficiency measurement principles.

Chapter 4 presents a study on the electrical characteristics of DBDs, which involves the methods adopted for the measurement of macro electrical parameters (voltage, current, transferred charge and discharge power based on a sinusoidal voltage cycle), and the impulsive discharge current and transient voltage measurement during a single micro-discharge. Moreover, the effect of the applied voltage amplitudes on the DBDs is discussed. Also, the electrical characteristics of DBDs energized by 100 Hz and 5 kHz AC sinusoidal

voltages were compared at the end of the chapter. In this chapter, an electrical model of the DBDs is developed and an equation for calculating the filamentary current is derived.

Chapter 5 is focused on the statistical analysis of the micro-discharge events in DBDs with different discharge gap lengths and different gas pressures. The filamentary currents in the discharge gaps are calculated based on the electrical model of DBDs derived from in Chapter 4. The statistical distributions of filamentary current magnitude, filamentary current duration, charge transferred during a single filament, single micro-discharge energy and the number of current pulses during one active discharge phase are provided. The pulse statistics of filamentary current under different gap lengths and different gas pressures are presented and compared. Moreover, the ozone generation efficiencies in the work are calculated and discussed in relation to the effects of the discharge gap length and gas pressure.

Chapter 6 provides a further study on the ozone performance under a continuous, high-frequency (kHz) AC power supply. The ozone concentrations and ozone generation efficiencies under different gas flow rates, different gas pressures, different discharge gap lengths and different applied voltages are presented. The ozone performances based on two different types of ozone generators, a plate-type DBD reactor and a cylindrical-type DBD reactor, are demonstrated and compared. Based on the cylindrical DBD reactor, the effects of the energisation frequency of the AC power supply on the micro-discharges and ozone generation are researched. At the end of this chapter, the ozone generation efficiency versus the ozone concentration curve achieved in the work is compared with the literature data. The optimum conditions for the ozone generation under the continuous AC power supply are obtained through the experimental work in this chapter.

Chapter 7 presents an investigation of pulsed power technology for ozone generation. Firstly, pulsed power technology is reviewed. Based on the review of pulsed DBDs, the rise rate of the voltage pulse is a key parameter in the pulse discharges, therefore an experimental study on the effects of the rise rate of voltage pulse DBDs is presented. In the following, the ozone generation using pulsed DBDs is investigated and the results are compared with those achieved by using the continuous AC power supply.

Chapter 8 concludes the work in this thesis and highlights the major outcomes of the experimental results. This chapter ends with recommended future work on ozone generation using DBDs.

2 BACKGROUND AND LITERATURE REVIEW

2.1 Introduction

Ozone is a strong oxidation agent, widely used in industrial applications including water treatment, deNOx(reduction of oxides of nitrogen), and pulp bleaching etc. With growing public pressure on environmental issues, the demand for decontamination of water is increasing. However, the efficiency of existing industrial ozone generators is low, which makes ozone expensive, and the high cost limits the application of ozone in industry. Commercial ozone generators have an efficiency less than 100 g/kWh at the concentration of 147.8 g/Nm^3 (10%, by weight) [4, 5]. Considering the theoretical efficiency of 1215 g/kWh (based on the enthalpy of formation of 1.48 eV per O_3 molecule [13]), only 12% of the input electrical energy is utilized for ozone synthesis, while the remainder is wasted as heat produced in the discharge gap. Because some of the energy losses as heat from chemical reactions which cannot be prevented, the maximum possible efficiency that can be achieved was ~30% [14, 15]. In order to improve the ozone generation efficiency, the physical and chemical processes of ozone generation have to be brought to light.

As ozone is very sensitive to temperature, non-thermal plasma discharges in air or oxygen have been employed for ozone generation. The most common method in industry is dielectric barrier discharges, because this type of discharge has advantages in generating large-volume non-equilibrium plasma, which is very beneficial for the chemical synthesis of ozone [16]. Other non-thermal plasma discharges used for ozone generation include DC corona discharges, atmospheric glow discharges and pulsed corona discharges. Pulsed corona discharge is an attractive method that has taken attentions of researchers in the past 20 years [10]. The advantages and disadvantages of both DBD and pulsed corona discharge for the ozone generation have been reviewed in this chapter.

Within this chapter, the properties of ozone, applications, and its historical generation technology are initially reviewed. Following the background material on ozone generation technology, a theoretical analysis of the ozone generation process is presented, with emphasis on the elementary process of electron collisions with other particles in discharges in oxygen. The chemical reactions involved in ozone generation and decomposition are demonstrated, followed by an energy balance analysis of ozone formation. The theoretical ozone generation efficiency is calculated based on the energy analysis, and methods to

improve the efficiency are discussed. Finally, different non-thermal plasma discharges for ozone generation are reviewed and compared.

2.2 Ozone Properties

Ozone consists of three oxygen atoms and its chemical symbol is O_3. Ozone gas is colourless and it has a characteristic pungent odour. Ozone was firstly discovered as a new chemical compound in 1840 by C. F. Schönbein [17]. After more than two decades, the structure of ozone was identified as triatomic oxygen in 1865 by J.-L. Soret [18]. Nowadays, the molar mass of ozone has been accurately measured to be 47.998 g/mol [19] and its density at standard conditions (0 °C and 101.325 kPa) is recognised as 2.144 g/L worldwide.

Ozone is one of the most powerful oxidants and it has higher oxidation-reduction potential (2.07 V) than other oxidants including chlorine (*Cl*, 1.36 V) and hydrogen peroxides (H_2O_2, 1.77 V). An ozone concentration of 0.1 mg/L is capable of inactivating 99.9% of a bacterial suspension within 1 min [20]. More importantly, ozone has a better environmental compatibility than other oxidants, since its eventual product after the oxidation reaction is oxygen. Ozone dissolves in many solvents such as water, which gives rise to its application in water disinfection. Ozone is unstable, it cannot be stored, and must be generated at its point of use; in normal swimming-pool water, it lasts just long enough to purify and disinfect the water (less than 1 second).

Ozone is generated naturally in the atmosphere from 15 km to 50 km above the earth (the ozone layer). The generation of ozone in the atmosphere is a result of solar UV radiation in the wavelength range between 240 nm and 300 nm, through the reactions below:

$$O_2 + \mathrm{UV} \rightarrow 2O \tag{2.1}$$

$$O + O_2 \rightarrow O_3 \tag{2.2}$$

The ozone layer in the atmosphere absorbs UV radiation from 200 nm to 360 nm, with the reaction below:

$$O_3 + \mathrm{UV} \rightarrow O_2 + O \tag{2.3}$$

The net result of the above equations is absorption of the harmful UV radiation from the sun. The ozone measurement method is mainly based on the absorption of the 254 nm UV radiation.

2.3 Typical Applications of Ozone

2.3.1 Water Treatment

Ozone is conventionally used for drinking-water treatment, as it is a strong oxidant and disinfectant. The main benefits of using ozone for water treatment are described below:

- **Disinfection**

Firstly, ozone can kill bacteria such as *E. coli* more effectively in drinking water compared with chlorine. It has been observed that 0.1 mg/L of ozone requires only 5 seconds to kill 6×10^4 *E. coli* cells in water, whereas 0.1 mg/L of chlorine requires 4 hours [21]. When the temperature was increased from 22 ºC to 37 ºC, the ozone inactivation time decreased from 5 seconds to 0.5 seconds. The disinfection by ozone takes place with rupture of the bacterial cell wall and the disinfection rate is dependent upon the ozone concentration, temperature, pH, and the type of organisms.

- **Iron and manganese removal**

Secondly, ozone can oxidize the heavy metals, including iron and manganese, in water supplies. Ozone oxidizes iron from Fe (II) to Fe (III), and Fe (III) hydrolyses to Fe $(OH)_3$, which precipitates to a solid form that can be filtered. As for the manganese, ozone oxidizes Mn (II) to MnO_2 (Mn IV), which is insoluble and can be filtered out of the water. The reaction equations are shown below:

$$2F^{2+} + O_3 + 5H_2O \rightarrow 2Fe(OH)_3 + O_2 + 4H^+ \quad (2.4)$$

$$Mn^{2+} + O_3 + H_2O \rightarrow MnO_2 + O_2 + 2H^+ \quad (2.5)$$

- **Bisphenol A removal**

Finally, oxidation of the micro-pollutant, Bisphenol A, is a very important application of ozone in recent years. Bisphenol A (BPA) is an endocrine-disrupting compound (EDC), which exists in surface water. An EDC is defined as “an exogenous substance or mixture that alters the functions of the endocrine systems and consequently causes adverse health effects in an intact organism, or its progeny or sub-populations” [22]. BPA has been widely used in making polycarbonate plastic and epoxy resins and it has been found in a wide range of

aquatic environments [23, 24]. Ozone has been found to be highly effective for the removal of BPA in water [25-28]. The proposed reactions pathways for the formation of oxidation products of BPA are shown in Fig. 2-1.

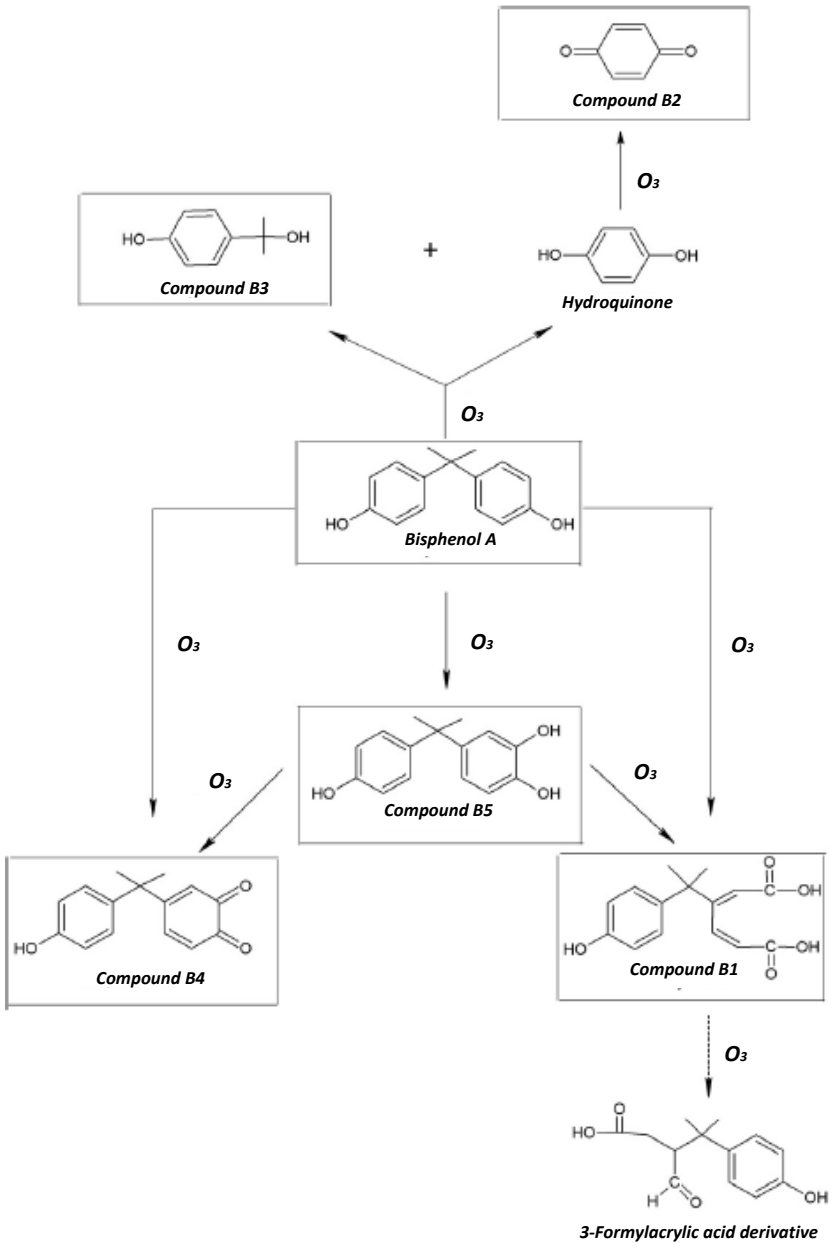

Fig. 2-1 Proposed reaction pathways for the formation of oxidation products of BPA [29, 30]

In the BPA ozonation pathways, compounds B1–B5 represent the initial transformation products. Fig. 2-2 shows the variation in the abundance of these compounds according to the ozone dose applied:

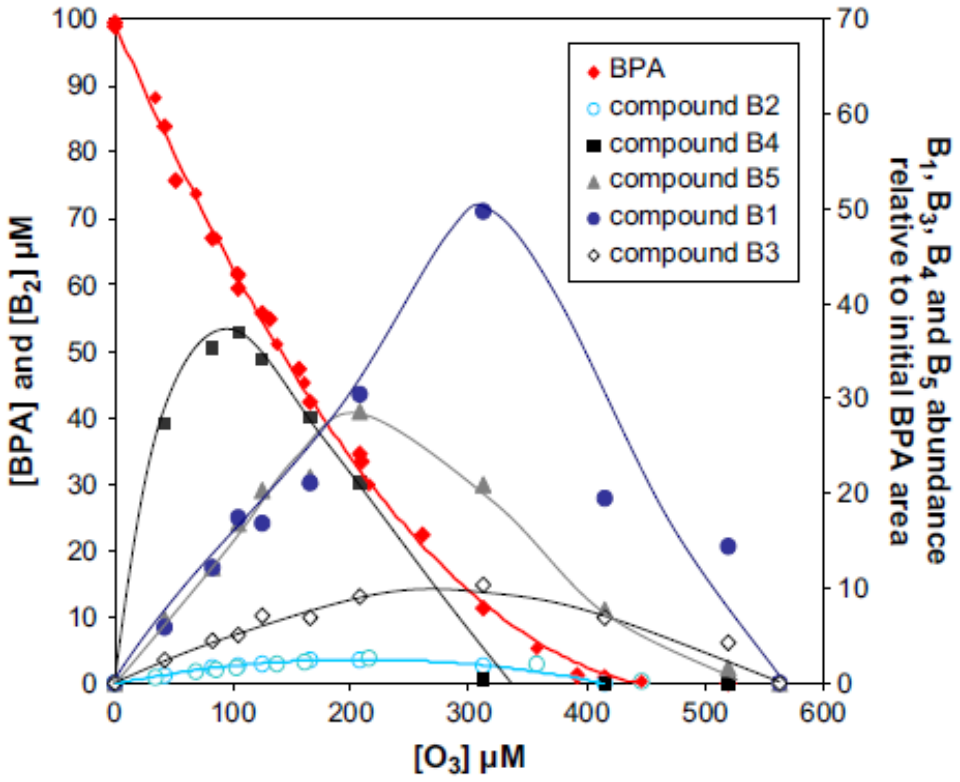

Fig. 2-2 Transformation product variation according to the ozone dose applied [30]

It was reported that the amount of each degradation product increased with increasing ozone dose and for each major transformation product identified, a progressive decrease in formation was observed before complete BPA removal [30]. Based on Fig. 2-2, it can be seen that for an initial BPA concentration of 100 µM, an ozone dose ≥ 570 µM is sufficient to remove the BPA and all major degradation products.

2.3.2 NO_x Reduction

NO_x is a generic term for oxides of nitrogen, mainly NO (nitric oxide) and NO_2 (nitrogen dioxide). These are pollutant gases that influence the quality of air, soil and water through acid rain, which affects human health. NO_x mainly impact respiratory conditions and long

term exposure can decrease lung function. NO_x are generated from the reaction of nitrogen and oxygen gases during combustion in power plants, automobiles or industrial boilers. The aim of ozone processing is oxidation of NO to NO_2, which is then further converted into N_2O_5. NO and NO_2 are relatively insoluble in water, but N_2O_5 is highly soluble in water, therefore NO_x can be reduced after this conversion process, with the final product (N_2O_5) treated by wet scrubbers. The main reactions involved in converting NO and NO_2 into N_2O_5 using ozone are shown in the following:

$$NO + O_3 \rightarrow NO_2 + O_2 \tag{2.6}$$

$$2NO_2 + O_3 \rightarrow N_2O_5 + O_2 \tag{2.7}$$

$$N_2O_5 + H_2O \rightarrow 2HNO_3 \tag{2.8}$$

Reduction of NO_x ($deNO_x$) is usually done by ozone processing, via one of the following two methods:

- Direct method: the exhaust flue gas that contains NO_x is fed through a non-thermal plasma discharge reactor. The ozone generated inside the reactor will convert NO and NO_2 into N_2O_5.
- Indirect method: ozone is generated from an ozone generator on-site and the ozone is injected into the exhaust flue gas stream that contains NO_x. The ozone then converts NO_x into N_2O_5, which will be absorbed in the water.

At present, there is one commercially-available $deNO_x$ technology, named LoTOx™ [31]. In this system, ozone is generated on-site and on demand by using an ozone generator. The ozone is injected into a reaction duct installed in the process gas stream and the amount of ozone injected can be automatically varied to maintain a pre-set amount of NO_x present in the output flue gas generated [31].

2.3.3 Pulp Bleaching

Ozone has been increasingly used in pulp mills for their bleaching process, because ozone has advantages in terms of effluent load reduction, usage simplicity and bleaching cost savings [32]. By destroying lignin, ozone makes paper whiter. For the same delignification efficiency, 1 kg of ozone can replace 2-4 kg of pure chlorine dioxide [33]. In addition, ozone is an ideal choice to limit the formation of chlorinated by-products (AOX) formed during conventional beaching processes.

Ozone bleaching is efficiently applied on hardwood and softwood pulps, on Kraft and sulphite pulps. It has been shown that, with 1% ozone concentration, dye decolourization in Kraft paper works very well [34]. Pulp bleaching is achieved through a continuous sequence of bleaching steps, utilizing different chemicals and operating conditions to remove residual lignin, and to destroy chromophoric groups [33]. Ozone is usually applied alone in a "Z" stage, or combined with chlorine dioxide in a "ZD" stage, depending upon the mill requirements.

2.4 Ozone Limits and its Brominated By-products

As ozone is a strong oxidant, it is toxic to human beings. The OSHA (Occupational Safety and Health Act) has established a time-weighted average permissible exposure level for workers for an eight-hour day of 0.1 ppm (~0.2 mg/Nm^3) and a short-term exposure limit of 0.3 ppm (~0.6 mg/Nm^3) for an exposure less than 15 minutes. The toxicity of ozone depends upon the ozone concentration and exposure time. The symptoms of exposure to ozone with concentration of 0.1 – 1 ppm ozone are headache, throat dryness and irritation of the respiratory passages. Exposure to ozone with concentration of 1 – 100 ppm ozone can cause asthma-like symptoms such as tiredness and lack of appetite. Short-term exposure to higher concentrations of ozone (>100 ppm) can cause throat irritations, haemorrhaging, and pulmonary edema. Oxidation of water by ozone can produce various by-products, such as brominated organics and bromate ion. Bromide is a chemical compound that is usually found in raw seawater. When the raw water is treated by ozone, some brominated by-products are generated. The simplified reactions of ozone with bromide are shown below:

$$O_3 + Br \rightarrow O_2 + OBr^- \tag{2.9}$$

$$O_3 + OBr^- \rightarrow 2O_2 + Br^- \tag{2.10}$$

$$2O_3 + OBr^- \rightarrow 2O_2 + BrO_3^- \tag{2.11}$$

Bromate (BrO_3^-) is classified as a potent carcinogen by the IARC (International Agency for Research on Cancer) [35]. Thus, a stringent limit on the maximum contaminant level (MCL) for bromate in drinking water (10 μg/L) has been set by authorities of the United States, China, the European Union, and others [36].

2.5 Analysis of Ozone Generation Kinetics

2.5.1 Fundamental Parameters in Kinetics of Ozone Generation

Collision is one of the most fundamental processes in a chemical reaction. All the new species in a chemical reaction are formed via the collision of atoms or molecules. The motion of charged particles in a gas in the presence of an external electrical field can lead to intensive collision of particles, which results in the synthesis of new species. The elementary processes in gas discharges, including ionization, excitation and dissociation, are caused by the collision of electrons with other particles. The elementary processes in gas discharges can be described in terms of the following six major collisional parameters: Collision cross-section, mean free path, mean kinetic energy, interaction frequency, reaction rate and reaction rate coefficient.

A. Reaction cross-section:

Reaction cross-section, σ, is the fundamental quantity that characterizes a reaction. It can be interpreted as follows. Assuming that moving particles such as electrons behave as solid spheres and they have a relative velocity v with the "target" particles, a specified reaction will take place if the "target particle" lies with its centre within an imaginary circle that comes with the moving particle with diameter d. The area of $\pi\ (d/2)^2$ is defined as the cross-section $\sigma(v)$ of the specified reaction [37].

B. Mean free path:

The average distance travelled by a particle between collisions is called the mean free path, λ. The mean free path of the elementary process A+B means that an interaction takes place if the cylindrical volume traversed by a particle A contains at least one particle B, which means that $\lambda\sigma N_B = 1$ [37]; N_B is the concentration of particle B. Rearranging of this equation allows the mean free path to be calculated:

$$\lambda = \frac{1}{N_B \sigma} \tag{2.12}$$

C. Collision frequency:

The collision frequency, *z*, is defined as the average number of collisions between two particles per unit time. Assuming that the velocity of a moving particle A is *v*, the collision frequency of collision partner A with the other collision partner (partner B) can be calculated [37]:

$$z_A = \frac{v}{\lambda} = N_B \sigma v \tag{2.13}$$

Taking into account the velocity distribution function, the collision frequency is usually calculated as an average value:

$$z_A = n_B \int \sigma(v) v f(v) dv = \langle \sigma v \rangle N_B \tag{2.14}$$

In the above relation, $<\sigma v>$ is the mean value of σv based on the velocity distribution function, *f(v)*.

D. Reaction rate coefficients:

The number of elementary processes that take place in a unit volume per unit time is called the elementary reaction rate, denoted as *w*. For the reaction of A+B, the reaction rate can be calculated by multiplying the interaction frequency of partner A with partner B, and the number of particles A in the unit volume [37]. Therefore:

$$w_{A+B} = z_A N_A \tag{2.15}$$

Substituting the equation (2.14) into the equation (2.15), the reaction rate of A+B can be rewritten as:

$$w_{A+B} = \langle \sigma v \rangle N_A N_B \tag{2.16}$$

The factor $<\sigma v>$ is termed as the reaction rate coefficient, denoted as *k*. The reaction rate coefficient of the reaction of A+B is:

$$k_{A+B} = \langle \sigma v \rangle = \int \sigma(v) v f(v) dv \tag{2.17}$$

From equation (2.17), it can be seen that the reaction rate coefficient is the mean value of the product of the reaction cross-section and the collision particle velocity, based on a relevant distribution function. The reaction rate coefficient *k* includes information on energy distribution functions and depends upon the temperatures or mean energies of the collision partners.

2.5.2 Elementary Processes of Ozone Generation in Oxygen Discharges

Ozone can be generated by discharges in oxygen. There are three key processes involved in the formation of ozone: ionization of O_2, dissociation of O_2 and O_3 formation. First of all, in the presence of an external electrical field, oxygen gas molecules are ionized by the seed electrons existing in the gas due to cosmic radiation and radioactive substances. Based on the Townsend discharge mechanism, an electron avalanche takes place. Increasing numbers of electrons will cause the dissociation of oxygen molecules and other reactions due to the electron collisions. Secondary, the oxygen atoms generated react with oxygen molecules and a third collision partner to form ozone. The third collision partner in the ozone formation process can be O atoms, O_2 molecules, O_3 molecules or the wall of the reactor. Ozone generation via discharges in oxygen consists of many particle reactions. The list of about 70 reactions taking place in the ozone generation process can be found in [14]. The main reactions considered in this work are shown below:

1) Electronic dissociation of O_2:

$$e + O_2 \xrightarrow{k_{1a}} O_2(\mathrm{A}\,^3\textstyle\sum_u^+) \rightarrow O(^3\mathrm{P}) + O(^3\mathrm{P}) + \mathrm{e} \qquad \text{(R1a)}$$

$$e + O_2 \xrightarrow{k_{1b}} O_2(\mathrm{B}\,^3\textstyle\sum_u^-) \rightarrow O(^3\mathrm{P}) + O(^1\mathrm{D}) + \mathrm{e} \qquad \text{(R1b)}$$

2) Formation of vibrationally-excited O_3:

$$O + O_2 + M \xrightarrow{k_2} O_3^* + M \qquad \text{(R2)}$$

(M = [O], [O_2], [O_3])

3) O_3 formation:

$$O_3^* + O \xrightarrow{k_3} O_3 + O \qquad \text{(R3)}$$

$$O_3^* + O_2 \xrightarrow{k_4} O_3 + O_2 \qquad \text{(R4)}$$

4) O_3 decomposition:

$$O + O_3^* \xrightarrow{k_5} 2O_2 \qquad \text{(R5)}$$

$$e + O_3 \xrightarrow{k_6} O_2 + O + \mathrm{e} \qquad \text{(R6)}$$

In reactions (R1)-(R6), k_x (x=1a, 1b, 2…6) is the reaction rate coefficient. From the reaction equations (R1a) and (R1b), it can be seen that two excited states of O_2 molecules $O_2(\mathrm{A}\,^3\Sigma_u^+)$ and $O_2(\mathrm{B}\,^3\Sigma_u^-)$), are formed, followed by the formation of O atoms ($O(^3\mathrm{P})$, $O(^1\mathrm{D})$). $O(^1\mathrm{D})$ is the excited state of an O atom and it is transformed into the ground state $O(^3\mathrm{P})$ atom within about 10 ns [14]. Following the dissociation of O_2 molecules, the O_3 molecules are formed initially into a vibrationally-excited state through the reaction equation (R2) [38, 39]. Most of these excited O_3^* molecules are quenched into O_3 molecules through the reactions (R3) and (R4), but some of them are transformed into O_2 through equation (R5). The ozone can also collide with an electron which causes the dissociation of the ozone, shown in reaction (R6). Fig. 2-3 shows the evolution of different particle species after a micro-discharge:

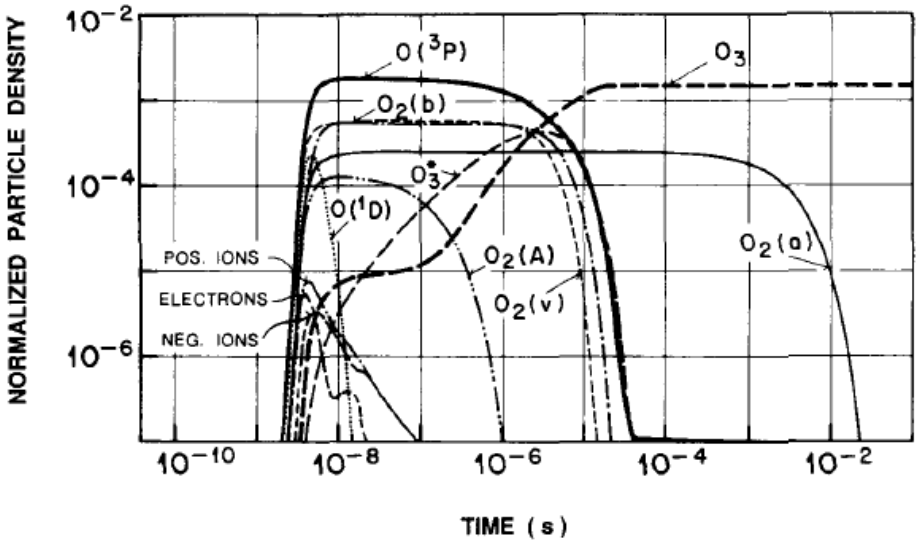

Fig. 2-3 Numerical simulation of ozone generation due to one micro-discharge in pure oxygen (homogeneous model, p=1 bar, T=300 K) [40]

It is shown that while the charge carriers (electrons, positive ions and negative ions) disappear typically in less than 10 ns, ozone formation takes a few μs [40]. It can be seen that within 10^{-4} s after a micro-discharge, the newly-formed ozone will be diluted by the flow

of gas to establish a background ozone concentration that will serve as the initial condition for subsequent micro-discharges. The chemical reactions with this background ozone concentration reduce the ozone generation efficiency. In the following analysis, the effect from the background ozone concentration can be ignored by keeping this concentration small ($[O_3]/N < 1\%$) [41]. The main results from Fig. 2-3 can be summarized as below [40]：

1) Dissociation of O_2 by electron impact is the main reaction path leading to ozone formation;

2) Ionic reactions contribute little to ozone formation;

3) There is optimum micro-discharge energy;

4) High ozone concentrations have to be built up by a large number of micro-discharges.

2.5.3 Energy Balance in Ozone Generation Process

The ozone generation process results from competing reactions involved in ozone formation and ozone decomposition. The energy balance involved in both of these reactions should be considered, as described in the following discussion:

1) Ozone formation

The processes for all of the chemical reactions include: breaking bonds, rearranging atoms and forming new bonds. The energy associated with chemical bonds is referred to as the bond energy. For ozone generation, the first step is to dissociate the oxygen molecules into oxygen atoms and therefore some energy is required to break the bonds between two oxygen atoms in an oxygen molecule. The process of oxygen dissociation is an endothermic reaction and it has a positive enthalpy change. When oxygen atoms are produced, ozone will be generated by the reaction of an oxygen molecule, an oxygen atom and a third particle. Heat is released when the bond between the oxygen atom and oxygen molecule is formed.

The process of ozone formation is exothermic and it has a negative enthalpy change. The standard molar enthalpy of formation of an oxygen atom, oxygen molecule and ozone molecule at standard temperature and pressure (25° C and 1 atm) are listed in Table 2-1 [42].

Table 2-1. Standard molar enthalpy of formation ($\Delta_f H^\circ$) of O, O_2 and O_3 [42]

Species	$\Delta_f H^\circ$ (kJ/mol)	$\Delta_f H^\circ$ (eV per molecule)
O	249.2	2.59 *eV*
O_2	0	0
O_3	142.7	1.48 *eV*

The enthalpy changes in the ozone generation processes have been calculated and are shown below:

$$O_2 \rightarrow O + O \quad \Delta H = 5.18\ e\text{V} \tag{2.18}$$

$$O + O_2 + M \rightarrow O_3 + M \quad \Delta H = -1.1\ 1e\text{V} \tag{2.19}$$

M is the third collision partner such as *O*, O_2, O_3 for an oxygen-fed ozone generator, and it absorbs the energy released in the ozone formation process. The net energy required to generate an ozone molecule can be calculated:

$$\Delta E = \frac{5.18 - 2 \times 1.11}{2} eV = 1.48\ e\text{V} \tag{2.20}$$

Based on the net energy of 1.48 eV for generating one O_3 molecule, 100% efficiency of ozone generation corresponds to a yield of 1215 g/kWh. For dissociation of oxygen by electron collision, an electron with a kinetic energy of at least 5.18 eV is required. Based on the cross-section theory, there exists an optimum electron energy range that provides a large oxygen dissociation cross-section value [43]. Fig. 2-4 shows the oxygen dissociation cross-sections measured by Cosby [44]. It shows that an electron with energy from 20 eV to 40 eV can provide a maximum cross-section value of about 0.6×10^{-16} cm^2 (mean value). Therefore, it is necessary to produce electrons with kinetic energy in the range between 20 eV and 30 eV in order to increase the dissociation rate of oxygen molecules.

2) Ozone decomposition

In gas discharges, ozone decomposition reactions take place during the discharges, and these reactions compete with the ozone generation processes. Therefore, it is necessary to prevent the ozone decomposition process as well as enhance the ozone generation process to increase

the ozone generation efficiency. The ozone dissociation equation and its enthalpy change are shown below:

$$O_3 + M \rightarrow O_2 + O + M \quad \Delta H = 1.11\,eV \tag{2.21}$$

From the enthalpy change in the ozone dissociation reaction, it can be seen that the energy required in breaking the chemical bond between the oxygen molecule and oxygen atom in an ozone molecule is 1.11 eV. In equation (2.21), the collision partner *M* is mainly an electron

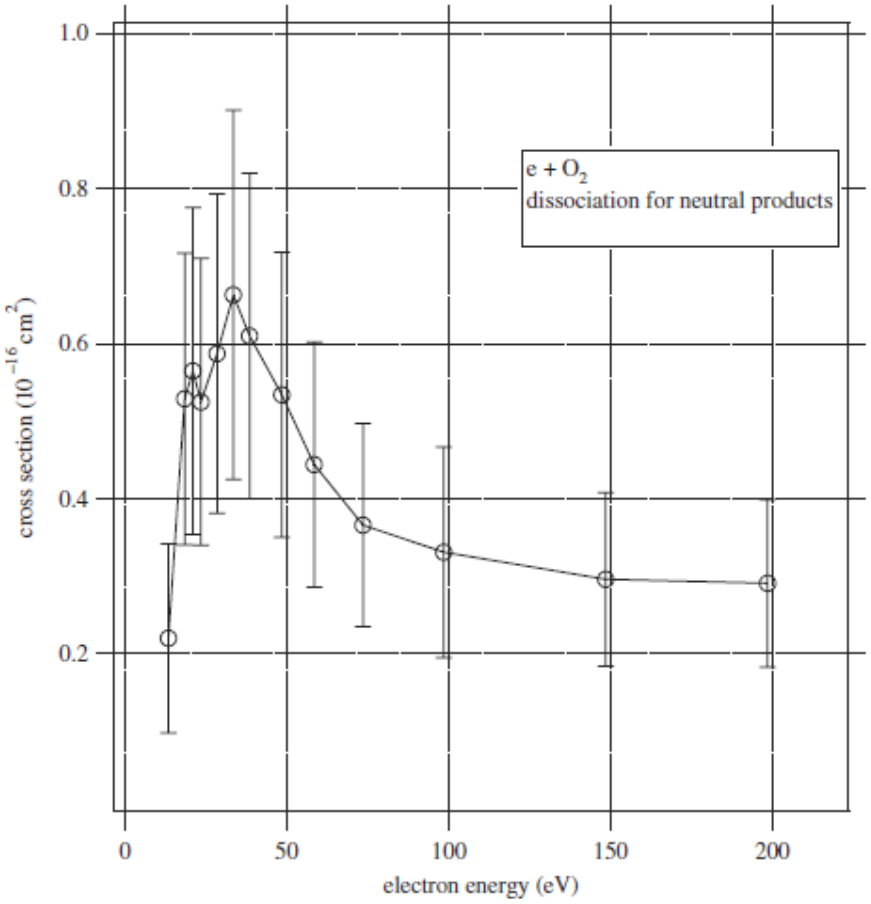

Fig. 2-4 Dissociation cross-section for the neutral products measured by Cosby [44]

or *O* atom. When electrons collide with ozone molecules, it has been found that the electrons that contribute to ozone decomposition mostly have energy between 1.06 eV to 3 eV [45, 46]. Therefore, to prevent ozone decomposition, it is necessary to reduce the kinetic energy of the gas particles (O_2 and *O*) to below 3 eV. As electrons with energy between 3 eV and 5.18 eV also do not contribute to ozone formation, the generation of electrons with energy

below 5.18 eV should be prevented. The reaction rate of the *O* atom collision with ozone, leading to ozone dissociation, is related to temperature, and it will be quantitatively presented in the following discussion.

2.5.4 Ozone Generation Efficiency Analysis

The efficiency of O_3 generation is defined as the ratio of the number of O_3 molecules produced to the total energy supplied. It depends on the efficiency of the *O* atoms formation and the conversion rate of oxygen atoms into O_3. The derivation of ozone generation efficiency is shown as below:

In an oxygen discharge with the electrical field strength *E*, the energy obtained by an electron per cm of path is given by:

$$\Delta E_e = eE \tag{2.22}$$

Assuming that the portion of energy carried by electrons is k_r, the total energy that is imparted to the discharge in the electric field per cm of path is given by:

$$\Delta E_t = \frac{\Delta E_e}{k_r} \tag{2.23}$$

In the literature, the portion of k_1 is estimated to be 0.5 in dielectric barrier discharges, because the dielectric barrier discharge is considered to be developed to the stage of the streamer discharge, where electrons and positive ions are produced evenly along the discharge columns [7, 15]. The ozone generation efficiency is calculated as:

$$\eta = \frac{N_1(O_3)}{\Delta E_t} = \frac{1}{2} \cdot \frac{N_1(O)}{\Delta E_e} \cdot C_1 \tag{2.24}$$

where $N_1(O_3)$ and $N_1(O)$ are the number of O_3 molecules and *O* atoms produced by one electron per cm of path, respectively. C_1 is the conversion ratio of *O* atoms into O_3 (the number of O_3 molecules formed per one *O* atom).

The *O* atoms are generated by collisions between O_2 molecules and electrons in the discharge space. It has been demonstrated in the reaction equations (R1a) and (R1b) that the O_2 molecules are transformed into two excited states $\mathrm{A}\,^3\sum_u^+$ (threshold energy: 6 eV) and $\mathrm{B}\,^3\sum_u^-$ (threshold energy: 8.4 *eV*), followed by dissociation. The number of oxygen atoms produced by one electron per cm of path can be calculated as below:

$$N_1(O) = 2(k_{1a} + k_{1b}) \cdot N \cdot v_d^{-1} \tag{2.25}$$

where N is the initial concentration of O_2 molecules with units of particles per cm^3, and v_d is the drift velocity of electrons with units of cm/s. The efficiency of the O atom formation process is given by the ratio of equation (2.25) and equation (2.22):

$$\frac{N_1(O)}{\Delta E_e} = \frac{2(k_{1a} + k_{1b})}{e v_d (E/N)} \tag{2.26}$$

In equation (2.26), E/N is defined as the reduced electric field, with units of *Td* corresponding to 10^{-17} V cm^2. Based on a set of electron impact cross-sections [47], Eliasson *et al* calculated the distribution of electron energy losses as a function of the reduced electric field, as shown in Fig. 2-5.

Fig. 2-5 shows that the electron energy losses are dominated by the 8.4 eV dissociation of O_2, corresponding to the process (R1b) when the reduced electric field E/N is larger than 60 *Td*. It was also calculated that about 80% of the electron energy was taken up by the O_2 dissociation processes (R1a) and (R1b), over a fairly wide range of reduced field (100 *Td* ≤ E/N ≤ 300 *Td*) [14]. This means that higher O atom formation efficiency ($n(O)/\Delta E_e$) can be achieved at the range of reduced electric field from 100 *Td* to 300 *Td*. From the reaction equations (R3) to (R6), it can be seen that not all O atoms produced are converted into O_3.

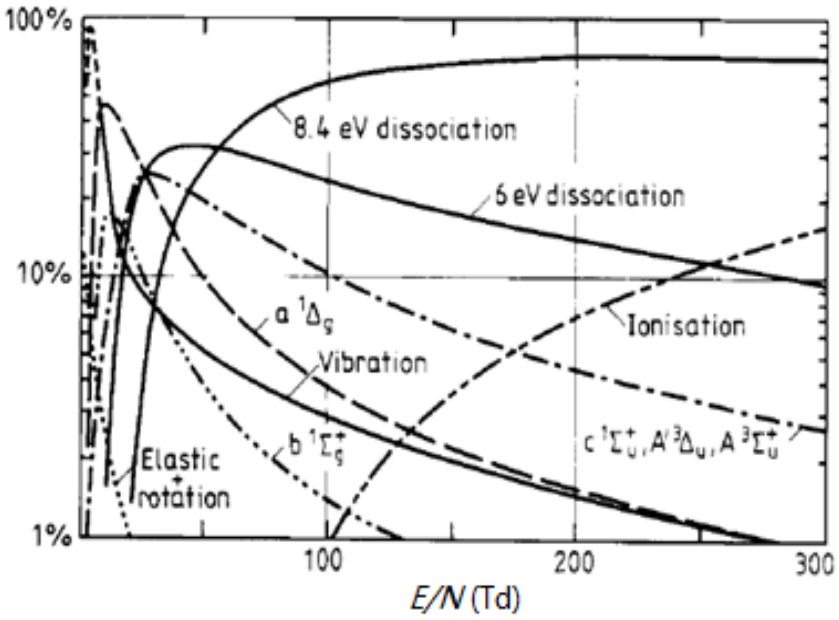

Fig. 2-5 Distribution of electron energy losses as a function of the reduced electric field: energy branching in oxygen [51]

The conversion ratio of *O* atoms into O_3 can be calculated as below:

$$\begin{aligned} C_1 &= \frac{k_3 N(O) N(O_3^*) + k_4 N(O_2) N(O_3^*)}{k_3 N(O) N(O_3^*) + k_4 N(O_2) N(O_3^*) + 2k_5 N(O) N(O_3^*)} \\ &= \frac{k_3 N(O) + k_4 N(O_2)}{k_3 N(O) + k_4 N(O_2) + 2k_5 N(O)} \\ &= \frac{1}{1 + \dfrac{2k_5 \dfrac{N(O)}{N(O_2)}}{k_3 \dfrac{N(O)}{N(O_2)} + k_4}} \\ &= \frac{1}{1 + \dfrac{2k_5 x_{10}}{k_3 x_{10} + k_4}} \end{aligned} \tag{2.27}$$

Where $N(O)$, $N(O_2)$ and $N(O_3)$ are the concentrations of *O* atoms, O_2 molecules and O_3 molecules, respectively, and x_{10} is the relative *O* atom concentration ($x_{10}= N(O)/ N(O_2)$). It is shown that the relative *O* atom concentration x_{10} determines the portion of *O* atoms that actually form O_3 molecules. The maximum conversion ratio, in which case every atom of oxygen reacts with molecular oxygen to form ozone, is obtained only if x_{10} is less than 10^{-4} [14, 15].

Substituting equation (2.27) and equation (2.26) into equation (2.24), the ozone generation efficiency is rearranged as below:

$$\eta = \frac{N_1(O_3)}{\Delta E_t} = \frac{(k_{1a} + k_{1b})}{v_d(E/N)} \cdot \frac{1}{1 + \dfrac{2k_5 x_{10}}{k_3 x_{10} + k_4}} \qquad O_3 \text{ molecules / eV} \tag{2.28}$$

As the reaction rate coefficients and the drift velocity of electrons can be obtained as a function of *E/N* by solving the Boltzmann equation [48], the ozone generation efficiency mainly depends upon the relative *O* atom concentration x_{10} and the reduced electric field *E/N*. Fig. 2-6 is the ozone generation efficiency calculation curve achieved by Eliasson *et al* [14] at different *E/N* and x_{10} - it shows that the theoretical maximum obtainable efficiency is 33%, corresponding to 0.22 O_3 molecules per eV or 400 g O_3 per kWh, which can be achieved when the *E/N* is 100 Td and the atomic concentration x_{10} is 10^{-4}. However, this theoretical maximum ozone generation efficiency curve was calculated assuming that no energy was lost to the ions in the micro-discharge pulse. Kitayama *et al* calculated the ozone generation efficiency versus *E/N*, with the portion of energy carried by electrons to be 0.55

[15]. The maximum ozone generation efficiency achieved via calculation and experimental measurement are shown in Fig. 2-7, which shows that the calculated maximum ozone generation efficiency is 230 g/kWh, based on 0.55 portion of the total energy carried by electrons, and the experimental ozone generation efficiency has a good agreement with this calculated result.

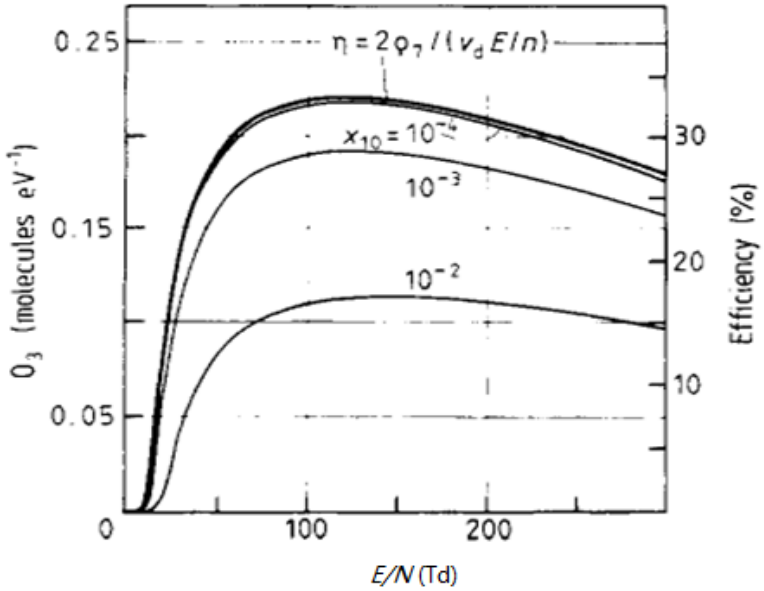

Fig. 2-6 Ozone generation efficiency as a function of *E/N* at different relative oxygen atom concentration in a micro-discharge column [14]

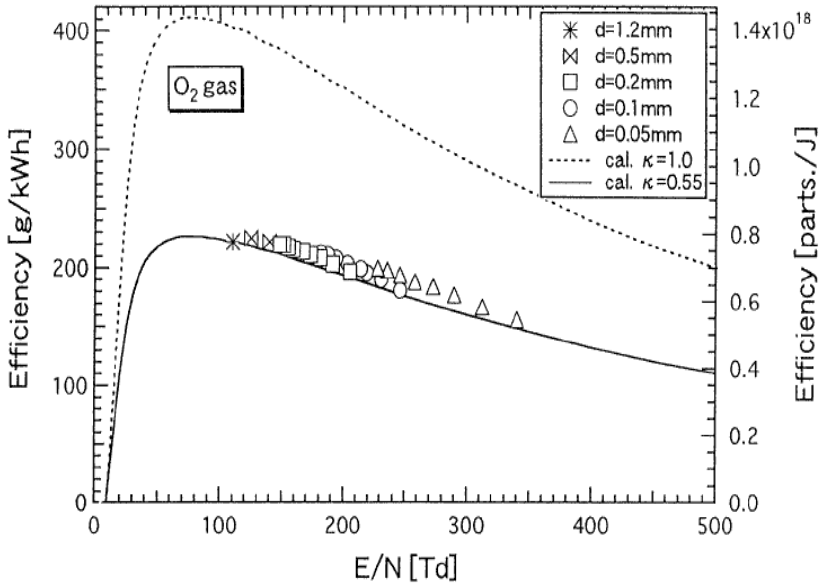

Fig. 2-7 Ozone generation efficiency as a function of *E/N* [15]

2.5.5 Temperature Effect on Ozone Generation

It is known that the reaction rate coefficient in the plasma-chemical reaction depends upon temperature. The reaction rate coefficients for ozone generation and decomposition are shown in Table 2-2.

Table 2-2 Reactions rate coefficients for ozone generation and decomposition [37]

Reaction	Reaction rate coefficients
$O + O_2 + O_2 \rightarrow O_3 + O_2$	$k_2(\mathrm{cm}^6/\mathrm{s}) = 6.9\times10^{-34}\times(300\mathrm{K}/T)^{1.25}$
$O + O_3 \rightarrow O_2 + O_2$	$k_5(\mathrm{cm}^3/\mathrm{s}) = 2\times10^{-11}\times\exp(-2300\mathrm{K}/\mathrm{T})$

Assuming ozone generation from oxygen at atmospheric pressure, the number density of oxygen molecules is 2.69×10^{19}. In addition, assuming that the oxygen atom concentration ($[O]/[O_2]$) is 10^{-4} and the ozone concentration is 500 ppm, the ozone generation reaction rate and the ozone decomposition rate at the gas temperatures of 300 K and 350 K can be calculated as below:

At 300 K:

$$\begin{aligned}\text{Ozone forming reaction rate} &= k_2 \cdot N(O)\cdot N(O_2)\cdot N(O_2)\\ &= 6.9\times10^{-34}\times2.69\times10^{19}\times10^{-4}\times(2.69\times10^{19})^2\\ &= 1.343\times10^{21}/\mathrm{cm}^3\cdot\mathrm{s}\end{aligned}$$

$$\begin{aligned}\text{Ozone decomposition reaction rate} &= k_5 \cdot N(O)\cdot N(O_3)\\ &= 2\times10^{-11}\times\exp(-2300/300)\times2.69\times10^{19}\times10^{-4}\times2.69\times10^{19}\times\frac{500}{10^6}\\ &= 3.39\times10^{17}/cm^3\cdot s\end{aligned}$$

At 350 K:

$$\begin{aligned}\text{Ozone forming reaction rate} &= k_2 \cdot N(O)\cdot N(O_2)\cdot N(O_2)\\ &= 6.9\times10^{-34}\times(300/350)^{1.25}\times2.69\times10^{19}\times10^{-4}\times(2.69\times10^{19})^2\\ &= 1.108\times10^{21}/cm^3\cdot s\end{aligned}$$

$$\text{Ozone decomposition reaction rate} = k_5 \cdot N(O) \cdot N(O_3)$$
$$= 2\times10^{-11} \times \exp(-2300/350) \times 2.69\times10^{19} \times 10^{-4} \times 2.69\times10^{19} \times \frac{500}{10^6}$$
$$= 1.01\times10^{18} / cm^3 \cdot s$$

From these calculated reaction rates, it can be seen that when the temperature increases by 50 K, the ozone decomposition reaction rate increases by 300%, and the ozone generation reaction rate decreases by 17.5%. Therefore, it is demonstrated that the increase of temperature promotes the decomposition of ozone. However, the extent of ozone generation efficiency drop with increasing the temperature depends upon the oxygen atom concentration, x_{10}, because from equation (2.28), it can be seen that the ozone generation efficiency is not only dependent on the ozone decomposition rate, k_5, but also directly dependent on the oxygen atom concentration, $x_{10.}$

Fig. 2-8 shows the influence of the gas temperature on the efficiency of the ozone generation at different oxygen concentrations. It shows that the ozone generation efficiency reduces with increasing temperature, and the extent of the ozone generation efficiency drop depends upon the oxygen atom concentration, x_{10}. It can be seen that when x_{10} is equal to 10^{-4}, the ozone generation efficiency is almost not changed when the temperature increases from 300 K to 350 K, although the ozone decomposition rate increases by three times from 300 K to 350 K. The ozone generation efficiency starts to drop from the temperature of 500 K when x_{10} is equal to 10^{-4}. When x_{10} is less than 10^{-4}, the ozone generation efficiency reduces as the temperature increases from a low value of 150 K.

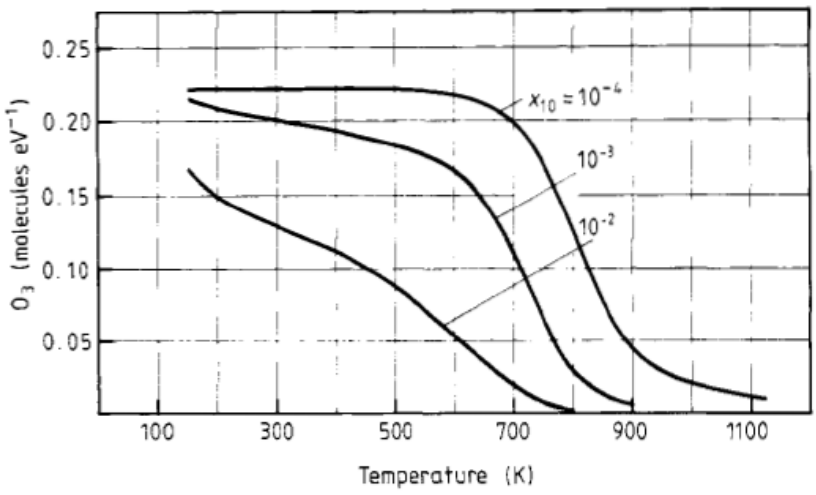

Fig. 2-8 The influence of the gas temperature on the efficiency of ozone generation [14]

It is important to prevent the temperature from rising during the ozone generation process, therefore the gas temperature inside the discharge gap of ozone generators has been investigated by some researchers [15, 49, 50]. An equation governing average gas temperature, shown in (2.29), was derived by J. Kitayama *et al* in [15],

$$T_{avg} = \frac{W/S}{3k} d + T_{wall} \tag{2.29}$$

where W is the discharge power, S is the discharge area (W/S is the discharge power density), d is the discharge gap length, k is the heat conductivity of oxygen (2.674×10^{-4} W cm^{-1} K^{-1} at 300 K), and T_{wall} is the temperature of the surface of the cooled electrode [15].

From (2.22), it can be seen that a narrow gap with a short discharge gap length d can provide lower gas temperature. In addition, based on numerical modelling [49, 50], it has been shown that the gas temperature increases along the length of the ozone generator. The reason for this is because gas particles gained energy every time a collision occurs, along length of reactor which led to higher temperature at the output of reactor. In [49], it was concluded that faster gas flow was beneficial for heat exchange in the ozone generator.

2.5.6 Humidity Effect on Ozone Generation

The humidity of the feed gas was also found to have an effect on the ozone generation performance. Rideal [51] recorded in 1920 that ozone generation efficiency could be increased by approximately 50% by using dry air rather than undried air with the dew point of 5.5 °C. In more recent data given by Sease [52], ozone generation from air at the dew point of −80 °C was found to be 50% greater than from air at the dew point of −5 °C. Up to the present time, it have been agreed that a feed gas with lower dew point can provide higher ozone generation efficiency. Humidity has a negative effect on ozone generation due to two major factors. The first factor is that the conductivity of a gas increases with increasing humidity, which results in stronger individual micro-discharges. Stronger micro-discharges provide too high a concentration of atomic oxygen (higher than 10^{-4}), which leads to a decrease in ozone generation efficiency. The other factor is that water vapour has a negative kinetic effect on ozone generation, due to the formation of OH and HO_2 radicals in plasma, leading to catalytic ozone destruction in the chain mechanism [43]:

$$OH + O_3 \rightarrow HO_2 + O_2 \tag{2.30}$$

$$HO_2 + O_3 \rightarrow OH + O_2 + O_2 \tag{2.31}$$

The typical dependence of ozone generation efficiency in an oxygen discharge on the gas humidity (dew point) is shown Fig. 2-9. The curve is still far from saturation at a dew point of about -20° C, and the efficiency of ozone generation is still growing with humidity reduction [43].

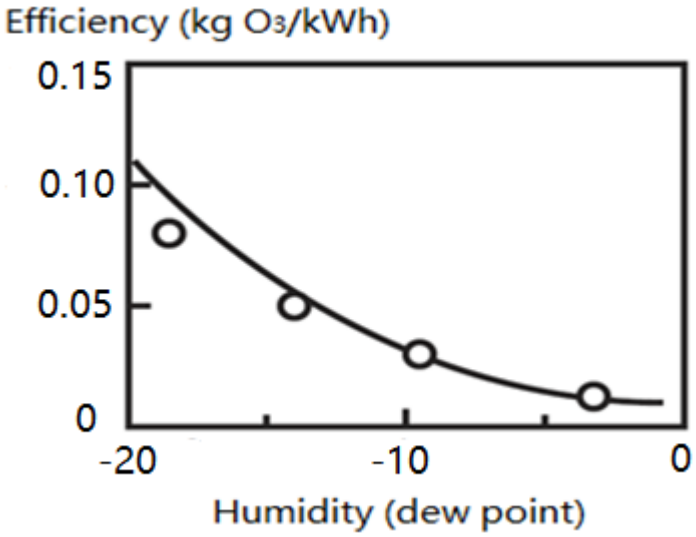

Fig. 2-9 Influence of humidity on ozone generation efficiency in a dielectric barrier discharge in room-temperature oxygen [53]

2.6 Review of Gas Discharge Theory

Gas breakdown phenomena are fundamental to ozone generation based on discharges in oxygen; therefore, gas breakdown mechanisms are reviewed in the following discussion. A gas discharge is a phenomenon observed when an electrical current flows through an ionized gas, or any process of ionization of the gas takes place, by the action of an applied electrical field [54]. The process of a gas discharge is explained as follows. When a high voltage is applied across two electrodes with a gas between them, an electrical field is formed. In the presence of this electrical field, free electrons in the gas will accelerate away from the cathode and toward the anode. In the path of an electron, it can collide with a gas molecule and transfer some of its energy to the molecule. If the energy obtained by the gas molecule is larger than its ionization energy, it will be ionized and free electrons will be produced. The new free electrons produced will follow the same collision process, then the multiplication of electrons proceeds along with their drift from the cathode to the anode, termed an electron avalanche.

The ionization coefficient α is defined as the number of electrons produced by an electron per unit length of path in the direction of the field [55]. For certain gases, known as electronegative gases, the molecules have a tendency to acquire a free electron to form a stable negative ion. The process of forming negative ions by the electron affinity of gas molecules or atoms is called electron attachment. The attachment coefficient β is defined as the number of attachments produced in the path of a single electron travelling a distance of 1 cm in the direction of the applied field [55]. When the applied voltage across the gap rises to a critical value (the breakdown voltage), where the ionisation coefficient α is equal to the attachment coefficient β, electrical breakdown occurs in the gas and an ionized state of the gas is formed.

The breakdown voltage of a uniform field gap is a unique function of the product of pressure and the electrode separation for a particular gas, as described by Paschen's law [55]. The breakdown voltage in an ozone reactor can be approximately calculated by the following equation [55]:

$$V_b = 6.72\sqrt{pd} + 24.36(pd)\ \text{kV} \tag{2.32}$$

where p is the absolute gas pressure in bar and d is the gap length in cm.

There are two gas breakdown mechanisms developed to explain the gas discharge phenomenon: the Townsend breakdown mechanism and the streamer breakdown mechanism. The breakdown mechanism developed by Townsend is a mechanism of ignition of a self-sustained discharge in a gap, controlled by secondary electron emission from the cathode [56]. The secondary electron emission in this mechanism is due to ions impacting the cathode. The theory explains well a great number of discharges observed at low pressure, approximately at pd < 200 Torr cm, but it fails at high pd and high overvoltage. It was found that at high pd, the breakdown in the gap developed much faster than that predicted by the Townsend mechanism. Another breakdown mechanism called streamer breakdown was developed by Loeb [57], Raether [58] and Meek and Craggs [59]. The theory is based on the concept of the growth of a thin ionized channel (streamer) between the electrodes, and it successfully explains discharge phenomena observed at pd > 4000 Torr cm, which cannot be explained by the Townsend mechanism [54]. While the two mechanisms are different, both start with an electron avalanche. Steamers are produced by an intensive primary avalanche if the space charge associated with this avalanche is high enough to create an electric field with strength of the order of the applied field. Electrons of numerous avalanches are pulled into the positive space charge trail left by the primary intensive avalanche, which leads to the formation of an ionized channel that bridges the electrodes.

The electrical gas discharge is the fundamental basis of plasma-chemical systems. Plasma is an ionized gas that includes electrons, ions and neutral particles, but shows almost zero net charge. Plasma-chemical systems are generally divided into thermal plasma and non-thermal plasma. In thermal plasma, also known as equilibrium plasma, electrons and heavy particles have a single high temperature. In non-thermal plasma, also known as non-equilibrium plasma, the electron temperature significantly exceeds that of heavy particles. Thermal plasma discharges have applications such as plasma torches and arc welding, in which the electron and neutral gas temperature exceed 3000 °C [60]. Non-thermal plasma discharges can provide electrons, ions and radicals that can initiate plasma-chemical reactions at a relatively low temperature [61], which is beneficial for ozone generation. Before a discussion on the elementary ozone generation in the plasma discharge, the fundamental parameters in the plasma-chemical process are first described.

2.6.1 Collision-energy Transfer

Electrons drift under the action of an applied electrical field, and when they collide with gas particles, part of the kinetic energy of the electron is converted into potential energy of the struck particle. According to the laws of energy and momentum conservation, the following equations can be obtained:

$$\frac{1}{2}mu_0^2 = \frac{1}{2}mu_1^2 + \frac{1}{2}MV^2 + W_p \tag{2.33}$$

$$mu_0 = mu_1 + MV \tag{2.34}$$

where m is the mass of the electron, M is the mass of the struck particle, u_0 is the initial velocity of the electron, u_1 is the velocity of the electron after the collision, V is the velocity of the struck particle after the collision, assuming that it was at rest before the collision, and W_p is the increase in potential energy of the struck particle. The maximum energy transfer for two colliding particles can be calculated based on equations (2.33) and (2.34), which is as shown below [55]:

$$W_{p\max} = \frac{M}{m+M}\frac{mu_0^2}{2} \tag{2.35}$$

For an electron, $m \ll M$, which means that almost all of the electron kinetic energy, $mu_0^2/2$, can be converted into potential energy. To cause ionization of the atom or molecule, the incoming electron must have a kinetic energy higher than the ionization potential. To cause

dissociation of the molecule, the incoming electron energy must be larger than the chemical bond energy between the atoms of molecule.

2.6.2 Electron Energy and Reduced Electric Field

For the electron energy, it is impossible to calculate the energy of a single electron, and usually a distribution function, $f(\varepsilon)$, is used to describe the probability density for an electron to have energy between ε and $\varepsilon + \Delta$ divided by Δ. The electron energy distribution function is usually given by the quasi-equilibrium Maxwell-Boltzmann distribution [37]:

$$f(\varepsilon) = 2\sqrt{\frac{\varepsilon}{\pi(k_B T_e)^3}}\exp(\frac{-\varepsilon}{k_B T_e}) \tag{2.36}$$

where k_B is the Boltzmann constant and T_e is the electron temperature.

Taking the first moment of the distribution function, the mean electron energy is shown as below:

$$\langle\varepsilon\rangle = \int_0^\infty \varepsilon f(\varepsilon) d\varepsilon = \frac{3}{2} k_B T_e \tag{2.37}$$

The reduced electric field is defined as the electric field divided by the gas density, represented as *E/N*, with units of Td (10^{-17} Vcm^2). *E/N* is an important parameter in plasma discharges, which determines the mean energy of the electrons [54]. The relation between the mean energy of an electron and the reduced electric field *E/N* is shown as below [43]:

$$\langle\varepsilon\rangle = \frac{3}{2} k_B \cdot (\frac{E}{N}) \cdot \frac{e}{\langle\sigma\rangle}\sqrt{\frac{\pi}{12\delta}} \tag{2.38}$$

where δ is a factor that characterizes the fraction of an electron's energy lost in a collision with a neutral particle. It is worthy of note that the linear relation between electron mean energy and the reduced electric field is only a qualitative one, and this relation is more complicated in reality [37, 43].

2.7 Industrial Ozone Generation Based on Electrical Discharges

2.7.1 Historical Ozone Generation Technology

Ozone was firstly generated using dielectric barrier discharges by W. V. Siemens in 1857 [2]. The ozone generator developed by Siemens consisted of two glass tubes. One glass tube was coated externally and the other was coated internally with a tin foil. The air feed gas was passed through the annular space between the two tubes. Ozone was generated when the air gas broke down by the application of AC high voltage. This ozone generator was the prototype of modern industrial large-scale ozone generators. Since 1857, ozone generation based on gas discharges has attracted the attention of more and more researchers. The effect of gas temperature on ozone generation performance was identified in the 1880s. Ozone generation under low temperature was investigated by Hautefeuille and Chappuis [62], who successfully obtained concentrations of 14.9% by weight of ozone at 0 °C, and 21.4% at −23 °C. High concentration ozone (350 g/Nm^3) can be achieved at −23°C due to the low ozone decomposition rate.

The development of large-scale ozone generators was continuously driven by the water treatment industry. In order to enhance the ozone production, increasing the number of discharges is important. Increasing the amplitude of applied voltage or increasing the energization frequency of voltage both results in an increase of the number of discharges. However, higher voltage adds more stress on the dielectric layer of DBD, so raising the frequency of AC power supply with a relative low voltage was considered be superior in large-scale ozone production. High-frequency (10 kHz) power supplies were first introduced into ozone generators by the Siemens Company in the 1930s, which greatly increased the ozone generator power capacity. Using a high-frequency power supply, high concentrations of ozone were achieved, but with low generation efficiency. It was reported by Kozhinov [63] that this model could only generate 8 mg/l of ozone, with an efficiency of 35 g/kWh. This ozone generator was not very successful because of its fragility and the requirement of a 50 Hz to 10 kHz converter set [18]. In the 1980s, with the development of power electronics technology and new dielectric materials, there was a major breakthrough in ozone technology in the United States and Canada. The ozone generator became more compact and provided a high power density at lower voltage, by using a high-frequency AC power supply. Ozone generators operating in modern medium frequency regimes (a few hundred Hertz) were successfully installed and operated in the Los Angeles Aqueduct Filtration Plant

[13], providing 10,000 kg ozone per day to treat two million cubic meters of drinking water per day.

In addition to the electrical gas discharge, ozone was also historically generated by other methods including UV radiation and electrolysis. However, these two methods are both inefficient for large-scale ozone generation. In photochemical reactions, the ozone generation efficiency depends upon the percentage of light for dissociation of oxygen (λ<242 nm) and for dissociation of ozone (200 nm < λ <254 nm). Practically, it is very difficult to produce light at shorter wavelengths to generate ozone without the simultaneous production of the longer wavelengths that cause photolysis of ozone. Therefore, UV radiation has rarely been used for industrial ozone generation. In the past twenty years, a narrow-band UV radiation at 172 nm, generated by a xenon excimer based on a dielectric barrier discharge, has been researched by B. Eliasson *et al*, and this method was found that to be very efficient for ozone generation [64]. However, this method is limited to small-scale ozone generators. Electrolysis of water is an electrochemical method for the ozone generation. By applying electric power to the water (H_2O), water is split into its basic elements and then part of the liberated oxygen is converted into ozone. Electrolytic ozone generator has also been investigated by many researchers in the past years since ozone was first discovered [65-68]. To date, however, the electrolytic process has only been tested in small cells of 1-5 m^3 electrode area [18]. Commercial electrolytic ozone generators are rare due to the low power efficiency.

2.7.2 Non-thermal Discharges for Ozone Generation

As non-thermal plasma discharges are highly effective in promoting electron-impact dissociation, excitation and ionization of background gas molecules, while keeping the gas at a low temperature, they have been widely used in ozone production. From the literature, ozone is mainly generated via the following non-thermal discharges:

- Dielectric barrier discharges
- Pulsed corona discharges

A. Dielectric Barrier Discharges

Dielectric barrier discharges (DBDs), also referred to as silent discharges, are characterized by placing at least one dielectric layer in the current path between two planar or cylindrical electrodes. Common DBD electrode configurations are shown in Fig. 2-10. The discharge

gap has a typical gap length from 0.1 mm to several centimetres, depending upon the application.

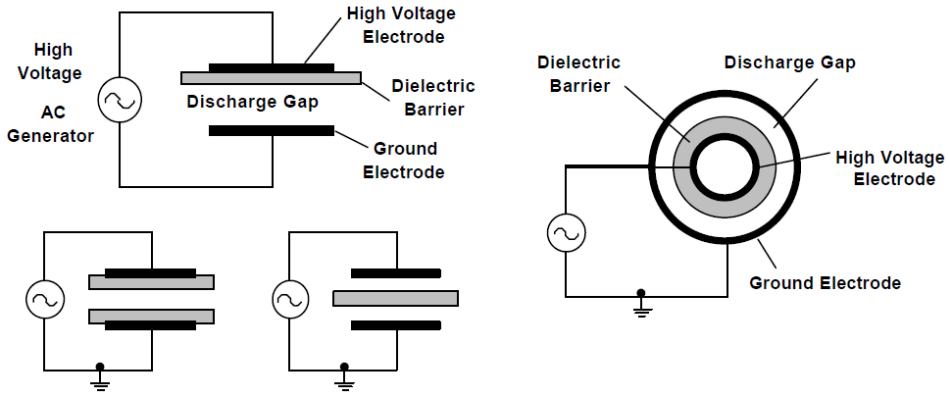

Fig. 2-10 Common dielectric-barrier discharge electrode configurations [69]

Dielectric barrier discharge is the most common method of ozone generation in industry. Gas spaces bounded by one or two dielectrics have practically the same breakdown voltage as if they were between metal electrodes. Because of the presence of the dielectric, only AC voltage or pulsed voltage can be applied to the electrodes. Typical gap length in the ozone reactor are from 0.5 to 5 mm [70]. With narrow gaps, the electrical field at breakdown can be strongly influenced by varying the gap spacing or the particle density in the gap [70]. The choice of gap length is a compromise between reducing the gap breakdown voltage and increasing the discharge volume for ozone formation. In addition, low-loss dielectrics of high breakdown strength such as glass, quartz or ceramic plates or tubes are used in DBDs, with the outer surface of the dielectric in contact with a metallic electrode [13].

Fig. 2-11 shows a schematic diagram of a typical DBD reactor for ozone generation.

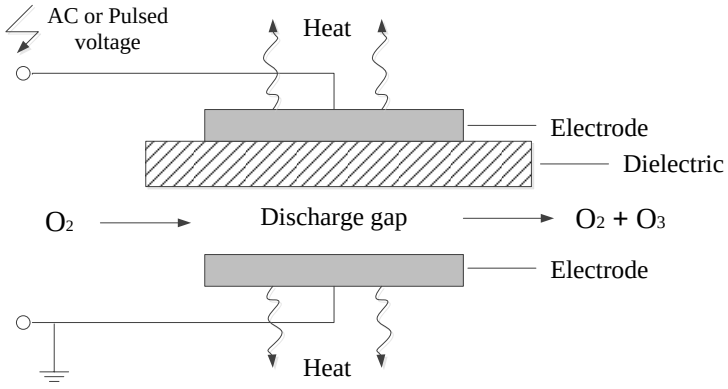

Fig. 2-11 Typical electrode configuration of the dielectric barrier discharges

A feed gas of oxygen or air flows through the discharge gap, with a high voltage applied across the electrodes. When the applied voltage rises to the gas breakdown value, there will be a large number of randomly-distributed micro-discharges, with duration of the order of nanoseconds, in the discharge gap. Fig. 2-12 shows a Lichtenberg figure, obtained by exposing photographic plates to the action of the discharge for about 1 ms, which enables charge patterns on a dielectric surface (the footprint of individual micro-discharges) to be visualised [70].

Fast image intensifiers reveal that each micro-discharge consists of a cylindrical current filament of about 0.1 mm radius in the discharge gap, which spreads into a surface discharge at the dielectric boundary [13]. Due to the charge accumulation on the dielectric, the electric field at the location of micro-discharges is reduced within a few nanoseconds of breakdown, which results in the termination of the current flow at this location. As long as the external voltage is rising, additional micro-discharges will occur at new positions, because the presence of accumulated charge on the dielectric reduces the electric fields at positions where micro-discharges have already occurred. When the applied voltage is reversed, the next micro-discharges will form at the locations of previous micro-discharges [13, 71]. The dielectric barrier limits the charge and energy deposited in a micro-discharge and distributes the micro discharges over the entire electrode surface [13, 70]. The typical properties of micro-discharges with a 1 mm air gap at 1 bar are summarised in the Table 2-3 [13, 14].

Fig. 2-12 Photographic Lichtenberg figure of micro-discharges taken in air [70]

Table 2-3: Typical parameters of micro-discharges with 1 *mm* air gap at 1 *bar*

Duration: 1-10 ns	Total Charge: 0.1-1 nC
Filament Radius: about 0.1 mm	Electron Density: $10^{14} – 10^{15}$ cm^{-3}
Peak current: 0.1 *A*	Mean Electron Energy: 1- 10 eV
Current Density: 100-1000 A/cm^2	Gas Temperature: close to ambient temperature

Compared with other non-thermal discharges, dielectric barrier discharges can produce highly non-equilibrium plasma in a controllable way, at atmospheric pressure and at moderate gas temperatures [72]. A DBD reactor has great flexibility with respect to its operational conditions, such as the range of applied voltages and gas pressures. Therefore, it is possible to achieve a wider range of reduced electric field to optimize the elementary electron collision process, compared with the DC corona discharge. Also, high discharge power can be achieved easily by using a high-frequency AC power supply (usually between 500 Hz and 5 kHz) to increase the concentration of ozone produced. Experimental DBD reactors can readily by scaled-up to large, industrial-scale ozone generators.

As DBDs have great advantages in ozone generation and other industrial applications such as excimer lamps, it has been studied by many researchers for many decades. In 1932, Buss discovered that DBDs in the air occurred as a large number of tiny, short-lived, current filaments [73]. The first photographic traces (Lichtenberg figures) of these micro-discharges and the oscilloscope waveforms of current and voltage were first achieved in his work. In 1943, T. C. Manley proposed a method for calculating the discharge power of DBDs by using a Lissajous figure [74]. Since then, the electrical characteristics of the micro-discharges associated with DBDs have been investigated by many researchers. The two-dimensional spatial distribution of micro-discharges in atmospheric-pressure DBDs in air was studied by Chirokov *et al.* In this work [75], the authors obtained micro-discharge images (Lichtenberg figures) by using photostimulable phosphors. In recent 20 years, with the aid of a high-speed ICCD camera, the spatial-temporal development of micro-discharges was studied by Kettlitz *et al.* [76]. The current of a single micro-discharge was measured and investigated by Eliasson *et al.*[14], by Heise *et al.* [77] and by Murata *et al.* [78]. All the results from their work showed that single micro-discharges generated a current impulse with duration of the order of nanosecond. The charge transferred by micro-discharges was measured experimentally by Drimal *et al.* [79, 80]. They claimed that the average charge

transfer of one series of micro-discharges increased with an increase of the gap voltage, and also increased with an increase of the gap length. In order to model the equivalent electrical circuit of a DBD, Chiper *et al.* [81] and Naudé *et al.* [82] used variable resistors to represent micro-discharge channels. Shuhai. Liu *et al.* represented the micro-discharge as a current source and derived an electrical model of a DBD under an arbitrary excitation voltage [83]. The discharge mode of DBDs has been investigated by researchers over the past 30 years, including the work from Kanazawa *et al.* [84] and Okazaki *et al.* [85] from Japan, Tepper *et al* [86] and Kozlov *et al.* [87] from Germany, and Ráhel *et al.* [88] from USA. The literature on the discharge mode of the DBDs was extensively reviewed by Kogelschatz [71]. Based on the work from these researchers, it is known that there are mainly two type of DBD discharge mode, filamentary mode and homogeneous (or diffuse) mode. A DBD usually exhibits filamentary behaviour at atmospheric pressure, but the homogeneous mode can be achieved when: helium dilution gas is used; pulsed power is employed; or a mesh high-voltage electrode is applied.

In the past 50 years, the research of the ozone generation based on DBDs has been contributed by many researchers such as Yagi *et al.* from Japan [7], Pietsch from Germany [89], Kogelschatz and Eliasson [1, 9, 14] from ABB in Switzerland, and by Kitayama *et al.* from Japan [15]. The mechanism of ozone formation in DBDs was mainly researched in [7, 14, 15]. From their research, it was known that a single micro-discharge resulted in a current pulse with tens of nanoseconds duration. They reported that oxygen dissociation was very fast and completed at the end of the current pulse, while the ozone formation was finished after about 10 microseconds. During the micro-discharges, Yagi *et al*. and Eliasson *et al.* both considered that half of the energy dissipated in the micro-discharge was consumed by ions, while Kitayama *et al.* considered that the portion of the energy consumed by ions in the micro-discharge was 0.55. Apart from the portion of the energy loss to the ions, another important parameter affecting the ozone generation efficiency in DBDs, claimed by Eliasson *et al*., is the oxygen atom concentration. They claimed that 10^{-4} was the optimum oxygen atom concentration for the ozone generation. The effect of the discharge mode of DBDs on the ozone generation efficiency was investigated by Okazaki *et al* [90]. In their work, it was reported that the ozone formation efficiencies in the homogeneous discharge were 10% higher than the values found in the filamentary DBD in air, and 15% higher in oxygen. It was explained that this increase was attributed to better collision efficiency among electrons and molecules, and to a lower increase in temperature than in discharge filaments of a silent electric discharge [90]. However, the rates of increase of ozone formation efficiencies

decreased at higher applied voltage (above 10 kV) at the 1.5 mm gap distance, and the reason was not clear. In recent years, DBDs with a mesh electrode for ozone generation were researched by Z. Buntat *et al.* [91]. They produced atmospheric pressure glow discharges by using a perforated-aluminium plate and fine-mesh stainless steel electrodes with a mica sheet as a dielectric barrier, and they concluded that the perforated-aluminium plate discharge system provided better glow discharge stability, which may be an effective means for improving the ozone generation efficiency. However, there is no ozone performance data provided in their work [91]. Nakai *et al.* also investigated the effect of the DBD discharge mode on ozone generation [92]. In their research, it was reported that, with the same specific input energy, the ozone generation efficiency under filamentary mode (247 g/kWh) in pure oxygen was much higher than that under homogeneous mode (33 g/kWh) in pure oxygen. The authors claimed that in the case of the homogeneous mode, the electrons cannot get enough energy to dissociate O_2 efficiently. To date, there is no definitive proof as to whether filamentary mode or homogeneous mode is better for ozone generation.

DBD reactors were historically energized by 50 Hz AC power, but with the development of power electronics in the last twenty years, an inverter-based *L*-*C* resonant circuit [93-96] has been employed as a high-frequency AC source for industrial DBD reactors. Since DBD-based ozone generator is characterised by a capacitive load, the series or parallel inductor in the circuit compensates the reactive power consumed by the DBD load, which greatly improves the efficiency of the power supply. Also, power density modulation (PDM) and pulse width modulation (PWM) techniques involved in the inverter allow digital control of the dissipated power of DBDs, which makes ozone concentration and ozone production readily adjustable.

DBDs can also be driven by pulsed voltages. Pulsed DBDs have some advantages over AC continuous discharges, such as preventing adverse temperature increase, limiting the energy loss to the ions, and increasing the reduced electric field of the discharge gap. Pietsch *et al.* found that a spatial homogeneous discharge occurred when pulsed voltage was applied to a DBD reactor [97]. It was explained that with rising reduced electric field, the number of avalanches starting from the cathode at the same time increased, and the discharge became more homogeneous due to overlapping of the heads of the avalanches. Liu *et al.* investigated the ozone generation efficiency under energization of DBDs by unipolar, sub-microsecond square pulses [98]. From their experimental result, it was found that micro-discharges only occurred on the rising edge and falling edge of the square pulse, that is, when the voltage is changing. The authors claimed that ozone generation efficiency under the energization of

unipolar square pulses improved by 30% compared with that when energized by AC sinusoidal voltage with same frequency of 2 kHz. However, Mericam-Bourdet *et al.* reported that the voltage waveform, sine wave or pulsed, has no influence on the ozone production by DBDs [99]. They considered that the duration and the peak of the micro-discharge current was self-controlled by the charge deposited on the surface of the dielectric, and that reduction of the pulse width has no effect on the micro-discharge, therefore the influence of the pulsed power supply on the ozone generation in DBDs was insignificant.

B. Pulsed Corona Discharge

A pulsed corona discharge is a discharge initiated by a short, high-voltage pulse in a highly non-uniform field geometry, such as a coaxial wire-to-cylinder arrangement [100], or a spiral wire-cylinder arrangement [101]. Such discharges have been investigated as an alternative method of ozone generation. The typical reactor configurations for a pulsed corona discharge are shown in Fig. 2-13. Pulsed corona discharges have advantages over DC corona discharges, because high voltage above the critical DC sparking voltage can be applied to the discharge gap without causing spark breakdown. Therefore, highly-energetic electrons can be generated, which is beneficial for *O* production in an ozone reactor. Also, a short pulse is effective to decrease the energy wasted via transfer to ions, since ions will be almost stationary if the duration of the applied pulse voltage is much shorter than the ion drift time. As less energy is thus transferred to ions and neutral gas molecules, the heat dissipation will be reduced, and a cooling system can be obviated [101].

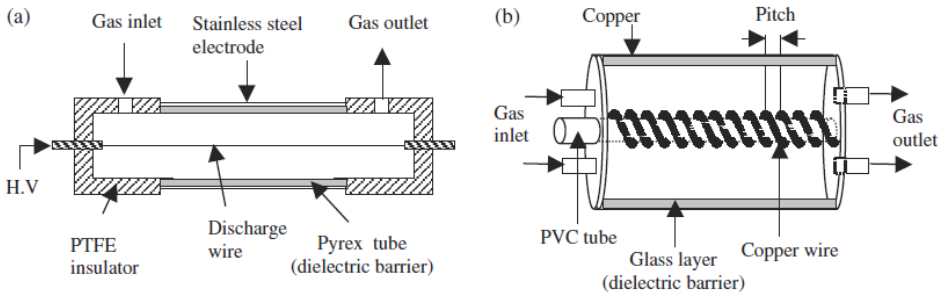

Fig. 2-13 Reactor configuration of pulse corona discharge (a) coaxial wire-cylinder and (b) spiral wire-cylinder [102]

A wire/cylinder pulsed ozone reactor was researched mainly by two groups, Chalmers *et al*. from the University of Strathclyde, and Samaranayake *et al*. from Kumamoto University. In the work of Chalmers *et al.* [10], a very fast pulse, with a rise time less than 5 ns and a pulse width of 40 ns, was applied to a wire/cylinder reactor, without a dielectric layer, for ozone generation. The results from [10] show that the radius of the inner electrodes has little effect on the ozone generation rate, for a given voltage. It was explained by Chalmers *et al.* that the ozone generation was not only influenced by the intensity of the corona, which increased as the radius of the inner electrode decreased, but also by the volume of the corona discharges, which increased as the surface area of the high-voltage electrode increased. The compensation of these two effects meant that the efficiency of ozone generation had no dependence on the dimensions of the inner electrode. In other work by Chalmers *et al* [100], the effect of the pulse width on ozone generation was investigated. It was claimed that the ozone generation efficiency was a constant value of around 100 g/kWh for pulses of width in excess of 80 ns, but the efficiency continuously increased as the pulse width was reduced below 80 ns, reaching a value of around 300 g/kWh with a 20-ns-wide pulse [100]. Fig. 2-14 shows the ozone generation efficiency versus the pulse width from the work [100].

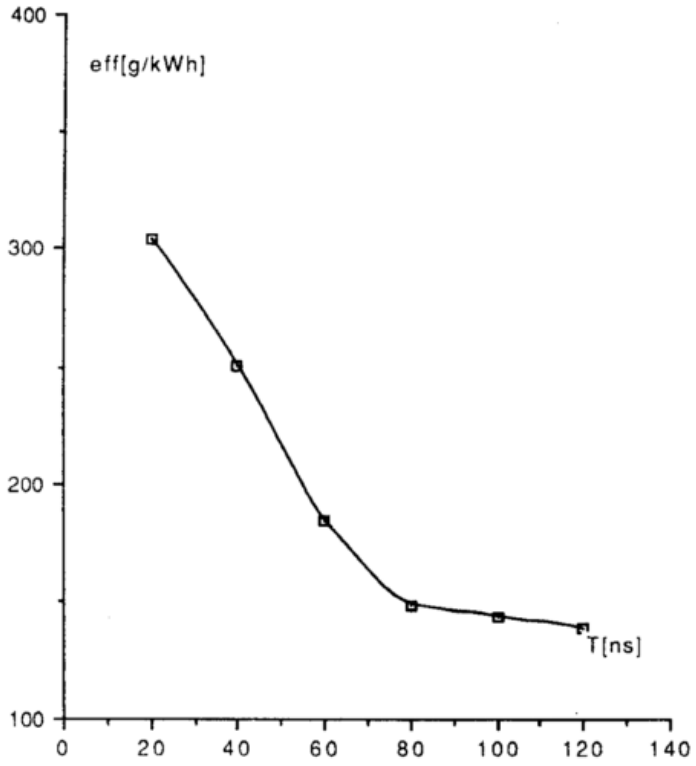

Fig. 2-14 Ozone generation efficiency versus pulse length [100]

However, due to the time required for the creation of atomic oxygen, and the statistical time lag required for the appearance of a primary electron to initiate the corona discharge, the authors found a limit for the pulse width for increasing the ozone generation: it was found that the ozone generation efficiency significantly decreased when the pulse width was 10 ns [100].

Samaranayake *et al.* also researched pulsed power energisation regimes for ozone generation [101, 103-105]. The authors investigated the ozone generated by a pulsed streamer discharge in a spiral wire-to-cylinder arrangement, with and without a dielectric layer. It is worthy of note that the pulsed streamer discharges described by Samaranayake *et al.* corresponds to the same discharge mechanism as a pulsed corona discharge but with a different name, because in the development of the pulsed corona discharge, the field adjacent to the inner electrode can be so high that the electron avalanche transforms into a streamer within a very short distance from the electrode [106]. Samaranayake *et al* researched the ozone concentration and generation efficiency through the variation of the pulse peak voltage, pulse repetition rate and the gas flow rate. They concluded that the ozone generation efficiency was strongly dependent upon the concentration of the ozone generated, and therefore on the applied voltage, pulse repetition rate and gas flow rate. They claimed that the highest ozone generation efficiency of 202 g/kWh (ozone concentration: 4700 ppm) was achieved using an oxygen-fed reactor with a dielectric layer, at the low pulse repetition rate of 25 pps, and with the (positive) peak voltage of 39 kV.

H. Tamaribuchi *et al*. investigated the ozone performance based on different pulse widths of 50 ns, 100 ns and 200 ns [107]. They found that the input energy into the discharge per pulse was increased with increasing pulse width, but the ozone concentration was not raised, which resulted in higher ozone generation efficiency at the shorter pulse width of 50 ns; the maximum ozone generation efficiency obtained in this work was 73 g/kWh. F. Fukawa *et al.* used a very short (FWHM) pulse with of ~1 ns to generate a pulsed corona discharge based on a wire-to-cylinder reactor, and the maximum ozone generation efficiency achieved was 190 g/kWh [108].

2.8 Conclusion

The background of ozone generation technology, ozone properties and ozone applications, have been comprehensively reviewed in this chapter. The main chemical kinetics associated with ozone generation were presented, followed by a discussion of the energy balance during ozone formation. Following the analysis of the physical process of ozone generation, theoretical methods to improve the ozone generation efficiency were discussed. The factors affecting the ozone generation efficiency are described as follows. Ozone generation efficiency strongly depends on the micro-discharge strength. The lower limit of micro-discharge strength in a DBD is related to electrons not having sufficient energy to dissociate oxygen molecules, and the upper limit is related to the chemical kinetics of ozone production. Minimising the energy lost to ions is important, as ionic reactions do not contribute to ozone generation. Increasing the proportion of high-energy electrons (>20 eV) can benefit oxygen dissociation, while simultaneously reducing the rate of ozone dissociation by electron collisions. Reduced electric field, *E/N*, in the range between 100 Td to 300 Td, is claimed to be optimal for ozone generation, based on a review of the literature. The concentration of atomic oxygen is the most important parameter in the chemical reactions facilitating ozone generation. When the atomic oxygen concentration is below 10^{-4}, most of these oxygen atoms contribute to the ozone formation, but when the concentration of atomic oxygen exceeds 10^{-4}, the ozone dissociation rate increases significantly. Restricting the concentration of the reactive oxygen atoms to below 10^{-4} can be achieved by optimizing the energy density of the micro-discharges. In addition, temperature and humidity both have a significant effect on ozone generation. Preventing increase of the temperature and maintaining a low dew point ($<-40\ ^{\circ}C$) of the feed gas are beneficial to ozone generation.

Following from the theoretical analysis of the ozone generation process, the development of industrial-scale ozone generation technology was also traced. A comprehensive review of the published literature on non-thermal discharges for ozone generation, DBDs and pulsed corona discharges, was conducted. Dielectric barrier discharges have two types of discharge mode, the filamentary mode and the homogeneous mode. The homogeneous DBD mode can be obtained at atmospheric pressure by using helium dilution gas, mesh electrodes, or pulsed energization mode, but this mode was not as efficient for ozone generation as the filamentary mode, based on the literature data [92]. The micro-discharge behaviours of DBDs have been studied by many groups, but measurement and characterisation of these random transient discharge current pulses is still a challenge for researchers. The energization modes of DBDs, AC sinusoidal voltage and pulse voltage, are reviewed and compared. The

advantages of pulsed dielectric barrier discharges, such as preventing the temperature increase and limiting the energy loss to the ions, were claimed in the literature, but there is also an opinion that voltage waveforms of DBDs have no influence on the ozone generation efficiency. Pulsed corona discharge is a promising method for low-concentration ozone production (below $10\ g/Nm^3$), but due to its low power consumption, pulsed corona discharge is not practical for large-scale industrial ozone generation. Therefore, in the present study, only dielectric barrier discharges for ozone generation are experimentally studied, and the experimental results are presented and discussed in the subsequent chapters.

3 EXPERIMENTAL SYSTEMS AND METHODOLOGIES

3.1 Introduction

This research project is focused on dielectric barrier discharges for ozone generation. Initially, a reliable pneumatic control system was designed and developed, which provided the possibility to investigate ozone generation under different gas flow rates and gas pressures. In order to study the electrical characteristics of DBDs and the ozone performances under different experimental conditions, different test cells were designed and developed for different experimental studies, as presented in the following chapters. In terms of the power energization system, four different power supplies were used, as listed below:

- 50-100 Hz AC power source
- 20-5,000 Hz linear AC power source
- High frequency power source (2.6 kHz and 20 kHz) based on series resonant circuit
- Pulsed power supply

Different power sources were employed to investigate the ozone generation performance in this research project and the results were compared, which will be demonstrated and discussed in the following chapters. The advanced electrical and optical measurement devices used to diagnose electrical and optical signals in the experiments are described in this chapter. The ozone concentration measurement principle and ozone generation efficiency calculation process are also included in this chapter.

3.2 Gas Handling System

A reliable gas handling system was important for ozone generation experiments, and it was designed and developed at the initial stages of this project. A schematic diagram of the gas handling system developed is shown in Fig. 3-1. The gas handling system consists of two main parts: a compressed oxygen cylinder and a pneumatic control board. As can be seen from Fig. 3-1, the compressed oxygen cylinder is connected to the pneumatic control board

by using a PVC tube with an outer diameter (OD) of ¼ inch, providing a feed gas of oxygen with a purity of 99.5% and a dew point of -40 °C.

The body of the pneumatic control board was made of PVC, and different equipment with different functions was mounted on the board. The details of the equipment and their functions were listed in Table 3-1. Due to the strong oxidation capability of ozone, stainless steel 316 or PTFE should be chosen for the construction of the ozone flowing path. In this work, all the gas flowing path in the gas board were made up of stainless steel 316. Once the ozone generated had been measured, an ozone destructor (ozone catalyst) was used to destroy the off-gas for safety.

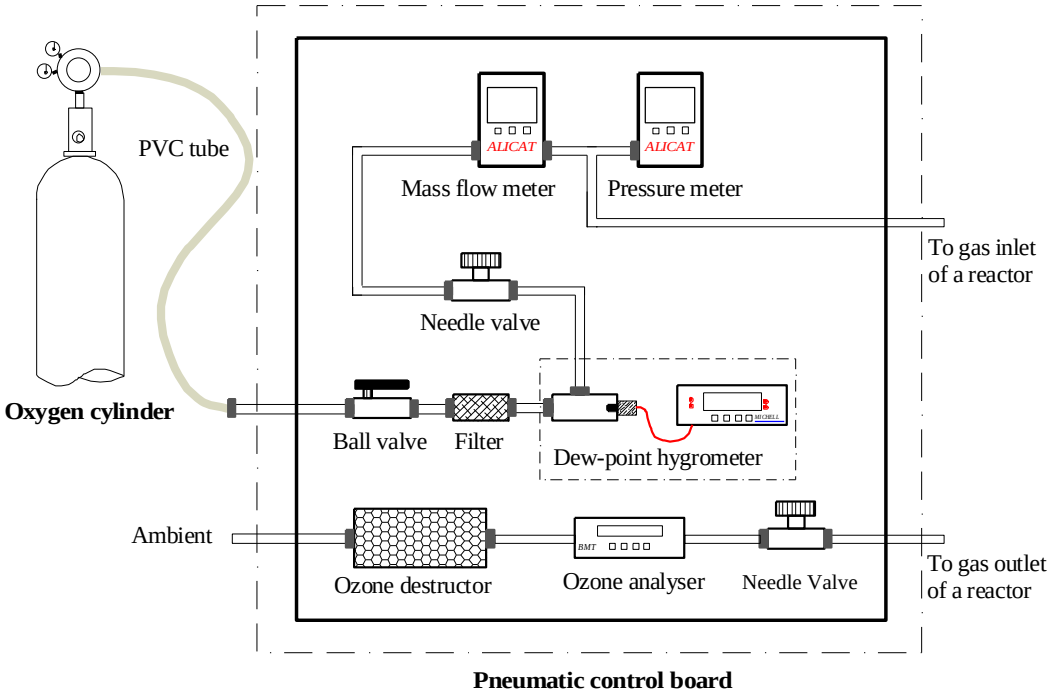

Fig. 3-1 Gas handling system for the ozone generation

A pneumatic control board was developed to control the pressure of a sealed vessel. As can be seen from Fig. 3-2, a compressed gas cylinder and a vacuum pump were both connected to a manifold though an on/off ball valve. The vacuum pump could provide an ultimate vacuum pressure of 1 mbar absolute, and was used to evacuate the reactor before injecting pure oxygen gas for the experiment. A pressure gauge was connected to the manifold to measure the vessel pressure. An exhaust port was connected to the manifold through a ball

valve and all exhaust gas was vented to atmosphere though this port when the ball valve was on. The connection ports in the board and the gas tube all have an outer diameter of 6 mm. This gas board was also used to adjust the breakdown voltage of a gas-filled triggered switch by controlling the gas pressure inside the switch.

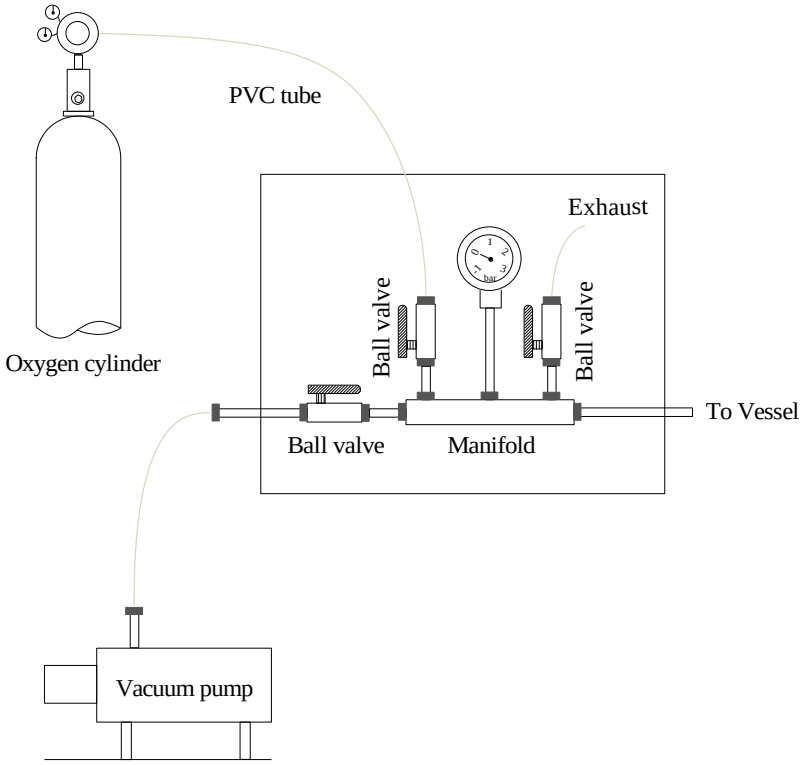

Fig. 3-2 Gas handling system for controlling the pressure in a vessel

Table 3-1: Details of equipment in the pneumatic control board

Name	*Manufacturer(Part name)*	*Function*	*Measurement range*	*Resolution*	*Accuracy*
Stainless steel tube	NERO ((¼ inch OD)	Gas flow connection	-	-	-
Ball valve	HOKE	Turn on/off of the feeding gas	-	-	-
Filter	HOKE	Filter the feeding gas	-	-	-
Hygrometer	MICHELL Instruments (Easidew Online)	Gas dew point measurement	-100°C dp - 20°C dp	0.1°C	±2°C
Needle valve	HOKE	Precision control of the gas flow rate and pressure in the reactor	-	-	-
Gas Flow meter	ALICAT (M Series)	Measure the mass flow rate of feeding gas	0-10 L/min	0.1 L/min	±0.8%
Pressure meter	ALICAT (P Series)	Measure the gas pressure of a reactor	0-2 bar absolute	0.001 bar	±0.25%
Ozone analyser	BMT (964)	Low ozone concentration measurement	0-20 g/Nm^3	0.01 g/ Nm^3	0.4% of measurement + 0.1% of scale
	INUSA (Mini HiCon)	High ozone concentration measurement	0-400 g/Nm^3	0.1 g/ Nm^3	±0.5 g/Nm^3
Ozone destructor	Workshop of HVT group	Convert the ozone into oxygen before it is vented into the atmospheric	-	-	-

3.3 Power Supply System

This section describes the power energization systems involved in this research project. Four types of power supply were employed throughout the project and their operational principles and circuit arrangements are described in the following sub-sections.

3.3.1 50 Hz Power Supply System

A high voltage ac power supply based on the mains frequency of 50 Hz was constructed by using an auto-transformer and a high voltage transformer (230 V/5 kV). The circuit diagram is shown in Fig. 3-3.

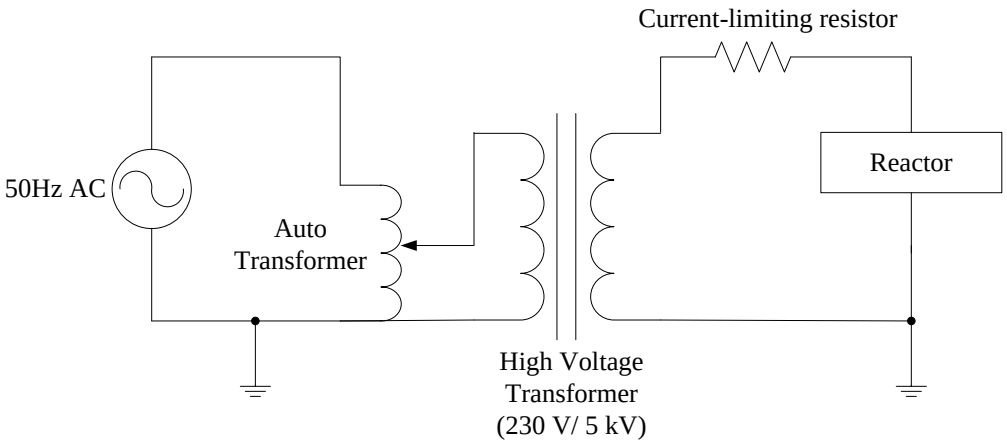

Fig. 3-3 Schematic diagram of high voltage AC power supply with the mains frequency of 50 Hz

Mains input voltage was supplied to the auto-transformer. The output voltage from the auto-transformer was stepped up by a high voltage transformer with a ratio of 1:22. The voltage applied to a reactor can be adjusted from 0 to 7 kV (peak value) by the auto-transformer. A 10 kΩ current-limiting resistor was connected in series with the reactor for short circuit protection.

This 50 Hz power supply was employed to conduct some calibration tests on the electrical and optical measurement equipment in this research project. Also, it was applied for ozone generation experiments; the ozone generation efficiency was compared with that by using a high frequency power supply.

3.3.2 High Frequency Sinusoidal Power Supply

A high frequency AC power supply system was constructed by using a linear AC power source and a high voltage transformer (300 V/ 6 kV). The circuit diagram is shown in Fig. 3-4:

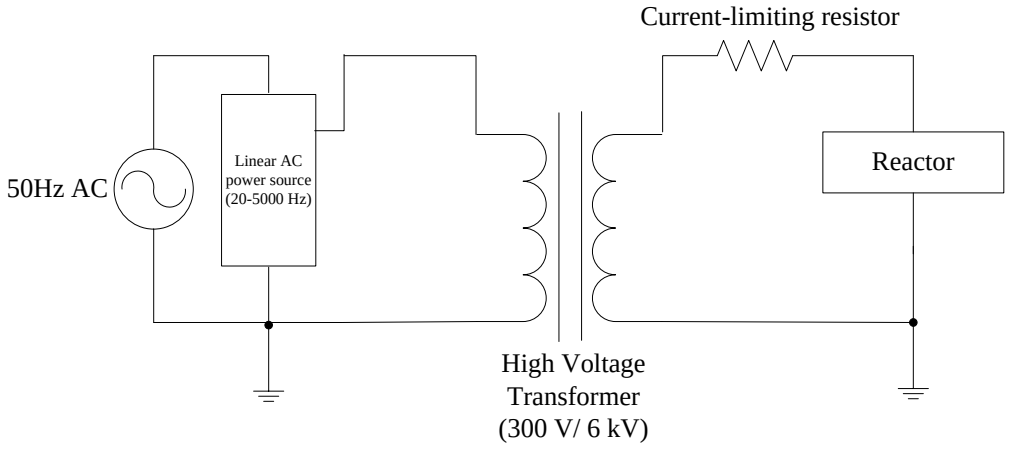

Fig. 3-4 Schematic diagram of high voltage ac power supply with a frequency range from 20 Hz to 5 kHz

The linear AC power source is from Pacific Power's AMX-Series (model No.: 112AMX). The output voltage and frequency of the 112AMX power source can be digitally adjusted. The output voltage has a range from 0-300 V and the output frequency has a range from 20 Hz - 5 kHz. A high voltage and high frequency transformer with the ratio of 1:20 was connected to the output of the AC power source, providing a 6 kV (peak value) voltage at 20 Hz to 5 kHz to the reactor. A 10 kΩ current-limiting resistor was connected in series with the reactor for short circuit protection.

This type of power source can provide a transient voltage output to the ozone reactor, which offered the possibility to investigate the ozone generation performance under different experimental conditions, with no need to consider the temperature effect. The experiment based on the transient applied voltage will be introduced in Chapter 5. Also, this power supply provided a continuous, high frequency (up to 5 kHz) AC voltage to the ozone reactor for comparing the ozone performance between different experimental conditions under the same gas temperature conditions (discharge power was kept the same). Experiments based on continuous AC voltage will be presented in Chapter 6.

3.3.3 High Frequency Series Resonant Inverter

A high frequency AC power supply based on a series resonant inverter was developed for ozone generation. The experiments based on this type of power supply will be presented in Chapter 6. Compared with the linear AC power source, this type of power supply circuit provided reactive power compensation by connecting an inductor in series with a capacitive DBD load. The working principle of this type of circuit is described in the following.

As shown in Fig. 3-5, V_{dc} is a direct voltage obtained by rectifying and filtering the mains voltage. The inverter consists of 4 IGBT switches, and each of them has a reversed parallel diode.

This circuit inverted direct voltage V_{dc} into a square wave AC voltage V_1 with a certain switching frequency. The switching frequency can be digitally adjusted from 500 Hz to 30 kHz. Also, the duty cycle and power density of the square wave can be digitally controlled, providing different voltage amplitudes and average power output. As seen from the circuit diagram, the square wave was exported to a high frequency and high voltage booster transformer, which stepped up the square wave voltage amplitude from 400 V to 6 kV. On the secondary side of the transformer, a resonant inductor was connected in series with the ozone generator which presented a capacitive load. When the switching frequency of the inverter equalled the resonant frequency of the *LC* circuit, the circuit would work at a resonant state and a sinusoidal voltage across the load was achieved. The frequency of the sinusoidal load voltage was the resonant frequency which was determined by the *LC* values. At the resonant state, the reactive power consumed by the ozone generator was compensated by the resonant inductor, such that the power supply efficiency can be increased based on this circuit topology.

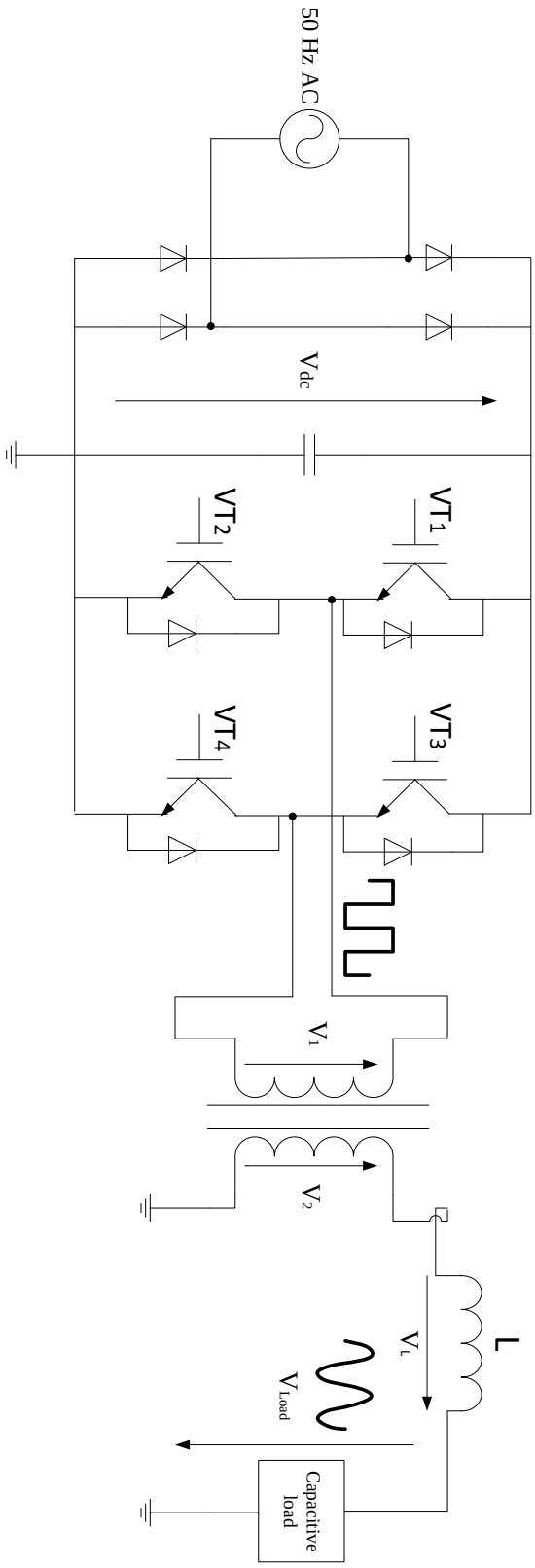

Fig. 3-5 Schematic diagram of high frequency power supply based on a series resonant inverter

3.3.4 Pulsed Power Supply System

A pulsed power supply was designed and developed in this project to investigate the ozone generation efficiency by using pulsed dielectric barrier discharges. The circuit diagram of the pulsed power supply is shown in Fig. 3-6.

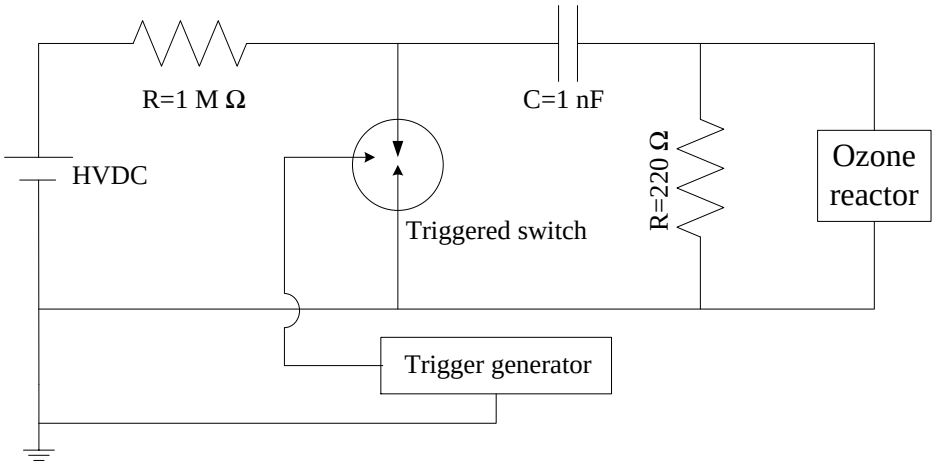

Fig. 3-6 Schematic diagram of the electrical circuit of the pulsed power supply

As seen from the circuit diagram, a pulsed high voltage was generated by charging a capacitor of 1 nF, fed by a 20 kV/10 mA high voltage DC power supply (manufacturer: Glassman EH series, 0-20 kV), via a 1 MΩ charging resistor. A 220 Ω resistor was connected in parallel with the ozone reactor for charging and discharging the capacitive load, and this determined the duration of the pulsed voltage across the reactor. The pulse duration is defined as the full-width half maximum (FWHM) of the pulsed voltage. In this circuit, a negative pulsed voltage with FWHM of 500 ns was achieved, and the rise time of the pulsed voltage was 40 ns. A three-electrode spark gap switch was triggered by a trigger generator to provide a pulse repetition rate up to 200 pps for the ozone production experiment. The experiment based on this type of power supply will be presented in Chapter 7.

3.4 Electrical and Optical Diagnostic Systems

In order to evaluate the ozone generation efficiency, proper diagnosis of the characteristics of the plasma discharges generated is important. In this research project, electrical and optical diagnostic systems were set-up to investigate the characteristics of DBDs. The electrical parameters of the DBD load, including the voltage, current, power dissipation and transferred charge, were measured and analysed. An optical signal was also measured in some experiments to detect discharge events. Details of the measurement devices involved in the diagnostic system are described in the following sub-sections.

3.4.1 Electrical Diagnostic Systems

The electrical measurement devices employed in this research are listed as below:

1) Voltage measurement

The applied voltage was measured by the voltage probes listed in Table 3-2.

Table 3-2: Types of voltage probes used in this research project

Type	Tektronix P6015A	LeCroy PPE 6kV	LeCroy PP005A
Maximum input voltage	20 kV DC & 40 kV Peak impulse	Measuring range: 0-6 kV DC	600 V (DC + peak AC)
Attenuation	1000:1	1000:1	10:1
Bandwidth	75 MHz	400 MHz	500 MHz
Rise time	4 ns	0.9 ns	0.7 ns

The Tektronix P6015A high voltage probe was used to measure the applied voltages in the scenarios where higher bandwidth and fast response time were not required, while the LeCroy PPE 6 kV high voltage probe, which has a higher bandwidth of 400 MHz and a faster rise time of 0.9 ns, was used to measure the transient voltage associated with a short-duration (<100 ns) discharge event. The LeCroy PP005A voltage probe was used to measure low voltages, such as the voltage across a charge measurement capacitor.

2) Current measurement

Two current measurement methods were involved in this project for measuring the discharge current in the external circuit. They are based on a current transformer (CT) and a 50 Ω shunt resistor. The measurement circuits based on these two devices, CT and 50 Ω shunt resistor, are shown in Fig. 3-7 and Fig. 3-8, respectively. The two circuits are introduced and compared as below:

- *Current measured by using a current transformer*:

A current transformer is a device that generates a secondary alternating or pulsed current that is proportional to the primary current. As shown in Fig. 3-7, the CT was placed around the ground electrode of the DBD reactor, and encircled the wire that was connected to ground. When there was a current flowing through the window of the CT, a secondary terminal voltage was induced and transmitted to the oscilloscope for measurement through a coaxial cable (RG214), with characteristic impedance of 50 Ω. The terminal input impedance of the oscilloscope was also 50 Ω, which prevented the reflection and deformation of the transmitted voltage signal. In terms of the selection of the CT, the sensitivity, bandwidth and rise time are important parameters that need to be considered. For the DBD short pulsed discharge current measurement, a CT with high bandwidth and fast response time should be chosen. As to the sensitivity of the CT, it was selected according to the range of the prospective discharge current. Based on these considerations, two CTs, shown in Table 3-3, were used for the discharge current measurement in this research project.

Table 3-3: The CTs used in the research project

	Pearson CT (model: 6585)	Bergoz FCT
Sensitivity	0.5 V/A into 50 Ω	5 V/A into 50 Ω
Maximum peak current	500 A	100 A
Maximum rms current	10 A	1.4 A
Bandwidth	400 Hz to 250 MHz	32 kHz to 1 GHz
Rise time	1.5 ns	0.78 ns
Output connector	BNC	SMA

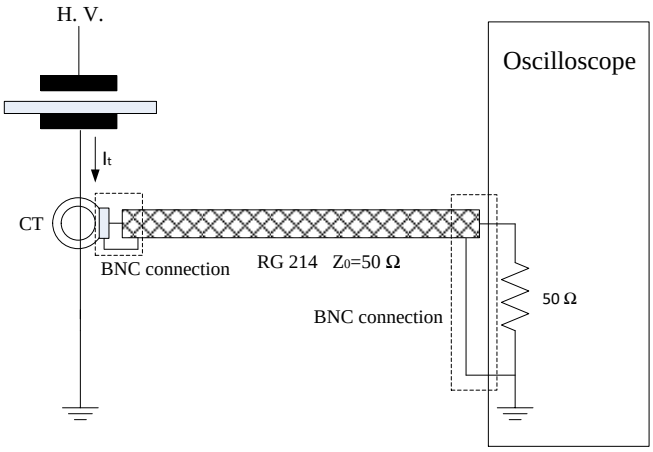

Fig. 3-7 Schematic diagram of current measurement based on current transformer

- *Current measured by using a 50 Ω shunt resistor:*

The discharge current was also measured by using a shunt resistor in this project. A non-inductive 50 Ω resistor (Caddock MP 820) was selected for the measurement. As shown in Fig. 3-8, the grounded electrode of the DBD reactor was connected to ground through the 50 Ω shunt resistor. The voltage across the shunt resistor was transmitted to the oscilloscope via a coaxial cable (RG405) with a characteristic impedance of 50 Ω, and terminated using a 50 Ω termination to prevent reflections. The discharge current can be calculated by the voltage across the shunt resistor, divided by the equivalent input impedance of 25 Ω, based on transmission line theory [109]. It is worth mentioning that the conductor wire for connecting the shunt resistor and transmission line was made as short as possible to reduce the stray inductance and capacitance.

Compared with the current transformer, the shunt resistor method provides the advantage of higher bandwidth (ideally infinite), which enables the measurement of a continuous AC current with low frequency (minimum is 50 Hz in this project), and a transient discharge current with duration of the order of ns. Current transformers have a limited bandwidth, and can only be used to reliably measure the current within this limited frequency range. The main advantages of current measurement based on a CT are that there is no need to break the current-carrying conductor at the point of measurements, and galvanic isolation from the power circuit is provided for the measurement.

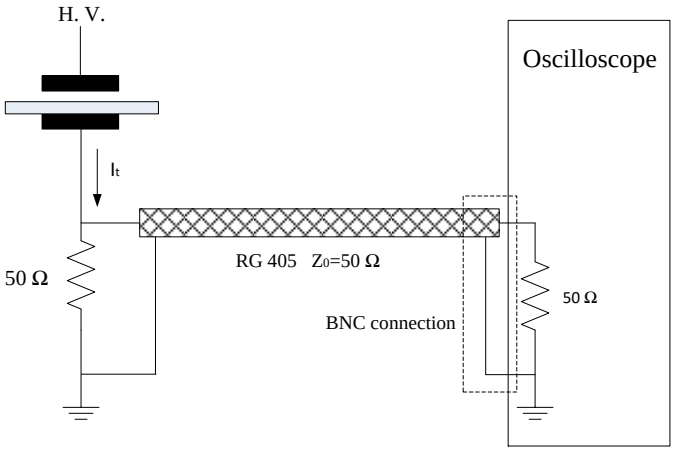

Fig. 3-8 Schematic diagram of current measurement based on a 50 Ω shunt resistor

Depending upon the discharge current range and power frequency, either the current transformer or shunt resistor approach was used for different experiments in this research project.

3) Transferred charge measurement

The charge transferred through a DBD reactor was measured by a capacitor connected in series with the DBD reactor. The charge transferred through the measurement capacitor, which is equal to the charge transferred though the DBD reactor, can be calculated by equation (3.1):

$$Q = C_m \cdot V \tag{3.1}$$

where C_m is the capacitance of the measurement capacitor and V is the voltage across the measurement capacitor.

A polypropylene film capacitor from Kemet was chosen as the measurement capacitor because of its low internal inductance and resistance values, which was beneficial for a transient voltage application [110]. The capacitance was selected to be about 500-1000 times larger than the equivalent capacitance of the DBD reactor, which provided a voltage that was adequately low for measurement.

4) Data acquisition and processing

A LeCroy oscilloscope (WaveRunner 625 Zi) was used for data acquisition. The key parameters of the oscilloscope are shown in Table 3-4.

Table 3-4: Parameters of the oscilloscope used in the experiment

Bandwidth	2.5 GHz
Maximum sample rate	40 GS/s
Maximum acquisition memory	128 Mpts
Resolution	8-bit

The high bandwidth of 2.5 GHz and sample rate of 40 GS/s provided an accurate measurement of the impulsive discharge current. The large acquisition memory of 128 Mpts offered the possibility to acquire a full cycle of the voltage and current signals (≥100 Hz) at a high sample rate (≥10 GS/s), which guaranteed the accuracy of the power calculation by digital integration of the sampled voltage and current data. Eight-bit vertical resolution provided an acceptable dynamic range for simultaneous measurement of high amplitude discharge current spikes and low amplitude background continuous current.

The voltage and current waveforms acquired by the WaveRunner 625 Zi oscilloscope were exported as CSV files, which were post-processed by data processing software, Matlab [111] and Origin [112].

3.4.2 Optical Diagnostic System

An optical diagnostic system was set up to detect the emitted light from the discharges, with the purpose of detecting discharge events, and also to investigate the DBD modes under different experimental conditions. The key component of the optical measurement system was a photomultiplier (PMT) from Hamamatsu (H10721-01). The H10721-01 PMT delivered high gain for measuring the light with wavelength from 230 nm to 870 nm. The predominant spectrum lines of oxygen are 777 nm and 844 nm, within the measurement range of the PMT [113]. The PMT had a rise time of 0.57 ns, which was fast enough to detect discharge events. The schematic diagram of the PMT detection system is shown in Fig. 3-9.

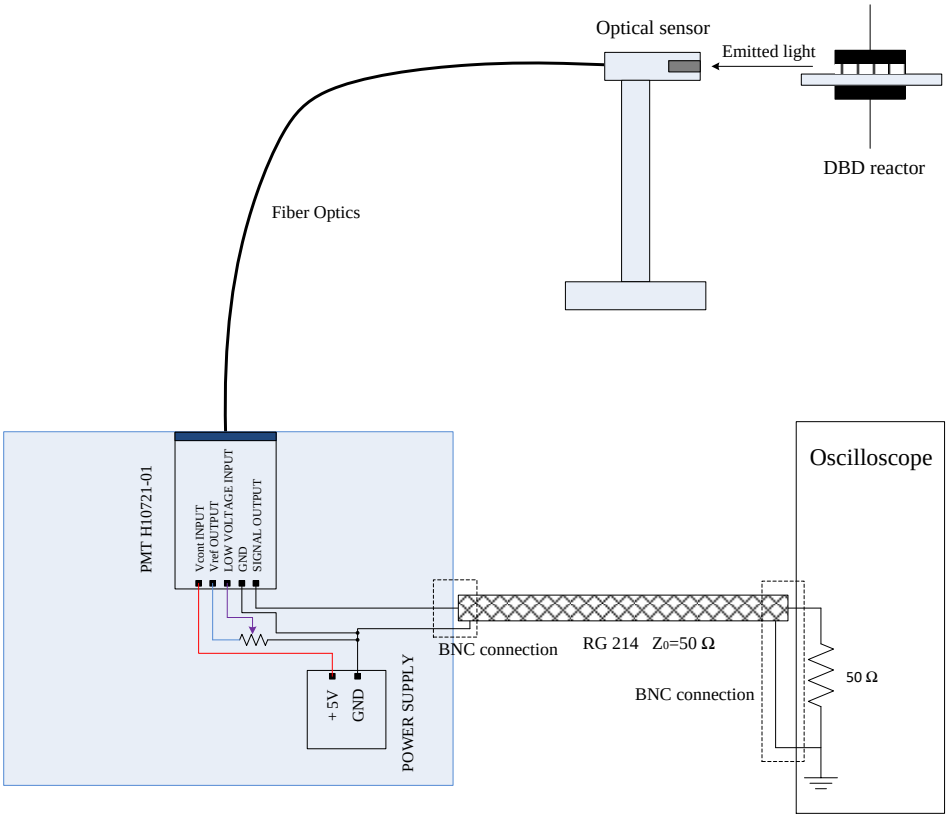

Fig. 3-9 Schematic diagram of optical signal detection system based on PMT

As shown in Fig. 3-9, the emitted light from the discharge was detected by an optical sensor, and the optical signal was transmitted through fibre-optic cables to the PMT. The optical signal was converted into an electrical signal by a built-in circuit, and the electrical signal was transmitted to the oscilloscope through a double-shielded RG214 coaxial cable. As the emission light was detected by a photocathode in the PMT, an electron current was produced such that a negative current pulse representing a light pulse was observed on the oscilloscope [114].

3.4.3 Calibration of the Propagation Time of the Coaxial Cables of Voltage and Current Measurement Devices

Although the measurement equipment had been calibrated by the manufacturer, different measurement devices (voltage probe, current sensor and PMT) have different cable lengths, so it was necessary to measure the propagation time delay of different cables and take this into account when experimental measurements were conducted.

Fig. 3-10 shows the circuit set-up for calibrating the propagation time delay of the cables of the high voltage probes (P6015A and PPE 6kV) and the transmission lines (RG405 & RG214) used for current measurements.

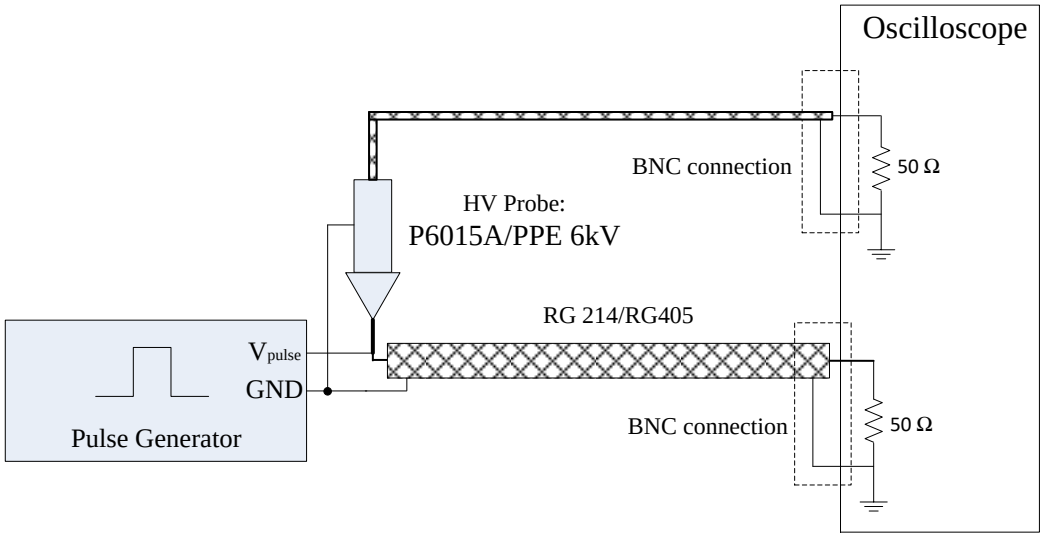

Fig. 3-10 Schematic diagram of circuit set-up for calibration of the voltage probe and the transmission line used for current measurement

By measuring the same calibration voltage pulse with duration of 80 ns generated by a pulsed voltage generator (Thurlby Thandar TG 105, 5Hz -5MHz), the signal propagation time delay between different cables was identified and the time delay was compensated. After the compensation of delay time by oscilloscope, the signals transmitted by two cables were synchronized which was shown in Fig. 3-11. For the optical signal measurement, there was an additional delay time of 7.5 ns due to the propagation of light signal along a 1.5 m fiber-optic link (propagation speed: 5 ns/m), and this delay time has also been compensated by oscilloscope in the measurement.

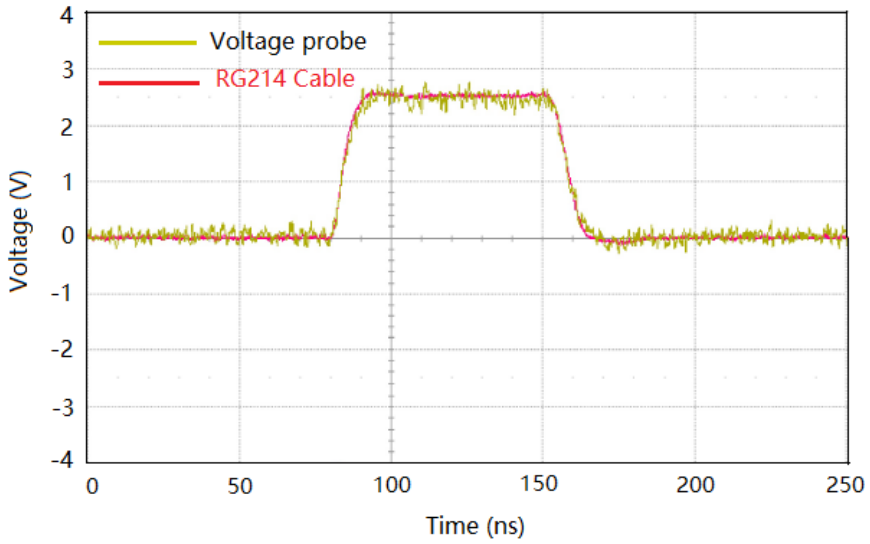

Fig. 3-11 synchronized signals transmitted by the coaxial cable of voltage probe and the transmission line (RG214) used for current measurement

3.5 Discharge Power Measurement

There are two methods to determine the DBD power: integration of the product of current and voltage; and a power formula derived from a Lissajous figure [74].

3.5.1 Integration of the Product of Current and Voltage

The discharge power of DBD is equal to the power injected to the reactor, provided that the dielectric loss of the dielectric barrier is negligible. The power injected to the reactor can be calculated as below:

$$P = \frac{1}{T} \cdot \int_0^T i_t(t) \cdot V_a(t) dt \tag{3.2}$$

where T is the period of the applied voltage V_a, and i_t is the current measured in the external circuit. The analogue signals of the voltage $V_a(t)$ and current $I_t(t)$ are sampled by the oscilloscope and converted into digital values, $V_a(k)$ and $I_t(k)$, respectively. Thus, equation (3.2) can be approximated by:

$$P = \frac{1}{T} \cdot \sum_{k=1}^{n} I_t(k) \cdot V_a(k) \cdot \Delta t \tag{3.3}$$

where n is the number of samples in one cycle and Δt is the sampling period.

The accuracy of the power measurement through the numerical integration of the product of current and voltage depends on the sampling rate and the quantization level of the oscilloscope. The oscilloscope that was used in this research project had a maximum sampling rate of 40 GS/s and 8-bit quantization range, providing a high degree of accuracy for the numerical integration of the current and voltage signals.

3.5.2 Power Formula Based on the Lissajous Figure

Equation (3.2) can be rewritten as follows:

$$\begin{aligned} P &= \frac{1}{T}\cdot\int_0^T i_t(t)\cdot V_a(t)dt \\ &= \frac{1}{T}\cdot\int_0^T V_a(t)\cdot\frac{dQ}{dt}dt \\ &= f\cdot\int_0^T V_a(t)\cdot dQ \end{aligned} \tag{3.4}$$

The charge transferred, Q, can be measured based on equation (3.1). The plot of the charge, Q, against the applied voltage, V_a, is called a Lissajous figure, an example being shown in Fig. 3-12. Equation (3.4) shows that the area inside the closed Lissajous figure, multiplied by the AC power frequency, f, is equal to the discharge power. Based on Fig. 3-12, the area of the Lissajous figure can be derived as follows:

$$A = 2V_b\cdot\Delta Q' + 2(V_{\max}-V_{\min})\cdot(\Delta Q-\Delta Q') \tag{3.5}$$

where $\Delta Q'$ is the charge required for a voltage reversal across the gap from V_b to $-V_b$, V_{max} is the maximum applied voltage and V_{min} is the minimum applied voltage required to sustain the discharge. The $\Delta Q'$ can be calculated by equation (3.6):

$$\Delta Q' = 2C_g\cdot V_b \tag{3.6}$$

Based on the geometry of the Lisssajous figure, the charge transferred, ΔQ, can be calculated as below:

$$\Delta Q = 2(V_{\max}-V_{\min})\cdot C_d \tag{3.7}$$

Substituting equation (3.6) and equation (3.7) into equation (3.5) and rearranging, the following equation can be achieved:

$$A = 4V_b\cdot C_d(V_{\max}-V_{\min}) \tag{3.8}$$

Therefore, the discharge power can be calculated by the equation as below:

$$P = 4 f V_b C_d (V_{\max} - V_{\min}) \tag{3.9}$$

The accuracy of equation (3.9) for power measurement is subject to errors in the reading of data from the Lissajous figure. Compared with the integration method, equation (3.9) can provide a quicker estimate of the discharge power, but as to the accuracy, the integration of the product of the current and voltage was found to be more accurate by using the oscilloscope with a high sampling rate and quantisation range.

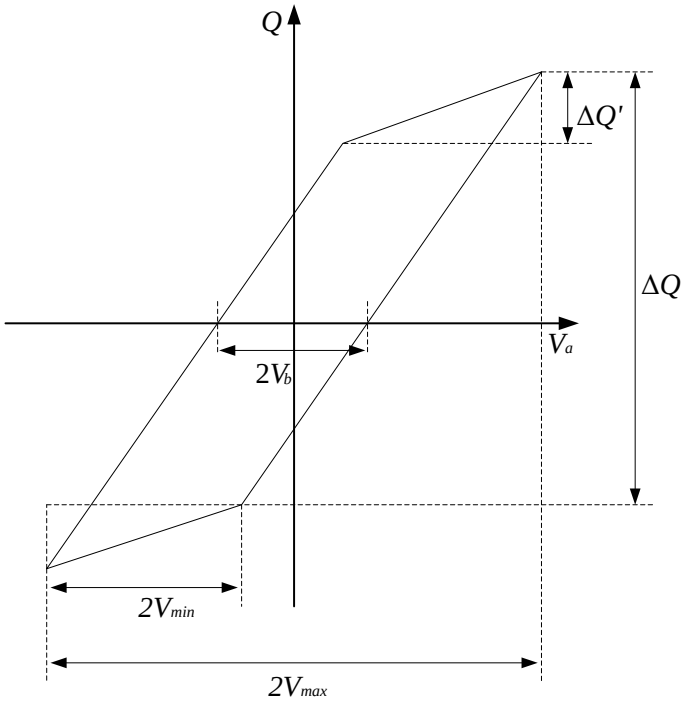

Fig. 3-12 Schematic presentation of Lissajous figure

3.6 Ozone Concentration Measurement

Ozone concentration was measured by an ozone analyser (BMT 964 & INUSA Mini Hi-Con). The measurement range and accuracy can be found in Table 3-1. The measurement principle is based on the fact that ozone has a strong absorption of 254 nm UV light. A low pressure mercury lamp is used as a source of radiation in the ozone analyser. Narrow band filters are used to ensure that only the mercury light with the wavelength of 254 nm is transmitted into a gas chamber for the measurement. The gas chamber is constructed with two parallel cuvette windows, transparent to 254 nm radiation. The distance between them defines the measurement range and the sensitivity of the instrument. The intensity of 254 nm radiation after passing through the sample gas (ozone plus carrier gas) is measured, and this value is compared with a reference measurement of ozone off-gas. From the ratio of the two values, the ozone concentration can be calculated. The ozone concentration was defined as mass of ozone per normal (or standard) volume of sample gas (oxygen or dry air). Its dimension is g/Nm^3, %Wt/Wt (weight concentration) or part per million volume (ppm_v, volume concentration).

In this research work, the ozone concentration at both steady state and transient state were measured. The steady state ozone concentration was measured when a continuous AC and pulsed voltage were applied, the results of which will be presented in Chapter 6 and Chapter 7. The transient ozone concentration was measured when a transient AC voltage was applied, as presented in Chapter 5.

For the transient ozone concentration measurement, real-time data with a sample period of 100 ms were transmitted to a computer via an RS232 interface. All the concentration data were acquired and saved by a LabVIEW program. These concentration data were processed for plotting the concentration curve, and for calculating the ozone generation efficiency using Matlab. Fig. 3-13 is an example of the ozone concentration curve when the ozone generator was energized by 200 voltage cycles at a frequency of 5 kHz and amplitude of 5.5 kV. The ozone generation efficiency calculation based on this concentration curve is illustrated in Section 3.7.

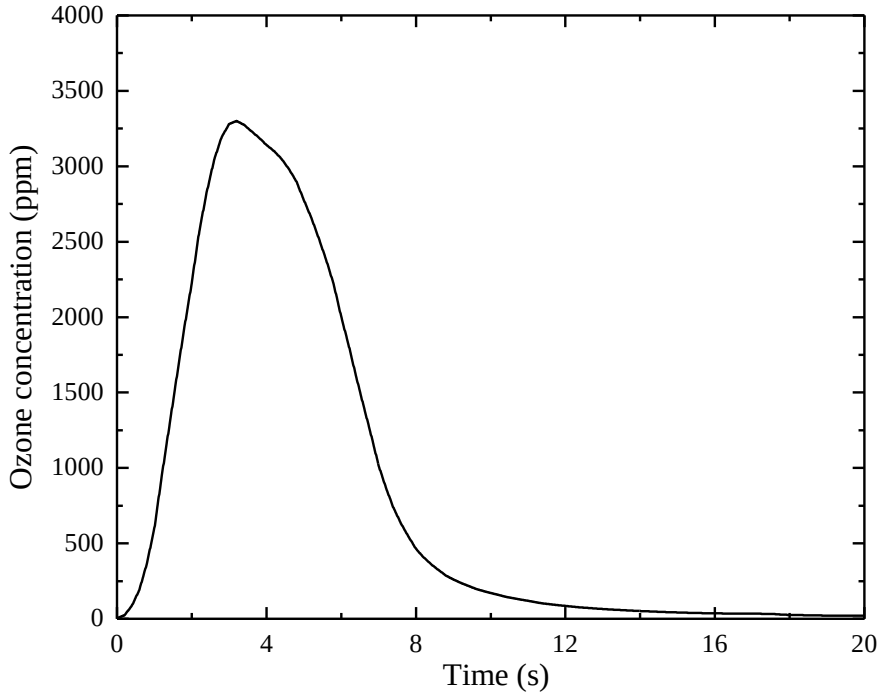

Fig. 3-13 Ozone concentration curve measured when transient voltages (200 cycles of 5 kHz sinusoidal voltage with the amplitude of 5.5 kV) was applied to the ozone reactor (0.5 mm gap length, with absolute pressure of 1 bar)

3.7 Ozone Generation Efficiency Calculation

3.7.1 Ideal Gas Law

The classical gas law was firstly discovered in an experiment by Boyle and Mariotte. It states that for a given amount of enclosed gas at a constant temperature, the product of pressure (P) and volume (V) is a constant:

$$pV = C = const \tag{3.10}$$

The ideal gas law is often written as [55]:

$$pV = nRT \tag{3.11}$$

In the above equation, n is the number of moles of gas atoms or molecules, R is the universal gas constant, which equals 8.3144621 $J/mol\ K$, and T is the thermodynamic temperature in K.

The molar mass of ozone was specified as 47.998 *g*/*mol* in Section 2.2. According to equation (3.11), the molar volume of ozone, *V*/*n*, is related to the pressure and temperature. At the standard condition of 1 *atm* and 0 °C, the molar volume of ozone gas is agreed to be 22.388 *L*/*mol*. Therefore, the density of ozone can be calculated as 2.144 g/L, which is a commonly-used figure. Also, the density of oxygen at these standard conditions is 1.429 g/L.

There is another reference condition that is also used in the ozone concentration measurement: 1 *atm* and 25° C. At these conditions, the oxygen and ozone densities are 1.308 g/L and 1.952 g/L, respectively, based on calculation through equation (3.11).

3.7.2 Calculation Based on a Steady-state Ozone Concentration

Ozone generation efficiency is defined as the weight of ozone generated per kWh, with units of g/kWh. The calculation process of ozone generation efficiency based on a steady state ozone concentration, with a constant gas flow rate, is illustrated below:

The oxygen volume flow rate (denoted as *r* with the unit of L/min) was measured by the ALICAT flow meter shown in Fig. 3-1. From the datasheet of the ALICAT flow meter, the volumetric flow rate value *r* was corrected to standard conditions of 25 °C and 1 atm. Under these conditions, the molar volume of an ideal gas is:

$$V_m = \frac{V}{n} = \frac{RT}{P} = 24.465\ L/mole \tag{3.12}$$

The number of moles of oxygen input per minute is:

$$n_1 = \frac{r}{24.465} \quad moles \tag{3.13}$$

The molar mass of oxygen is 31.9988 g [42], so the mass of the input oxygen per minute is:

$$m = n_1 \cdot 31.9988 \tag{3.14}$$

The ozone concentration value measured by an ozone analyser was based on a standard condition of 0 °C and 1 atm. Under this condition, the molar volume of ozone gas is 22.388 L/mole and the ozone density is 2.144 g/L. Given the ozone concentration measured is *c* (with units of g/Nm^3), the number of moles of ozone is:

$$n_2 = \frac{c}{47.9982} \tag{3.15}$$

According to (3.11), the molar volume of the mixture gas (ozone and oxygen) from the ozone reactor at the condition of 0 °C and 1 atm is:

$$V_{mixture} = \frac{V}{n} = \frac{RT}{P} = 22.414 \quad \text{L/mole} \tag{3.16}$$

Therefore, the number of moles of the mixture gas at the above condition is:

$$n_{mixture} = \frac{1000}{22.414} = 44.615 \tag{3.17}$$

The number of moles of oxygen in the output mixture gas is:

$$n_3 = n_{mixture} - n_2 \tag{3.18}$$

The weight concentration of ozone in the mixture gas is:

$$x = \frac{c}{c + n_3 \cdot 31.9988} \tag{3.19}$$

According to the mass conservation law, the total weight of the mixture gas at the output of the ozone reactor is the same as the weight of the input oxygen gas which is shown in (3.14). So the weight of the ozone generated per hour can be calculated as below:

$$m_1 = m \cdot x \cdot 60 \tag{3.20}$$

Given that the discharge power is *P*, the ozone generation efficiency is calculated as below:

$$\eta = \frac{1000 \cdot m_1}{P} \quad \text{g/kWh} \tag{3.21}$$

The ozone generation efficiency calculation process shown above was written as an *m* file, executed by Matlab. The commands of the *m* file are shown in APPENDIX C for reference.

3.7.3 Calculation Based on Transient Ozone Concentration Value

The ozone generation efficiency based on a transient ozone concentration value shown in Fig. 3-13 is calculated as below:

According to (3.13), the amount of oxygen input per second is:

$$n_1^{'} = \frac{r}{24.465 \times 60} \quad \text{moles} \tag{3.22}$$

The mass of oxygen flowing per second is:

$$m^{'} = n_1^{'} \cdot 31.9988 \tag{3.23}$$

Considering the concentration of ozone measured at the moment *t* as $x^{'}$ ppm, the weight concentration by the conversion of volume concentration of $x^{'}$ ppm is:

$$c = \frac{x' \cdot 2.144}{(10^6 - x') \cdot 1.429 + x' \cdot 2.144} \tag{3.24}$$

The weight of ozone generated per second can be calculated:

$$m_0 = c \cdot m \tag{3.25}$$

The total ozone generated can be calculated by the integration of m_0 over time:

$$m_t = \int_0^T m_0 dt \tag{3.26}$$

The injected energy is defined as W_t with units of J, and the ozone generation efficiency is calculated as below:

$$\eta = \frac{m_t \cdot 3.6 \times 10^6}{W_t} \quad \text{g/kWh} \tag{3.27}$$

The equations were written in an *m* file, executed by Matlab, and the commands are shown in APPENDIX C for reference.

4 ELECTRICAL CHARACTERISTICS OF DIELECTRIC BARRIER DISCHARGES

4.1 Introduction

Dielectric barrier discharges, also referred to as silent discharges, are the most conventional method of ozone generation. The advantage of these discharges is that a large number of high energy electrons can be generated at a low gas temperature, which is advantageous for ozone formation [15, 72]. The electrical characteristics of DBD have been investigated for more than one hundred years, since the first prototype DBD reactor was used by W. Siemens for ozone generation [2]. Much progress has been made in the past 50 years, due to the evolution of power electronics technology. High frequency AC switch mode power supplies highly improve the discharge power of DBD in the voltage range 5-10 kV, which offers great advantages over the bulky, step-up transformers traditionally used for generating high concentrations of ozone. In recent years, large ozone generating facilities have the capability to produce several hundred kilograms of ozone per hour, with a power consumption of several megawatts [9]. Also, a modern power supply based on a resonant inverter can provide active power compensation for the dielectric barrier discharges, which improves the power supply efficiency [93-96].

However, despite considerable progress in generating DBD in an efficient way and in understanding the electrical properties of DBD, nowadays the knowledge of this subject still cannot provide an adequate quantitative theoretical description of the filamentary DBD behaviour [72]. One of the main reasons for this situation is the difficulty to investigate experimentally the dynamics of the discharge filaments, which have a short duration of tens of nanoseconds. Also, it is difficult to diagnose the discharge parameters inside the discharge gap. In this research, with the benefit of advanced DAQ equipment, WaveRunner 625 Zi, which provides the capability to acquire a large amount of sample data at a high sample rate and quantization level, the voltage and discharge current signals of DBD in the external circuit were accurately measured. Based on the accurate measurement of the electrical and optical signals from the discharge, the electrical characteristics of DBD were analysed, and these characteristics are discussed quantitatively in this chapter. An equivalent electrical model of a DBD was derived based on energy balance, and an equation governing the discharge current in the gap was derived. Also, the electrical characteristics of the DBD

under different applied voltages and frequencies were investigated, and these are compared at the end of this chapter.

4.2 Test Cell and Experimental Set-up

4.2.1 Test cell

A plate-type DBD reactor (Type-A) was designed and developed for this part of the work. A schematic drawing of this reactor is shown in Fig. 4-1. As can be seen from the drawing, two stainless steel electrodes with the diameter of 30 mm were housed inside a sealed acrylic vessel. The maximum fill pressure was 2 bar absolute in this part of work. Because AC voltage was applied to the DBD reactor and the polarity of the electrode was changed every half cycle, the discharges characteristics of DBD were the same regardless of which electrode the dielectric barrier was on. In the experiments, the earth elected was covered by a

.

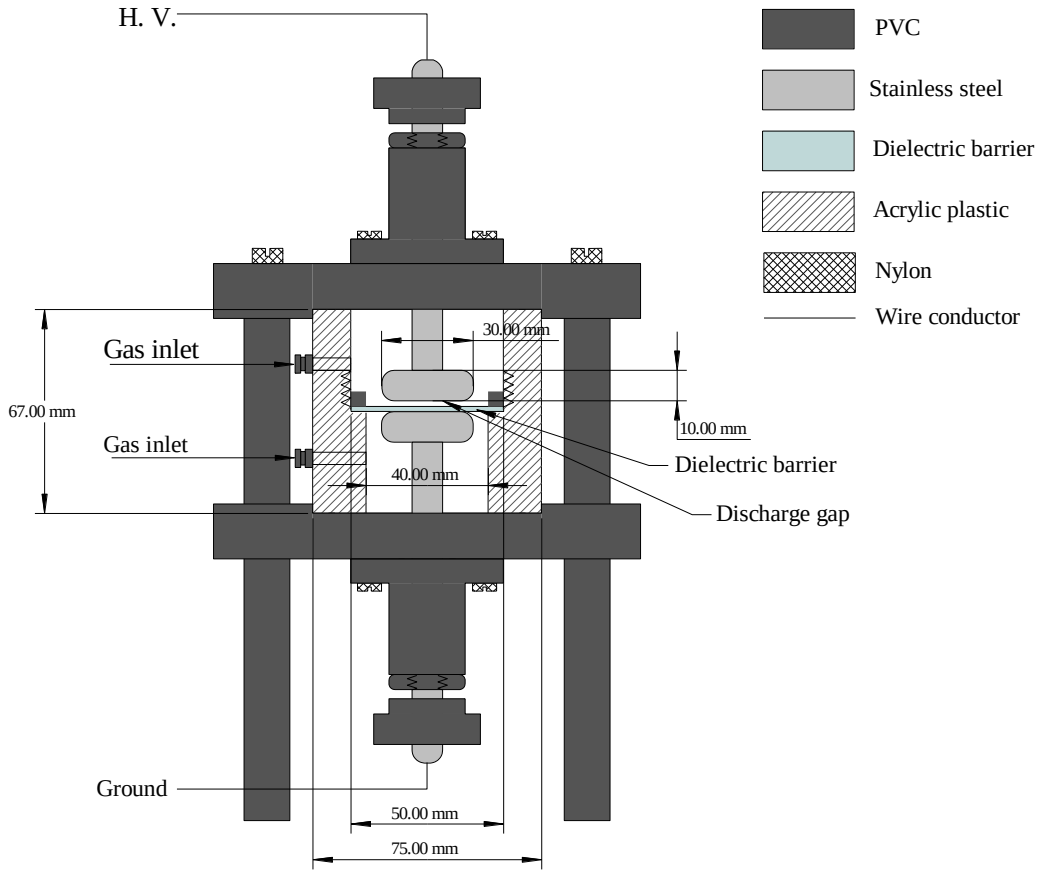

Fig. 4-1 Schematic diagram of Type-A plate DBD reactor

glass barrier with a thickness of 1 mm and a diameter of 50 mm. Three different types of glass barriers were compared in the experiments. Their dielectric constants and effective equivalent capacitance are shown in Table 4-1. The effective equivalent capacitances of the glass barriers were calculated based on equation (4.1):

$$C = \varepsilon_0 \varepsilon_r \frac{A}{d} \tag{4.1}$$

Where A is the effective area of the electrode and d is the thickness of the dielectric barrier or the discharge gap distance. An adjustable discharge gap was formed between the glass and the grounding electrode. The discharge gap could be adjusted by varying the height of the grounding electrode. Four different discharge gap lengths were investigated. The equivalent capacitance of discharge gaps were calculated, as presented in Table 4-2

Table 4-1: Dielectric constants of different glasses

Type	Quartz glass	Soda lime glass	Borosilicate glass
Dielectric constant	3.8	7.2	4.6
Effective equivalent capacitance (pF)	23.8	45.0	28.8

Table 4-2: Equivalent capacitance of discharge gaps with different lengths

	0.2 mm	0.4 mm	0.6 mm	0.8 mm
Effective Equivalent capacitance (pF)	31.3	15.6	10.4	7.8

4.2.2 Experimental Set-up

A 100 Hz - 5 kHz AC power supply with Type-A plate DBD reactor was set up to investigate the electrical characteristics of dielectric barrier discharges. Because soda lime glass had the largest capacitance due to the largest dielectric constant, the portion of applied voltage across the discharge gap was highest which was good for the ignition of discharges. Therefore, the soda lime glass with a thickness of 0.5 mm was chose as the dielectric barrier of DBD reactor and the length of the discharge gap was 0.2 mm. A non-inductive 50 Ω shunt resistor in conjunction with a RG 405 transmission line was employed to measure the discharge current in the external circuit. The experimental set-up for the current

measurement was as shown in Fig. 4-2. As can be seen in the figure, the external discharge current is denoted as I_t, and the applied voltage is denoted as V_a. The light emission from the discharge was detected by a PMT from Hamamatsu (H10721-01), to confirm the occurrence of discharge events. The charge transferred in the external circuit was measured by using a measurement capacitor connected in series with the DBD reactor, as shown in Fig. 4-3. The capacitance of C_m was chosen to be 22 nF, and the charge transferred was calculated by equation (3.7) in Chapter 3.

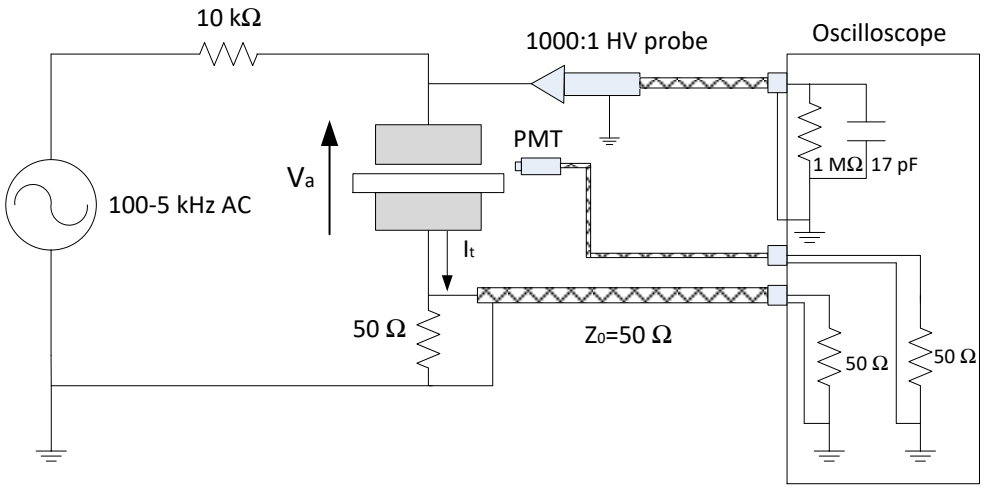

Fig. 4-2 Schematic diagram of the circuit set up for the DBD current measurement in the external circuit

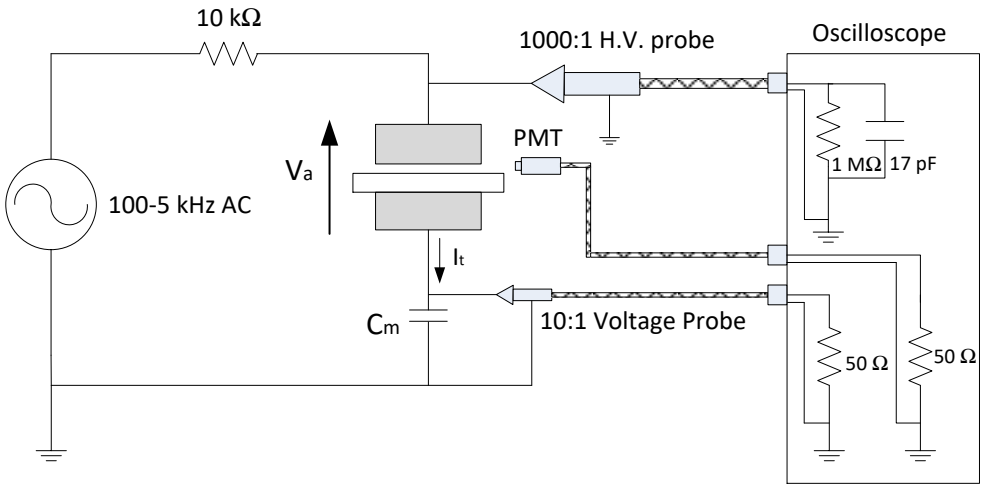

Fig. 4-3 Experimental set-up for transferred charge measurement (gap length: 0.2 mm; dielectric barrier: soda lime glass)

4.3 Measurement of Macro Electric Parameters

This section introduces the measurement of the macro electric parameters of DBD. These parameters include the discharge current in the external circuit, ignition voltage, discharge voltage across the gap, voltage across the dielectric barrier, transferred charge during half of a voltage cycle, and the discharge power. The discharge process was analysed from the discharge current waveforms and the Lissajous figure measured in the external circuit.

4.3.1 Discharge Current in the External Circuit

The discharge current in the external circuit based on 5 kHz AC power supply was measured. The applied voltage and current waveforms are shown in Fig. 4-4. It is shown that the current measured in the external circuit has impulsive discharge current superimposed on a continuous AC current. The continuous AC current is the capacitive current resulting from the capacitive impedance of the DBD reactor, and the impulsive current is the discharge current in the external circuit, induced by the micro-discharges in the gap. As can be seen from Fig. 4-4, one voltage cycle can be divided into four parts, including two non-discharge periods and two discharge periods. When the applied voltage rose from the negative peak to the ignition voltage, the DBD reactor started to discharge, corresponding to the occurrence of a positive impulsive current. The discharge stopped when the applied voltage rose to the positive peak of the applied voltage. This can be explained as follows: when the applied voltage was rising, additional micro-discharges were initiated at new locations as the build-up of charge deposited on the dielectric barrier had reduced the electric field at positions where micro-discharges had already occurred. No further micro-discharges were initiated when the voltage stopped rising, which lead to the termination of the impulsive current at the peak of the applied voltage. After the positive peak, the applied voltage started to decrease and there was no discharge until the voltage dropped to a certain level, at which the reversed net electric field was high enough to break down the gas, with the help of the residual charge deposited on the surface of the dielectric barrier. The impulsive current occurred when the discharge began in the falling part of the applied voltage waveform, and it was terminated at the negative peak of the applied voltage.

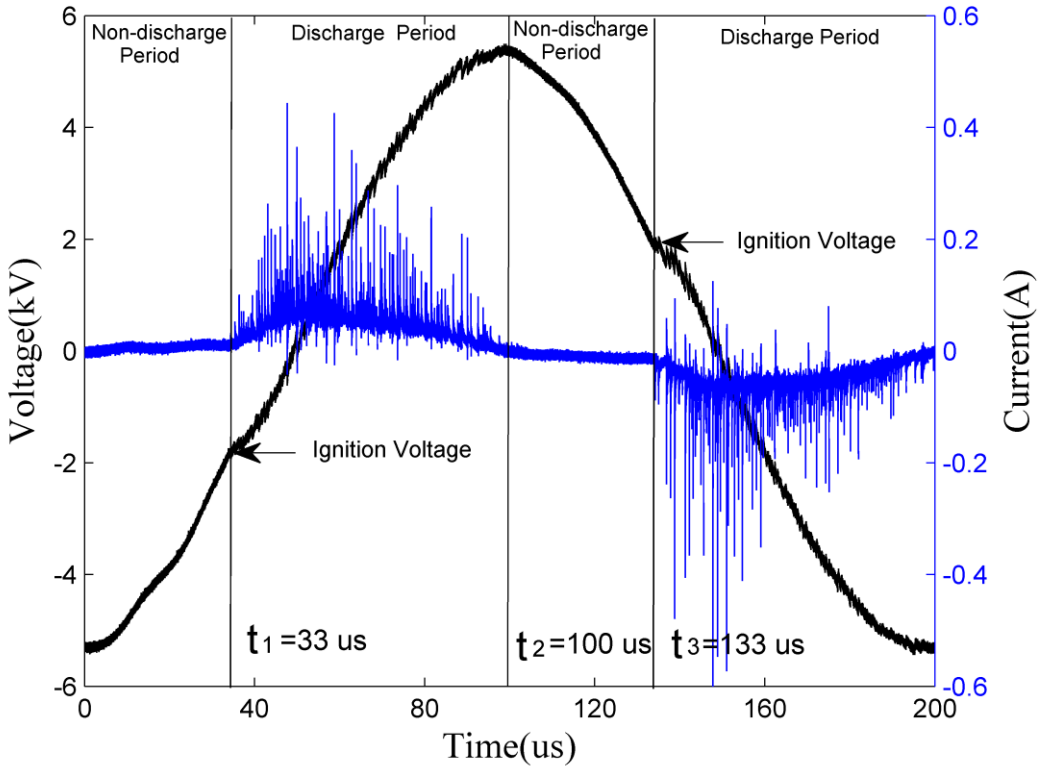

Fig. 4-4 Waveforms of applied voltage and discharge current in the external circuit (5 kHz AC power supply, 0.5 mm gap, soda lime glass as dielectric barrier)

4.3.2 Voltage across the Discharge Gap and Dielectric Barrier

Further to investigating the electrical characteristics of the DBD, the voltage across the discharge gap, V_g, and the dielectric barrier, V_d, were measured. Fig. 4-3 shows the experimental set up used for measuring the transferred charge, Q. C_m is the measurement capacitor, connected in series with the DBD reactor. The DBD reactor was considered as two capacitors connected in series, C_g and C_d, as shown in Fig. 4-5. As introduced in Chapter 3, the charge transferred through C_m was equal to the charge transferred through the DBD reactor. The charge stored by the dielectric barrier capacitance, C_d, was equal to the charge stored by the measurement capacitor, C_m. Based on this, the voltage across the dielectric barrier and the discharge gap were measured through equations (4.2) and (4.3):

$$V_d = \frac{C_m \cdot V_m}{C_d} \tag{4.2}$$

$$V_g = V_a - V_d \tag{4.3}$$

where V_m is the voltage across the measurement capacitor and V_a is the applied voltage. The waveforms of V_a, V_d and V_g are shown in Fig. 4-6.

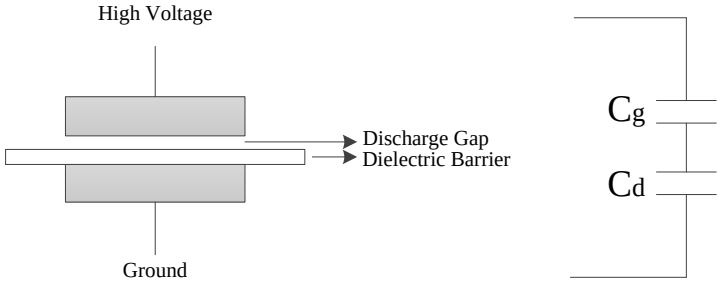

Fig. 4-5 Equivalent capacitance of DBD reactor (C_g is the equivalent capacitance of the discharge gap and C_d is the equivalent capacitance of the dielectric barrier)

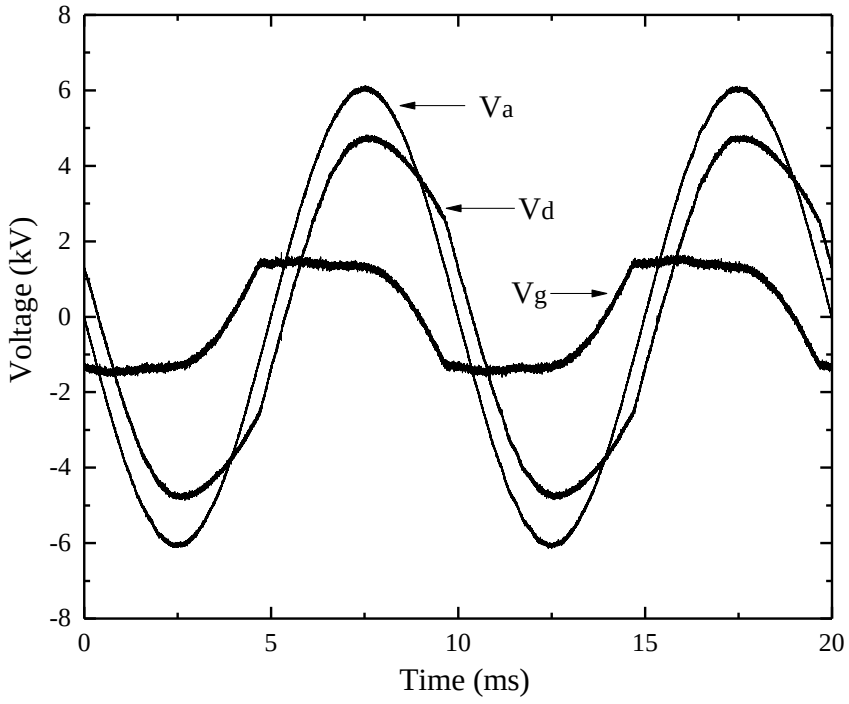

Fig. 4-6 Waveforms of applied voltage (Va), discharge gap voltage (Vg) and dielectric barrier voltage (Vd)

It can be seen that the discharge voltage was constant at 1.4 kV during the active discharge phase. The discharge voltage was found to be close to the gas breakdown voltage (1.45 kV) calculated according to equation (4.4), based on Paschen's law [55]:

$$V_b = 6.72\sqrt{pd} + 24.36(pd)\ \text{kV} \tag{4.4}$$

where p is 1.01 bar and d is 0.02 cm in the experiment. From Fig. 4-6, it was also observed that the dielectric barrier voltage lagged the applied voltage waveform by 10º. The capacitive current leads the dielectric barrier voltage by 90º; therefore, the capacitive current leads the applied voltage by 80º. Based on this, it can be considered that the DBD load had an equivalent resistive component. During the discharge period, the discharge gap can be represented as a resistor, with resistance value that varied with time in order to keep the gap voltage constant [81, 115].

4.3.3 Charge Transfer through the Discharge Gap

A. Presentation of Q-V Plot

A Lissajous figure is a very useful plot; apart from the discharge power, other important electrical parameters associated with a DBD that can be derived from it, such as C_g, C_d and V_b. This sub-section is focused on the derivation of the accumulated charge on the dielectric surface at different operating points of dielectric barrier discharges.

A Lissajous figure measured from the experimental set up of Fig. 4-3 is shown in Fig. 4-7:

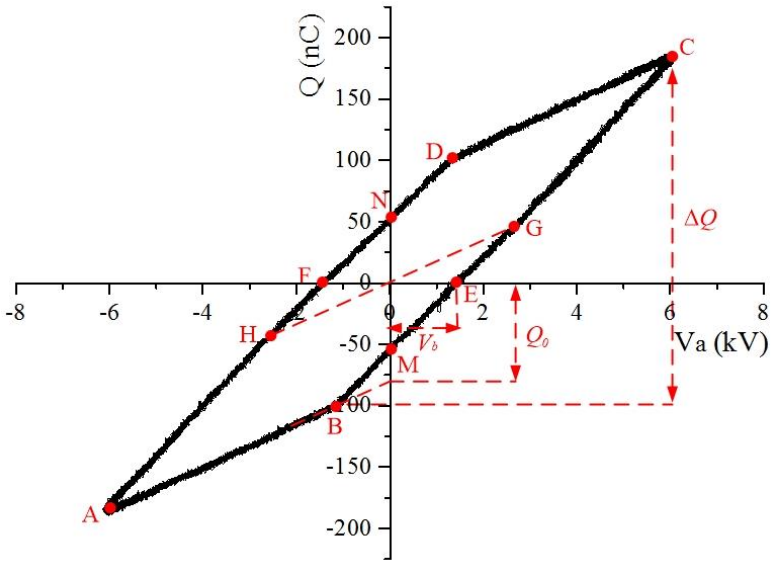

Fig. 4-7 Lissajous figure of dielectric barrier discharges

The *y*-axis represents the charge, *Q*, measured by the capacitor C_m, and the *x*-axis represents the applied voltage. It is worthy of note that the charge, *Q*, is equal to the charge stored by the dielectric barrier capacitor, since it was connected in series with the measurement capacitor. It can be seen that the Lissajous figure is a parallelogram, consisting of four straight line segments. The segments of A-B and C-D correspond to the non-discharge phases, and they can be described by equation (4.5):

$$Q(t) = C_t \cdot V_a(t) \pm Q_0 \tag{4.5}$$

where Q_0, shown in Fig. 4-7, is the charge induced in the external circuit by the accumulated charges on the dielectric surface, Q_{ac}, in the dark phase. Equation (4.5) was derived based on the fact that in the dark phase, the charge, *Q*, stored by the dielectric barrier capacitor was contributed by two components, which are the charges from the external power supply, and the induced charge due to the accumulated charge on the dielectric surface. The positive and negative signs are applied for different polarities of charges at the C-D and A-B phases. According to equation (4.5), the slopes of the line segments A-B and C-D represent the total capacitance of the DBD reactor, C_t. It was calculated that C_t was equal to 18 pF, based on the data from the Lissajous figure of Fig. 4-7.

The active discharge phases are represented by the segments of B-C and D-A, and they are described by equation (4.6):

$$Q(t) = C_d (V_a(t) \pm V_g(t)) \tag{4.6}$$

Equation (4.6) was derived based on the fact that, during the active discharge phase, the charge stored by the dielectric barrier capacitor was equal to its capacitance value, C_d, multiplied by its voltage value, V_d, which is equal to V_a (*t*) ± V_g (*t*). The positive and negative signs are applied for different polarities of gap voltages at the D-A and B-C phases. From Section 4.3.2, it is known that the discharge gap voltage was a constant value, V_b, during the discharge phase. From equation (4.6), it can be seen that, when *Q*(*t*) is equal to zero, the applied voltage is equal to the gap voltage. Therefore, from the Lissajous figure, the gap discharge voltage, V_b, can be read from the points E and F, where the line segments of B-C and D-A intersect with the *x*-axis. The slopes of the B-C and D-A line segments represent the dielectric capacitance, C_d. It was calculated that C_d was equal to 39 pF, based on the data from the Lissajous figure of Fig. 4-7. This capacitance was ~13% less than the theoretical value of 45 pF in Table 4-1, which might be related to the change of dielectric constant of soda-lime glass at high frequency of Giga Herz.

The discharge gap capacitance, C_g was equal to 33 pF, calculated using equation (4.7):

$$C_g = \frac{C_t \cdot C_d}{C_d - C_t} \tag{4.7}$$

B. Charge accumulation on the dielectric surface

This sub-section is focused on the quantitative analysis of the charge deposited on the dielectric surface. The schematic diagram of Fig. 4-8 is shown to identify and designate the related charge parameters.

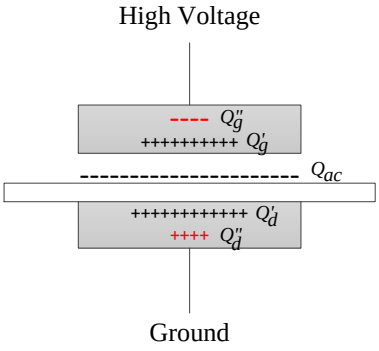

Fig. 4-8 Illustration of the charge distribution of DBD

In Fig. 4-8, Q_{ac} represents the net accumulated charge on the dielectric surface. As indicated previously, the charges stored in the electrodes resulted from two sources: the external AC source, and the accumulated charge on the dielectric surface. The charges provided by the external AC source are denoted as Q_g" and Q_d" (g and d represent the charge stored in the high voltage electrode and ground electrode respectively); and they are marked in red on Fig. 4-8. The induced charges are denoted as Q_g' and Q_d'; and they are marked in black on the electrodes in Fig. 4-8. The total charge stored in the ground electrode is equal to $-Q$ (the minus sign represents the opposite polarity of the charge measured by C_m), described by equation (4.8):

$$Q_d'' + Q_d' = -Q \tag{4.8}$$

Q_g" and Q_d" can be calculated by the following equation:

$$Q_g'' = -Q_d'' = C_t \cdot V_a \tag{4.9}$$

Only considering the charge induced by the accumulated charge, the external AC source is short-circuited according to the superposition theorem, which is shown in Fig. 4-9 (a):

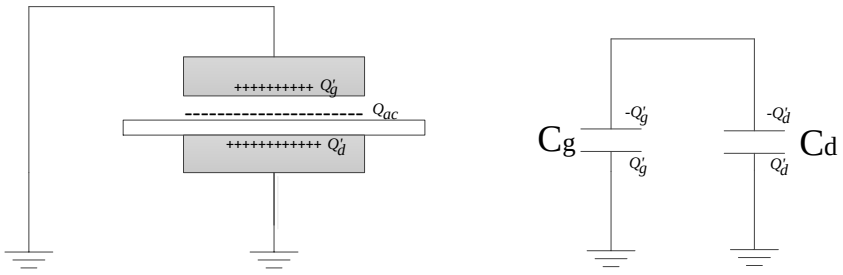

(a) (b)

Fig. 4-9 (a) Schematic presentation of the accumulated charge and induced charge (b) electric model of the charge distribution between two capacitance, C_g and C_d

Based on the electric model shown in Fig. 4-9 (b), the equations below can be derived:

$$-(Q_g^{'} + Q_d^{'}) = Q_{ac} \tag{4.10}$$

$$\frac{Q_g^{'}}{Q_d^{'}} = \frac{C_g}{C_d} \tag{4.11}$$

According to equation (4.10) and equation (4.11), the induced charge Q_g' and Q_d' are related to the accumulated charge Q_{ac} as follows:

$$Q_g^{'} = -Q_{ac} \cdot \frac{C_g}{C_g + C_d} \tag{4.12}$$

$$Q_d^{'} = -Q_{ac} \cdot \frac{C_d}{C_g + C_d} \tag{4.13}$$

Five typical operating points, shown as B, M, E, G and C on Fig. 4-7, are chosen for the analysis of the accumulated charge. Based on the equations from (4.8) to (4.13), the charge parameters of a DBD at these typical operation points were calculated, as listed in Table 4-3. The schematic presentations of the charge distribution at different operation points are shown in Fig. 4-10 (a) to Fig. 4-10 (e).

Table 4-3 Charge parameters of DBD at the typical operation points

	B	M	E	G	C
V_a (V)	-1151	0	1400	2625	6000
Q (nC)	-99	-54	0	47.5	181
Q_g''(nC)	-20.7	0	25.2	47.5	108
Q_d''(nC)	20.7	0	-25.2	-47.5	-108
Q_g'(nC)	66.3	45.7	21.3	0	-61.8
Q_d'(nC)	78.3	54	25.2	0	-73
Q_{ac}(nC)	-144.6	-99.7	-46.5	0	134.8

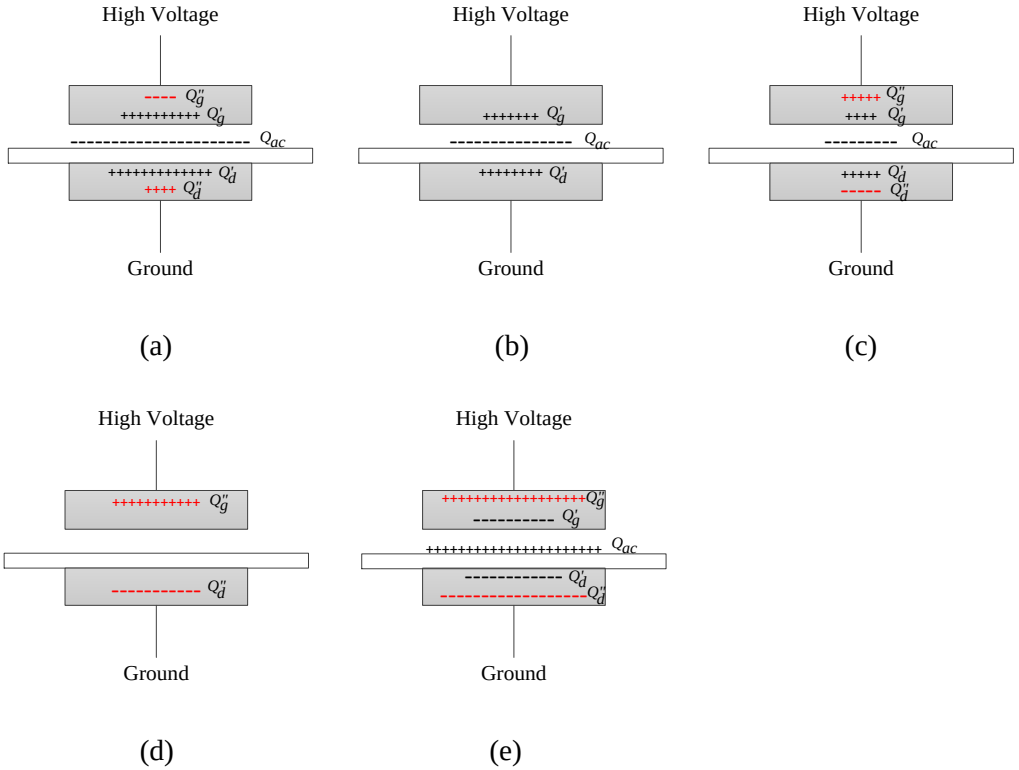

Fig. 4-10 Schematic presentation of charge distributions of DBD ((a), (b), (c), (d) and (e) correspond to the operation points of B, M, E, G and C)

Because the discharge process repeated every half voltage cycle, the amount of charge deposited on the dielectric surface at the operating points D, N, F, H and A, were the same as at the points B, M, E, G and C, respectively, but with opposite charge polarity.

C. Charge transfer

Let the accumulated charge on the dielectric surface at the operating point *B* be $Q_{ac\text{-b,}}$ and the accumulated charge at the operating point *C* be $Q_{ac\text{-c}}$. The charge transferred through the discharge gap is equal to $Q_{ac\text{-c}} - Q_{ac\text{-b.}}$ The calculation of $Q_{ac\text{-c}} - Q_{ac\text{-b}}$ is shown as follows:

At point *B*:

$$-Q_{ac-b} \cdot \frac{C_g}{C_g + C_d} + C_t \cdot V_{a-b} = V_b \cdot C_g \tag{4.14}$$

At point *C*:

$$-Q_{ac-c} \cdot \frac{C_g}{C_g + C_d} + C_t \cdot V_{a-c} = V_b \cdot C_g \tag{4.15}$$

In equations (4.14) and (4.15), $V_{a\text{-}b}$ and $V_{a\text{-}c}$ are the applied voltages at the points *B* and *C*, respectively. From both equations, the charge transferred through the discharge gap can be derived as below:

$$Q_{ac-c} - Q_{ac-b} = (V_{a-c} - V_{a-b}) \cdot C_d \tag{4.16}$$

From the Lissajous figure of Fig. 4-7, it can be seen that the term of $(V_{a\text{-}c} - V_{a\text{-}b}) \cdot C_d$ is equal to ΔQ. Therefore, it is verified that the charge transferred in the external circuit is equal to the charge transferred through the discharge gap. From Table 4-3, it can be seen that the external charge, *Q*, measured at the point *C* and *B* are 181 nC and −99 nC respectively, so the total charge transferred in the external circuit is 280 nC. The accumulated charge, Q_{ac}, on the dielectric surface at the points *C* and *B* is 134.8 nC and −144.6 nC, respectively. The charge transferred through the discharge gap can be calculated to be 279.4 nC, which quantitatively verifies that the charges transferred inside and outside of the discharge gap are the same.

4.4 Impulsive Discharge Current and Transient Voltage Drop

The transient impulsive discharge current and the voltage drops across the DBD reactor due to micro-discharges were measured, and are discussed in this section. The experimental set

up was the same as that in Fig. 4-2. The discharge gap was 0.5 mm and the dielectric barrier used was a quartz glass. This section was divided into three parts. Firstly, the impulsive current and the corresponding optical signals from the micro-discharges are presented and discussed. Secondly, the voltage drops in the external circuit and in the discharge gap are demonstrated and discussed. Finally, an electrical model of a DBD is derived, and the discharge current in the gap is calculated and presented.

4.4.1 Single Micro-discharge Current Measurement in the External Circuit

The single micro-discharge current in the external circuit and emitted light output was measured based on the experimental set up shown in Fig. 4-2. The initial test result is shown in Fig. 4-11.

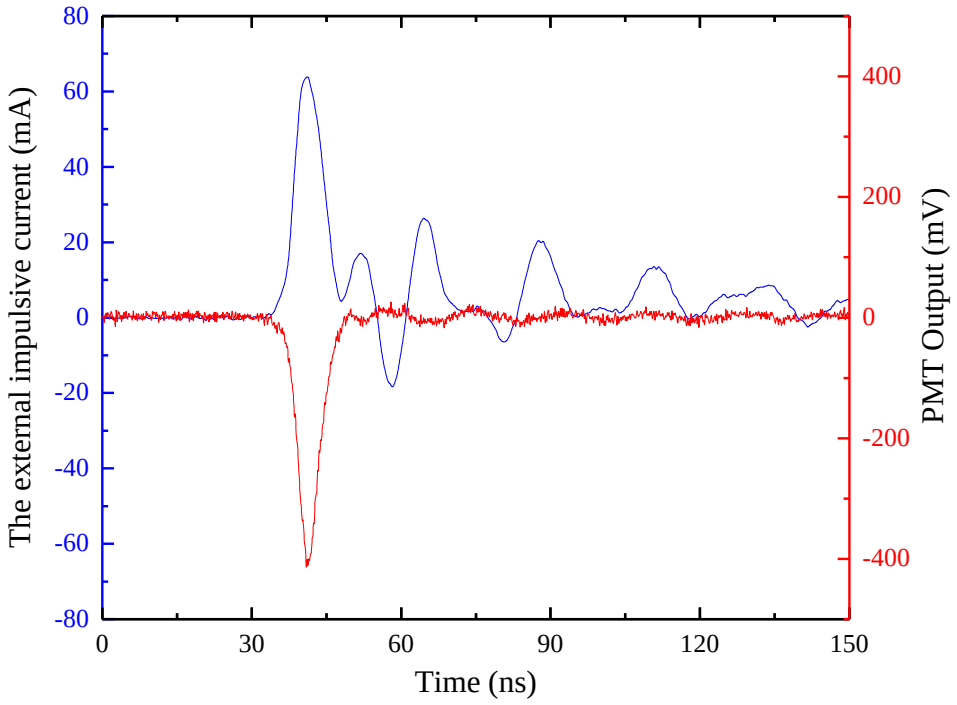

Fig. 4-11 External impulsive current and the PMT output signal measured initially

As can be seen in Fig. 4-11, a current pulse corresponds to an emitted light pulse signal, but when the amplitude of the light pulse signal dropped down to 0 V, the current showed some irregular oscillations, rather than settling at 0 A. The settling of the light pulse at 0 V indicated that the micro-discharge process was complete, which implies that the oscillations

on the current were due to the external circuit, rather than as a direct result of the discharge. This is thought to be due to the stray inductance in the current measurement circuit loop. After shortening the current measurement circuit loop to the minimum length (1.4 meters), a second test was carried out and the result is shown in Fig. 4-12.

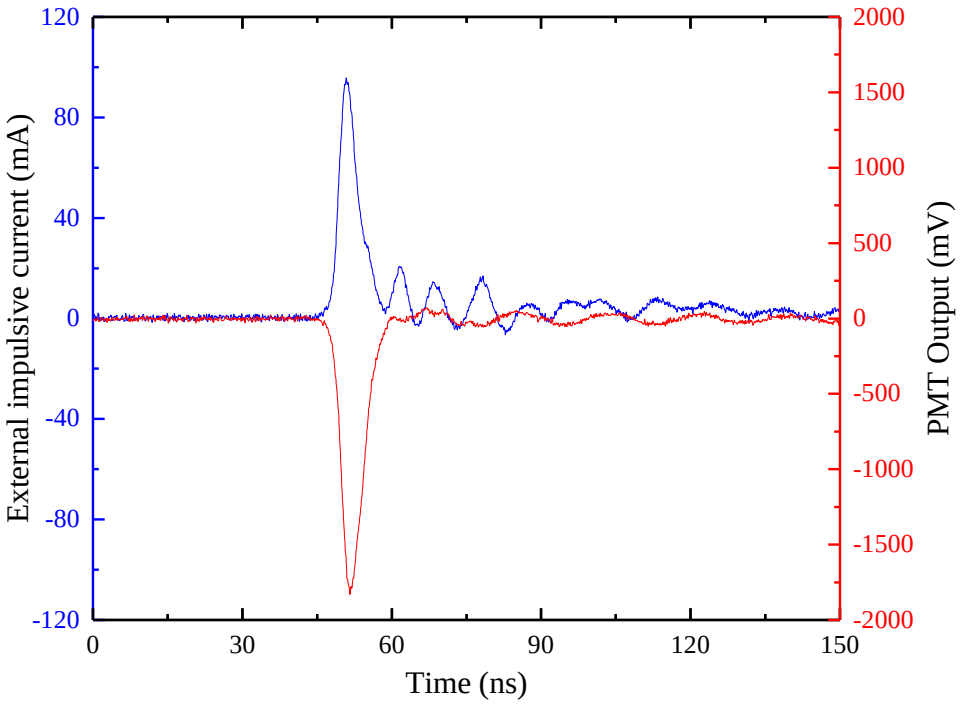

Fig. 4-12 External impulsive current and PMT output signal measured after shortening the circuit loop

At this time, the magnitudes of the oscillations associated with the impulsive current were reduced, confirming the preceding reasoning for the presence of the oscillations. Also, the rise time and the duration of the impulsive current are shorter in Fig. 4-12 compared with those in Fig. 4-11. It was not possible to eliminate the oscillations on the current waveform completely, as the circuit loop always had a certain value of stray inductance. For the impulsive current measured from the second test (Fig. 4-12), the rise time was 5 ns and the duration was 20 ns. The micro-discharge process associated with the impulsive current waveform can be explained as follows. The current started to rise at the instant of breakdown of the discharge gap, when the electric field in the gap was increased to the critical value where the ionisation coefficient was equal to the attachment coefficient. As soon as the current flow was initiated, charge accumulated at the location where the micro-discharge hit the dielectric surface. The accumulated charge generated an internal electrical field that was

opposite in direction to the external applied electrical field, which led to a decrease of the net electric field at the location where the micro-discharge occurred. When the field dropped below a certain value where the attachment coefficient was larger than the ionization coefficient, the current flow stopped.

It was found that a new micro-discharge could take place before the previous one was extinguished. Fig. 4-13 shows a negative transient current due to a group of micro-discharges.

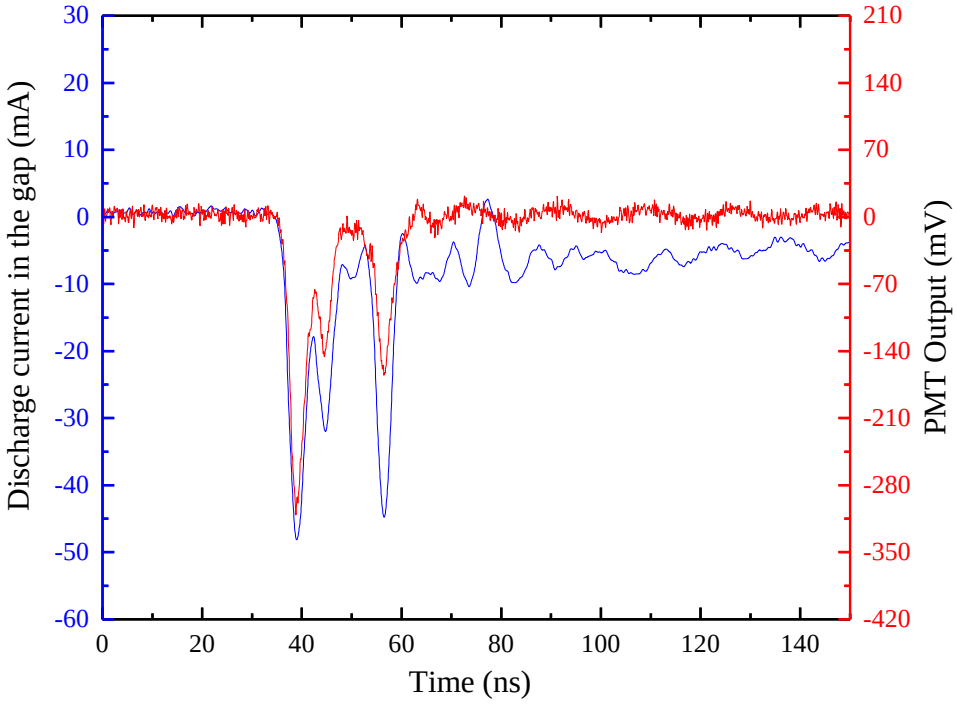

Fig. 4-13 External transient current and PMT output signal due to a group of micro-discharges

From the PMT output signal, it can be confirmed that the second current peak resulted from the occurrence of another micro-discharge before the first one was extinguished. A third micro-discharge also took place, as indicated by the PMT and current signals. The reason for the occurrence of a group of micro-discharges is that the UV emission from a preceding micro-discharge pre-ionizes the air and triggers succeeding micro-discharges [78].

4.4.2 Voltage Drops during Micro-discharge

The transient voltage drop and the corresponding impulsive current in the external circuit during a single micro-discharge event are shown in Fig. 4-14:

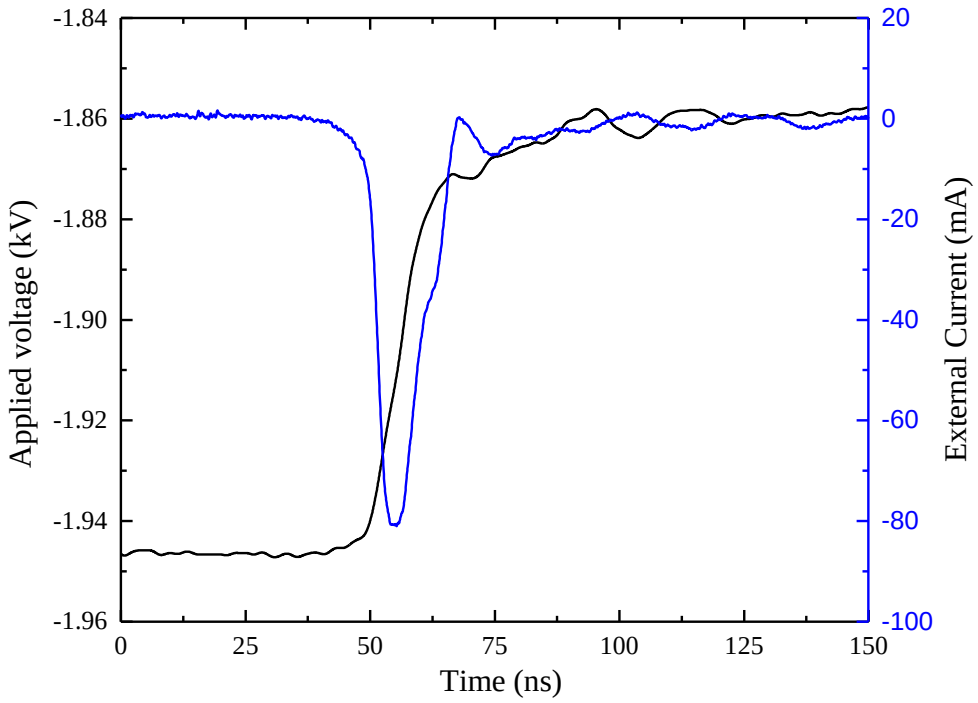

Fig. 4-14 Waveforms of applied voltage and impulsive discharge current in the external circuit

It can be seen that the applied voltage dropped at the same time as the impulsive current rose when a single micro-discharge took place in the negative voltage half-cycle. The impulsive current had duration of 20 ns and a magnitude of 80 mA, and the applied voltage was found to drop by about 82 V. The voltage drop across the dielectric barrier can be measured using an oscilloscope and equation (4.17):

$$\Delta V_d = \frac{1}{C_d}\int_0^t i_t(t)dt \tag{4.17}$$

The discharge gap voltage can be calculated by the applied voltage subtracted by the voltage drop across the dielectric barrier. The waveforms of the voltage drop across the dielectric barrier and the discharge gap are shown in Fig. 4-15 and Fig. 4-16, respectively:

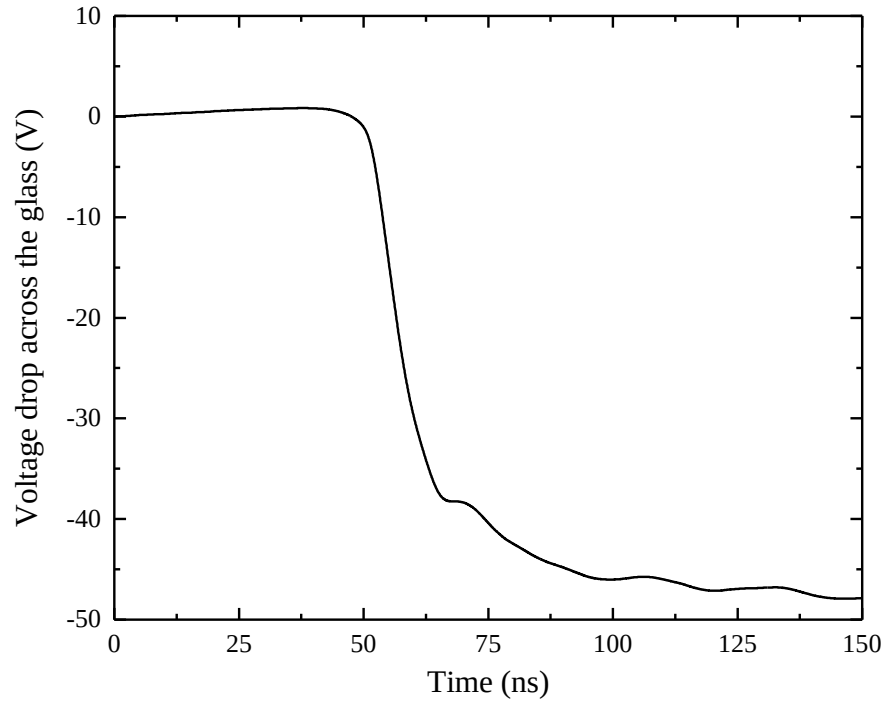

Fig. 4-15 Voltage drop across the dielectric barrier during a single micro-discharge

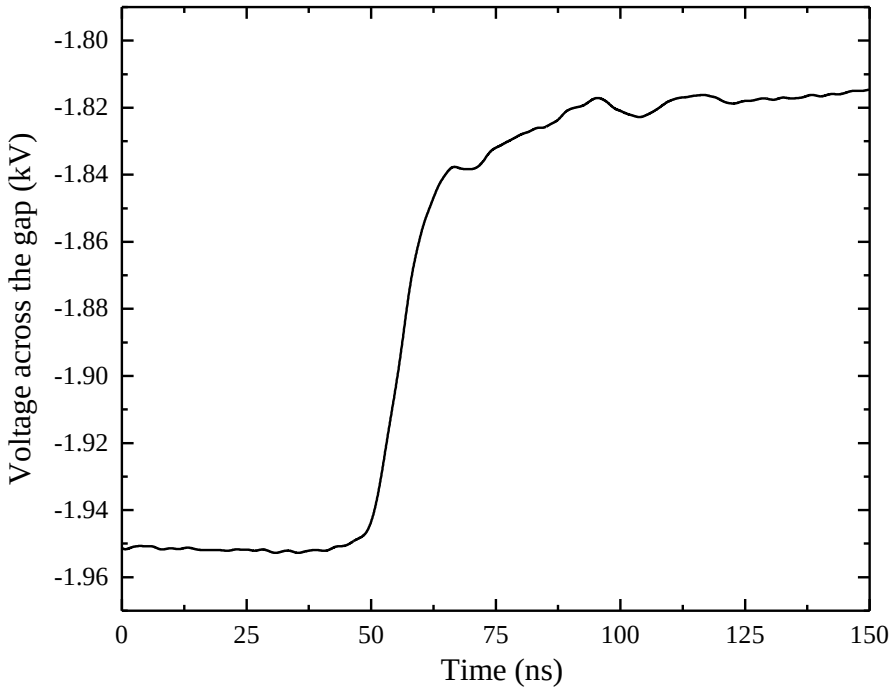

Fig. 4-16 Voltage drop across the discharge gap during a single micro-discharge

From both figures, it can be seen that, during the discharge, the voltage across the discharge gap dropped by ~130 V, while the voltage across the dielectric barrier increased by 45 V in the negative half-cycle.

From the voltage changes in the DBD reactor, it can be understood that every time a micro-discharge took place, the dielectric barrier was charged such that its voltage was increased suddenly by a certain voltage. The voltage increase across the dielectric barrier is related to the amount of charge deposited on the dielectric surface from a single discharge. The impulsive current measured in the external circuit is the charging current seen by the dielectric barrier. From the applied voltage drop, external impulsive discharge current, and the capacitances of the discharge gap and dielectric barrier, the filamentary current in the gap can be derived, as discussed in Section 4.4.3.

4.4.3 Filamentary Current in the Gap

The equivalent circuit of a DBD during the active discharge phase is shown in Fig. 4-17:

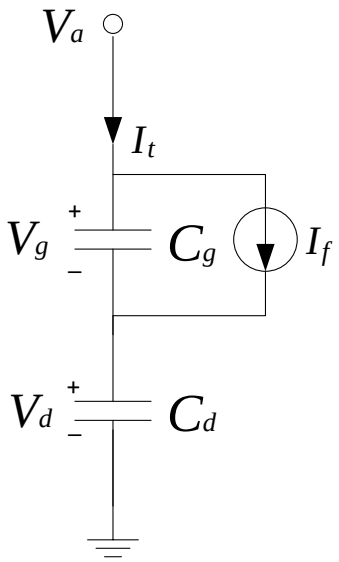

Fig. 4-17 Equivalent Circuit of a DBD

As can be seen, the filamentary current in the gap, denoted as I_f, can be modelled as a pulsed current source in parallel with the gap capacitance, C_g. Based on energy balance, the following equation can be derived [58]:

$$V_a(t)I_t(t) = \frac{d(\frac{1}{2}C_g V_g^2(\mathrm{t}))}{dt} + V_g(t)I_f(t) + \frac{d(\frac{1}{2}C_g V_d^2(t))}{dt} \tag{4.18}$$

In addition:

$$V_a = V_g + V_d \tag{4.19}$$

$$I_t = C_d \frac{dV_d(t)}{dt} \tag{4.20}$$

Based on the above equations from (4.18) to(4.20), the filamentary current in the gap can be calculated and its equation is shown as below；

$$I_f = (1+\frac{C_g}{C_d})I_t(t) - C_g \frac{dV_a(t)}{dt} \tag{4.21}$$

The capacitances of the discharge gap and the dielectric barrier, C_g and C_d, were extracted from the Lissajous figure, and their values are shown below:

$$C_g = 15 \text{ pF} \tag{4.22}$$

$$C_d = 22 \text{ pF} \tag{4.23}$$

Therefore, the filamentary current can be calculated using Matlab, based on equation (4.21). The waveform of the filamentary current is shown in Fig. 4-18. From the figure, it can be seen that the magnitude of the filamentary current is about 230 mA, which is about 3 times higher than the impulsive current measured in the external circuit. The calculated filamentary current provides further information on the electrical characteristics of the micro-discharges in the gap; the charge transferred during a single micro-discharge, which is a key parameter determining ozone generation performance, can be calculated by the integration of the filamentary current in the gap. In this experiment, the charge transferred by one single micro-discharge in the gap was calculated to be ~4 nC.

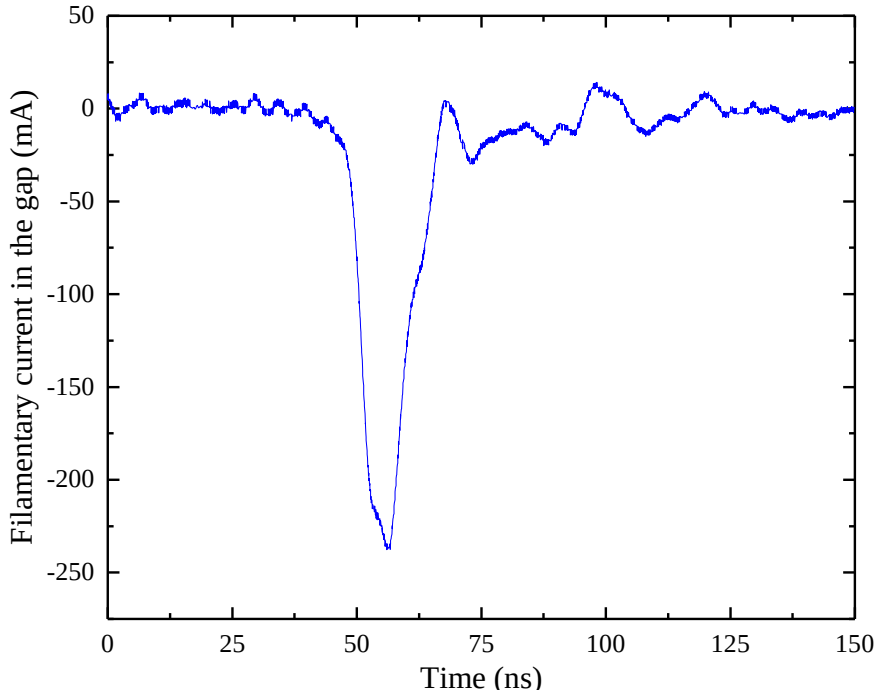

Fig. 4-18 Filamentary current in the gap

4.5 Effects of Applied Voltage Amplitude

The effects of the amplitude of the applied voltage on the discharge ignition voltage and the charge transferred in a DBD were investigated in this section. A schematic diagram of the experimental set up is shown in Fig. 4-2. A pair of cylindrical electrodes (copper) with a diameter of 30 mm was used. The dielectric barrier was soda lime glass and the discharge gap length was 0.2 mm. The frequency of the applied voltage waveform was 100 Hz, and the peak applied voltages were 4 kV, 5 kV, 6 kV and 7 kV.

The discharge ignition voltages under different applied voltages were measured. The positive and negative ignition voltages over 1000 voltage cycles with the same peak amplitude were recorded. The distributions of the ignition voltages under different applied voltages are plotted in Fig. 4-19 and Fig. 4-20.

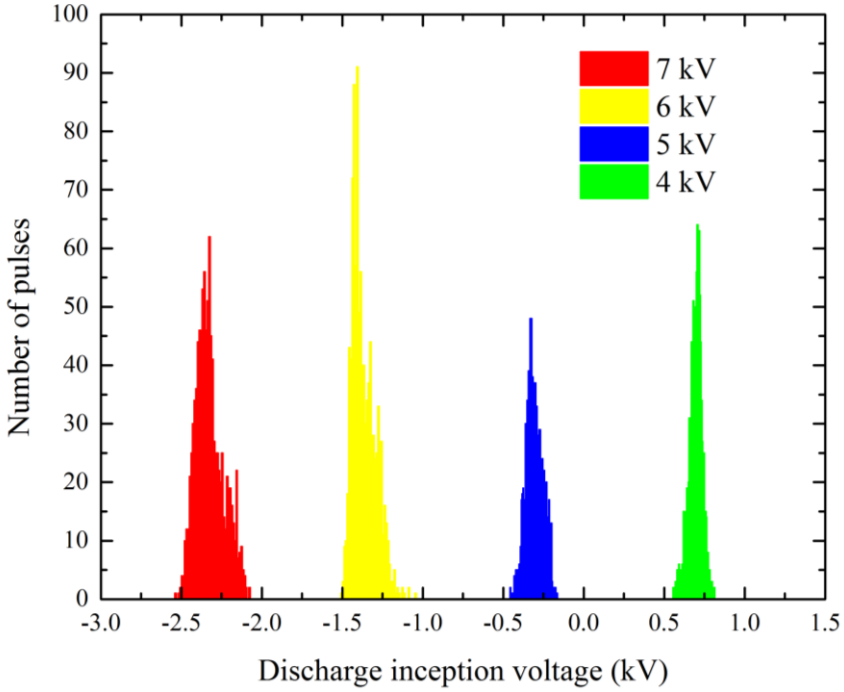

Fig. 4-19 Discharge ignition voltage during the rise time of applied voltages with different peak values

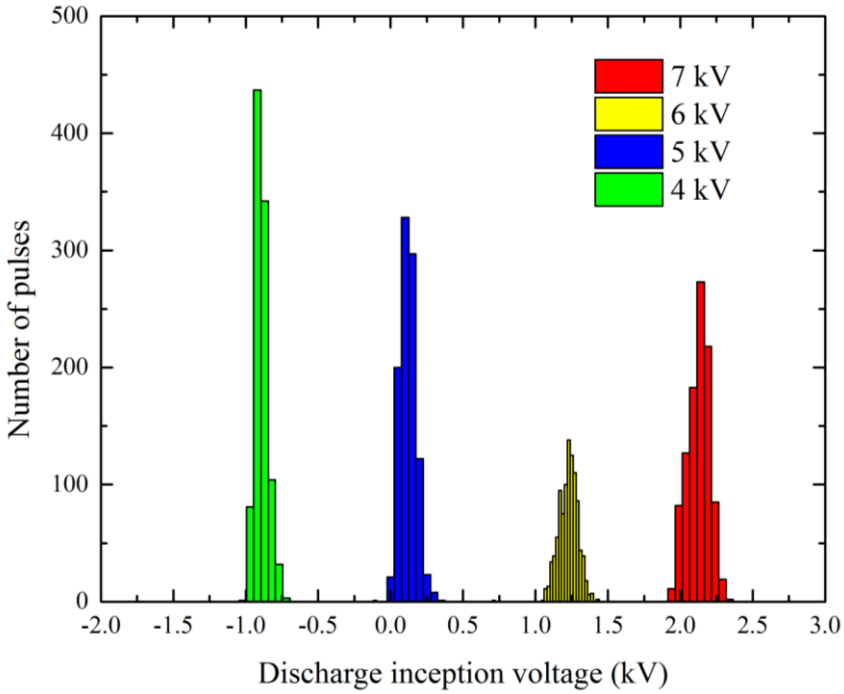

Fig. 4-20 Discharge ignition voltage during the fall time of applied voltages with different peak values

From the figures it is clear that the ignition voltages under different applied voltages all showed narrow distributions, which means that the ignition voltages were stable. The mean value and standard deviation of the ignition voltage distributions under different applied voltages were calculated, and are shown in Table 4-4. In the table, positive discharge refers to the discharge phase when the external discharge current had a positive value, and negative discharge refers to the discharge phase when the external discharge current had a negative value.

Table 4-4 Mean value of the discharge inception voltage distribution at different applied voltages at a frequency of 100 Hz

Voltage amplitudes (kV)	4	5	6	7
Positive inception voltage (V)	701	-312	-1387	-2347
Negative inception voltage (V)	-900	116	1231	2134

From Table 4-4, it can be seen that when the amplitude of the applied voltage increased to 5 kV and above, the ignition voltage of positive discharges occurred at negative voltage values, and the ignition voltage of negative discharges occurred at positive voltage values. The values of the ignition voltages under different applied voltages in Table 4-4 are plotted in Fig. 4-21and Fig. 4-22.

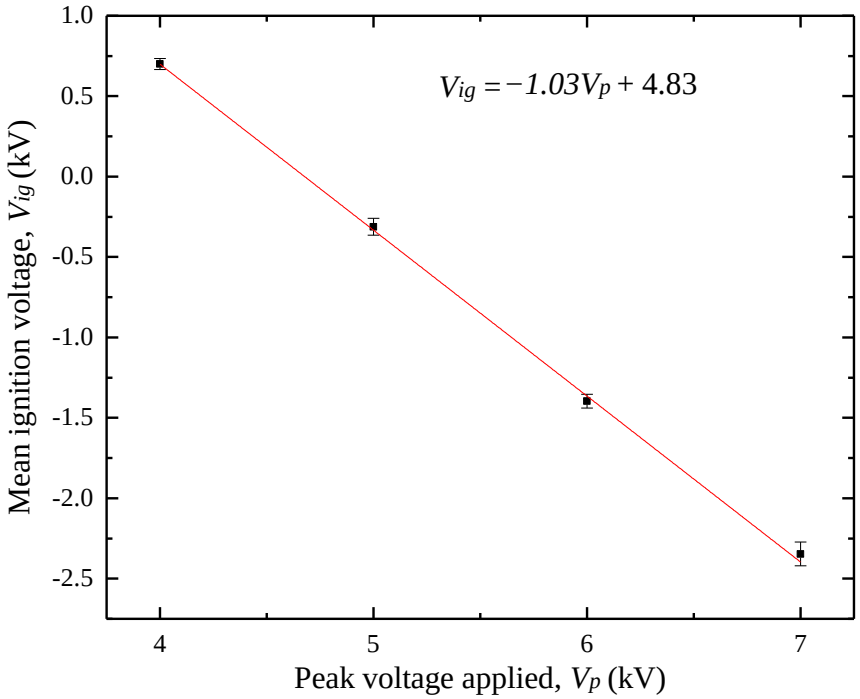

Fig. 4-21 Mean discharge ignition voltages during the rise time of applied voltages with different peak values

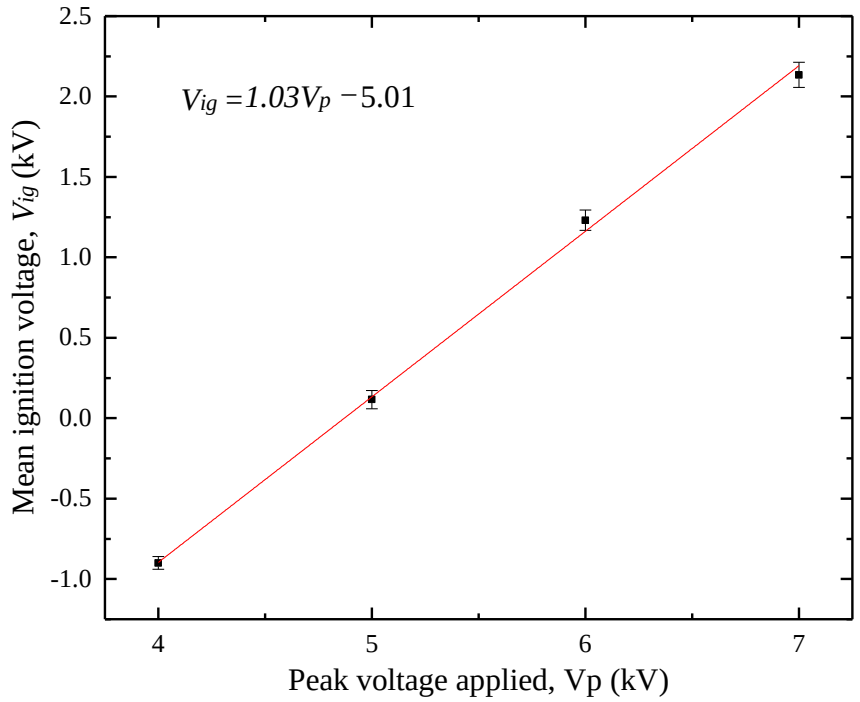

Fig. 4-22 Mean discharge ignition voltages during the fall time of applied voltages with different peak values

It can be seen that the applied voltage required for igniting the discharge decreased linearly with the increase of the peak voltage applied, for both polarities. The reason for this is due to the increased accumulated charge on the dielectric surface at higher peak voltages. The increased accumulated charge on the dielectric surface enhances the internal electrical field that is opposite in direction to the external electrical field. At a fixed gap length, the net electrical field for gas breakdown was the same; therefore, the discharge was ignited at lower external applied voltage when the internal opposite electrical field was raised, due to the larger amount of accumulated charge.

It was also found that the negative ignition voltage was higher than the positive ignition voltage by approximately 200 V, which is reflected in the fitting functions in Fig. 4-21 and Fig. 4-22. The reason for this is as follows. As the accumulated charge on the dielectric surface has the same polarity, the charge deposited from one micro-discharge repels its adjacent charge deposited from another micro-discharge. Therefore, the accumulated charge from one micro-discharge accumulates until the discharge extinguishes, and the electrical field around the accumulated charge from an individual micro-discharge is non-uniform, such that a polarity effect is apparent in the breakdown of the gas [55].

The Lissajous figures measured for DBD under different applied voltages are shown in Fig. 4-23.

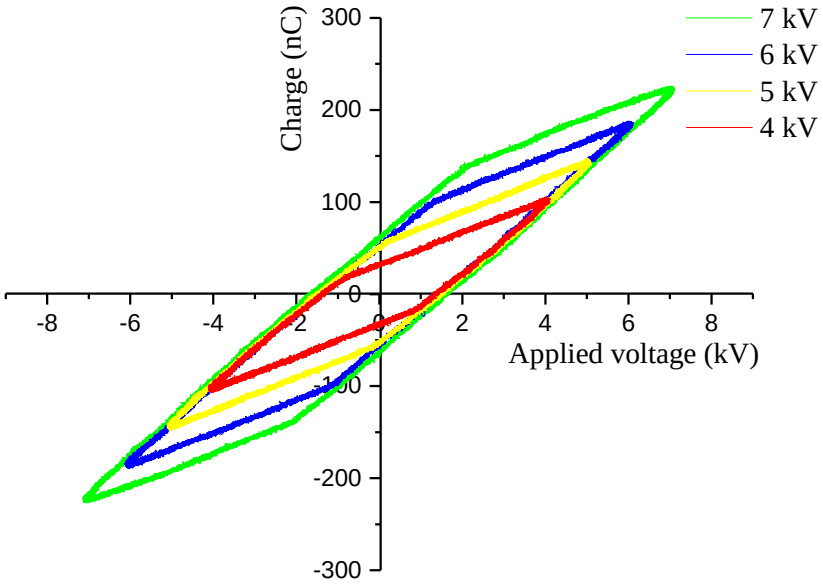

Fig. 4-23 Lissajous figures of DBD under different applied voltages

Fig. 4-23 shows that the non-discharge sides of the Lissajous figure are the same under different peak voltages. The reason for this is that the length of the non-discharge side is equal to $2V_{min}$, and V_{min}, the minimum voltage to sustain the discharge, is only related to the discharge gap breakdown voltage and the capacitances of DBD based on equation (4.24).

$$V_{\min} = \frac{V_b}{C_d}(C_g + C_d) \tag{4.24}$$

The charge transferred under different peak voltages is shown in Table 4-5, and plotted in Fig. 4-24.

Table 4-5 Charge transferred in half voltage cycles under different peak voltages at 100 Hz

Peak voltage (kV)	4	5	6	7
Charge transferred (nC)	120	197	285	364

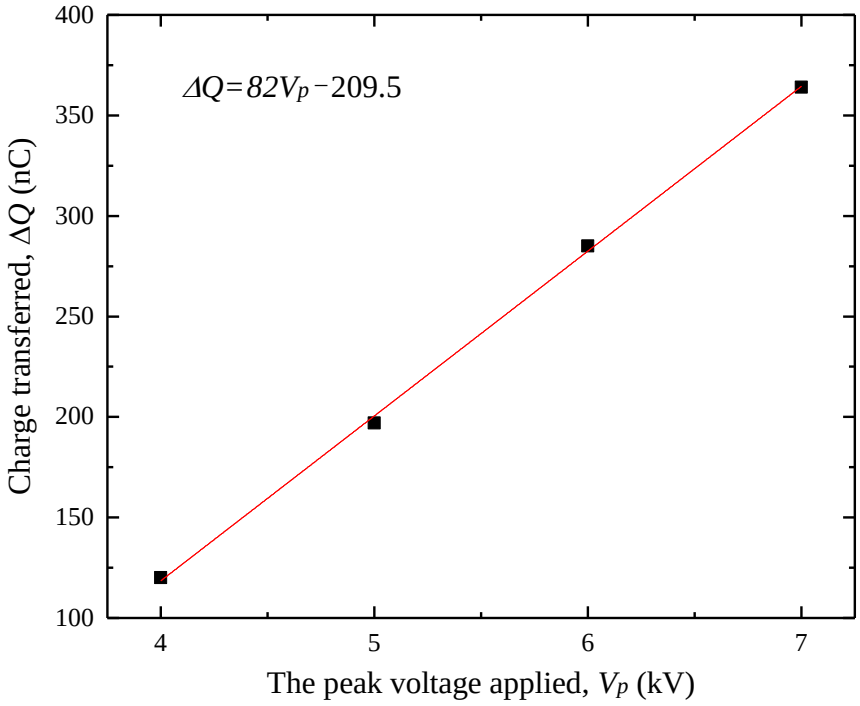

Fig. 4-24 Charge transferred during one active discharge phase under different peak voltages

Fig. 4-24 shows that the charge transferred during one active discharge phase is linearly related to the peak voltage applied, which is in an agreement with the relationship between the discharge ignition voltage and peak voltage applied.

4.6 Frequency Effect on Discharge Characteristics

The discharge characteristics of a DBD at 100 Hz and 5 kHz are compared in this section. The experimental set-up was the same as that in Section 4.5. The discharge ignition voltages and the charge transferred were measured at 5 kHz and compared with those at 100 Hz. Also, the external impulsive current distributions for both frequencies were measured and compared.

4.6.1 Ignition Voltage and Charge Transfer

The discharge ignition voltages at 5 kHz are presented in Table 4-6.

Table 4-6 Mean and standard deviation of the discharge inception voltage distribution at different applied voltages

Voltage amplitudes	Positive discharge		Negative discharge	
	Mean (V)	Standard deviation (V)	Mean (V)	Standard deviation (V)
4 kV	-561	240	0	310
5 kV	-1640	190	1010	334
6 kV	-2670	160	2090	290
7 kV	-3630	130	3120	360

Plots of the ignition voltages under different peak voltages with the frequencies of 5 kHz and 100 Hz are shown in Fig. 4-25 and Fig. 4-26.

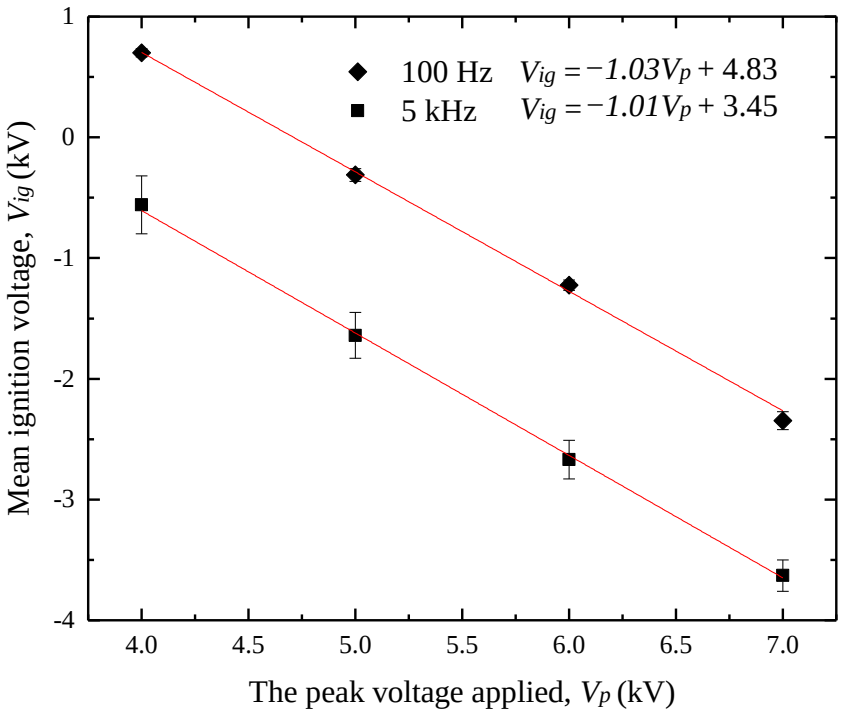

Fig. 4-25 Positive discharge ignition voltages under different peak voltages at frequencies of 100 Hz and 5 kHz

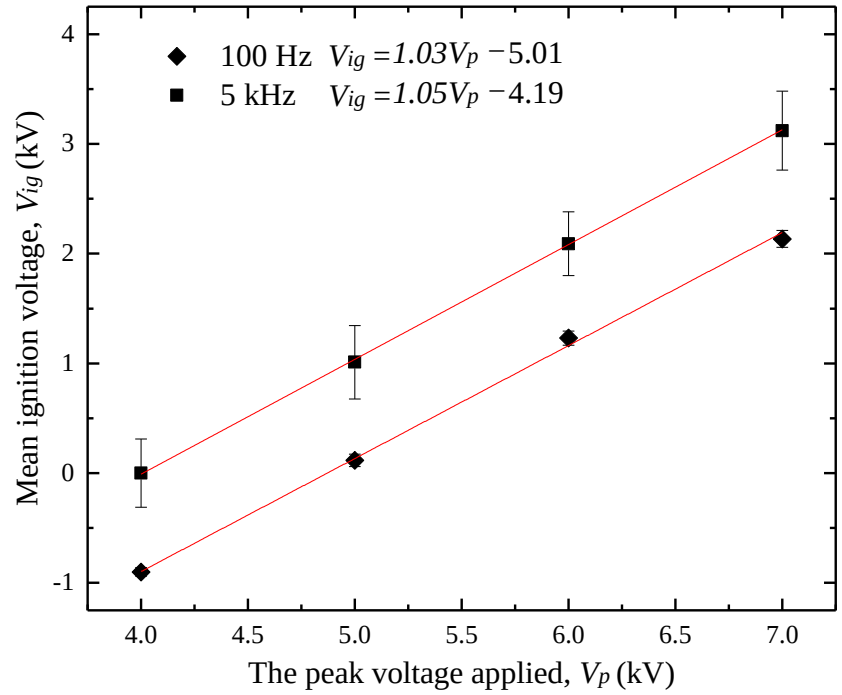

Fig. 4-26 Negative discharge ignition voltages under different peak voltages at frequencies of 100 Hz and 5 kHz

As can be seen from these figures, DBD had slightly lower ignition voltages at 5 kHz compared to those at 100 Hz. The reason for this is thought to be due to the faster rise rate of the voltage waveform at 5 kHz compared to that at 100 Hz, which results in a lower gas breakdown voltage. The charges transferred during one discharge phase under different peak voltages at 5 kHz were measured and are presented in Table 4-7, and these values are plotted in Fig. 4-27 along with the charges transferred during one discharge phase at 100 Hz.

Table 4-7 Charge transferred in one active discharge phase under different peak voltages at 5 kHz

Peak voltage (kV)	4	5	6	7
Charge transferred (nC)	139	222	305	390

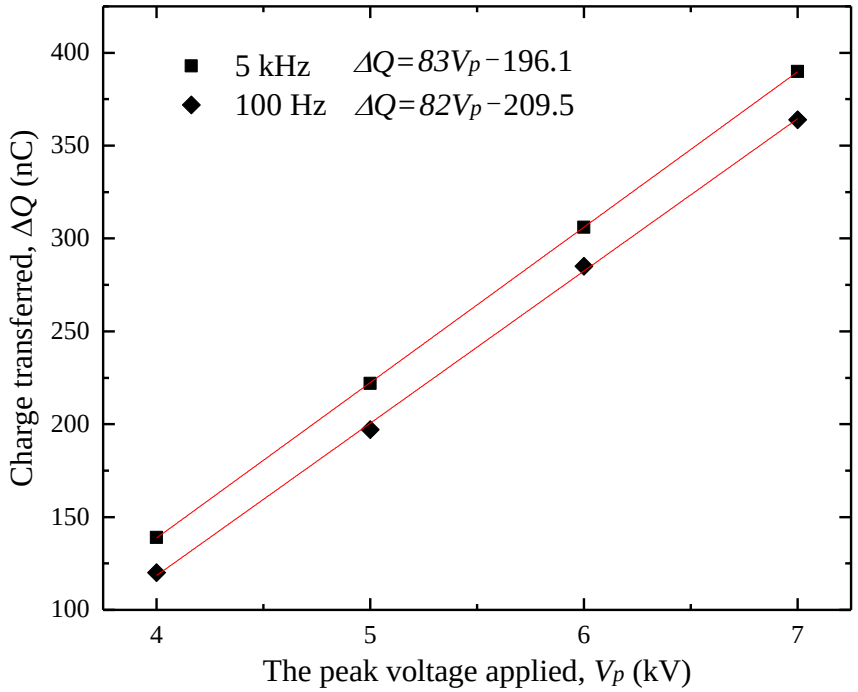

Fig. 4-27 Charge transferred during one discharge phase under different peak voltages at 100 Hz and 5 kHz

It can be seen that the charge transferred at both frequencies has a linear relation with the peak voltage applied, and the slopes of both linear lines is almost the same, but the amount

of charge transferred during one discharge phase at 5 kHz was found to be ~14% higher than that at 100 Hz.

4.6.2 Comparison of the Impulsive Discharge Current Magnitude

The voltage and current waveforms of DBD measured at 100 Hz and 5 kHz are shown in Fig. 4-28 and Fig. 4-29, respectively. As can be seen, the current at 5 kHz has impulsive current superimposed on a small capacitive current, while the current at 100 Hz only shows the impulsive current; this is because the DBD reactor has lower impedance at 5 kHz than at 100 Hz. The impulsive discharge current at both frequencies measured in the external circuit occurred randomly in time, so the statistics of the impulsive current magnitudes over 2000 pulses was conducted at both frequencies for comparison. Fig. 4-30 and Fig. 4-31 are the pulse statistics of the impulsive current magnitudes at 100 Hz and 5 kHz, respectively:

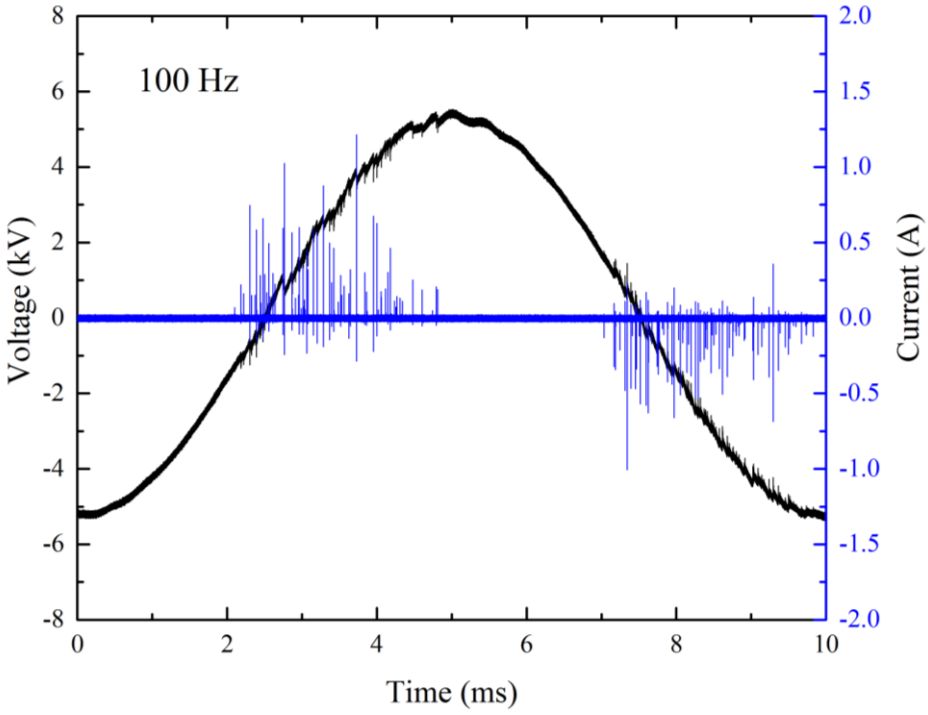

Fig. 4-28 Voltage and external current waveforms at 100 Hz

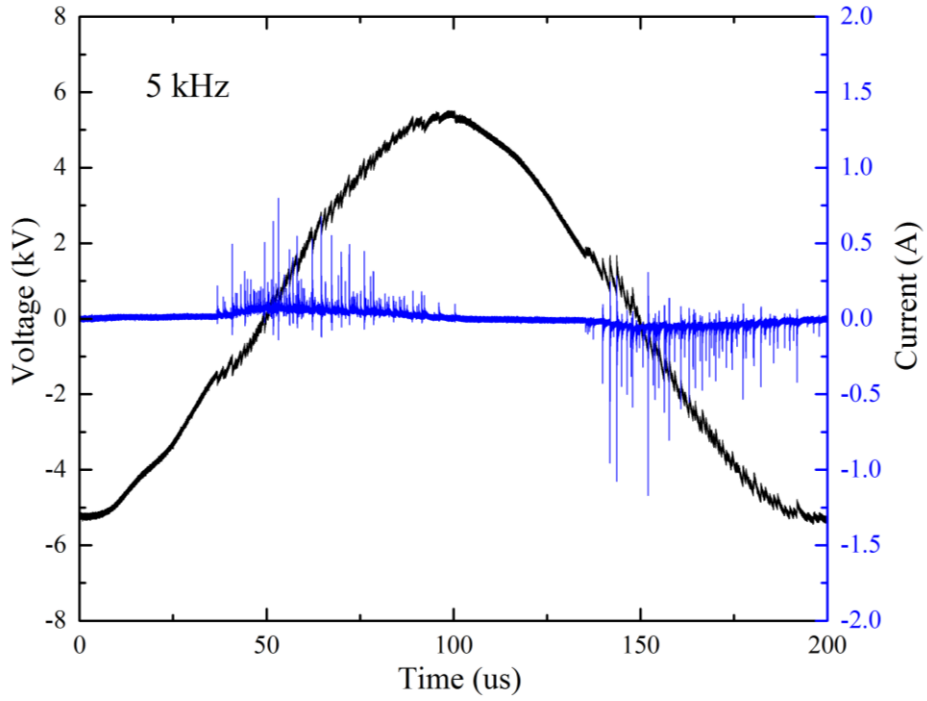

Fig. 4-29 Voltage and external current waveforms at 5 kHz

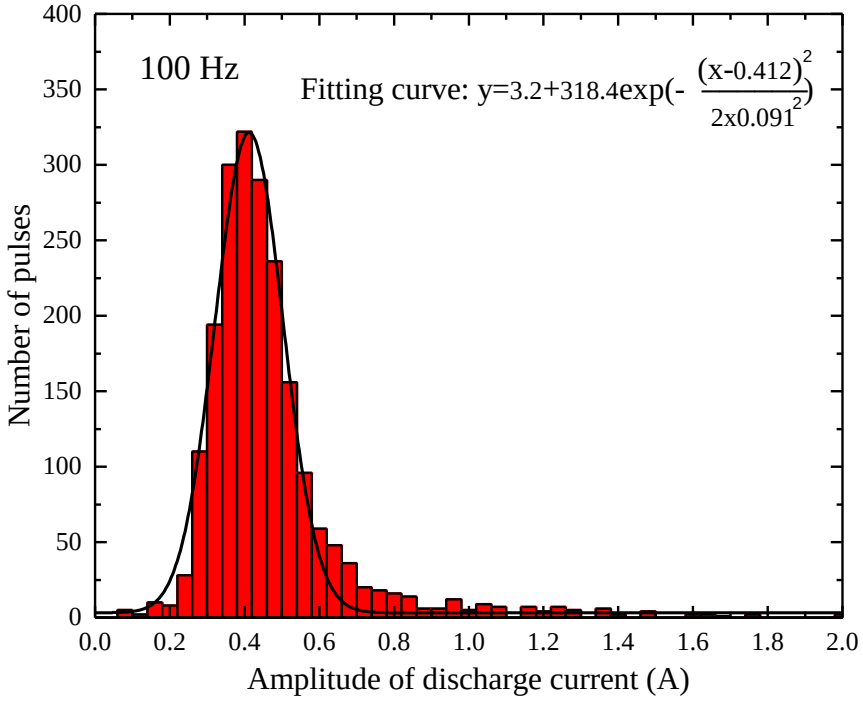

Fig. 4-30 Distributions of external impulsive current amplitude at 100 Hz

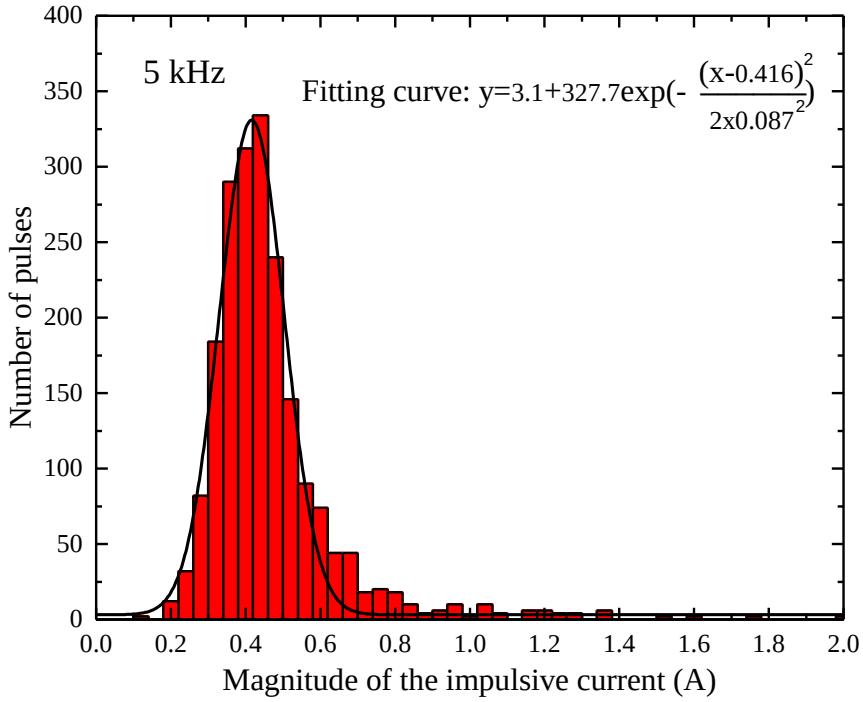

Fig. 4-31 Distributions of external impulsive current amplitude at 5 kHz

Gaussian fitting curves were applied to the data in Fig. 4-30 and Fig. 4-31 to provide the mean impulsive current magnitude and the standard deviation of the statistical distributions, as shown in Table 4-8. The impulsive currents measured at 100 Hz and at 5 kHz have similar statistical distributions, for which the mean values and standard deviations are almost the same.

Table 4-8 Mean value and standard deviation of impulsive current magnitude

Frequency	Mean value (A)	Standard deviation
100 Hz	0.412	0.091
5 kHz	0.416	0.087

4.7 Conclusion

Measurement techniques to determine the electrical parameters of DBD have been described, and the electrical characteristics of DBD were quantitatively analysed in this chapter. The recorded current waveforms demonstrated that the DBD showed a filamentary discharge mode in this work. The discharge impulsive currents associated with DBD were found to conform to a Gaussian distribution. It was also found that the current associated with one single micro-discharge corresponded to one pulsed emitted light signal. A group of micro-discharges was detected occasionally, showing that a new micro-discharge can occur before the previous one is extinguished. The results herein showed that the duration of a single micro-discharge was in the range from 20 ns to 40 ns. The charge transferred through the discharge gap was verified to be equal to the charge transferred in the external circuit, through the quantitative analysis of the accumulated charge on the dielectric surface. Based on the electrical model of DBD, an equation for calculating the discharge current in the discharge gap was derived, which is important for the further study on the discharge parameters in the gap that are related to the ozone generation efficiency.

Different applied voltages with different amplitudes were applied for energizing the DBD, and it was shown that the discharge ignition voltages and the charge transferred during one active discharge phase had a linear relation with the amplitudes of the applied voltages. The electrical characteristics of the DBD energized by AC voltages at 100 Hz and 5 kHz were compared, and the results showed that the amount of charge transferred was 14% higher at 5 kHz than at 100 Hz, but the distribution of the impulsive current under both power frequencies showed similar behaviour.

Following the background and literature review of DBDs, this part of the experimental work provided an in-depth understanding of the electrical characteristics of DBDs. The methodologies developed in this chapter for the measurement of discharges parameters of DBDs can be applied to the investigation of electrical properties of ozone generator in the next stage of this research project.

5 STATISTICAL ANALYSIS OF PULSED MICRO-DISCHARGES AND OZONE GENERATION

5.1 Introduction

It is the interest of this research work to optimize dielectric barrier discharges in order to increase ozone generation efficiency. From Chapter 4, it is known that the behaviour of pulsed micro-discharges is the key feature of DBDs. The charge transferred by one micro-discharge (Q_c) inside the discharge gap and the micro-discharge energy determines the amount of dissociation of oxygen by electron impact and, thus, the efficiency of ozone generation [79]. Therefore, optimization of pulsed micro-discharges is the best approach to increase the ozone generation efficiency [13]. However, numerous pulsed micro-discharges in DBDs take place randomly in the discharge gap, making their electrical characterization difficult in two aspects: measuring the filamentary current, and understanding its distribution over the applied voltage cycles. Over the last 30 years, much research has been dedicated to the electrical characterization of micro-discharges. Two approaches to measure the filamentary current have been identified in the literature: direct measurement, by incorporation of a well-shielded, fast, current probe into the ground electrode, to measure the current of an individual micro-discharge in the gap [14, 77, 116]; and indirectly, by measuring the external impulsive current and then calculating the filamentary current, I_f, in the gap [79, 83, 117, 118], as shown in equation (5.1),

$$I_f = (1+\frac{C_g}{C_d})I_t - C_g \frac{dV_a}{dt} \tag{5.1}$$

where C_g and C_d are the capacitances of the gap and the dielectric barrier, respectively, I_t is the total external current, and V_a is the applied voltage.

Disadvantages associated with direct measurement include the fact that it can only provide information on the filamentary current in one specific location, and it is difficult to construct a ground electrode to incorporate a well-shielded current probe without undesirable modification of the original field distribution. Dřímal *et al.* [79] and Liu *et al.* [83] derived an equation relating the filamentary current to the applied voltage and external impulsive current. In the work of Dřímal *et al.* [79], a term incorporating the derivative of applied voltage was neglected, however, leading to inaccurate calculation of the filamentary current

and the transferred charge, since there are always abrupt fluctuations in the applied voltage when a discharge occurs [70]. In the work of Liu *et al.* [83], both the external current and the derivative of the applied voltage were considered, but only the calculated filamentary current waveform in one cycle was presented; the statistical distribution of the filamentary current over several voltage cycles was not discussed. Jidenko *et al.* provided a statistical distribution of the electrical characteristics over 500 micro-discharges in [118], but only the factor $(1+C_g/C_d)$ was taken into account for calculation of the filamentary current in the gap, the derivative of applied voltage being neglected.

In the present work, the instantaneous applied voltage and the impulsive current in the external circuit were measured by an oscilloscope with a bandwidth of 2.5 GHz and maximum sampling rate of 40 GS/s. The oscilloscope memory allows the acquisition of 200 cycles of voltage and current information with sampling rate of 5 G/s, when operating at 5 kHz. Subsequent processing of the recorded data using Matlab revealed the statistical distribution of important electrical parameters of pulsed micro-discharges during the 200 voltage cycles. In contrast to previous studies in the literature, the statistical distribution of filamentary current, considering both the factor $(1+C_g/C_d)$ and the derivative of applied voltage, has been analyzed in this chapter. The electrical parameters associated with the filamentary current recorded include the magnitude of the current, the duration of the current, the charge transferred, the micro-discharge energy, and the number of current pulses during one active discharge phase (occurring in half of a voltage cycle). To optimize the pulsed micro-discharges in the barrier discharge for improved ozone generation efficiency, different experimental conditions (different discharge gap lengths, different gas pressure, and different applied voltages) were investigated, and the ozone generation data was recorded simultaneously during the filamentary current measurement. The ozone generation efficiency for different discharge gaps, gas pressures and applied voltages was investigated, with consideration for the effect of the statistical characteristics of the filamentary current under different conditions.

5.2 Experiment Set-up and Methodology

5.2.1 Test Cell

A new plate type DBD reactor (Type-B) with larger discharge area was designed and developed, in order to study the statistical characteristics of micro-discharges and ozone generation in oxygen-fed dielectric barrier discharges. A schematic drawing of this reactor is shown in Fig. 5-1, which shows that the reactor consisted of three pairs of electrodes with the dimensions of 50 mm (L) × 10 mm (W) × 30 mm (D). The dielectric barriers were composed of rectangular soda-lime glass of thickness 0.5 mm, with the dimensions of 75 mm × 50 mm. The discharge gap was constructed in a sealed PTFE chamber and the gap length could be accurately controlled from 0.2 mm to 0.6 mm by the inclusion of different spacers, which were made of Pyrex glass. The maximum fill pressure was 2 bar absolute. The effective gap and dielectric barrier equivalent capacitances with different gap lengths were calculated, and are shown in Table 5-1.

Table 5-1: Equivalent capacitance of discharge gaps and dielectric barrier with different lengths

	0.2 mm	0.3 mm	0.4 mm	0.5 mm	0.6 mm
Dielectric barrier equivalent capacitance (pF)	191.2	191.2	191.2	191.2	191.2
Discharge gap equivalent capacitance (pF)	199.0	132.8	99.6	79.7	66.4

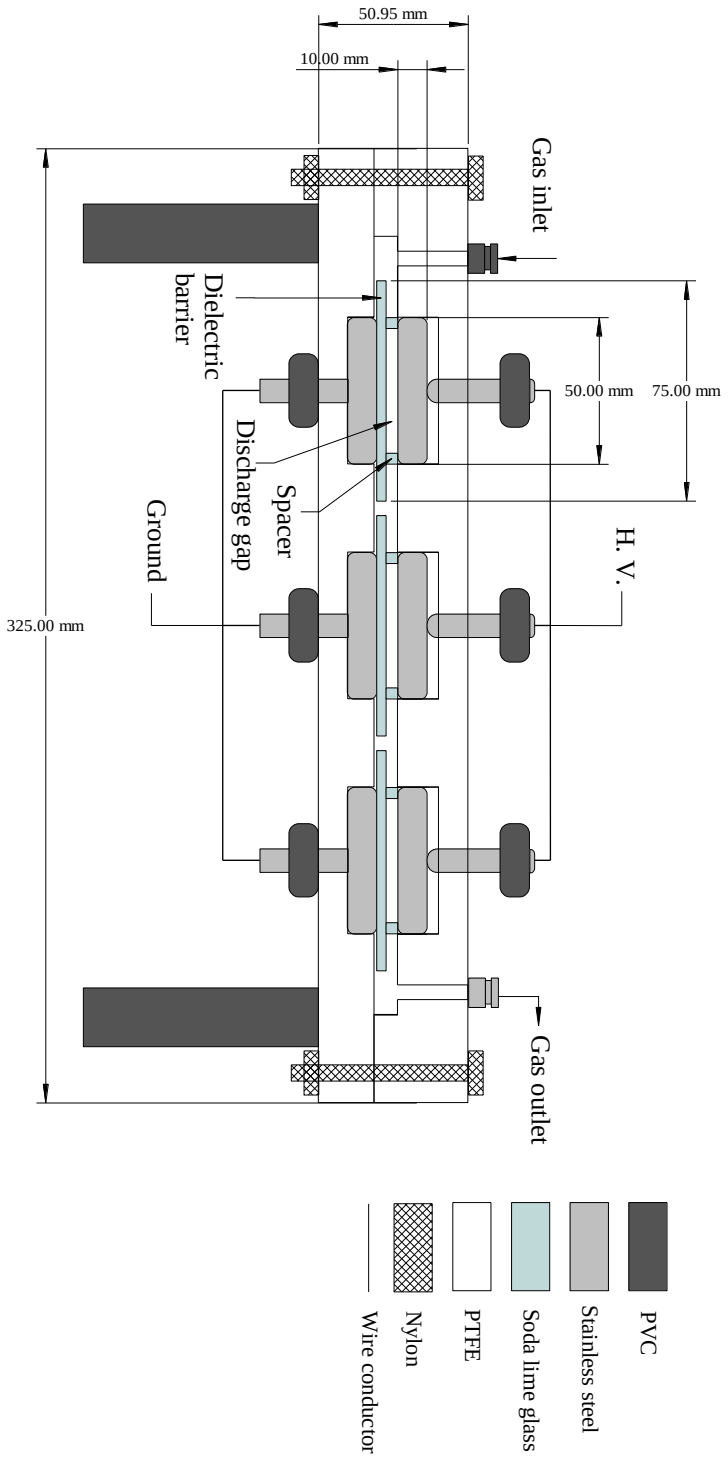

Fig. 5-1 Schematic diagram of Type-B plate DBD reactor

5.2.2 Experimental Set-up

The experimental set-up was as shown in Fig. 5-2.

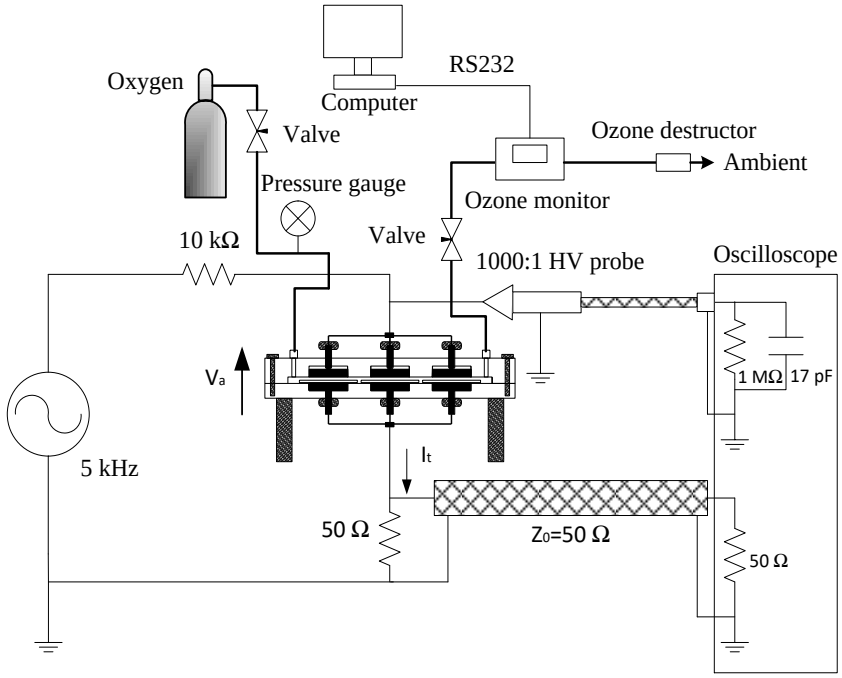

Fig. 5-2 Schematic diagram of experimental set-up

The ozone generator was energized by 200 cycles of a sinusoidal voltage with amplitude of 5.5 kV, at a frequency of 5 kHz. The AC power supply employed was the Pacific 112AMX, the output voltage of 300 V being stepped up to 5.5 kV by a high-frequency transformer. A detailed schematic diagram of this power supply can be found in Chapter 3. Experiments were conducted in an oxygen environment, with absolute pressure from 1 bar to 2 bar, and the ambient temperature of 25 °C. The internal gas pressure was controlled through two needle valves located before and after the ozone reactor. The flow rate was fixed at 0.5 L/min in all experiments. The external current was measured through a 50 Ω coaxial cable (RG405), with a bandwidth of 18 GHz. The voltage across the ozone reactor was measured using a LeCroy PPE6kV high-voltage probe (400 MHz). The measurement data were acquired by an oscilloscope (LeCroy WaveRunner 625 Zi) with a bandwidth of 2.5 GHz and maximum sampling rate of 40 GS/s. The ozone concentration was measured using an ozone monitor (BMT964) and the data was transferred to a computer for real-time integration, to calculate the total ozone production during the application of 200 voltage cycles.

5.2.3 Experimental Methodology

A transient sinusoidal voltage of 200 cycles was employed in the work. The choice of applying 200 voltage cycles fulfils the following requirements:

- it reduces the heating effects in the ozone-synthesis process;
- electrical measurement data can be acquired and recorded at a high sampling rate (≥5 GS/s).

The parameters measured and recorded during the application of 200 voltage cycles included the applied voltage, V_a, and the total current, I_t, in the external circuit, and the ozone concentration as a function of time. The measured data were processed using Matlab to obtain the electrical parameters of each filament and their statistical distributions. The numerical treatments in this work are described as below:

1) Separation of the impulsive current

The measured current in the external circuit consists of two components: a displacement current at the applied voltage frequency of 5 kHz; and an impulsive current with duration of the order of ns. A high-pass filter with lower cut-off frequency of 10 kHz was used in Matlab to separate the impulsive current component.

2) Calculation of the filamentary current in the gap

The filamentary current in the discharge gap was calculated using(5.1). The high sampling rate of the oscilloscope enabled the derivative of the applied voltage V_a to be obtained numerically using Matlab.

3) Calculation of the micro-discharge energy

The energy dissipated by the micro-discharge (W_0) in the gap can be calculated in the following, as shown in equation (5.2):

$$W_0 = \int_0^t I_f(\tau) V_g(\tau)\,\mathrm{d}\tau \tag{5.2}$$

where V_g is the gap voltage and t is the duration of the micro-discharge.

4) Statistical treatment of the filamentary current and micro-discharge energy over a representative 25 cycles

Limited by the maximum acquisition memory of the oscilloscope, 25 cycles of voltage and current waveforms at the sampling rate of 5 GS/s were acquired. The representatives 25 cycles were taken from the middle of the 200 cycles of voltage and current. The number of discharges per cycle (n_0), the amplitude of the filamentary current (I_p), the duration of the filamentary current pulse (t_d), the transferred charge associated with a filament (Q_c), and the individual micro-discharge energy (W_0) over the representative 25 cycles were statistically analyzed.

5) Reduced electric field calculation

The reduced electric field, *E/N*, is an important quantity that determines the electron energy distribution function and reaction rate coefficients [15, 37, 40]. It is the interest of this work to investigate the characteristics of filamentary current and ozone generation efficiency over a range of *E/N* values (100 Td – 200 Td), calculated using equation (5.3):

$$E / N = V_g / (d_g \cdot N) \tag{5.3}$$

where N is the gas density calculated from the ideal gas equation [55], d_g is the gap length and V_g is the gap voltage. The reduced electric field *E/N* as a function of gap length and gas pressure were investigated in the study.

6) Ozone generation efficiency calculation

The ozone concentration was monitored in real-time via a computer-based system. Ozone generation efficiency was calculated as the integral of the ozone produced over 200 cycles divided by the discharge energy over 200 cycles.

5.3 Experimental Results

5.3.1 Filamentary Current Pulses Statistics

Fig. 5-3 shows the waveforms of the applied voltage and external impulsive current measured at discharge.

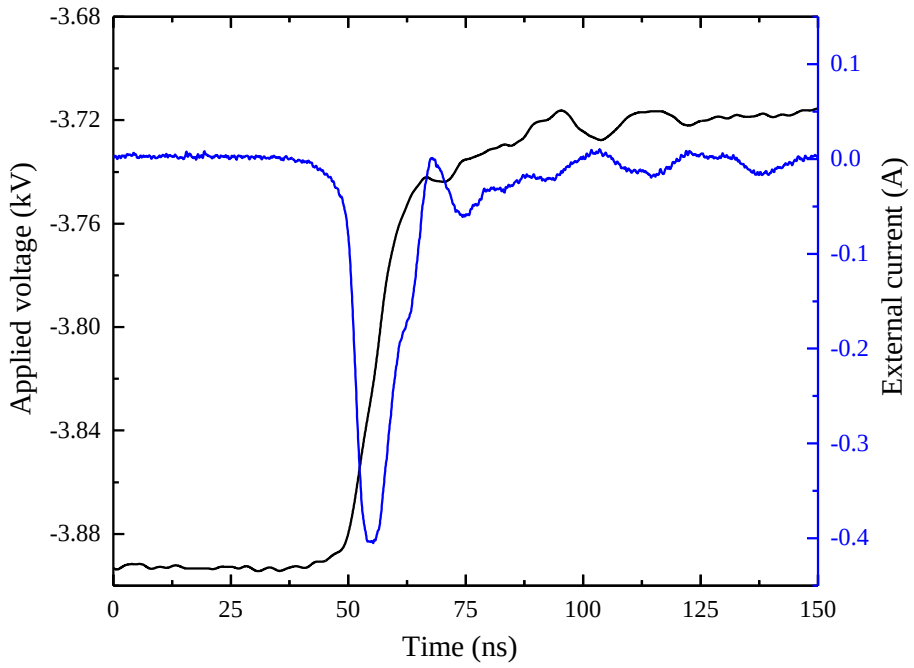

Fig. 5-3 Applied voltage and external impulsive current (at 0.5-mm gap length and 1 bar absolute, with 5.5-kV applied voltage at 5 kHz)

The filamentary current was calculated using equation (5.1) and plotted in Fig. 5-4:

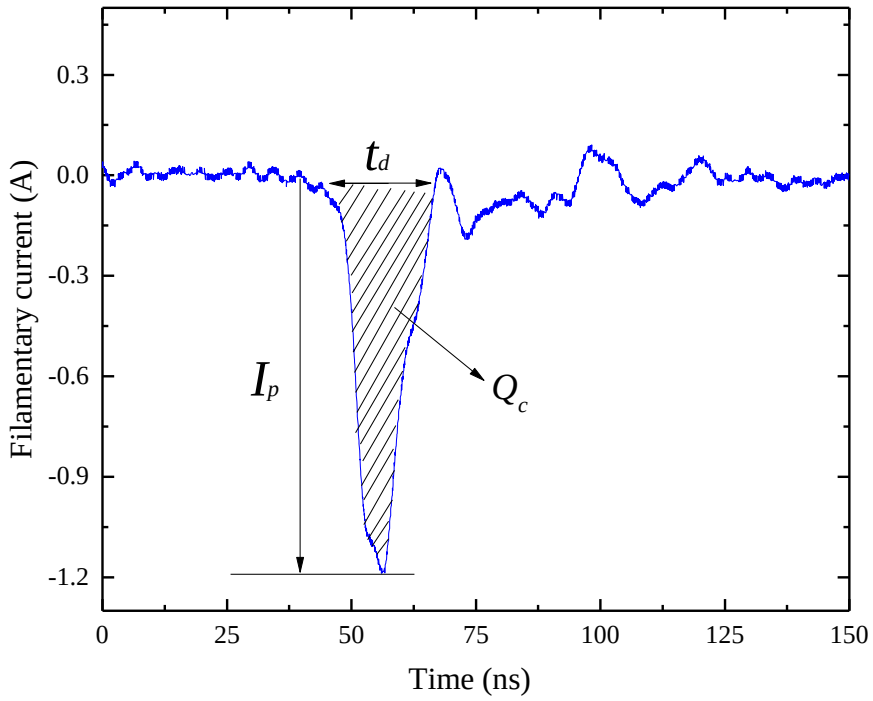

Fig. 5-4 Calculated filamentary current in the gap (at 0.5-mm gap length and 1 bar absolute, with 5.5-kV applied voltage at 5 kHz)

As can be seen in Fig. 5-4, t_d is the filamentary current duration, defined as the time interval starting from where the current rises from zero to where the current falls to zero. I_p is the amplitude of the filamentary current pulse, and Q_c is the transferred charge which is equal to the area integrated over the time interval defined by t_d.

Fig. 5-5 shows the filamentary current of one voltage cycle, obtained when the peak voltage applied was 5.5 kV and the gap distance was 0.5 mm, at the absolute pressure of 1 bar.

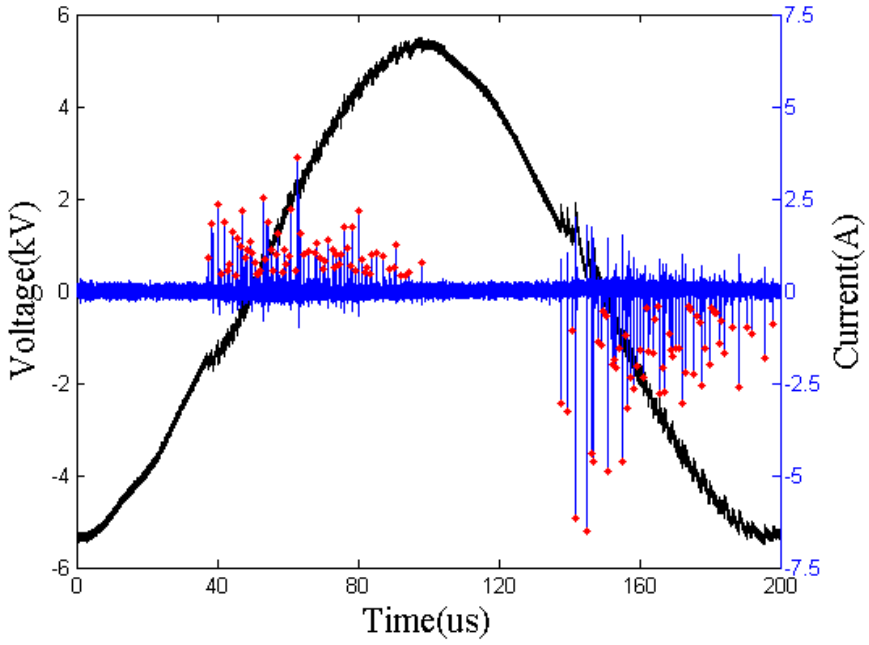

Fig. 5-5 Filamentary current of one voltage cycle (at 0.5 mm gap length and 1 bar absolute, with applied voltage 5.5 kV at 5 kHz)

The detected filamentary currents are marked using red dots on Fig. 5-5. The detection limit applied was ±0.2 A. The important parameters of individual filamentary currents, I_p, t_d, Q_c and W_0, over the representative 25 cycles were statistically analysed and the histograms of these parameters are presented in Fig. 5-6 to Fig. 5-9.

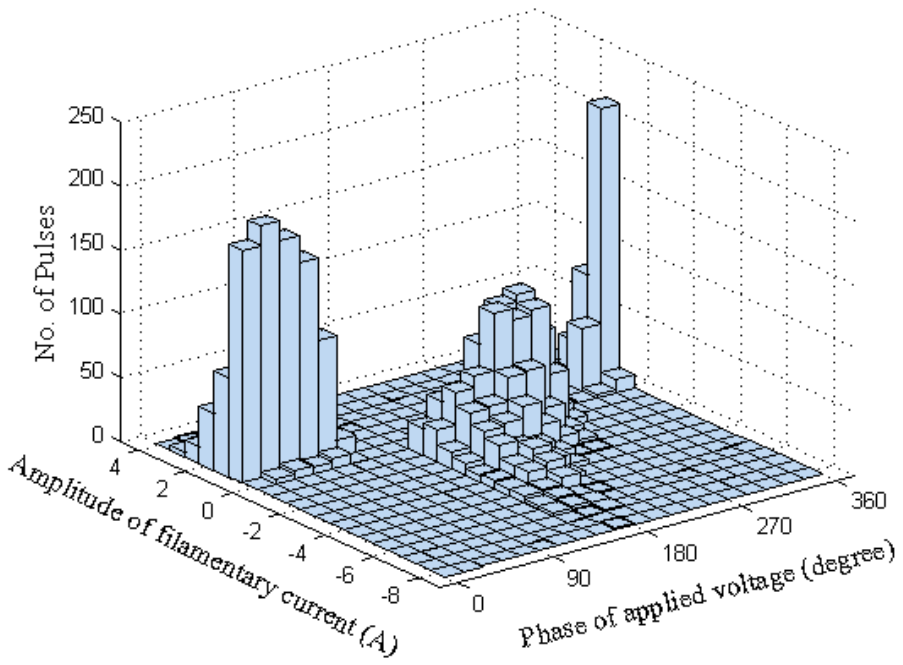

Fig. 5-6 Histogram of amplitude of filamentary current I_p (at 0.5 mm gap length and 1 bar absolute)

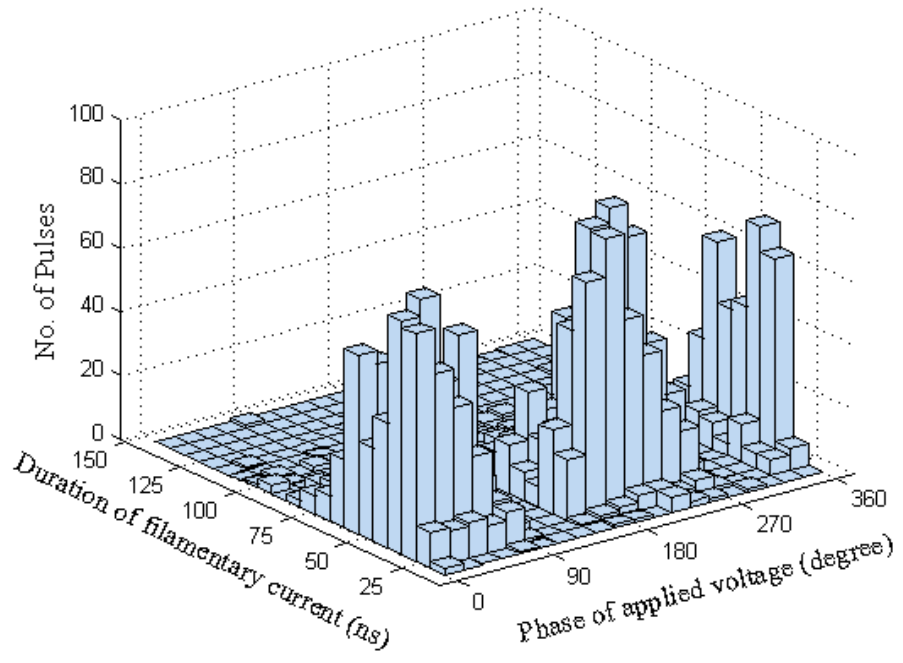

Fig. 5-7 Histogram of duration of filamentary current t_d (at 0.5 mm gap length and 1 bar absolute)

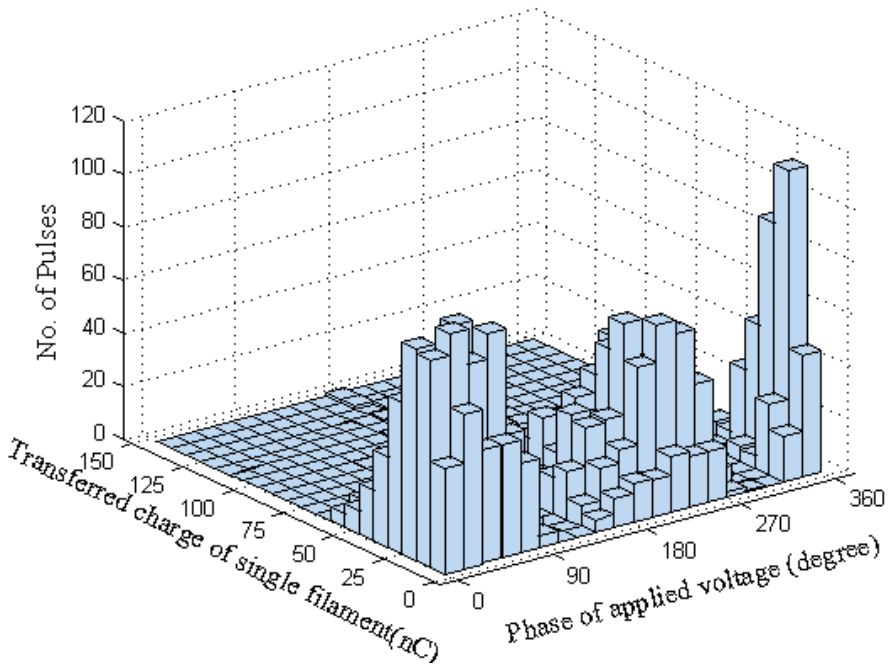

Fig. 5-8 Histogram of transferred charge of filamentary current Q_c (at 0.5 mm gap length and 1 bar absolute)

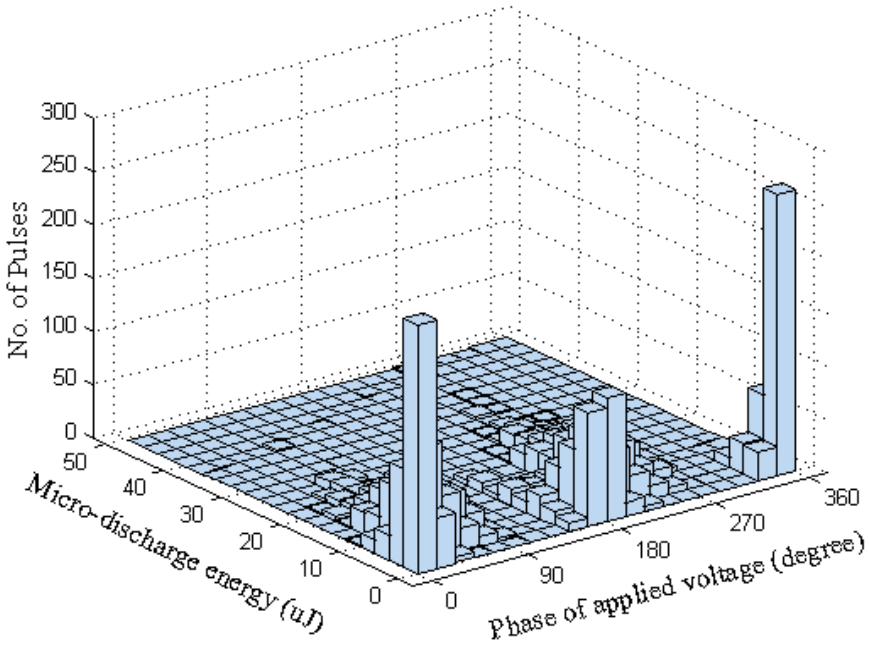

Fig. 5-9 Histogram of micro-discharge energy W_0 (at 0.5 mm gap length and 1 bar absolute)

In Fig. 5-6, the amplitude of positive filamentary currents demonstrates more consistency than that of negative filaments. The amplitudes of most positive current pulses are about 1 A, and few are higher than 2 A. The amplitudes of negative current pulses are widely spread, and up to 6 A. It can be observed from Fig. 5-6 that the current pulses measured at the start of the negative voltage half-cycle (phase angle of 180°) have higher amplitudes, whereas the current pulses occurring at around 270° have relatively consistent amplitude of about 1 A. The corresponding charge transfer is presented in Fig. 5-8. The statistical distribution of charge is similar to that of current pulse amplitude, which shows that the charge transferred in negative filamentary currents is spread more widely than that of the positive filaments, and that the higher charge transfer took place at around 180°. Different from the wide range of current amplitudes, the current duration shows a narrow distribution for both positive and negative half-cycles, as shown in Fig. 5-7. Most of the current pulse durations are around 46 ns. Fig. 5-9 gives the distribution of energy dissipated by micro-discharges. It is found that the micro-discharges occurring at the beginning of the discharge period, where the voltage phase angle is 0° and 180°, consumes similar amount of energy; but when the voltage is close to its peak (90° and 270°), the micro-discharge energy becomes higher, and the distribution is spread wider. The mean values of the parameters presented in Fig. 5-6, Fig. 5-7, Fig. 5-8 and Fig. 5-9 are specified in Table 5-2.

Table 5-2 Mean values of electrical parameters of micro-discharges (0.5 mm, 1 bar absolute)

Parameters	Positive	Negative
I_p	1.0 A	1.6 A
t_d	47 ns	46 ns
Q_c	21 nC	32 nC
W_0	7.2 μJ	7.6 μJ
n	68	65

5.3.2 Comparison of the Characteristics of Micro-discharges for Different Gap Lengths

The negative filamentary current was selected for comparison at different gap lengths and gas pressures. Fig. 5-10 to Fig. 5-13 show the mean values and standard deviations of negative filamentary current pulse amplitude, duration, charge transfer and individual micro-

discharge energy, respectively, for different gap lengths at the same absolute pressure of 1 bar.

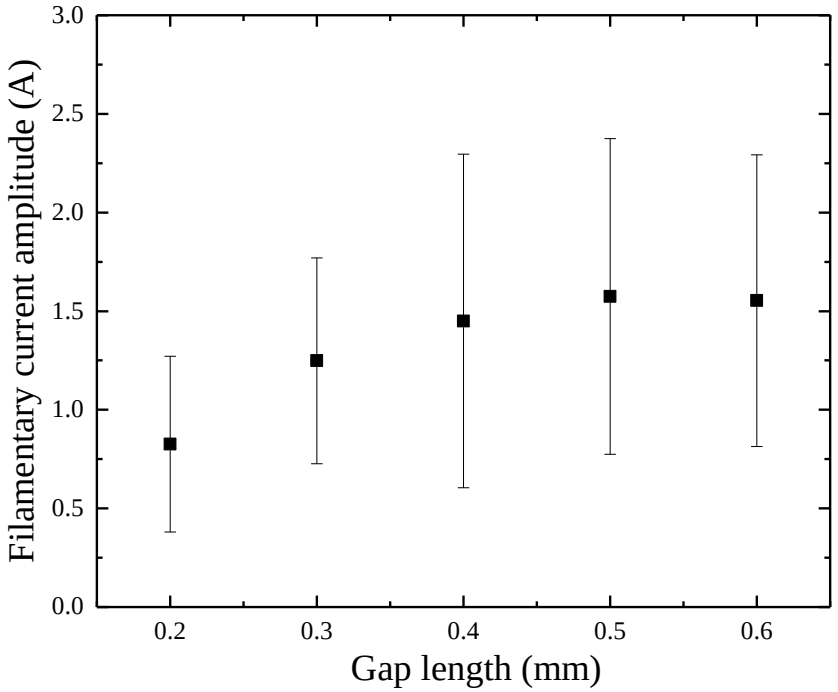

Fig. 5-10 Mean filamentary current amplitude for different gap lengths (at 1 bar absolute)

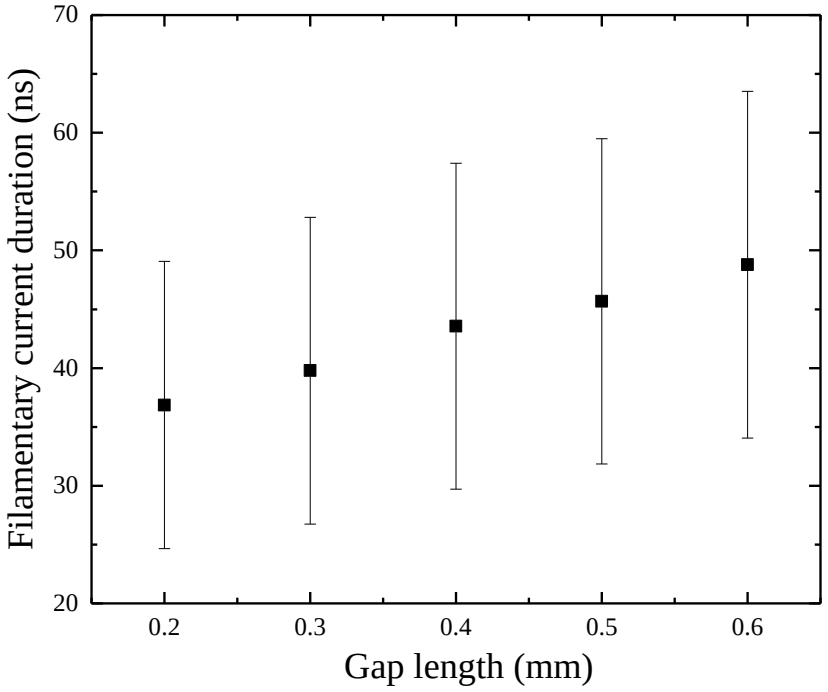

Fig. 5-11 Mean filamentary current duration for different gap lengths (at 1 bar absolute)

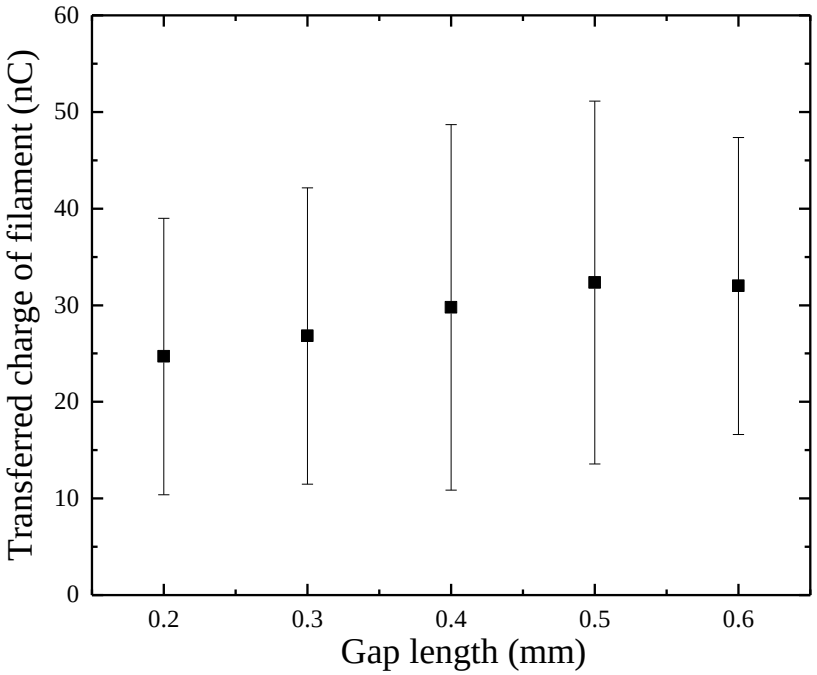

Fig. 5-12 Mean transferred charge of filament for different gap lengths (at 1 bar absolute)

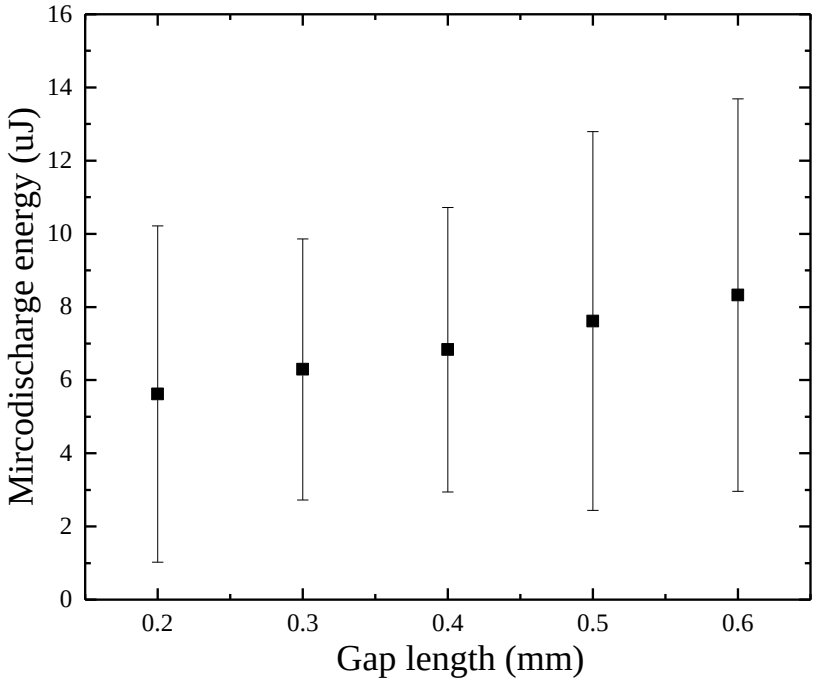

Fig. 5-13 Mean micro-discharge energy for different gap lengths (at 1 bar absolute)

The mean values generally increase with an increase in gap length. The mean filamentary current amplitude increases from 0.8 A with gap length of 0.2 mm, to 1.6 A with gap length of 0.5 mm, corresponding to an increase in mean charge transfer from 24 nC to 32 nC, as shown in Fig. 5-10 and Fig. 5-12, respectively. It was observed that the mean current amplitude increases with increasing gap length for shorter gaps (0.2 mm to 0.4 mm), before plateauing for longer gaps (0.5 mm and 0.6 mm). The mean current pulse duration increases from 37 ns with gap length of 0.2 mm, to 49 ns at gap length of 0.6 mm, and the micro-discharge energy increases from 5.6 μJ to 8.3 μJ, as shown in Fig. 5-11 and Fig. 5-13, respectively. All the data points shown in the figures contained a large standard deviation, which means that the distribution of these data was spreading. The pulse statistics of each electrical parameter of filaments for different gap lengths can be found in the Appendix A.

5.3.3 Comparison of the Characteristics of Micro-discharges at Different Gas Pressures

The mean values and standard deviations of filamentary current amplitude, duration, and transferred charge, and of individual micro-discharge energy, at different pressures with the same gap length of 0.5 mm are displayed in Fig. 5-14 to Fig. 5-17, respectively.

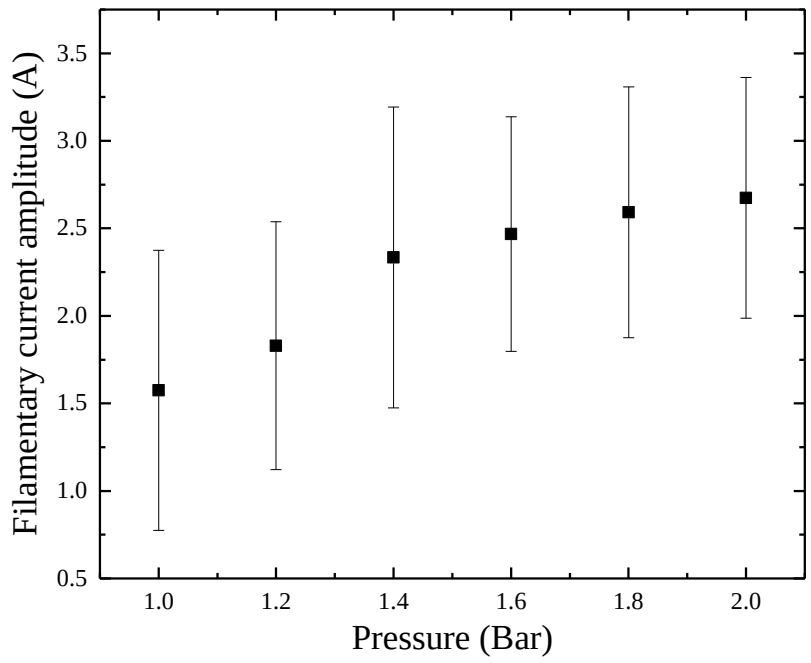

Fig. 5-14 Mean filamentary current amplitude at different (absolute) gas pressures (at 0.5 mm gap length)

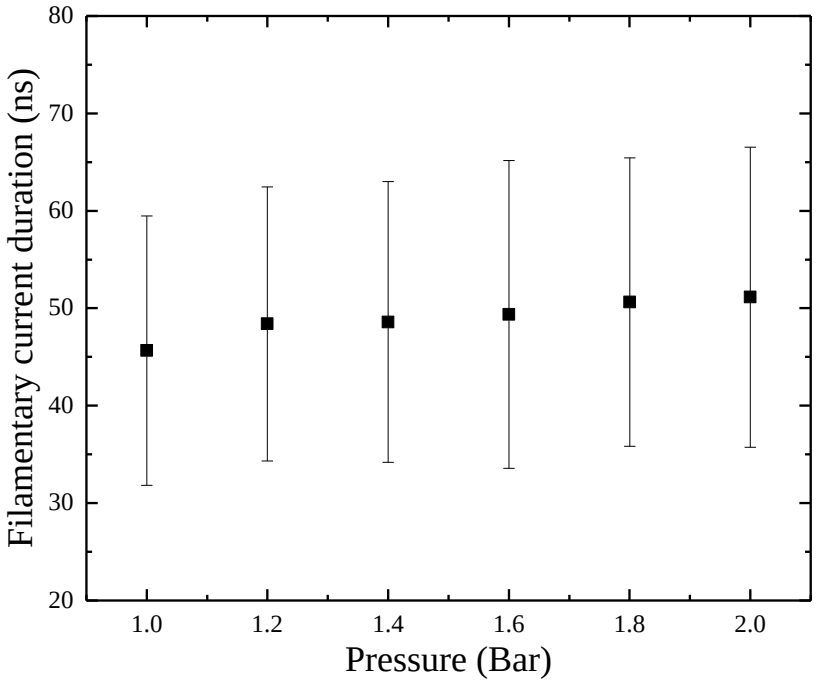

Fig. 5-15 Mean filamentary current duration at different (absolute) gas pressures (at 0.5 mm gap length)

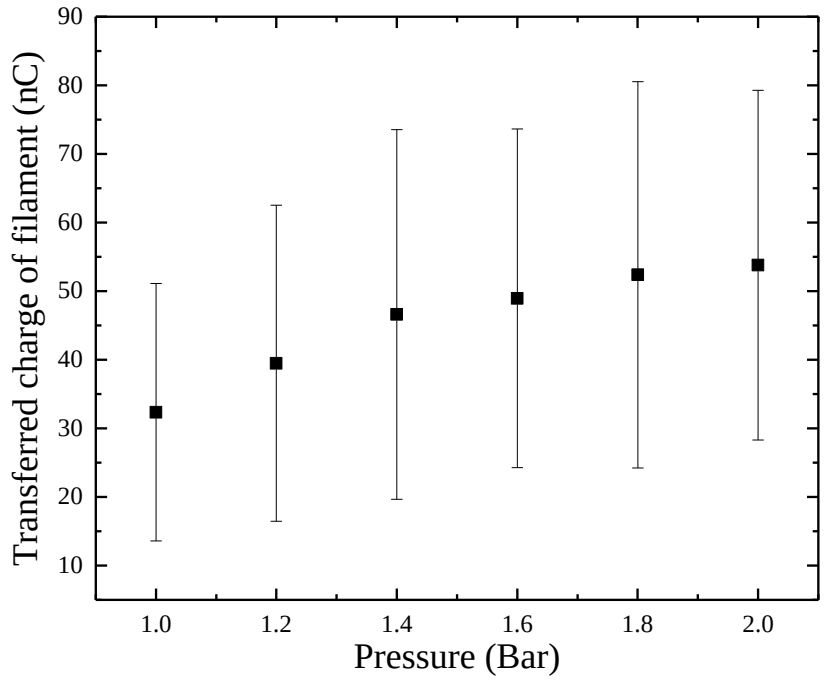

Fig. 5-16 Mean transferred charge of filament at different (absolute) gas pressures (at 0.5 mm gap length)

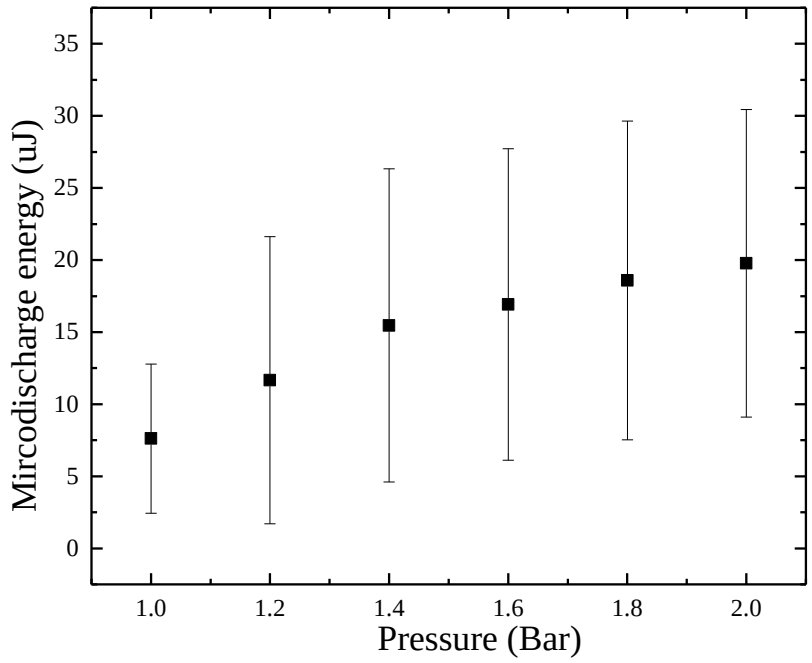

Fig. 5-17 Mean micro-discharge energy at different (absolute) gas pressures (at 0.5 mm gap length)

It can be seen in Fig. 5-14 that the mean filamentary current amplitude increases from 1.6 A at 1 bar absolute to 2.6 A at 2 bar absolute, corresponding to an increase in charge transfer from 32 nC to 54 nC, as shown in Fig. 5-16.

Fig. 5-15 shows that the mean pulse duration is generally within the range from 45 ns to 50 ns, demonstrating that the duration of the filamentary current pulse is not affected by gas pressure. Fig. 5-17 shows that the mean value of individual micro-discharge energy increases from 7.6 μJ at 1 bar absolute to 19.8 μJ at 2 bar absolute. Similar to the results for different gap lengths, the standard deviation of the distribution of these parameters was of the same order as the mean values, which means that the distribution of the filamentary current pulses was spread over the voltage phases from 150º to 270º. The pulse statistics of each electrical parameter of filaments at different gas pressures can be found in APPENDIX B.

5.3.4 Comparison of the Characteristics of Micro-discharges at Different Amplitudes of Applied Voltages

The characteristics of micro-discharges under different peak voltages from 3.5 kV to 5.5 kV at the same frequency of 5 kHz were investigated. The experiments were conducted with a fixed discharge gap length of 0.5 mm, and at the absolute pressure of 1 bar. The mean values and standard deviations of filamentary current amplitude, duration, and transferred charge; individual micro-discharge energy; and of the discharge current pulse number during half of a voltage cycle are shown in Fig. 5-18 to Fig. 5-22, respectively.

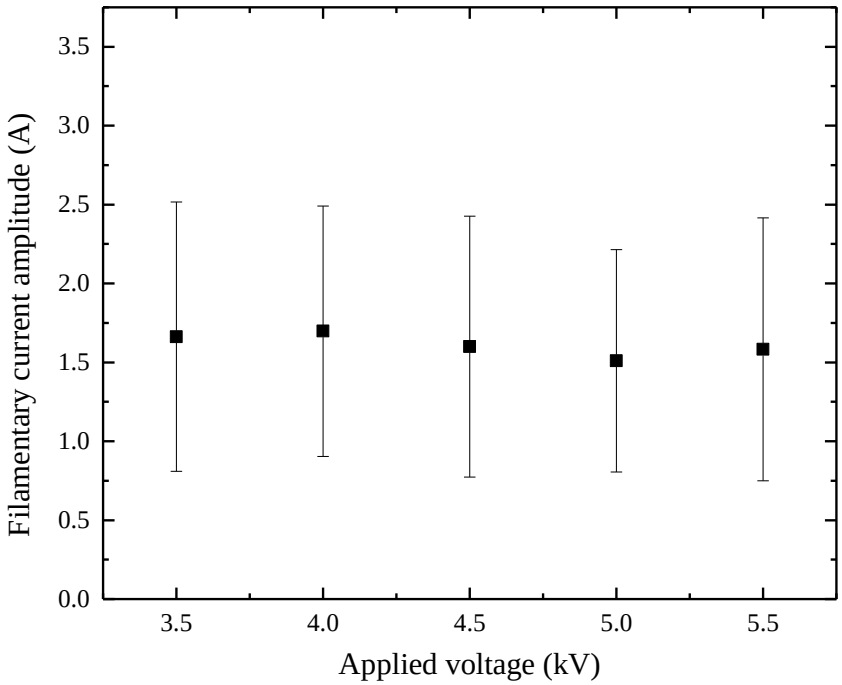

Fig. 5-18 Mean filamentary current amplitude at different applied voltages (at 0.5 mm gap length and 1 bar absolute)

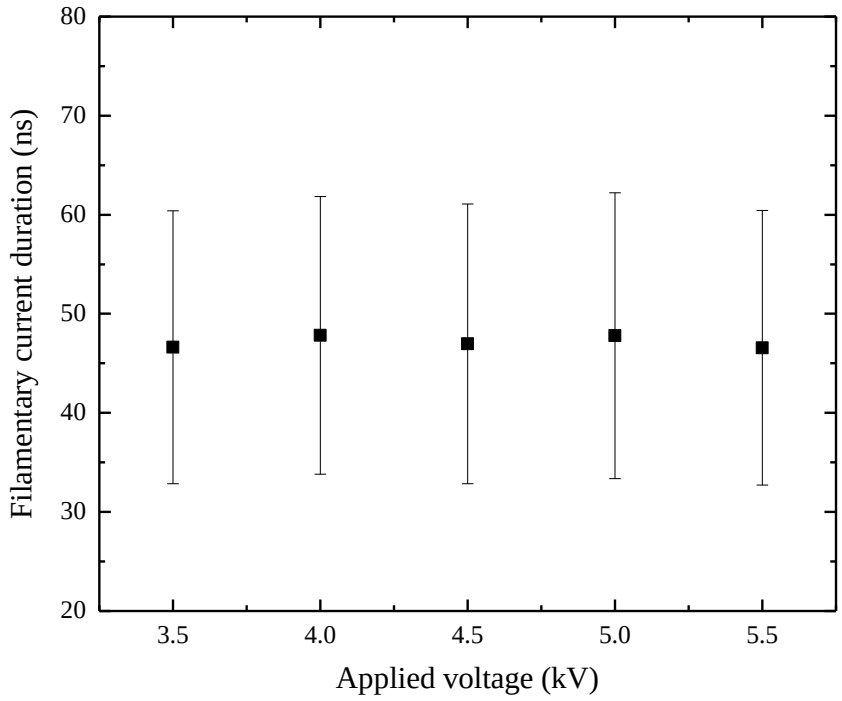

Fig. 5-19 Mean filamentary current duration at different applied voltages (at 0.5 mm gap length and 1 bar absolute)

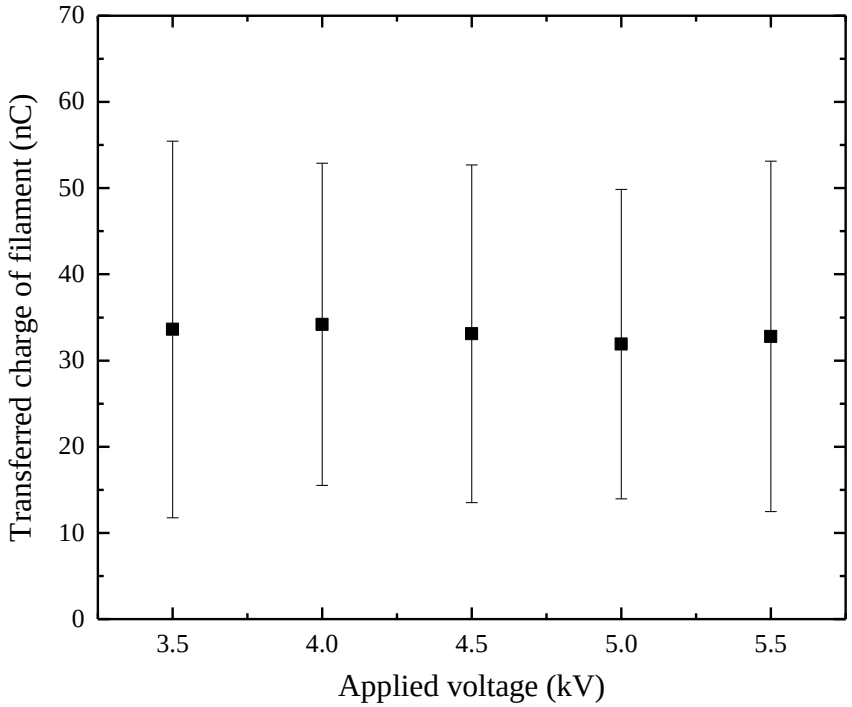

Fig. 5-20 Mean transferred charge of filament at different applied voltages (at 0.5 mm gap length and 1 bar absolute)

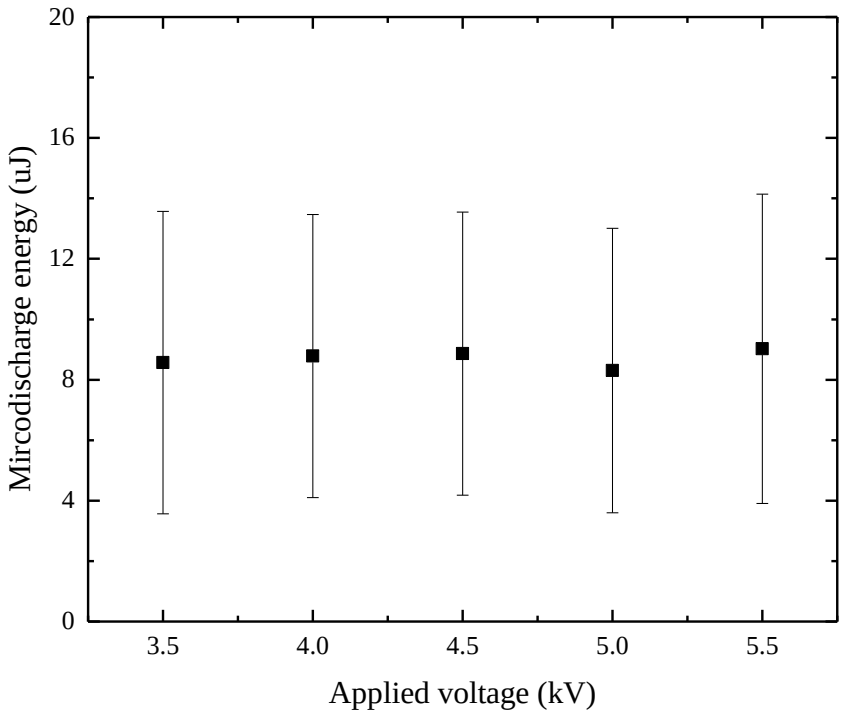

Fig. 5-21 Mean micro-discharge energy at different applied voltages (at 0.5 mm gap length and 1 bar absolute)

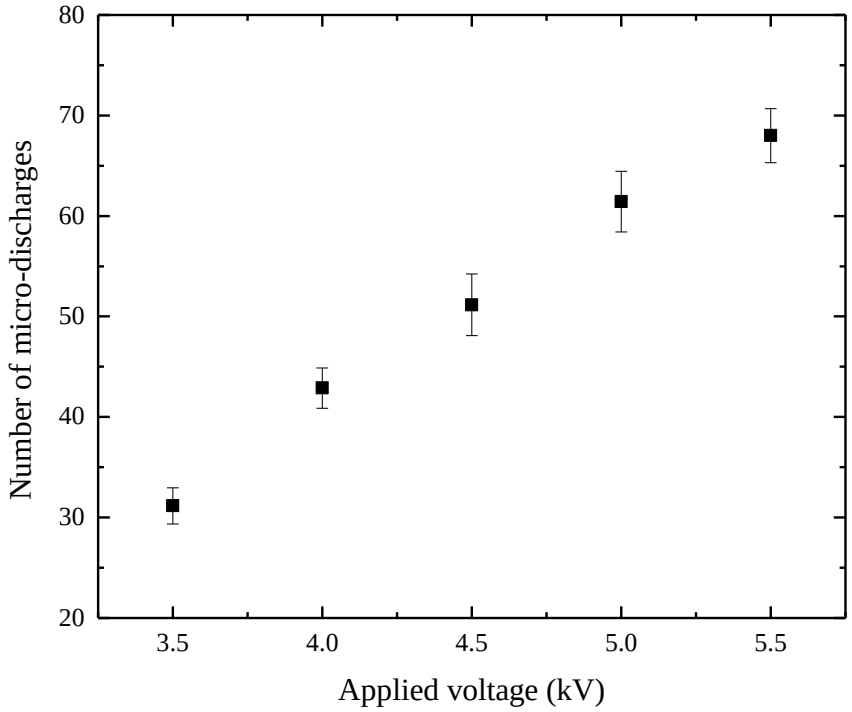

Fig. 5-22 Mean number of micro-discharge events during one active discharge phase

As can be seen, the filamentary currents under different peak voltages have a similar mean value of ~1.6 A and a standard deviation of ~0.8 A. The mean current pulse duration, the mean charge transferred by a filament and the mean micro-discharge energy were also found to be almost the same under different applied voltages. However, the number of micro-discharges during one active discharge phase is different under different applied voltage amplitudes, which is reflected in Fig. 5-22. The discharge number under an applied voltage of 3.5 kV is ~31, increasing to ~68 when the amplitude was raised to 5.5 kV. As can be seen from Fig. 5-22, the standard deviation of the number of micro-discharges under all test voltages is ~3, which demonstrates that the number of micro-discharges during one active discharge phase was quite consistent. The average number of micro-discharges increased with increasing applied voltage amplitude. With the same frequency of the applied voltage, an increase in the amplitude means an increase of the voltage rise rate. The results show that with increasing rate of voltage rise, the frequency of the micro-discharges increase; hence, the number of micro-discharges increased during one half of a voltage cycle. Because the charge transferred during one single micro-discharge is almost the same, an increase of the micro-discharge number under higher applied voltage results in increased total charge transferred, which agrees with the results in Table 4-5 in Chapter 4.

5.3.5 Ozone Generation Performance

The concentration curves for ozone generated by transient voltages (200 cycles) were recorded by real-time data acquisition software under different experimental conditions (different gap lengths, different gas pressures and different applied voltages). Fig. 5-23 shows a typical ozone concentration curve recorded in these experiments.

As can be seen, the ozone concentration curve is a pulse with a long tail of up to 20 ms overall duration. The oxygen feed gas had a fixed flow rate of 0.5 L/min under all test conditions. The process of calculating the ozone generation efficiency under the transient state can be found in Section 3.7.3 in Chapter 3.

Fig. 5-24 shows that the ozone generation efficiency increased with increasing gap length from 0.2 mm to 0.5 mm and then saturated, with the highest ozone efficiency obtained being 166 g/kWh.

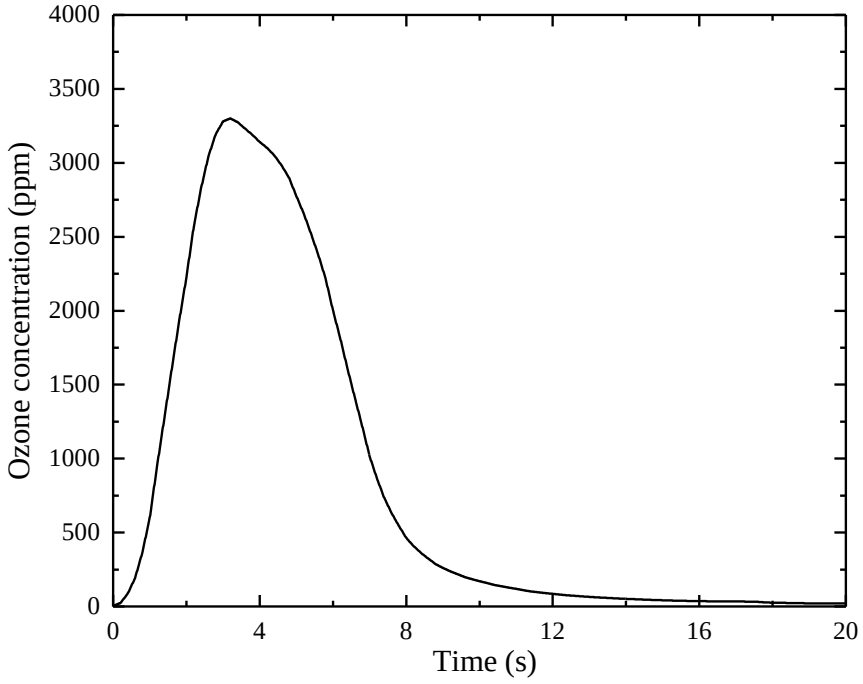

Fig. 5-23 Ozone concentration curve measured when transient voltages (200 cycles of 5 kHz sinusoidal voltage with the amplitude of 5.5 kV) was applied to the ozone reactor (0.5 mm gap length, with absolute pressure of 1 bar)

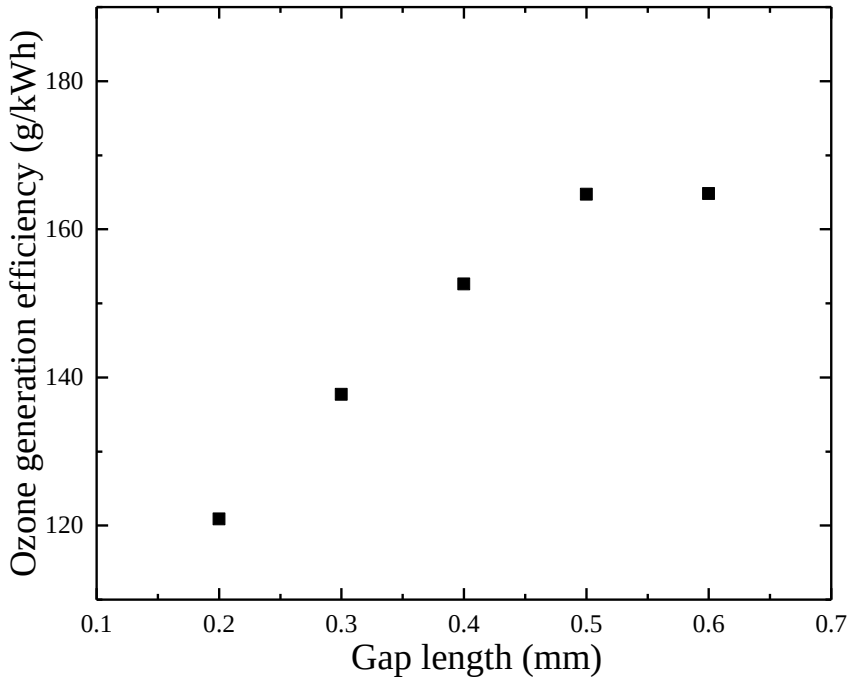

Fig. 5-24 Ozone generation efficiency with different gap lengths at 1 bar absolute, under applied voltage of 5.5 kV at 5 kHz

It has been reported by a number of researchers that shorter gap length can result in better heat removal, which leads to increased ozone concentration and generation efficiency [7, 15]. In the present work, however, due to the application of 200 voltage cycles with the frequency of 5 kHz, the applied power duration is only 40 ms, therefore the heating effect in the reactor can be neglected. Fig. 5-25 shows the dependence of ozone generation efficiency on gas pressure, demonstrating that the ozone efficiency increases with increasing gas pressure. The highest ozone generation efficiency of 217 g/kWh was achieved at pressure of 2 bar absolute. The ozone generation efficiency at 1 bar absolute was 165 g/kWh, which was 24% less than that achieved at 2 bar absolute.

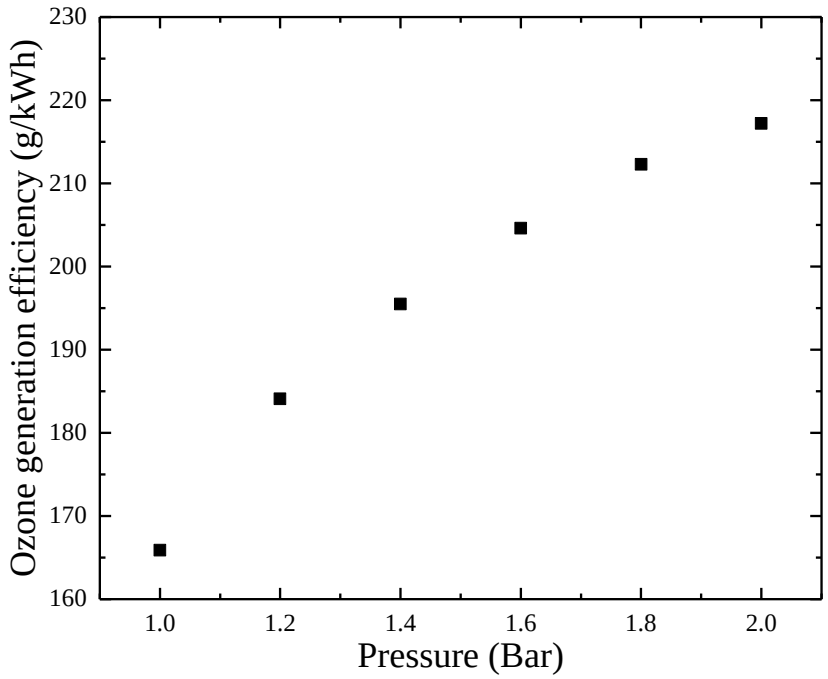

Fig. 5-25 Ozone generation efficiency with different (absolute) pressures for 0.5 mm gap length, under applied voltage of 5.5 kV at 5 kHz

Fig. 5-26 shows that the ozone generation efficiency increased with decreasing applied voltage amplitudes. The ozone generation efficiency under 5.5 kV applied voltage was 166 kg/kWh, which increased by 20% when the amplitude of the applied voltage was reduced to 3.5 kV. This result shows that the micro-discharges generated with lower applied voltage amplitudes are more effective for ozone formation, the reason for which is related to the frequency of the occurrence of the micro-discharges. Another reason might be due to the

lower temperature at lower applied voltage amplitude. Due to the sealed nature of the reactor used, however, the gas temperature could not be monitored during the experiments.

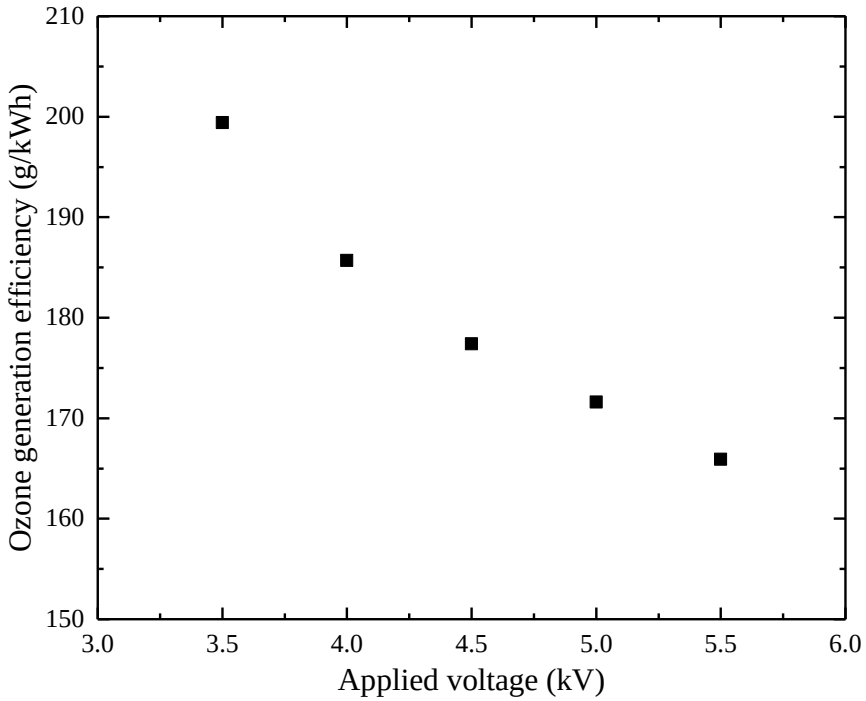

Fig. 5-26 Ozone generation efficiency with different applied voltages for 0.5 mm gap length, with the pressure of 1 bar

5.4 Discussion

5.4.1 Micro-discharge Characteristics

1) Establishment of Stationary Dielectric Barrier Discharges

Fig. 5-27 shows the waveform of the discharge current measured in the external circuit at the initial stage of the dielectric barrier discharges energised by 200 voltage cycles.

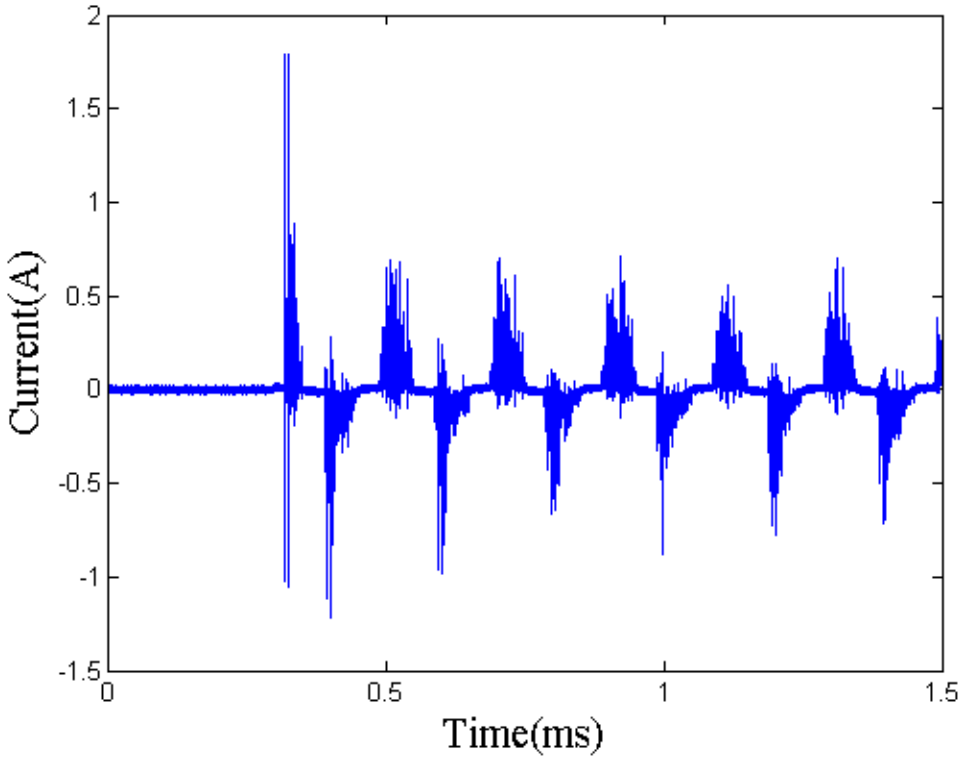

Fig. 5-27 Discharge current measured in the external circuit at the initial stage of the dielectric barrier discharges energised by 200 voltage cycles

From the discharge current waveform, it can be seen that the first cycle of the discharge current had a larger spike, which can be attributed to the transition of non-discharge state to gas discharge state. The accumulated charge on the barrier from the first cycle leads to the establishment of a steady state dielectric barrier discharge. From Fig. 5-27, it is shown that the discharge current waveform after the first cycle had a regular spike pattern. Therefore, it can be considered that a stationary dielectric barrier discharge was established from the

second cycle. As this research work was focused on the low-concentration ozone generation process, without considering the effects of temperature, the ozone generation efficiency is considered to be consistent once a stationary oscillatory discharge current was established.

2) Characteristics of Filamentary Current Distribution over One Voltage Cycle

From the histograms of filamentary current pulse amplitude (Fig. 5-6) and transferred charge (Fig. 5-8) of a single filament in Section 5.3, a polarity effect of micro-discharges has been observed. The results show that the negative filamentary current amplitude is about 2 times higher than that of the positive filamentary current. This observation can be explained as follows. Before the positive discharge cycle starts, there are negative ions deposited on the surface of the dielectric barrier from the previous half-cycle. The accumulated negative charges can be considered as numerous individual point charges distributed over the dielectric barrier surface, which results in local electric field distortion. When the external electrical field decreases to a certain value before zero volts, the local electrical field around the accumulated point charge is high enough to initiate positive discharges, representative of a glow-like mode. When the positive discharge stops, the charges accumulated on the barrier surface are positive. The numerous positive point charges deposited on the surface result in a local electrical-field distortion that is different from the negative point charge [55], which leads to a filamentary discharge mode. The filamentary discharge mode results in higher impulsive current than the glow-like discharge mode. This polarity effect was also found by Murata *et al*. in [78], who attributed it to the different mobility of electrons and ions accumulated on the glass surface.

It was found that, at the same voltage phase angle, the negative discharge current pulse amplitude values were dispersed. The average amplitudes around the voltage phase angles of 0° or 180°, the initial stage of the discharge period, were relatively higher compared to those around the voltage phase angles of 90° or 270°, the final stage of the discharge period. This can be explained as follows. At the initial stage of the discharge period for each half-cycle, the charge accumulated on the dielectric surface from the previous half-cycle contributes to the development of a filament, and also the charge with opposite polarity transported in the filament at this stage has more space to develop, leading to a higher-amplitude current pulse. At the final stage of the discharge period, as the dielectric surface has accumulated a certain amount of charge, the charge with the same polarity transported in the filament has a limited space to develop due to the repulsion by nearby charge, which results in a lower current pulse amplitude.

It was also observed that the filamentary current in the gap is about 4 times higher than the induced pulsed current measured in the external circuit, which is mainly due to the high dV_a/dt at the moment of discharge (see equation (5.1)). The calculated charge transferred per filament was about 10 times higher compared with that from a previous study [79], in which the rapidly changing voltage at the moment of discharge was not considered.

3) Effects of Discharge Gap Length and Gas Pressure on the Micro-discharges

Without considering the ionic current component in the filament current due to its small contribution [14], the current density, j, and the transferred charge, Q_c, of the filament can be calculated from (5.4) and (5.5), respectively:

$$j = e \cdot N_e \cdot v_d \tag{5.4}$$

$$Q_c = e \cdot F_c \cdot \int_0^{t_d} v_d \cdot N_e dt \tag{5.5}$$

where N_e, v_d and F_c are the electron density, electron drift velocity, and the cross-section of the micro-discharge channel, respectively. Referring to (5.4) and (5.5), it can be deduced that the increase of filamentary current and transferred charge with increasing gap length and gas pressure results from the joint effects of the electron density and electron drift velocity at different gap lengths and gas pressures. The electron density and the electron drift velocity distribution are related to the reduced electric field E/N [37, 119]. Values for E/N at different gap lengths were calculated and plotted in Fig. 5-28.

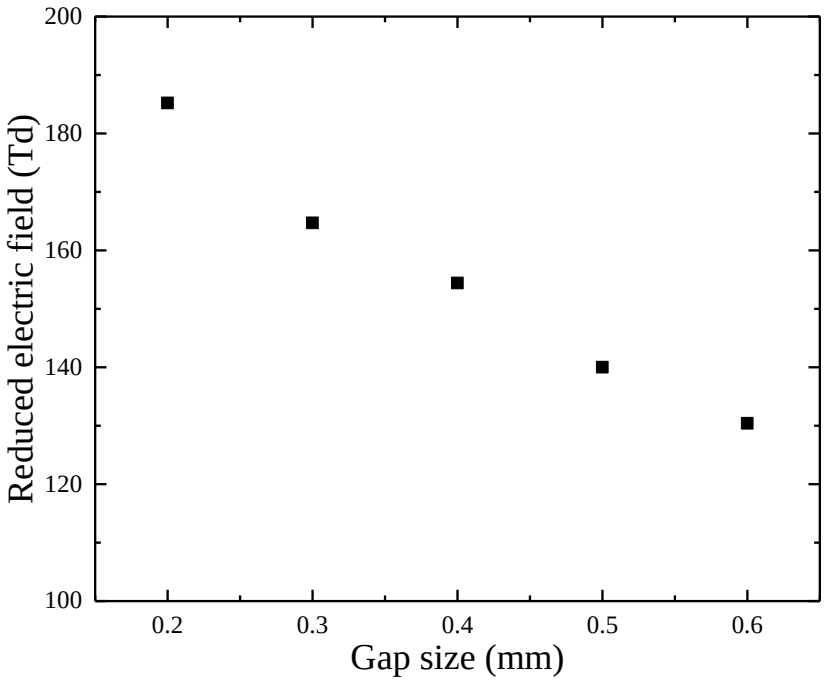

Fig. 5-28 The dependence of *E/N* on gap length (at 1 bar absolute)

Fig. 5-28 shows that the *E/N* decreases from 185 Td to 130 Td when the gap length increases from 0.2 mm to 0.6 mm. It is interesting to find that at lower electric field of 130 Td, the amplitude, transferred charge, and dissipated energy of filaments are higher compared with those at the higher electric field of 185 Td. The *E/N* at different gas pressures was calculated and plotted in Fig. 5-29, which shows that the *E/N* decreases slightly from 136 Td at 1 bar absolute to 126 Td at 2 bar absolute. Similar to the results obtained for different gap lengths, Fig. 5-29 demonstrates that the filamentary current amplitude, transferred charge, and individual micro-discharge energy are higher at lower levels of electrical field.

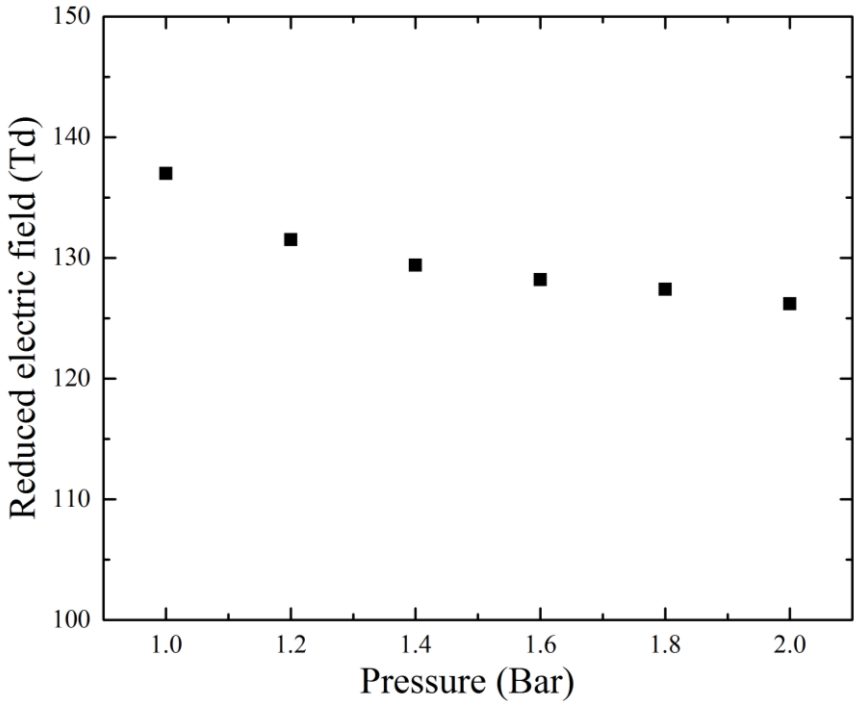

Fig. 5-29 The dependence of *E/N* on (absolute) gas pressure (for 0.5 mm gap length)

The effect of *E/N* on the distributions of electron density and electron drift velocity is complicated and requires further advanced plasma diagnostic techniques or application of the Particle-in-Cell method for numerical simulation [120, 121]. The filamentary current pulse duration represents the time taken for a reverse electrical field to be established by accumulated charge that is high enough to terminate the discharge. From experimental results, it is known that when the discharge gap is longer, more time is needed to establish the reverse electrical field to extinguish the discharge, but the filamentary current pulse duration is not affected by increasing gas pressure.

The effects of discharge gap distance and gas pressure on the characteristics of micro-discharge have also been investigated by other researchers. Using a numerical method, Braun *et al.* reported that the radius of the micro-discharge increased with increasing gap length, and decreased with increasing gas pressure [11]. For longer gap length, with larger micro-discharge radius, the transferred charge of a single filament and the micro-discharge energy both increase. However, the pressure effect cannot be explained by this argument.

5.4.2 Ozone Generation Efficiency versus *E/N*

Ozone generation results from two main opposite reactions: a reaction of ozone formation from oxygen and a reaction of ozone destruction. The key reactions (R1a to R6) in the ozone generation have been illustrated in Chapter 2. Assuming that the portion of the input energy carried by electrons is 0.5 [7, 15], the ozone generation efficiency was calculated by equation (5.6), based on the reactions from (R1a) to (R6).

$$\eta = \frac{(k_{1a} + k_{1b})}{v_d(E/N)} \cdot \frac{1}{1 + \dfrac{2k_5 x_{10}}{k_3 x_{10} + k_4}} \quad O_3 \text{ molecules/}ev \tag{5.6}$$

where x_{10} is the oxygen atom concentration (x_{10}= $N[O]$/ $N[O_2]$) [14], N is the initial concentration of O_2 molecules (particles cm^{-3}) and v_d is the drift velocity of electrons. According to this equation, it can be seen that the ozone generation efficiency is related to *E/N*. In the present work, different values of *E/N* were achieved by adjusting the gap length and gas pressures. Based on the ozone generation efficiency measured for different conditions, shown in Fig. 5-24 and Fig. 5-25, the ozone generation efficiency as a function of *E/N* is presented in Fig. 5-30.

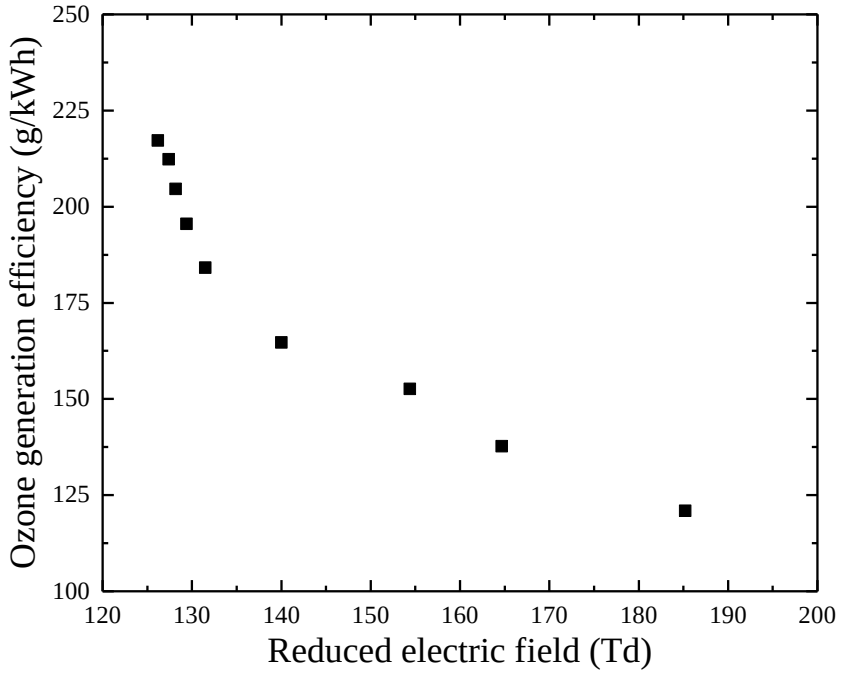

Fig. 5-30 Ozone generation efficiency at different *E/N*

It can be seen that the ozone generation efficiency decreases with increasing reduced electric field in the range from 126 Td to 185 Td. This result is in agreement with the findings of Kitayama *et al*, who reported that the maximum ozone yield decreased gradually with increasing value of the reduced electric field strength, when *E/N* >100 Td [15]. It should be noted that the parameters of $k_{1a,}$ $k_{1a,}\lambda$ and v_d are all affected by *E/N*, and therefore changes in ozone generation efficiency at different *E/N* are as a result of the joint effect of all of the parameters in equation (5.6).

From the statistical analysis of micro-discharge properties, it has been found that the micro-discharge energy is higher for longer gaps and higher gas pressures. Therefore, the ozone efficiency increases when the micro-discharge is more intense. The highest ozone generation efficiency of 217 g/kWh occurred when the mean value of individual micro-discharge energy was 20 μJ, at *E/N* of 126 Td. Increased micro-discharge energy means that more oxygen atoms are produced in the micro-discharge channel, such that more ozone can be generated subsequently, based on reactions R1a, R1b and R2 (see Section 2.5.2). Therefore, the ozone generation efficiency can be improved when the individual micro-discharge energy is increased. However, there exists an optimum value of oxygen atom concentration that is beneficial for ozone generation, which is 10^{-4} when *E/N* is about 100 Td, according to Elisasson *et al.*[14]. While the oxygen atom concentration could not be measured in the present work, the optimum *E/N* for ozone generation was found to be 126 Td. The highest ozone generation efficiency achieved by Elisasson *et al*. was 250 g/kWh, using an AC power supply [14]. Compared to this efficiency, the maximum ozone production efficiency measured in the present work was about 13% lower.

5.5 CONCLUSION

The statistical characteristics of micro-discharge and ozone production under different gap lengths, different gas pressures and different applied voltages were studied in this chapter. A polarity effect was found, with negative discharge current twice as large as positive discharge current. The dV_a/dt at the moment of discharge was considered, and the filamentary current in the discharge gap was calculated. It was shown that the amplitude of the filamentary current was about four times higher than that of the external pulsed current.

Statistical analysis of representative pulses showed that the mean values of the filamentary current amplitude, transferred charge and micro-discharge energy all increased as the gap length or gas pressure was increased. The filamentary current pulse duration increased with increasing gap length, but was not affected by gas pressure. The characteristic of the filamentary current was found to be almost the same under different applied voltages, but the number of micro-discharges increased as the amplitude of the applied voltage increased.

The *E/N* was calculated for different gap lengths and gas pressures, and it was observed that the filamentary current amplitude, transferred charge of an individual filament, and individual micro-discharge energy were higher at lower values of *E/N*, and also that the ozone generation efficiency was found to increase with decreasing *E/N*, in the range from 126 Td to 185 Td. The ozone generation efficiency was higher when the micro-discharge energy was higher in the energy range from 5 μJ to 20 μJ. Also, the ozone generation efficiency was found to increase by 20% under the lower applied voltage amplitude of 3.5 kV, compared with the higher amplitude of 5.5 kV. The maximum ozone production efficiency achieved in the work was 217 g/kWh with a gap length of 0.5 mm, 2.0 bar absolute pressure, and an applied voltage of 5.5 kV at 5 kHz.

6 INVESTIGATION OF OZONE GENERATION USING A CONTINUOUS AC POWER SUPPLY

6.1 Introduction

Different ozone generators, or a single ozone generator operating under different gas conditions, can have different curves of generation efficiency versus concentration. The objective of optimization of ozone generation is to achieve the highest ozone generation efficiency at a specific ozone concentration, for a given application. High concentration of ozone, around 10% w/w (150 g/Nm^3), is usually used in water treatment and pulp bleaching applications [34]. The concentrations of ozone to be used for food preservation are low, because at higher concentration (above 0.2 mg/Nm^3 air), fruit discoloration or surface damage may occur [122]. There are several parameters that can be adjusted to generate ozone with different concentrations, such as the flow rate, gas pressure, and the discharge power. A parametric study on the ozone generation concentration and efficiency was performed using a triggered dielectric barrier discharge in [123]. This study showed that ozone concentration increases in direct proportion to the inverse gas flow and pulse number, before the ozone concentration reaches a saturation value at about 40 g/Nm^3. The authors concluded that the saturation concentration depends upon only: the geometric configuration of the reactor; the reduced electric field; and the gas temperature. In another study [124], it was reported that the ozone concentration at each applied voltage increased as the gap length increased, and reached a saturated value of around 30 g/Nm^3 at d=0.4 mm; the optimum gap length was found to be in the range of 0.6-0.8 mm. In [125], the authors claimed that use of a single dielectric barrier results in a higher ozone generation rate as compared with the use of double dielectric barriers.

Optimization of the curve of ozone generation efficiency versus ozone concentration is important. In this chapter, the performance of an ozone generator based on DBDs energized by a continuous AC power supply was investigated and optimized under a sealed gas flow system. Two types of reactor (Type-B plate DBD reactor and Type-C cylindrical DBD reactor) were employed in this study. Firstly, the effects of gas flow rate, gas pressure, applied voltage, energisation frequency and discharge gap length, on the ozone concentration and generation efficiency were investigated, using a plate type DBD reactor (Type-B). The curves of ozone concentration versus specific energy under different experimental conditions

are plotted and discussed herein. The aim of this part of the work is to compare the concentration of ozone generated under different conditions, but with the same specific energy. Secondly, the ozone generation performance achieved with a cylindrical DBD reactor (Type-C) with a water-circulating cooling system was studied, and the ozone concentration and generation efficiency were measured and compared with the plate type reactor, energized by a conventional AC power source. Finally, attention was paid to the effects of the energisation frequency on the ozone generation performance. The industrially-used frequency of 50 Hz, along with high energization frequencies of 2.6 kHz and 20 kHz were compared, not only with respect to the ozone concentration and ozone generation efficiency, but also in terms of the practical aspects such as the power density and the construction of the ozone generator.

6.2 Ozone Generation Based on Plate DBD reactor

6.2.1 Experimental Set-up

The experimental set-up used for this work is shown in Fig. 6-1.

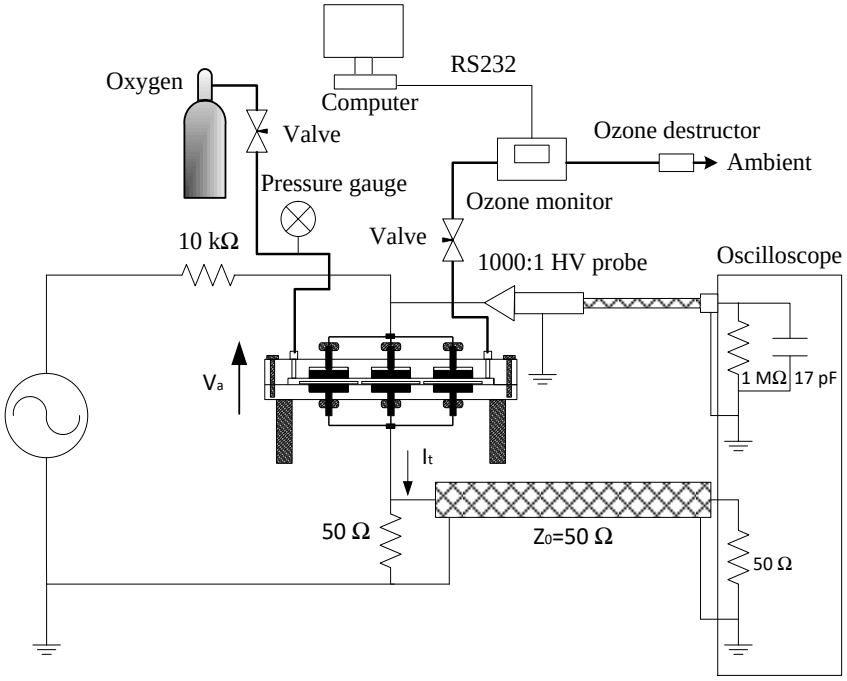

Fig. 6-1 Schematic diagram of experimental set-up

The Type-B plate DBD reactor with a variable gap length, energized by an AC power supply (Pacific 112AMX) with a frequency of up to 5 kHz was employed in this part of the study. Experiments were conducted under an oxygen flowing system, at an ambient temperature of 25 °C. The oxygen fed into the reactor had 99.5% purity, and dew point of −40 °C. The flow rate of the gas flowing through the reactor was controlled using two needle valves which were located before and after the ozone reactor (see Fig. 3-1 in Section 3.2). The gas flow rate was controlled from 0.3 L/min to 1 L/min, measured by a mass flow meter, and the gas pressure was controlled from 1 bar absolute to 2 bar absolute, measured by a digital pressure gauge. The ozone concentration in this work was monitored by an ozone analyser from IN-USA (Series: Mini-HiCon), and the concentration data was transferred to a computer for processing. The discharge power, specific energy and ozone generation efficiency were then calculated.

6.2.2 Experimental Results

1) The effects of gas flow rates on ozone generation

Experiments investigating the effect of gas flow rate on ozone generation were conducted at a constant applied voltage of 5.5 kV at 3 kHz, and at a constant gas pressure of 1 bar absolute. The ozone concentration and ozone generation efficency under different flow rates were measured and calculated, as shown in Fig. 6-2. It can be seen that as the flow rate increases from 0.4 L/min to 1 L/min, the ozone concentration decreases linearly from 87.7 g/Nm^3 to 60.5 g/Nm^3, respectively. However, calculation of the ozone generation efficiency revealed that this increases from 57.9 g/kWh to 100.5 g/kWh with increasing flow rate from 0.4 L/min to 1 L/min. These experimental observations can be explained as follows. As the gas flow rate is raised, the gas residence time inside the discharge gap decreases; therefore, the amount of ozone being destroyed by the discharges decreases, which results in an increase in the ozone generation efficiency.

2) The effects of applied voltage on ozone generation

Experiments investigating the effect of applied voltage on ozone generation were conducted at 3 kHz, with constant gas flow rate of 0.5 L/min and constant gas pressure of 1 bar absolute. The ozone concentration and ozone generation efficency under different applied voltage were measured and calculated, as shown in Fig. 6-3.

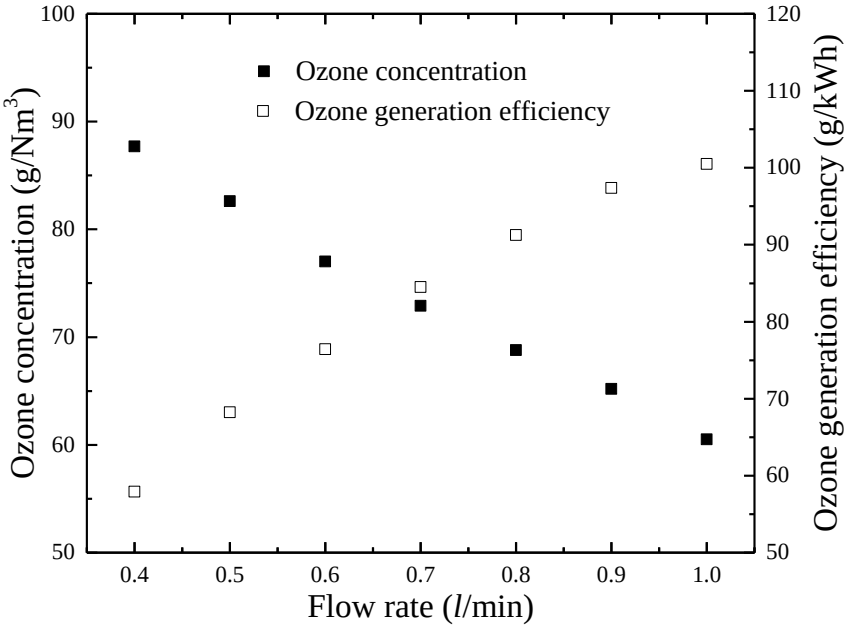

Fig. 6-2 Ozone concentration and generation efficiency at different flow rates (at constant applied voltage amplitude of 5.5 kV at 3 kHz and constant gas pressure of 1 bar absolute, with gap length of 0.5 mm)

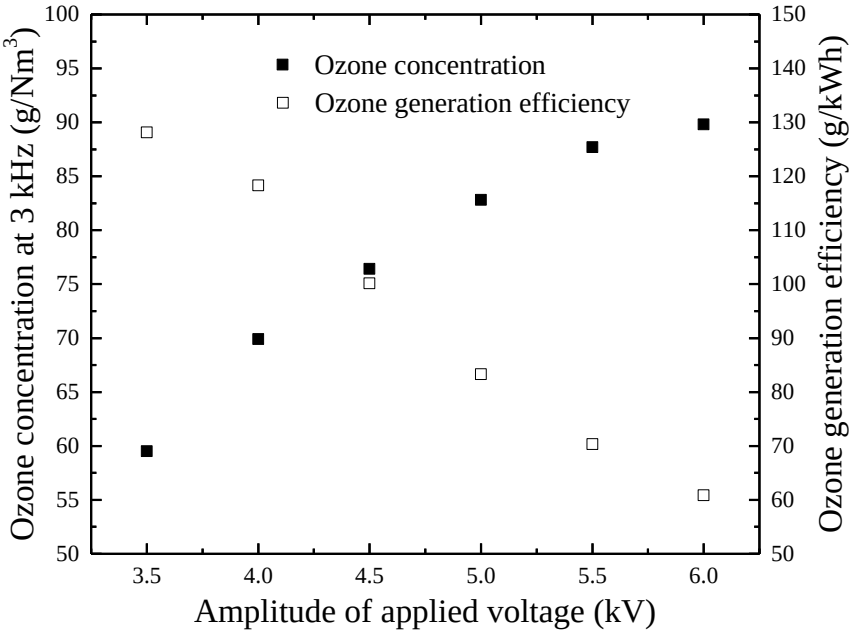

Fig. 6-3. Ozone concentration and generation efficiency under different applied voltages (at constant gas flow rate of 0.5 L/min and constant gas pressure of 1 bar absolute, with gap length of 0.5 mm)

The results show that the ozone concentration increased from 60 g/Nm^3 to 90 g/Nm^3 as the applied voltage was increased from 3.5 kV to 6 kV (constant flow rate), but the ozone generation efficiency decreases as the applied voltage increases. The ozone generation efficiency achieved under the lowest applied voltage of 3.5 kV was 128.1 g/kWh, more than twice higher than the ozone generation efficiency of 60.8 g/kWh achieved under the highest applied voltage of 6 kV. This can be attributed to the increase of the discharge power with increasing peak voltage. The discharge power with respect to the peak voltage is plotted in Fig. 6-4. It can be seen that the discharge power under the peak voltage of 6 kV was about 3 times higher than the discharge power under the peak voltage of 3.5 kV. Higher power results in higher temperature, and higher temperature leads to ozone decomposition, which causes the drop in ozone generation efficiency [15].

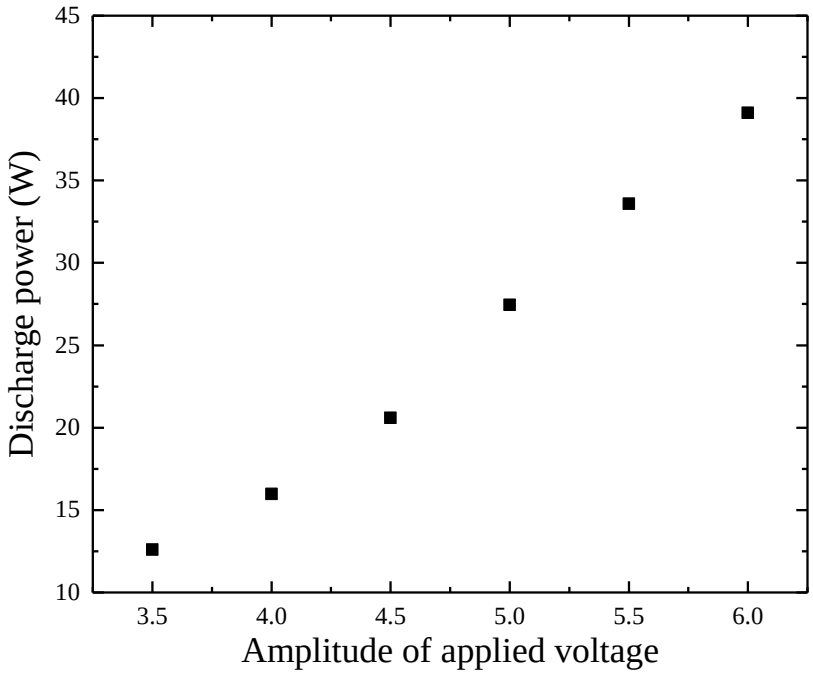

Fig. 6-4. Discharge power under different applied voltage amplitudes

3) Comparison of the effects of adjusting discharge power and adjusting gas flow rate on ozone generation

The same specific energy can be achieved by adjusting the gas flow rate at a constant discharge power, or by adjusting the discharge power at a constant flow rate. It was within the interest of this study to experimentally determine the balance of discharge power and gas

flow rate required to provide optimal ozone performance. Both the ozone concentration and ozone generation efficiency are plotted as functions of specific energy in Fig. 6-5 and Fig. 6-6, respectively. The specific energy is defined as the injected energy per unit volume of feed gas, calculated using equation (6.1):

$$W / Q = \frac{P \cdot 60}{F} \tag{6.1}$$

where F is the flow rate of the feed gas in L/min.

It is clear that, at the same specific energy, the ozone concentration and the ozone generation efficiency were both slightly higher when the gas flow rate was kept constant (0.5 L/min), compared with when the discharge power was kept constant (34 W). However, it can be seen that, for both cases (constant flow rate or constant power), the ozone concentration tended to saturate at ~87 g/Nm^3 when the specific energy reached 5 kJ/L, at which point the ozone generation efficiency fell to 58 g/kWh.

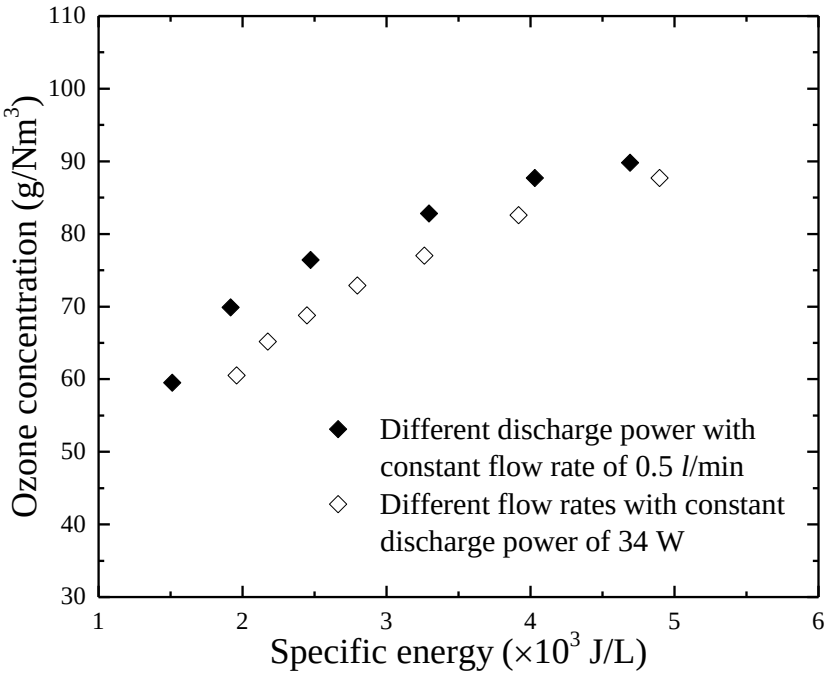

Fig. 6-5. Ozone concentration with respect to the specific energy under two conditions: different discharge power with a constant flow rate of 0.5 L/min and different flow rates with a constant discharge power of 34 W, with gap length of 0.5 mm

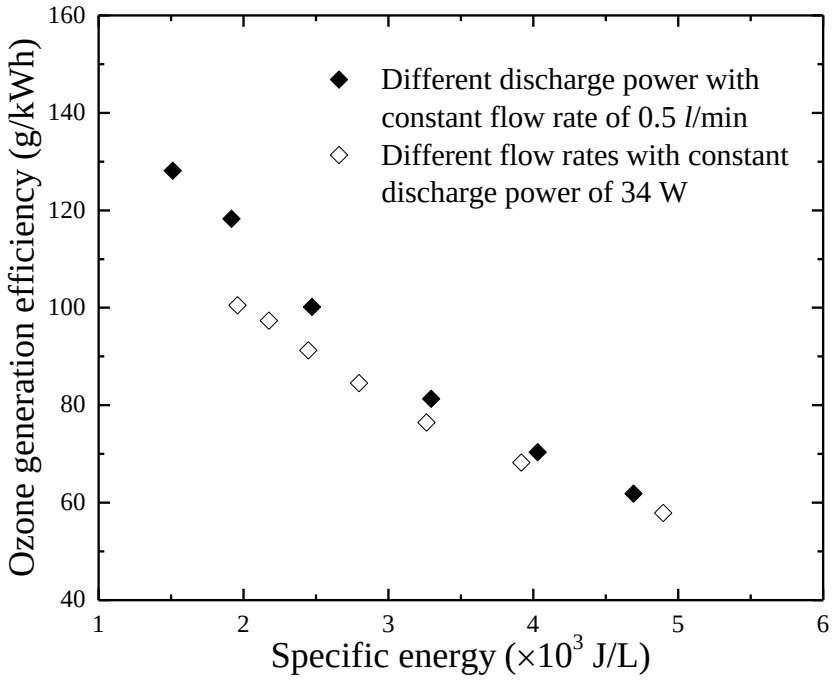

Fig. 6-6. Ozone generation efficiency with respect to the specific energy under two conditions: different discharge power with a constant flow rate of 0.5 L/min and different flow rates with a constant discharge power of 34 W, with gap length of 0.5 mm

4) The effect of frequency on ozone generation

Experiments were carried out to compare the relative ozone performance at 5 kHz and 3 kHz. The amplitude of the applied voltage was kept constant at 5.5 kV, but the flow rate was varied from 0.4 L/min to 1 L/min, for both frequencies. The ozone concentration as a function of specific energy is shown in Fig. 6-7. It can be seen that, with the same specific energy applied, the ozone concentration was higher at 3 kHz compared to that at 5 kHz. The results show that, at the same specific energy of 4.9 kJ/L, the ozone concentration achieved at 5 kHz is 75.5 g/Nm^3, while the ozone concentration achieved at 3 kHz is 87.7 g/Nm^3, 16% higher. It can be deduced that, at the same specific energy, the ozone generation efficiency at 3 kHz was higher than that at 5 kHz. The ozone concentration as a function of ozone generation efficiency is shown in Fig. 6-8. Fig. 6-8 shows that, at the same ozone concentration, the ozone generation efficiency at 3 kHz is ~55% higher than that at 5 kHz. From the figure, it can be seen that, at the ozone concentration of 68 g/Nm^3, the ozone generation efficiency achieved at 3 kHz is 91 g/kWh, while the ozone generation efficiency achieved at 5 kHz is 59 g/kWh. This can be explained as follows. Under the same applied voltage of 5.5 kV, the discharge power at 5 kHz was 57.4 W, ~76% higher than the

discharge power at 3 kHz, which was 32.6 W. No cooling system was deployed in these experiments; therefore much more heat would be produced in the gap at 5 kHz, contributing to increased ozone decomposition. The ozone decomposition rate at 5 kHz was higher than that at 3 kHz, which results in the lower ozone generation efficiency at 5 kHz.

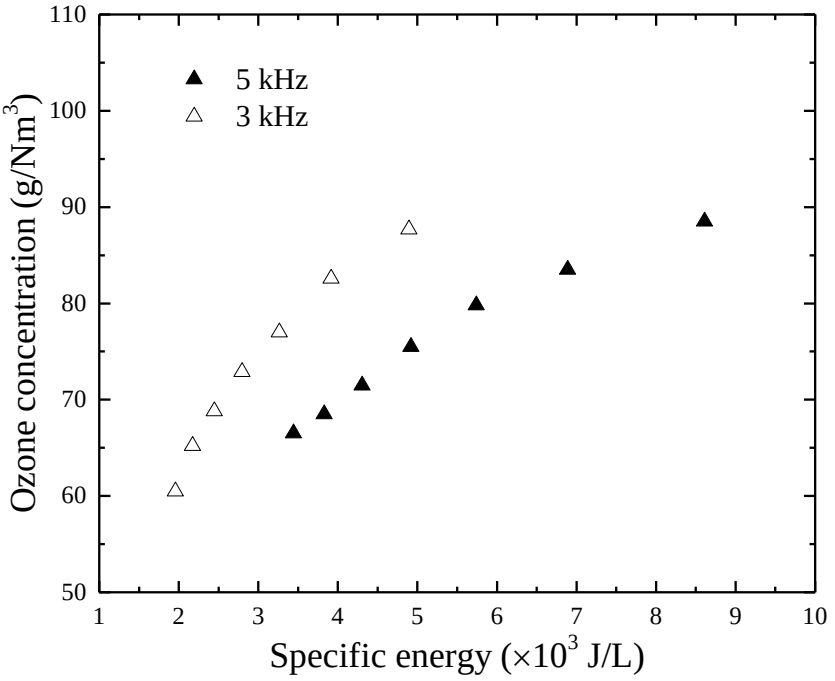

Fig. 6-7. Ozone concentration with respect to the specific energy at 3 kHz and 5 kHz with the same voltage amplitude of 5.5 kV (pressure: 1bar absolute; gap length: 0.5 mm)

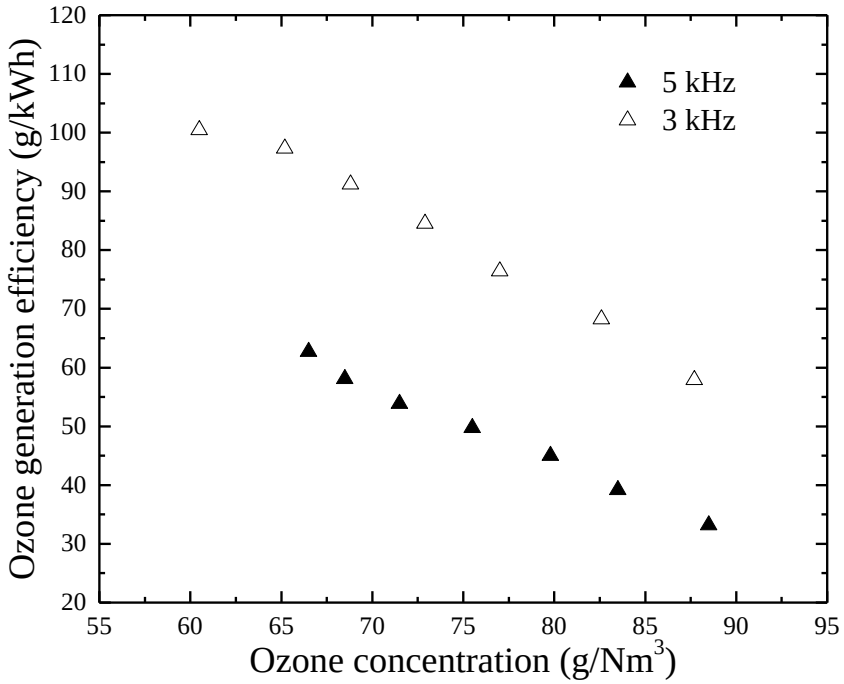

Fig. 6-8. Ozone generation efficiency with respect to ozone concentration at 3 kHz and 5 kHz with the same voltage amplitude of 5.5 kV at the gas pressure of 1 bar absolute

5) The effects of gas pressure on ozone generation

Experiments were undertaken to compare the ozone performance at 1 bar absolute gas pressure and 2 bar absolute gas pressure, with the same gas flow rate. The results are shown in Fig. 6-9 and Fig. 6-10. From Fig. 6-9, it can be seen that, at the same specific energy, the ozone concentration at 2 bar absolute is ~12.7% higher than that at 1 bar absolute, when the specific energy is less than 4.5 kJ/L. When the specific energy was raised to 5 kJ/L, the ozone concentration at 2 bar absolute was 81.7 g/Nm^3, 8.2% higher than that at 1 bar absolute (75.5 g/Nm^3). From the ideal gas law [55], it is known that the gas density increases linearly with increasing gas pressure at a constant temperature. As the volumetric flow rate was the same for both gas pressures, the number of gas particles flowing through the discharge area at 2 bar absolute was twice that at 1 bar absolute. Higher gas density results in increased reaction rates of oxygen dissociation and ozone formation. As the specific energy increases, the ozone dissociation rate increases for both gas pressures, but the ozone dissociation rate at 2 bar absolute increases at a faster rate due to the higher gas density, which manifests in a reduced ozone concentration difference between 2 bar absolute and 1 bar absolute at higher values of specific energy. The ozone generation efficiency as a function of ozone concentration is plotted in Fig. 6-10, which shows that, at the same ozone

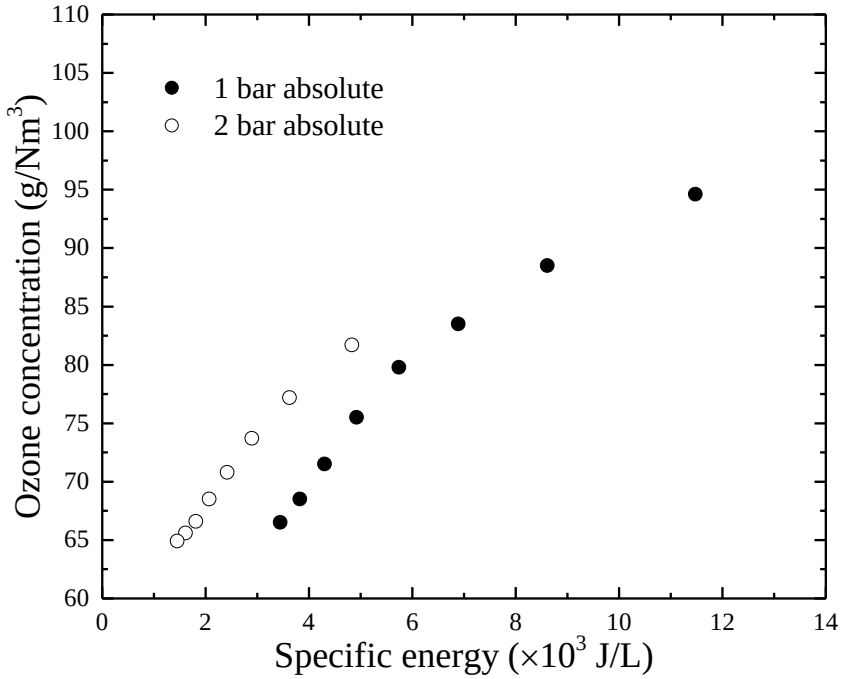

Fig. 6-9. Ozone concentration with respect to the specific energy at 1 bar absolute and 2 bar absolute (applied voltage: 5.5 kV at 5 kHz; gap length: 0.5 mm)

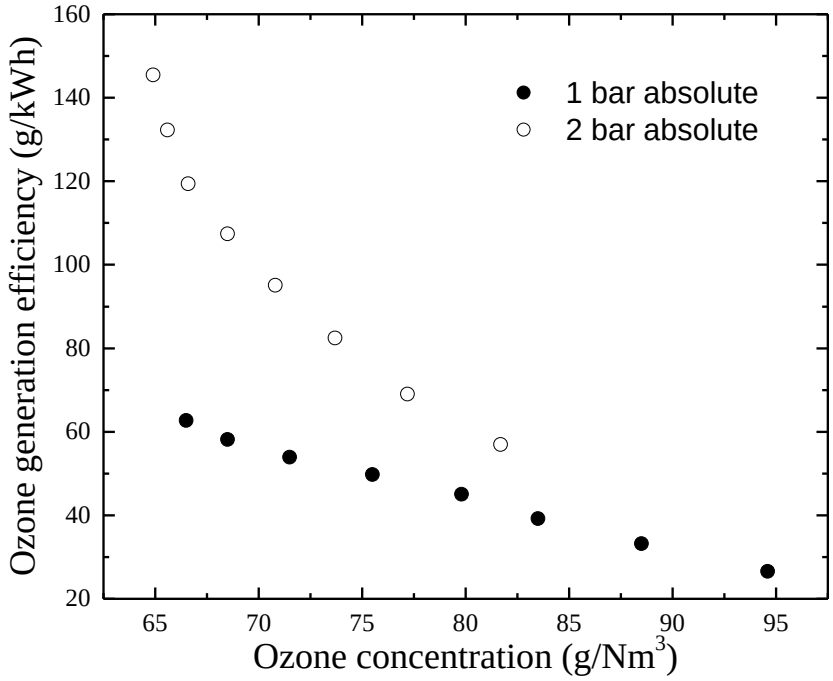

Fig. 6-10. Ozone generation efficiency with respect to ozone concentration at 1 bar absolute and 2 bar absolute gas pressures (applied voltage: 5.5 kV at 5 kHz; at 0.5 mm gap length)

concentration, the ozone generation efficiency at 2 bar absolute was higher than that at 1 bar absolute. It can be seen that the maximum ozone generation efficiency at 2 bar absolute was 145.4 g/kWh when the ozone concentration was 65 g/Nm^3, while the maximum ozone generation efficiency at 1 bar absolute was 62.7 g/kWh when the ozone concentration was 67 g/Nm^3. As the ozone concentration was increased, the ozone generation efficiency under both gas pressures dropped. This is due to increased ozone decomposition rate, but the decomposition rate increased faster at 2 bar absolute, resulting in the ozone generation efficiency dropping at a faster rate at 2 bar absolute than at 1 bar absolute. The ozone generation efficiency fell to 57 g/kWh at ozone concentration of 82 g/Nm^3 at 2 bar absolute, and the ozone generation efficiency decreased to 45 g/kWh at ozone concentration of 80 g/Nm^3 at 1 bar absolute. The ratio of the ozone generation efficiency at 2 bar absolute to that at 1 bar absolute reduced from 2.3 at ozone concentration of 65 g/Nm^3, to 1.3 at ozone concentration of 82 g/Nm^3.

6) The effects of gap length on the ozone generation

The ozone performances with different gap lengths were investigated under different applied voltages at a fixed frequency of 3 kHz, a constant gas flow rate of 0.5 L/min and a constant gas pressure of 1 bar absolute. The results are shown from Fig. 6-11 to Fig. 6-13.

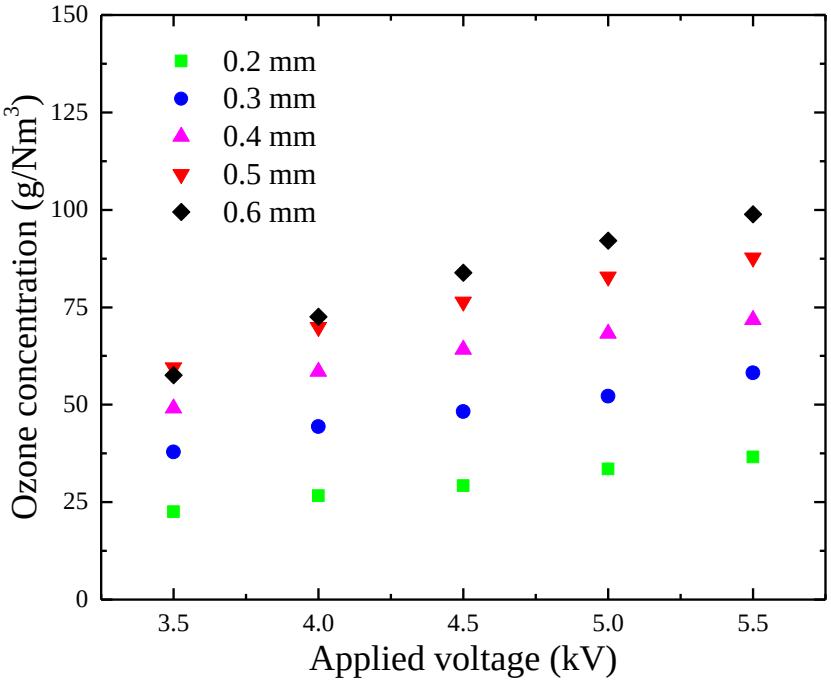

Fig. 6-11. Ozone concentration measured under different applied voltages for different gap lengths

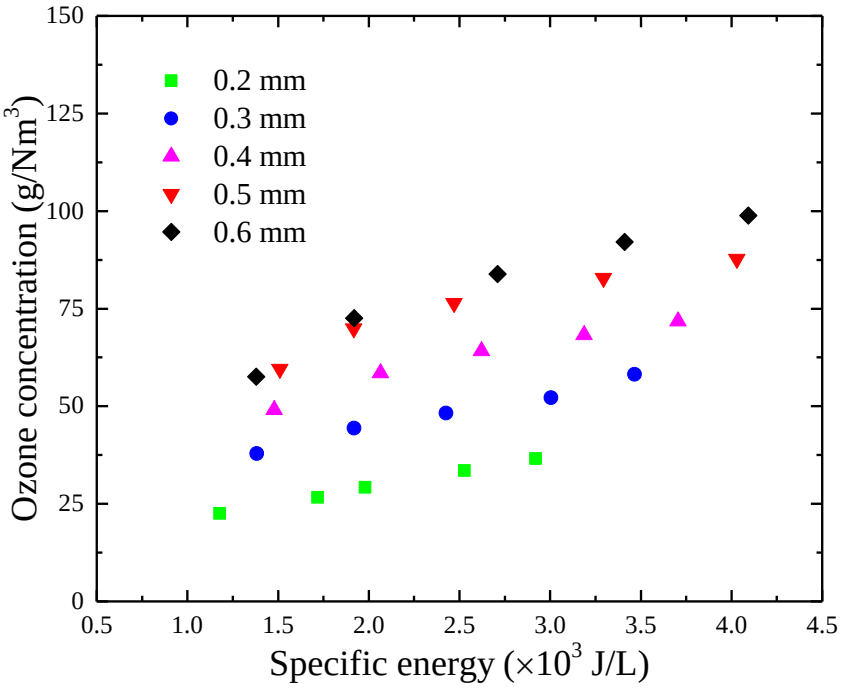

Fig. 6-12. Ozone concentration as a function of different specific energy for different gap lengths (applied voltage: 5.5 kV at 3 kHz; pressure: 1 bar absolute)

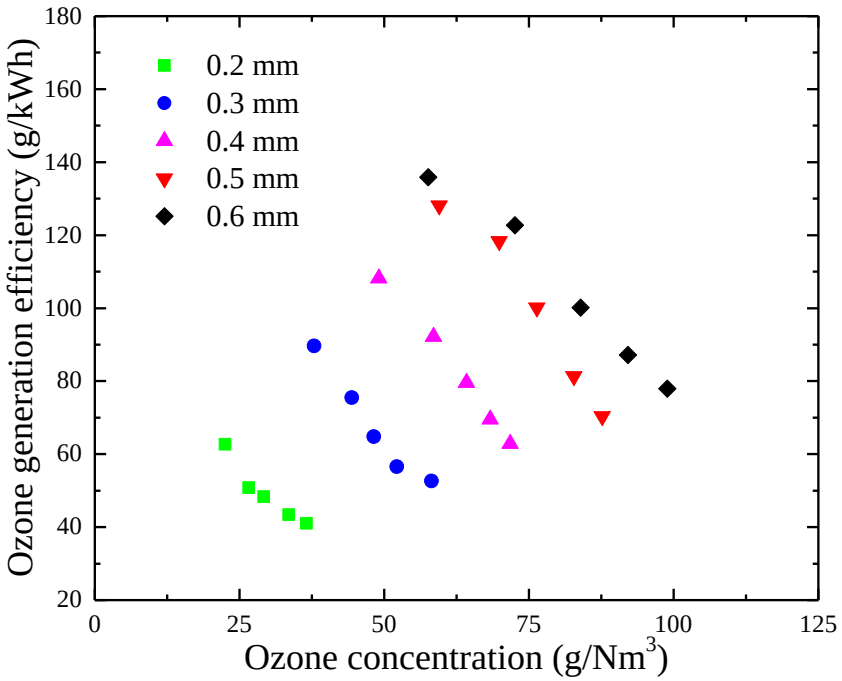

Fig. 6-13. Ozone generation efficiency as a function of ozone concentration for different gap lengths (applied voltage: 5.5 kV at 3 kHz; pressure: 1 bar absolute)

Fig. 6-11 shows the ozone concentration measured under applied voltages from 3.5 kV to 5.5 kV, for different gap lengths from 0.2 mm to 0.6 mm. It can be seen that the ozone concentration increased with increasing applied voltages, for all tested gap lengths. At voltages from 4 kV to 5.5 kV, the ozone concentration increased with increasing gap length. The ozone concentration was 98.9 g/Nm^3 with gap length of 0.6 mm and applied voltage of 5.5 kV, 2.7 times higher than the ozone concentration of 36.6 g/Nm^3 achieved with the gap length of 0.2 mm at the same applied voltage. The ozone concentration is plotted as a function of specific energy for different gap lengths in Fig. 6-12, which shows that, at the same range of specific energy, from 1.4 kJ/L to 2.9 kJ/L, the ozone concentration increased with increasing gap length from 0.2 mm to 0.5 mm. The ozone concentration with the gap length of 0.6 mm started to be higher than that with the gap length of 0.5 mm when the specific energy reached 1.9 kJ/L and above. The ozone generation efficiency as a function of ozone concentration is shown in Fig. 6-13. It can be seen that the ozone generation efficiency dropped with increasing ozone concentration for all tested gap lengths. With the same ozone concentration, in the range from 50 g/Nm^3 to 60 g/Nm^3, the ozone generation efficiency increased with increasing gap length from 0.3 mm to 0.6 mm, but the rate of this increase reduced from 0.5 mm to 0.6 mm; at almost the same ozone concentration, about 58 g/Nm^3, the ozone generation efficiencies achieved with gap lengths from 0.3 to 0.6 mm were 53 g/kWh, 92 g/kWh, 128 g/kWh and 136 g/kWh, respectively. As the ozone concentration was increased, the ozone generation efficiency dropped more slowly with the longer gap length of 0.6 mm, compared to with the gap length of 0.5 mm. The ozone generation efficiency at the maximum ozone concentration of 98.9 g/Nm^3, with the gap length of 0.6 mm, was 77.9 g/kWh.

6.2.3 Discussion

The theoretical ozone generation efficiency can be calculated using equation (6.2):

$$\eta = \frac{(k_{1a} + k_{1b})}{v_d (E/N)} \cdot \frac{1}{1 + \dfrac{2k_5 x_{10}}{k_3 x_{10} + k_4}} \quad O_3 \text{ molecules/eV} \tag{6.2}$$

It can be seen that the ozone generation efficiency depends on the relative *O* atom concentration x_{10}, the reduced electric field (*E/N*), the reactions rates coefficients (k_{1a}, k_{1b}, k_5, k_6 and k_7) and the drift velocity of electrons (v_d). As the *O* atoms are generated inside micro-

discharges, x_{10} depends on the energy density of these micro-discharges (W_0) [70]. In this work, the feed gas parameters (gas flow rate and gas pressure), physical parameter (gap length) and electrical parameters (applied voltage and frequency) were adjusted, which leads to the change of the internal gas discharge parameters (E/N, k_{1a}, k_{1b}, k_5, k_6, k_7, v_d and W_0), hence influencing the ozone generation efficiency and ozone concentration. Higher gas flow rate results in shorter ozone residence time in the discharge gap, which avoids the occurrence of ozone decomposition. Increasing the discharge power or reducing the gas flow rate both resulted in increased specific energy. With an increase in specific energy, the gas temperature increases, which results in saturation of the ozone concentration when the ozone dissociation rate is equal to the ozone formation rate, explaining the results in Fig. 6-5 and Fig. 6-6. The same trend was found in [126] and [127].

In [126], the ozone concentration was found to increase with increasing specific energy, but tended to saturate when the specific energy was raised higher than 2 kJ/L, where the ozone concentration was ~30 g/Nm^3. In [127], when the flow rate was 20 L/hour (~0.33 L/min), the ozone concentration started to saturate at ~35 g/Nm^3, when the specific energy was higher than 7 kJ/L. Changing the amplitude of the applied voltage also resulted in different ozone performance. It was found that the ozone generation efficiency at lower voltage amplitude was higher than that at higher voltage amplitude, which mirrors the results achieved using transient voltages in Chapter 5. This is due to the fact that the gas temperature increases with increasing voltage amplitude, which promotes ozone decomposition. The same reasoning can explain why the ozone generation efficiency was higher at 3 kHz than at 5 kHz.

Pressure effects on the ozone performance result from the influence on the reactions rates coefficients (k_{1a}, k_{1b}, k_5, k_6 and k_7), and also on the E/N in equation (6.2). In this work, higher ozone generation efficiency was achieved at 2 bar absolute compared with 1 bar absolute. The E/N calculated at 2 bar absolute and 1 bar absolute in this work were 126 Td and 137 Td, respectively, reflecting higher ozone generation efficiency at lower E/N. It was found that longer gap length results in higher ozone generation efficiency, which can also be attributed to the change of E/N. The E/N achieved at 0.6 mm was 130 Td, compared with 185 Td at 0.2 mm.

6.3 Ozone Generation Based on Cylindrical DBD Reactor with a Water Cooling System

6.3.1 Test Cell

As ozone is sensitive to temperature increase, an improved cylindrical DBD reactor (Type-C) with a circulating water-cooling system was designed and developed, in order to keep the reactor at a constant low temperature of 15º C. A schematic diagram of the new reactor is shown in **Fig. 6-14**.

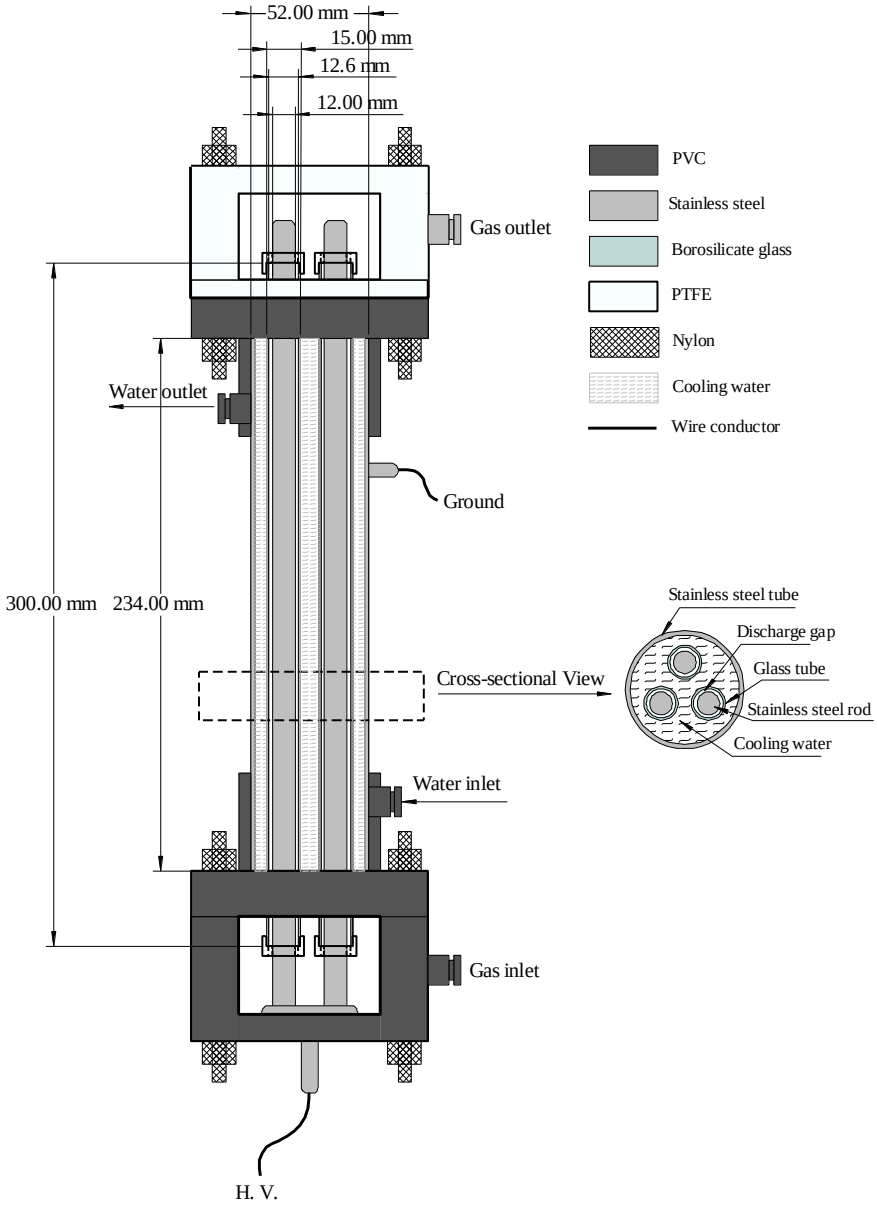

Fig. 6-14 Schematic diagram of Type-C cylindrical DBD reactor

Three borosilicate glass tubes of 300 mm in length were used as dielectric barriers. The tubes had an outer diameter of 15 mm and thickness of 1.2 mm. The active discharge length of the reactor was 234 mm. These glass tubes were placed inside a stainless steel pipe, with surrounding water acting as grounding electrodes. Stainless steel rods with diameter of 12 mm served as high voltage electrodes, located inside each glass tube. The discharge gap distance between the dielectric barrier and high voltage electrode was 0.3 mm. The temperature of the circulating water was kept at a constant value of 15 °C in these experiments. The end caps of the main stainless steel vessel consisted of two gas chambers made of PVC (oxygen side) and PTFE (ozone side). The maximum gas fill pressure was 2 bar absolute, and the water circulating system was sealed. The equivalent capacitances of the dielectric barrier and discharge gap of the Type-C DBD reactor were calculated using equation (6.3):

$$C = \frac{2\pi\varepsilon_r\varepsilon_0 l}{\ln(\frac{r_2}{r_1})} \quad (r_1\text{: Inter radius, } r_2\text{ : Outer radius}) \tag{6.3}$$

The calculated values are as shown below:

$$C_{d3} = 3\times 0.343 = 1.03 \text{ nF} \tag{6.4}$$

$$C_{g3} = 3\times 0.267 = 0.80 \text{ nF} \tag{6.5}$$

where C_d and C_g are the equivalent capacitances of the dielectric barrier and the discharge gap, respectively.

The electric field distribution of coaxial Type-C cylindrical reactor can be calculated by the following equation [55]:

$$E(x) = \frac{V}{In(r_2 / r_1)}\frac{1}{x} \tag{6.6}$$

For the annular gap in the Type-C reactor, r_1 is equal to 6 mm and r_2 is equal to 6.3 mm. V is the voltage across the annular discharge gap. Therefore, the maximum and minimum electric field in the annular gap can be calculated as below:

$$E_{\max} = \frac{1000V}{6In(6.3/6)} \tag{6.7}$$

$$E_{\min} = \frac{1000V}{6.3In(6.3/6)} \tag{6.8}$$

The ratio of maximum electric field and minimum electric field is:

$$\frac{E_{\max}}{E_{\min}} = \frac{6.3}{6} = 1.05 \tag{6.9}$$

It can be seen that the electric field distribution in the annular gap of Type-C reactor was approximately homogenous, giving rise to a gas discharge mechanism in the cylindrical reactor similar to that in the plate-type reactor.

6.3.2 Experimental Set-up

The experimental set-up is shown in Fig. 6-15.

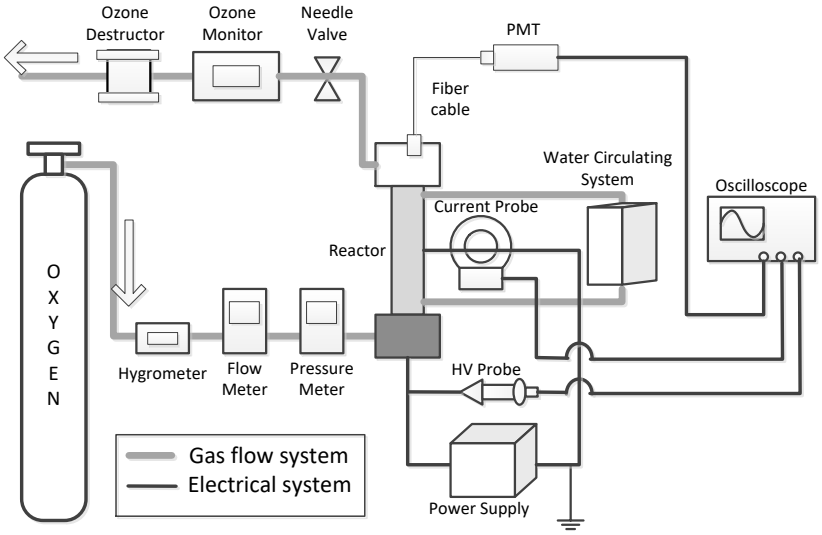

Fig. 6-15 Schematic diagram of the experimental system based on Type-C reactor with a circulating water-cooling system

The high frequency power supply used in this part of the work is based on a series resonant circuit, and two resonant frequencies - 2.6 kHz and 20 kHz - were applied in these experiments. The circuit diagram of the power supply is shown in Fig. 3-5 in Section 3.3.3 in Chapter 3. The peak output voltage from this power supply circuit was 6 kV when it was connected to the Type-C reactor for both frequencies (2.6 kHz and 20 kHz). The power output from the power supply was adjusted by power density modulation (PDM) control. In the experiment, a photomultiplier (ET 9125 B) was used together with a current probe

(Pearson CT 6585) to monitor the discharge characteristics. All the experiments in this work were carried out at atmospheric pressure.

6.3.3 Results and Discussion

1) Discharge Current and PMT Signal Measurement

Fig. 6-16 and Fig. 6-18 are the applied voltage and external current waveforms with the frequencies of 2.6 kHz and 20 kHz, respectively, and Fig. 6-17 and Fig. 6-19 are the applied voltage and PMT signals with the frequencies of 2.6 kHz and 20 kHz, respectively.

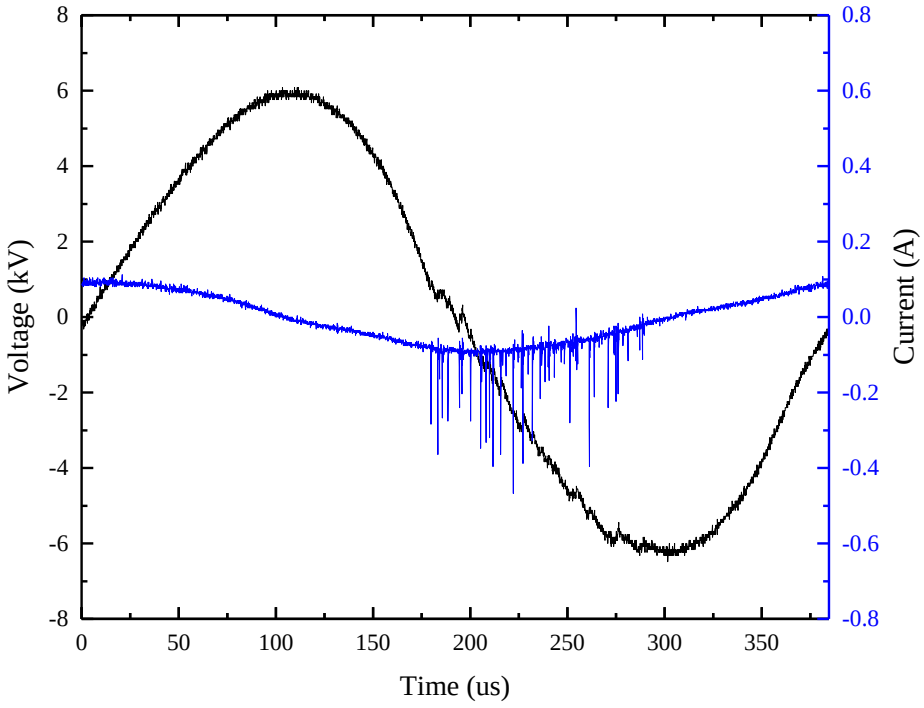

Fig. 6-16 Applied voltages and current measured in the external circuit when Type-C cylindrical DBD reactor was energized by inverter-based 2.6 kHz AC power supply

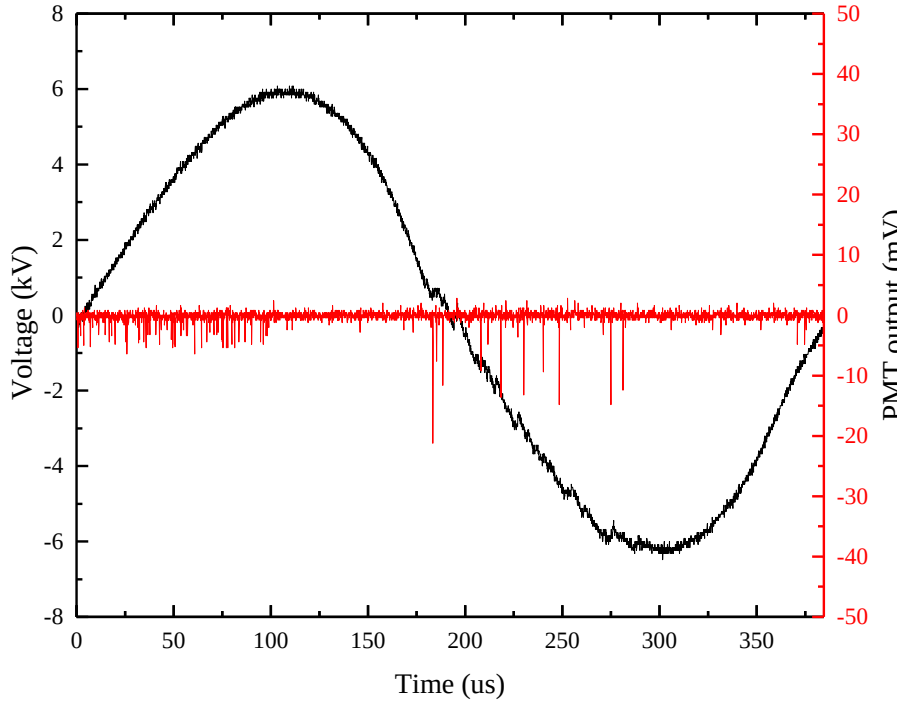

Fig. 6-17 Applied voltages and the corresponding PMT signal when Type-C cylindrical DBD reactor was energized by inverter-based 2.6 kHz AC power supply

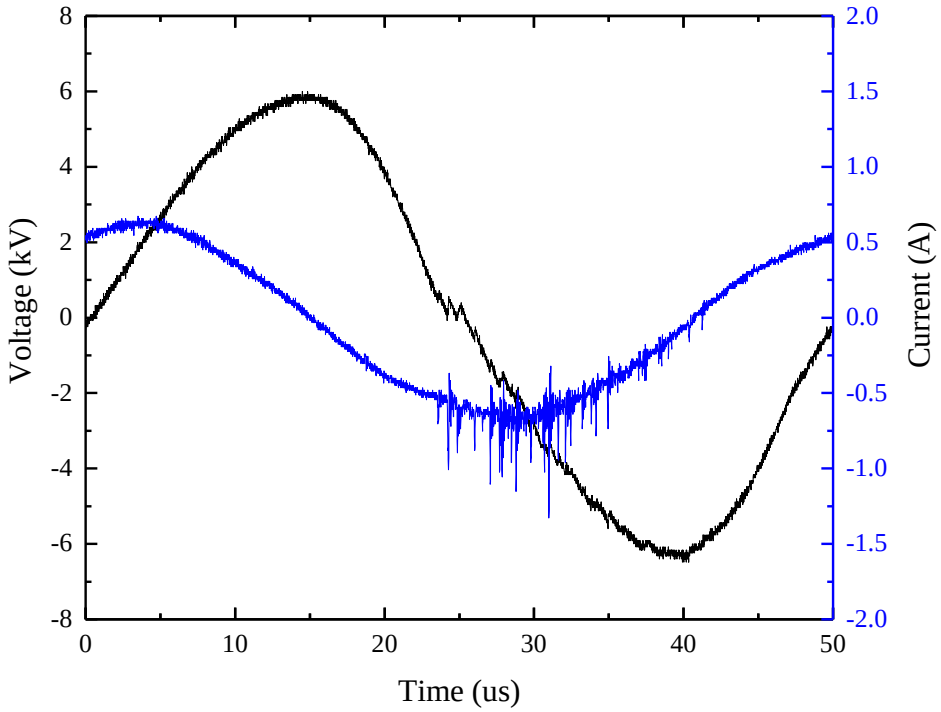

Fig. 6-18 Applied voltages and current measured in the external circuit when Type-C cylindrical DBD reactor was energized by inverter-based 20 kHz AC power supply

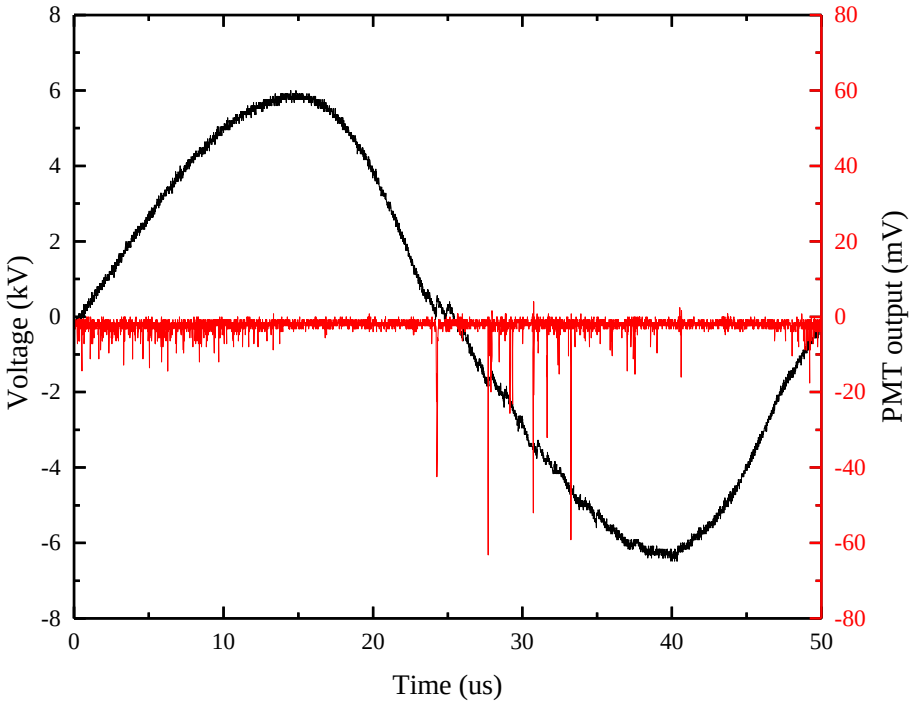

Fig. 6-19 Applied voltages and the corresponding PMT signal when Type-C cylindrical DBD reactor was energized by inverter-based 20 kHz AC power supply

As can be seen, for both tested frequencies, the transient currents are significantly lower during the positive voltage half-cycle as compared with those during the negative voltage half-cycle. From the optical measurements, it can be seen that PMT signals during the positive half-cycle have lower amplitude, but are distributed more homogeneously compared to the higher magnitude signals during the negative half-cycle. The reason for this may result from the pulsed glow-like discharge mode during the positive half-cycle and filamentary discharge mode during the negative half-cycle. When the polarity of the applied voltage is positive, there are a large number of pre-ionization electrons deposited uniformly on the surface of the dielectric barrier from the previous half-cycle. Large electron density causes the overlap and coalescence of primary avalanches, resulting in a pulsed glow-like discharge [71, 88]. During the positive half-cycle, the electrons are neutralized by the positive high voltage electrode, so when the polarity of the high voltage electrode reverses to negative, the density of electrons left in the discharge space is much lower. So, the discharge shows filamentary mode during this negative half-cycle.

Fig. 6-20 shows an exploded view of the discharge current pulse and the PMT output signal. It was found that each PMT pulse corresponded to an individual current pulse, but not every individual current pulse had a corresponding PMT pulse. The reason for this is that the ozone reactor had an annular discharge gap, and the light detector of the PMT can only detect the discharge emitted light coming from a specific discharge space. In Fig. 6-20, the secondary current pulse was emitted from out-with the detection region of the PMT, so no emitted light was detected.

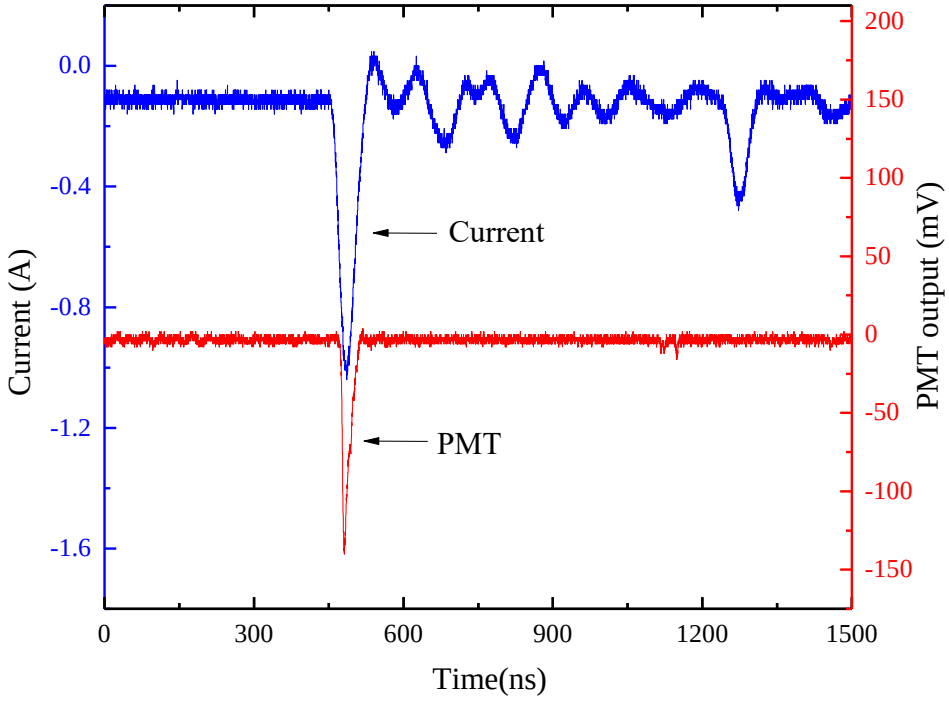

Fig. 6-20 Discharge current in the external circuit and the corresponding PMT output signal

2) Comparison between the ozone generation performances of Type-C reactor with a cooling system and Type-B reactor without a cooling system

The ozone generation performances achieved using the Type-C reactor with a cooling system and using the Type-B reactor without a cooling system were compared. Fig. 6-21 shows the ozone concentrations with respect to specific energy, for both types of ozone generator.

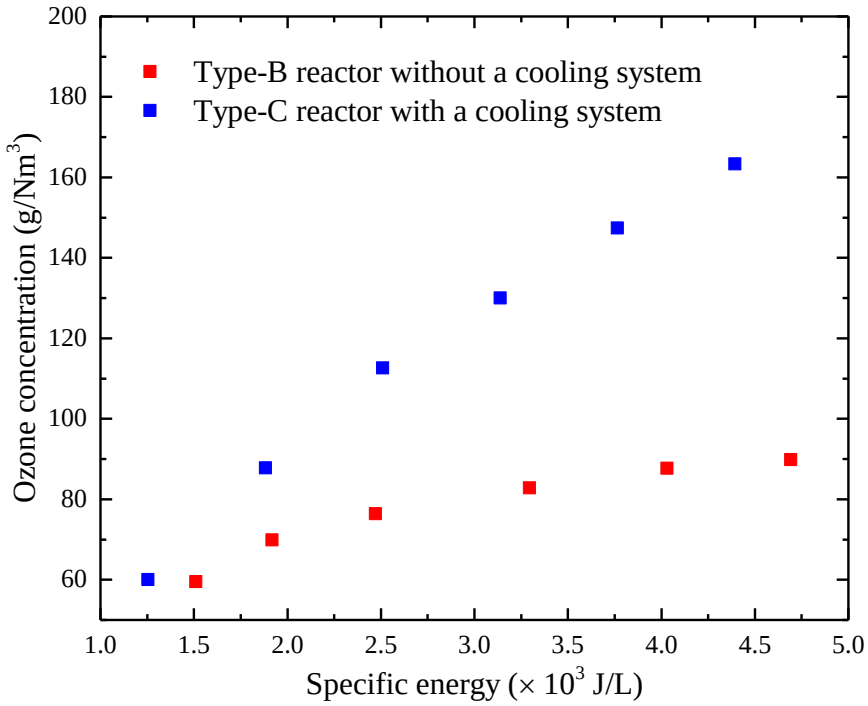

Fig. 6-21 Comparison of the ozone concentration with respect to the specific energy by using different ozone generation reactors

It is shown that the ozone concentration in the Type-C reactor increased with an increase of the specific energy at an approximate rate of 37 (g/Nm^3) / (kJ/L), and the ozone concentration of the Type-B reactor increased more slowly, before saturating at specific energy levels higher than 2.5 kJ/L. As the specific energy increases, the difference between the ozone concentration using the Type-C and Type-B reactors was increasingly larger. At the specific energy of ~1.8 kJ/L, the ozone concentration in the Type-C reactor was 26% higher than that in the Type-B reactor, but at the specific energy of ~4.4 kJ/L, the ozone concentration in the Type-C reactor was 85% higher than that of the Type-B reactor. The reason for this is that, as the specific energy increased, the temperature of the feed gas in the Type-B reactor was increasing, which favoured the ozone decomposition in the gap, while the heat produced in the discharge gap of the Type-C reactor was taken away by the circulating cooling-water surrounding the reactor; therefore, the ozone decomposition at higher specific energy can be prevented in the Type-C reactor. Fig. 6-22 compares the ozone generation efficiency with respect to the specific energy for the Type-B and Type-C reactors.

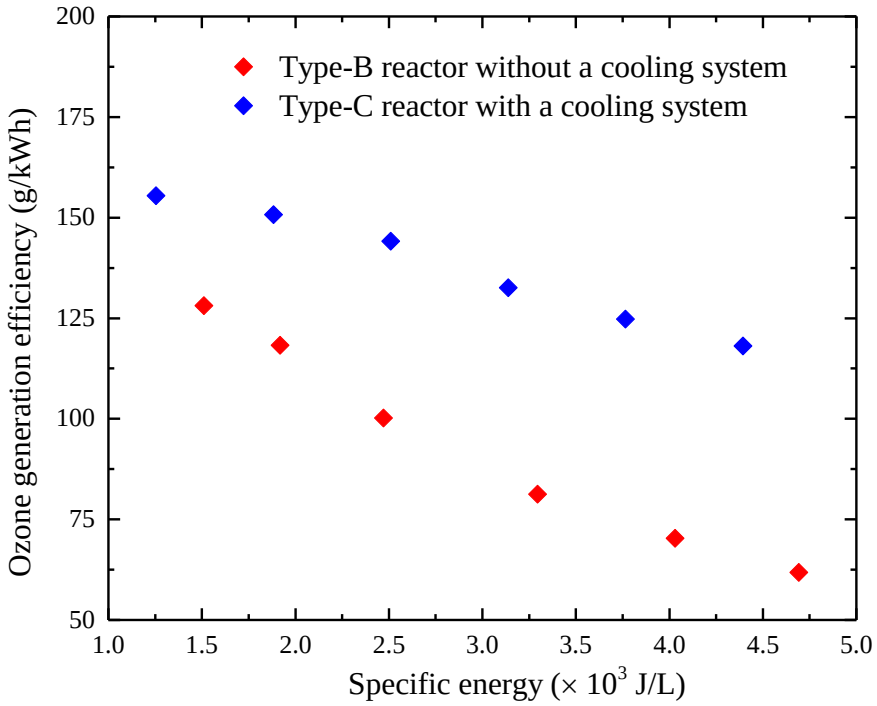

Fig. 6-22 Comparison of the ozone efficiency with respect to the specific energy by using different ozone generation reactors

As can be seen, the ozone generation efficiency reduced with an increase of the specific energy for both reactors, and the ozone generation efficiency for the Type-C reactor was about twice as high as that of the Type-B reactor when the specific energy was 4.5 kJ/L.

Fig. 6-23 shows the ozone generation efficiency with respect to the ozone concentration for both reactors. It is shown that the ozone generation efficiency for the Type-B reactor dropped by ~50% when the ozone concentration increased from 60 g/Nm^3 to 90 g/Nm^3, while the ozone generation efficiency for the Type-C reactor only dropped by ~1% for the same range of ozone concentration. At the concentration of 90 g/Nm^3, the ozone generation efficiency of the Type-C reactor was ~150 g/kWh, while the ozone generation efficiency for the Type-B reactor was only ~62 g/kWh. As the ozone concentration increased, the ozone generation efficiency of the Type-C reactor reduced to 118 g/kWh at the concentration of 163 g/Nm^3.

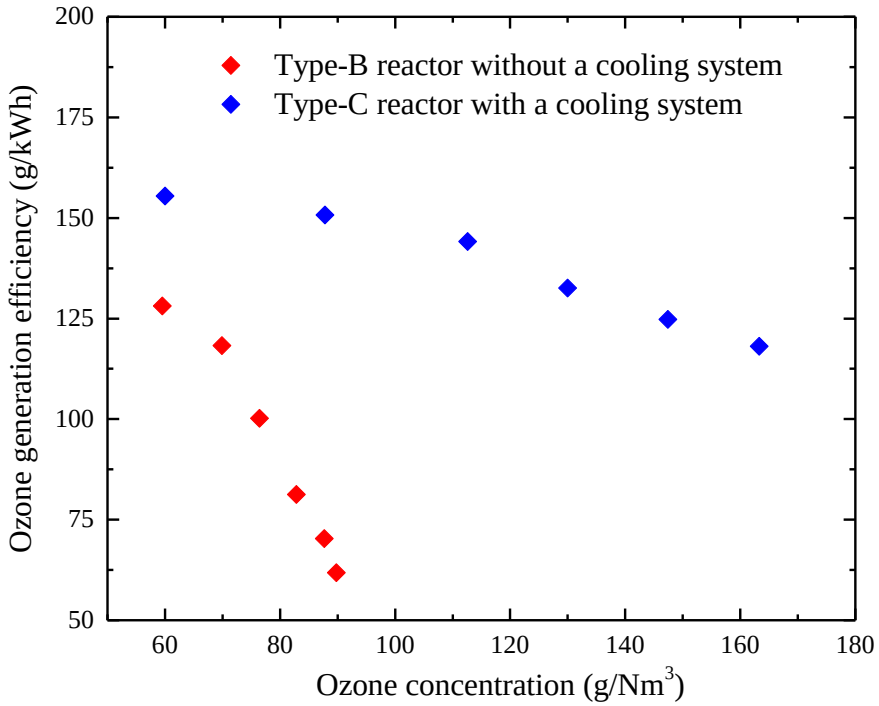

Fig. 6-23 Comparison of the ozone efficiency with respect to the ozone concentration by using different ozone generation reactors

From the above comparison, it can be seen that the incorporation of a water-cooling system into the ozone reactor can significantly improve the ozone generation performance for higher discharge powers. The Type-C ozone reactor with a water-cooling system reflected higher ozone generation efficiencies compared with the Type-B reactor without a cooling system.

Compared with the plate DBD reactor (Type-B), it was easier to integrate a water-cooling system into the cylindrical DBD reactor (Type-C). However, the plate-type reactor had advantages in terms of ready adjustment of the gap length for the investigation of the effect of varying gap length on the ozone generation efficiency. In terms of the discharge characteristics, pulsed glow-like discharge mode has been found in the positive half-voltage-cycle in the Type-C cylindrical reactor (shown in Fig.6-18), compared with filamentary modes on both half-voltage-cycle in the Type-B plate reactor.

6.4 Frequency Effect on Ozone Generation

Dielectric barrier discharges are commonly energized by a continuous AC power supply in industry. The frequency of the AC power supply is a key parameter affecting ozone generation. In this section, the effect of frequency on the ozone generation performance was investigated. The ozone concentration and ozone generation efficiency at the frequencies of 50 Hz, 2.6 kHz and 20 kHz were measured and compared, using the same experimental set-up (Fig. 6-15), same test cell (Type-C), and same applied voltage, with peak amplitude of 6 kV.

6.4.1 Ozone Generation with 50 Hz AC Power Supply

The ozone concentration and generation efficiency for different flow rates at 50 Hz are shown in Fig. 6-24:.

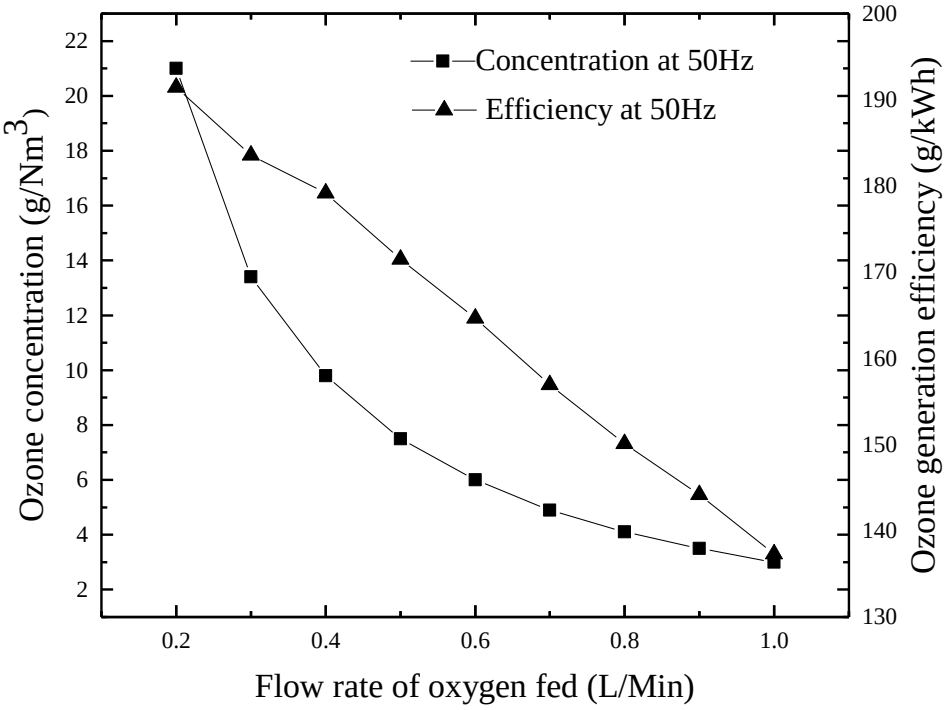

Fig. 6-24 Ozone concentration and generation efficiency for different flow rates by using Type-C reactor at 50 Hz

As can be seen from Fig. 6-24, the ozone concentration and ozone generation efficiency both decrease with increasing feed gas flow rate. The highest ozone concentration achieved at 50

Hz is 21 g/Nm^3, at a flow rate of 0.2 L/min, corresponding to the highest ozone generation efficiency of 192 g/kWh. When the flow rate was increased to 1 L/min, the ozone concentration dropped to 3 g/Nm^3, with corresponding ozone generation efficiency of 135 g/kWh. Fig. 6-25 shows the ozone generation efficiency with respect to the ozone concentration at 50 Hz, and it can be seen that the ozone generation efficiency increased with increasing ozone concentration.

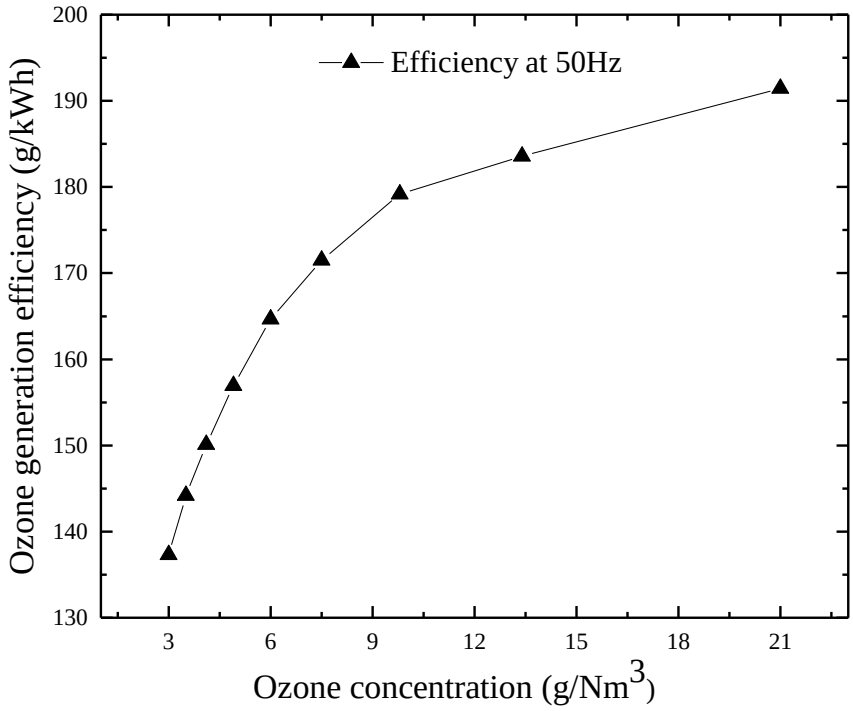

Fig. 6-25 Ozone generation efficiency with respect to ozone concentration using Type-C reactor at 50 Hz

6.4.2 Ozone Generation with kHz AC Power Supply

The ozone generation performance with frequencies of 2.6 kHz and 20 kHz is shown in Fig. 6-26 and Fig. 6-27.

For both tested frequencies of 2.6 kHz and 20 kHz, it is shown that the ozone concentration decreases with an increase of the feed gas flow rate, while the ozone generation efficiency increases with an increase of the feed gas flow rate. The highest ozone concentrations achieved at 2.6 kHz and 20 kHz were 271 g/Nm^3 and 250 g/Nm^3, respectively, at a flow rate of 0.2 L/min. The ozone concentration at 2.6 kHz was ~8% higher than that at 20 kHz at a flow rate of 0.2 L/min, but this rate (~8%) reduced as the flow rate increased, as shown in

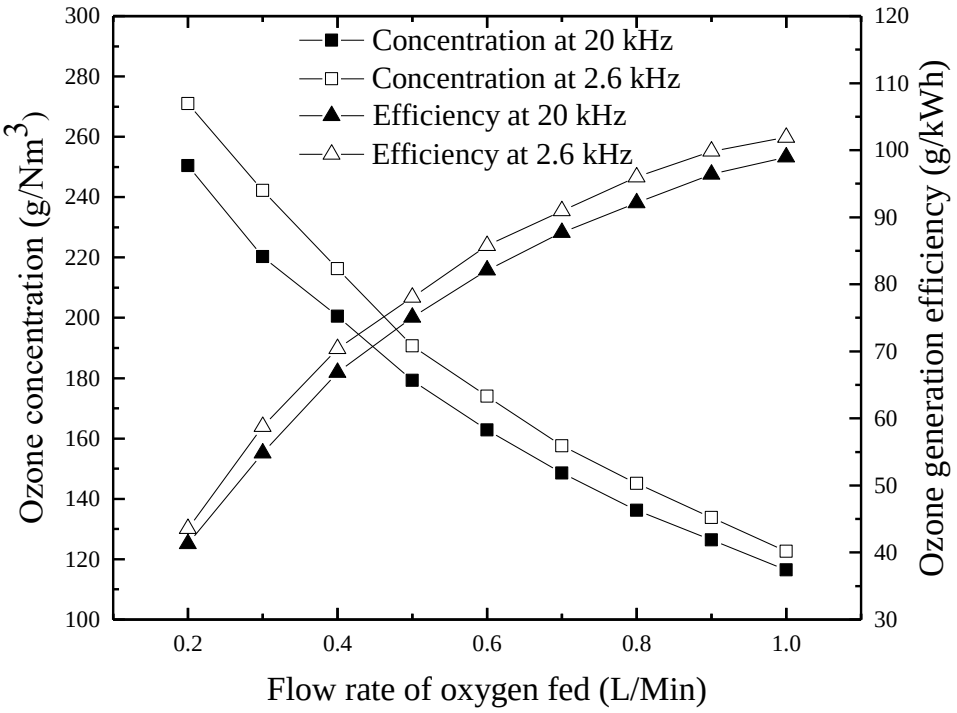

Fig. 6-26 Ozone concentration and generation efficiency at different flow rates using Type-C reactor at 2.6 kHz and 20 kHz

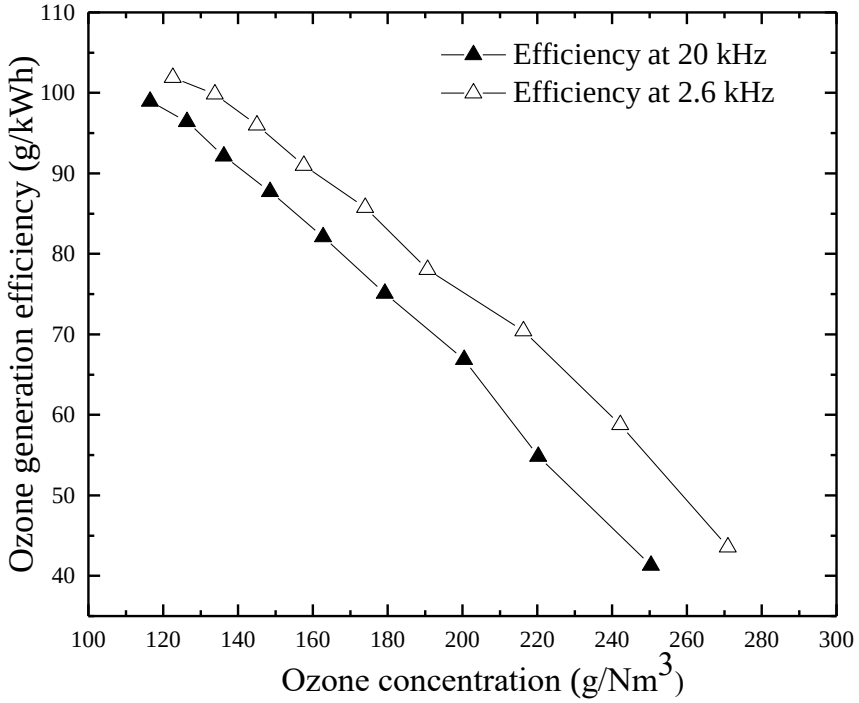

Fig. 6-27 Ozone generation efficiency with respect to ozone concentration using Type-C reactor at 2.6 kHz and 20 kHz

Fig. 6-26. The highest efficiencies achieved at 2.6 kHz and 20 kHz were 101.9 g/kWh and 99.0 g/kWh, respectively, at the flow rate of 1 L/min, when the ozone concentrations were 122 g/Nm^3 and 116 g/Nm^3, respectively. From Fig. 6-27, it can be seen that, for both frequencies, the ozone generation efficiency decreased with an increase of the ozone concentration. The ozone generation efficiency dropped to below 50 g/kWh when the ozone concentration was raised to be higher than 250 g/Nm^3. The reason for this is that the dissociative attachment of electrons in ozone increases with an increase in the concentration of ozone [128, 129], which results in the drop of ozone generation efficiency at high ozone concentrations.

6.4.3 Discussion of Frequency Effect

1) Comparison of the Ozone Performance at 50 Hz, 2.6 kHz and 20 kHz

From the experimental results, it was found that the ozone efficiency increased with an increase of the ozone concentration at 50 Hz, while at 2.6 kHz and 20 kHz, the ozone generation efficiency decreased with an increase of the ozone concentration. The reason for this can be explained according to the reactions below:

$$O + O_2 + M \xrightarrow{k_2} O_3^* + M \qquad \text{(R2)}$$

(M = [O], [O_2], [O_3])

$$O + O_3^* \xrightarrow{k_5} 2O_2 \qquad \text{(R5)}$$

$$e + O_3 \xrightarrow{k_6} O_2 + O + \mathrm{e} \qquad \text{(R6)}$$

As the background ozone concentration increases to a certain level (20 g/Nm^3), the ozone dissociation reaction rates (k_5 and k_6) become comparable with the ozone generation rate (k_2), and the reaction rates increase further as the ozone concentration increases [1, 14], which causes a drop in the ozone generation efficiency. However, while the ozone dissociation reaction rates are negligible at the low ozone concentrations achieved at 50 Hz, the ozone generation reaction rate (k_2) increases due to an increase of the oxygen dissociation rate. The increase of the oxygen dissociation rate is due to the longer residence time of the oxygen feed gas when the gas flow rate is lower. Therefore, at lower gas flow rate, the ozone concentration was higher, and the ozone generation efficiency was also higher at 50 Hz.

Samaranayake *et al* also had the same discovery in [130], finding that the ozone generation efficiency increased with increasing concentration of ozone until reaching a maximum, upon which the efficiency declined slightly. The ozone concentrations investigated in [130] were from 0 to 10,000 ppm (~21 g/Nm^3), which is in the same range of ozone concentrations generated at 50 Hz in the present study.

Fig. 6-27 shows that, at the same ozone concentration, the energisation frequency of 2.6 kHz resulted in slightly higher ozone production efficiency, as compared with the energisation frequency of 20 kHz. The reason for this is likely related to the different power modulation modes for the two tested frequencies. To provide the same discharge power as that provided by the 2.6 kHz AC power supply, the duty cycle of the 20 kHz AC power supply was set at 13%, while the duty cycle of the 2.6 kHz AC power supply was 100%. Under the 20 kHz power supply, the charges accumulated on the dielectric surface would decrease with time (due to ion-pair recombination) during the 87% shut-off period of the power supply, which might be the cause of the lower ozone generation efficiency compared with the 2.6 kHz power supply, with 100% duty cycle.

2) Lissajous figure and power density

With the same amplitude of applied voltage (6 kV), the charge transfer during one voltage cycle was the same at 50 Hz, 2.6 kHz and 20 kHz, which was confirmed by the measurement of the Lissajous figure of DBDs at the three different energization frequencies. The Lissajous figures at the frequencies of 50 Hz, 2.6 kHz and 20 kHz were the same, as shown in Fig. 6-28.

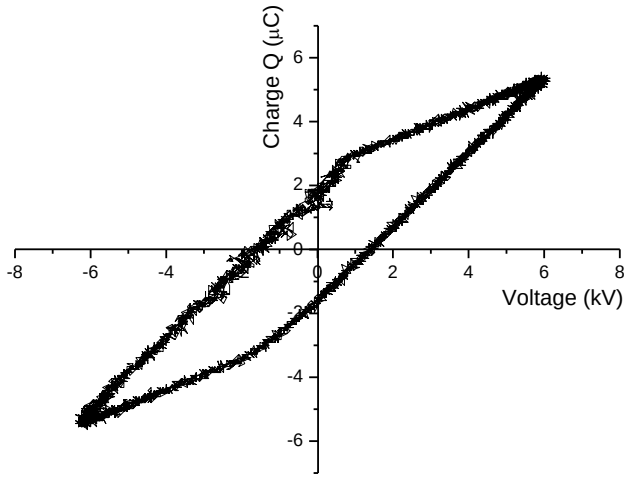

Fig. 6-28 Superimposed Lissajous figure of DBDs based on Type-C reactor energized by 6 kV AC power supplies with the frequencies of 50 Hz, 2.6 kHz and 20 kHz

As discussed in Section 3.5.2, the area inside the closed Lissajous figure multiplied by the AC power frequency is equal to the discharge power, as described by equation (6.10):

$$P=f\cdot\int_0^T V_a(t)\cdot dQ \tag{6.10}$$

which shows that, with the same amplitude of the applied voltage, increasing the AC power frequency, *f*, can increase the discharge power linearly. Based on this, application of an AC power supply operating in the kHz regime can result in a compact ozone generator, with a high power density. The power density is defined as the average power divided by the discharge surface area of the ozone reactor. For the same type of ozone generator (Type-C), the power densities achieved at 50 Hz, 2.6 kHz and 20 kHz are shown in Table 6-1.

Table 6-1 Average power densities at different frequencies

Power supply	50 Hz	2.6 kHz	20 kHz
Average Power Density	44.2 W/m^2	2.37 kW/m^2	2.29 kW/m^2

From Table 6-1, it can be seen that, compared to the industrial frequency of 50 Hz, high energization frequencies of 2.6 kHz and 20 kHz provide much higher power density, which results in the generation of high concentrations of ozone. By using kHz energization frequencies, the applied voltage required to produce ozone with concentrations higher than 200 g/Nm^3 - which has been demonstrated in this work - can be reduced to the range of about 6 kV., Reducing the applied voltage can practically eliminate the risk of dielectric breakdown in the ozone generator. In industry, it is found that the typical operating frequencies of modern high-power ozone generators are between 500 Hz and 5 kHz, and the typical power densities reach 1–10 kW/m^2 [16]. In terms of the physical size, an ozone generator operating in the kHz regime is more compact, enabled by the use of compact ferrite core transformers, while ozone generators operating at 50 Hz are larger due to the bulky, power-frequency transformer.

6.5 Comparison of the Ozone Generation Performance with the Literature Data

The optimum performance of the ozone generator in this work is based on the Type-C cylindrical ozone reactor, fitted with a water-cooling system. The ozone generation efficiency with respect to the ozone concentration using the Type-C reactor at 2.6 kHz is presented in Fig. 6-29.

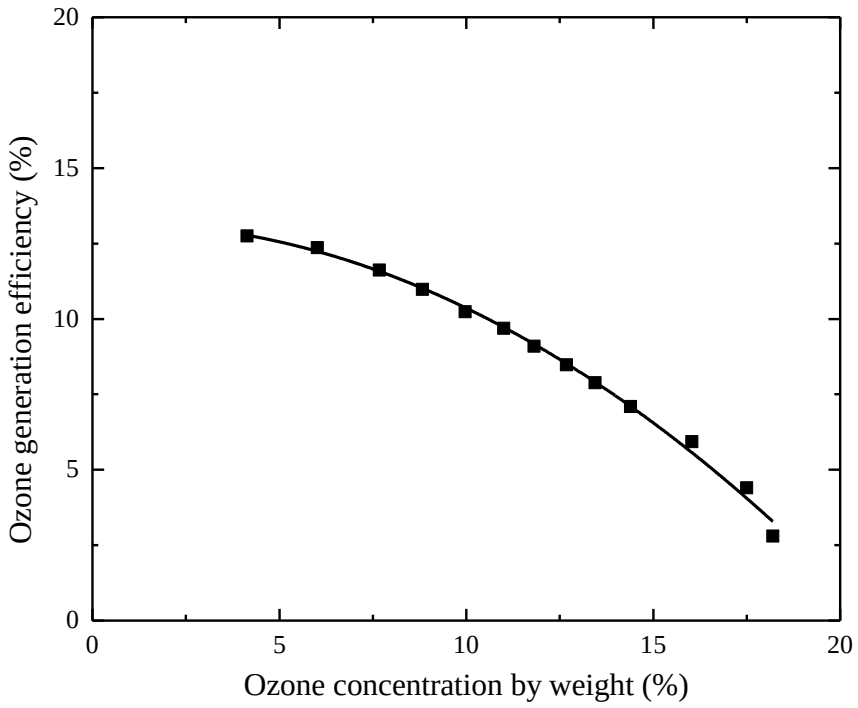

Fig. 6-29 Ozone generation efficiency versus ozone concentration (100% efficiency corresponds to a specific power consumption of 0.82 kWh/kg [1])

In the figure, the ozone concentration value with the dimension, %*wt*/*wt* (mass of ozone per mass of sample gas), was calculated from the dimension, g/Nm^3. The conversion process of these two dimensions can be found in APPENDIX C. From Chapter 2, it is known that 100% efficiency of ozone generation corresponds to the efficiency of 0.82 kWh/kg. Based on this, the ozone generation efficiencies were converted into a percentage value and plotted in Fig. 6-29. The ozone generation efficiency versus concentration curve of Fig. 6-29 was compared with the curve achieved in [1], which is shown in Fig. 6-30.

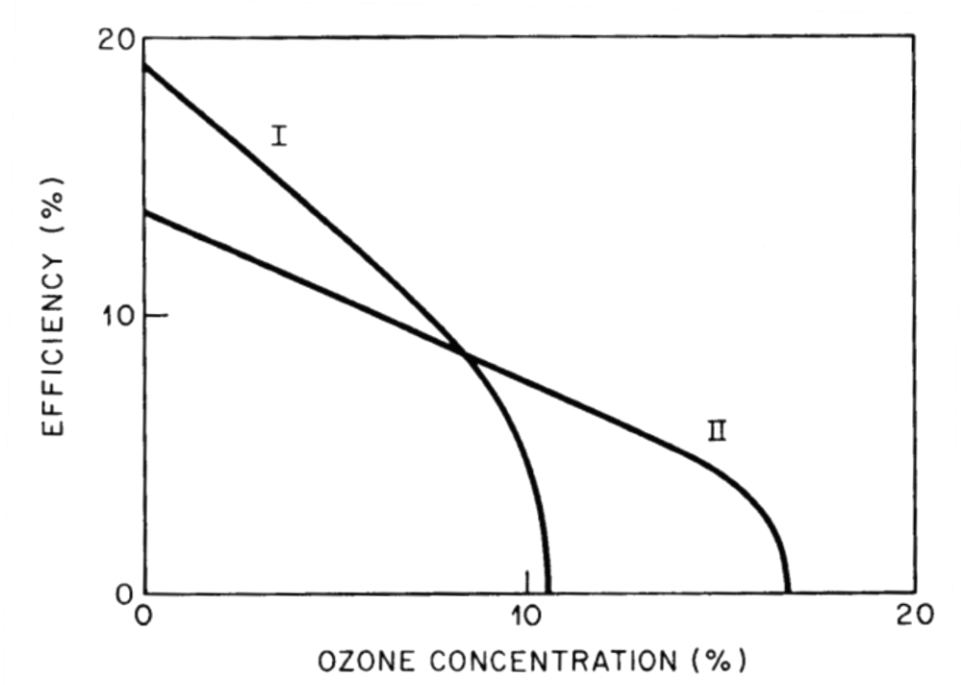

Fig. 6-30 Ozone generation efficiency versus ozone concentration (100% efficiency corresponds to a specific power consumption of 0.82 kWh/kg) [1]

As Fig. 6-30 shows, two ozone performance curves, curve I and curve II, were presented. Curve I is the choice for the demand of high efficiencies at low ozone concentrations, while curve II is the choice for high ozone concentration [1]. Compared with curve II in Fig. 6-30, the curve in Fig. 6-29, which was achieved in the present study, provided ~20% higher ozone generation efficiency at the same ozone concentration. At the typical ozone concentration of 150 g/Nm^3 (10% by weight) used in industrial applications, the maximum efficiency of this work is ~10%, corresponding to ~8.2 kWh/kg, while the efficiency from curve II is ~8%, corresponding to ~10.25 kWh/kg. From curve II, it can be seen that the maximum (saturated) ozone concentration was at 17.2%, corresponding to 260 g/Nm^3, while the maximum (saturated) ozone concentration in the present study was 18.1%, corresponding to 278 g/Nm^3. The results show that the Type-C ozone reactor with a water-cooling system provided promising ozone efficiency.

6.6 Discussion and Conclusion

Two types of ozone reactor, plate type and cylindrical type, have been investigated in this work. The plate type reactor (Type-B) was used because it was beneficial for adjusting the discharge gap length of the reactor, which provided the feasibility to investigate the effect of discharge gap length on the ozone performance. The cylindrical type reactor (Type-C) provided the feasibility of integrating a water-cooling system, which made it possible to generate higher ozone concentrations. Based on the plate type reactor, several experiments were conducted to investigate the ozone generation performance with different physical conditions and electrical conditions. The results showed that, in order to increase the ozone concentration, either the feed gas flow rate must be reduced, or the discharge power must be raised. While both methods will increase the specific energy injected into the ozone generator, adjusting the discharge power to achieve different ozone concentration was more efficient than adjusting the flow rate. However, when the discharge power increases, more heat will be generated, which requires an active heat dissipation system. The Type-C reactor with cylindrical configuration was integrated with a circulating water-cooling system, which provided a better ozone generation performance. It is also possible to integrate an air-cooling system for the plate type ozone generator, but for large-scale industrial ozone generation systems, a water-cooling system is necessary. Compared with plate type ozone generators, the cylindrical ozone generator also has a superior feed gas flowing system, because the gas turbulence in the plate type discharge gap can be avoided in the annular discharge gap. Based on these reasons, most modern large ozone generators use cylindrical discharge tubes, enclosed inside large steel tanks with a circulating water-cooling system [16].

The effect of frequency on the ozone generation performance was also investigated in this chapter. The results showed that the discharge characteristics of DBDs and the ozone generation efficiency were not affected by the energisation frequency. In the work done by Starke [131], it was also indicated that the ozone generation efficiency was independent of the applied frequency. However, the power density of an ozone generator is proportionally related to the energisation frequency. Compared with the power-frequency of 50 Hz, energisation frequency of 20 kHz with the same amplitude of applied voltage provides much higher power density, which results in higher ozone concentration. For a given ozone output, a power supply operating in the kHz regime has lower applied voltage (usually below 10 kV) compared with a 50 Hz power supply. For a 50 Hz ozone generator, the typical applied voltage is between 12 kV and 25 kV. As the voltage increases, the stress on the dielectric

barrier will increase, which reduces the service life of the ozone generator. Other advantages of using high frequency (kHz) ozone generators are as listed below:

- the ozone production amount can be easily increased with less electrode surface area, so for a given ozone output, the size of the ozone generator is small;
- using modern power electronics control strategies, a resonant frequency can be automatically detected and applied, which provides optimum reactive power compensation in the power supply circuit;
- voltage and frequency are both readily adjustable, which make it easy to control the ozone production amount.

In terms of the effect of the feed gas conditions on ozone generation, it was found that a higher pressure of 2 bar absolute provided a superior ozone performance as compared with atmospheric pressure. The reason for this may be due to the increase of the oxygen dissociation rate with an increase in the oxygen feed gas density. In addition, it is important to use an oxygen feed gas with high purity and low dew point for ozone generation. In this work, the dew point of the oxygen was limited to −40ºC by the laboratory conditions, but for commercial ozone generators it is recommended to use feed gas with a dew point of −60ºC.

In terms of the effect of discharge gap length on ozone generation, it was found that, based on a plate type ozone generator, longer discharge gap length (0.6 mm) provided higher ozone generation efficiency at the same ozone concentration, as compared with the shorter discharge gap (0.2 mm). In commercial ozone generators, 0.5–1 mm annular discharge gaps are commonly used in tubular ozone generators [16]. Larger discharge gaps (>1 mm) are rarely used, because they requires higher gas breakdown voltage. For narrow discharge gap lengths (<0.5 mm), geometrical tolerances on the stainless steel electrodes and the glass tube are important issues in industrial ozone generators, because local deviations from the design gap length have an important influence on micro-discharge properties, the gas flow and the heat flow, which can cause drastic reductions of the ozone generation efficiency [16].

In conclusion, this chapter presented a detailed study of high concentration ozone generation. Both a plate type and a cylindrical type ozone generator were investigated and compared in this work. The cylindrical ozone generator with a circulating water-cooling system showed a promising ozone generation efficiency of ~8.2 kWh/kg at the typical industrial ozone concentration of 150 g/Nm^3, which is ~20% higher than the typical ozone generation efficiency in the literature [1]. It was observed that the ozone generation efficiency was very sensitive to increases of the discharge power, and increasing the applied voltage or frequency

will cause the ozone generation efficiency to drop, unless the heat produced in the gap can be dissipated effectively. The maximum ozone concentration value (271 g/Nm^3 in this work) was also strongly limited by the heat dissipation capability of the generator. In addition, inverter-based power supplies operating in the kHz regime can provide much higher power density for ozone generation, and both the ozone generation efficiency and discharge characteristics were found to be independent of the AC energisation frequency.

7 INVESTIGATION OF OZONE GENERATION USING A PULSED POWER SUPPLY

7.1 Introduction

Ozone is produced through the dissociation of O_2 molecules by electrons and a subsequent three-body reaction involving an O atom, O_2 molecule and a third particle, M [14]. Electrons in micro-discharges play a key role in ozone formation, as they produce the oxygen atoms necessary for ozone formation. Therefore, in order to optimize the ozone production efficiency, control of the electron energy in micro-discharges is important. It is known that the mean energy of electrons distributed in a gas-filled gap is determined by the reduced electric field [*E/N*] in the gap [132]. The use of impulse voltages with fast rate-of-rise permits the application of over-voltage across the discharge gap without resulting in electrical breakdown [55]. Hence, higher *E/N* can be achieved under impulse voltage energisation. The effects of *E/N* on the ozone generation efficiency and pulsed DBD for ozone generation have been studied by several researchers. Eliasson *et al.* demonstrated the dependence of ozone production efficiency on *E/N* through numerical calculations, and showed that the optimum *E/N* for ozone production was from 100 Td to 200 Td [14]. Shuhai Liu *et al.* reported that the discharge onset voltage was about three times higher than the DC breakdown voltage under square pulse energisation (rise time of 14 ns), and the ozone synthesis efficiency was improved by 30% compared with sinusoidal excitation [98]. In addition, short-duration (of the order of ns) pulsed discharges can decrease the energy wasted in the movement of ions, which can prevent the temperature of ions and neutral gas molecules from increasing [133]. Many studies on pulsed ozone production have been carried out, with the aim of improving ozone production efficiency [10, 100, 104, 126]. In these studies, ozone was produced using pulsed streamer discharges in a coaxial wire cylinder [10, 100] or spiral cylinder with or without a dielectric barrier [104, 126]. The ozone production efficiency reported in these studies was promising: Chalmers reported an efficiency of 300 g/kWh using pulses of 20 ns duration [100]; Samaranayake reported an efficiency of 202 g/kWh at a pulse repetition rate of 25 pps [104]. However, these experiments were conducted at low ozone concentration (below 10 g/Nm^3). From the results achieved in these studies, it can be seen that the efficiency drops quickly when the ozone concentration is above 10 g/Nm^3. It is the interest of this research to investigate the

generation efficiency of ozone with higher concentration (>10 g/Nm^3), when using impulsive energisation voltages.

In this chapter, pulse discharge technology and its applications in ozone generation are initially reviewed, followed by an investigation of the effects of the rate-of-rise of the voltage impulse on oxygen-fed dielectric barrier discharges. The reduced electric field and charge transferred inside the gap under voltage rise rates of 300 V/ns and 500 V/ns were calculated, and the effect of the applied voltage impulses on ozone production is discussed. Secondly, a comparative study of ozone generation by using pulsed and continuous AC dielectric barrier discharges is presented. Ozone production efficiency for ozone concentrations up to 50 g/Nm^3 were investigated, and the DBD discharges modes and ozone production efficiencies under both energisation regimes are compared. The ozone generation performance achieved in this work is also compared with the literature data.

7.2 Pulsed Power Technology and its Applications in Ozone Generation

7.2.1 Pulsed Power Technology

Pulsed power technology is based on the conversion of a low-power, long-duration input into a high-power, short-duration output [134]. An impulse voltage generation circuit usually consists of a DC power source, an energy storage component and a high-power switch. A large amount of electrical energy is initially accumulated in the energy storage component, capacitor or inductor, and then this stored energy is delivered to a load within a short period by the opening or closure of the switch. As pulsed power can provide a high peak power in a short time, it has found a large number of civilian and military applications, including pulsed UV sterilization [135, 136], pulsed discharge for surface treatment [137, 138], and electromagnetic guns [139, 140]. In the past twenty years, pulsed power has also been investigated for ozone generation [101, 106, 141]. The pulse discharge mechanism and its applications in ozone generation are reviewed in the following sections.

7.2.2 Breakdown under Impulse Voltage

For the initiation of breakdown, an electron must be available to start the avalanche as discussed in Section 2.6. In the case of slowly varying fields, there is usually no difficulty in finding an initiatory electron from natural sources such as cosmic rays. Under an impulse

voltage of short duration, a gas gap may not break down as the applied voltage reaches the lowest (static) breakdown value (V_s) [55] because there is no initiatory electron while the voltage is applied. The time that elapses between the application of a voltage sufficient to cause breakdown to a gap and the occurrence of breakdown is called the time lag (t), which is illustrated in Fig. 7-1.

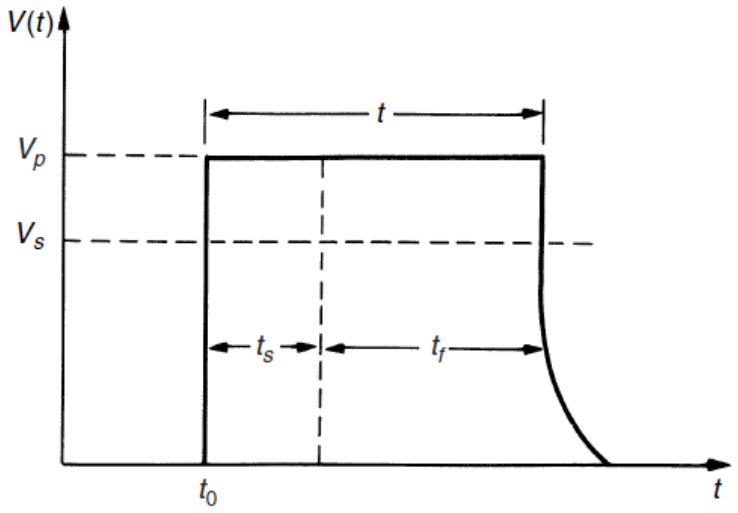

Fig. 7-1 Time lag components under a step voltage. V_s is minimum static breakdown voltage; V_p is the peak voltage; t_s is the statistical time lag and t_f is the formative time lag [55]

The time lag, t, consists of two components, t_s and t_f . t_s is called the statistical time lag, which is the time elapsed during the voltage application until a primary electron appears to initiate the discharge. t_f is called the formative time, which is the time required for the breakdown channel to develop once initiated. Fig. 7-2 shows an impulse voltage of a peak value higher than V_s.

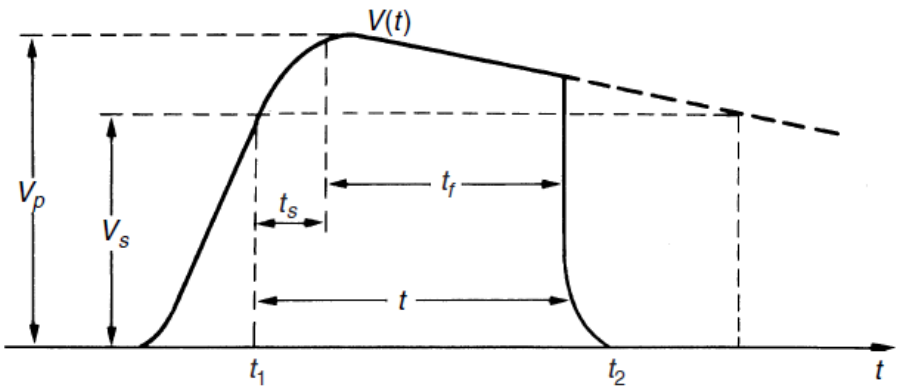

Fig. 7-2 Breakdown under impulse voltage [55]

For breakdown, it is necessary that the spark develops during the interval of the overvoltage ($V(t)$-V_s), which means that the overvoltage duration must exceed the time lag [$t<(t_2-t_1)$] [55]. Increasing the rise rate of the impulse voltage results in a decrease of the statistical time lag, and the voltage at breakdown will also be higher for faster rise times [142].

7.3 Effects of Rise Rate of Voltage Impulses on DBDs

7.3.1 Experimental Procedure

The Type-A plate reactor was used in this experiment. Its schematic diagram is shown in Fig. 4-1 in Chapter 4. The schematic diagram of the impulse generation and measurement circuit used is shown in Fig. 7-3.

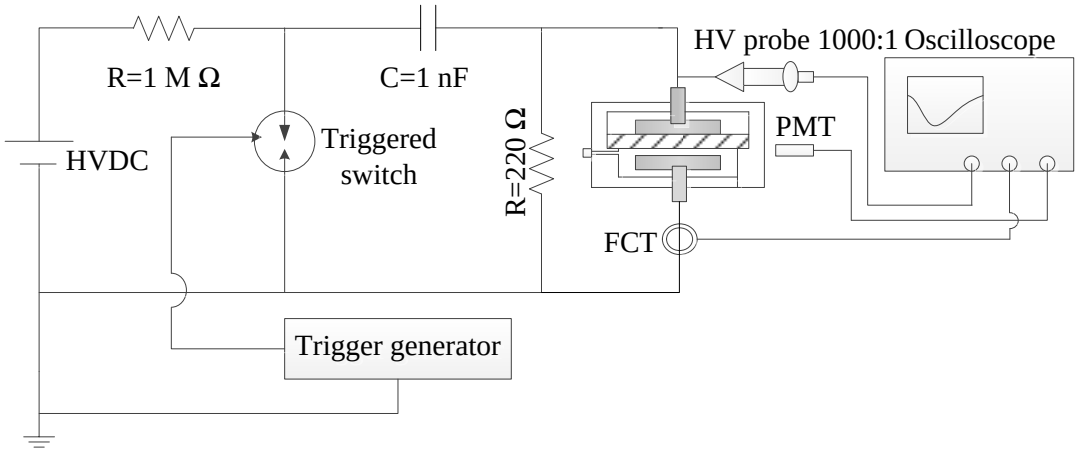

Fig. 7-3 Schematic diagram of impulse generation and measurement circuit

The feed gas in this experiment was oxygen, and the gas handling systems are shown in Fig. 3-1 and Fig. 3-2 in Chapter 3. In the experiment, the reactor was evacuated before being filled with oxygen with the purity of 99.5% and the dew point of -40℃. The pressure of the gas inside the reactor was adjusted to be one bar absolute. The voltage across the gap before the occurrence of a discharge, V_g, can be calculated from equation (7.1). V_a is the applied voltage across the reactor. C_g and C_d are the equivalent capacitance of the gap and dielectric, respectively.

$$\frac{V_g}{V_a} = \frac{C_d}{C_d + C_g} \tag{7.1}$$

The reduced electric field can be calculated as below:

$$\frac{E}{N} = \frac{V_g}{d_g \cdot N} \tag{7.2}$$

where N is the gas density calculated from the ideal gas equation and d_g is the gap distance. As shown in Fig. 7-3, negative voltage impulses were generated by charging a capacitor of 1 nF, fed by a high voltage DC power supply via a 1 MΩ charging resistor. A 500 Ω resistor was connected in parallel with the DBD reactor. A triggered switch, activated by a repetitive trigger generator, was used in the experiment, providing a pulse repetition rate of 50 pps. The rise time of the voltage impulse across the load was 40 ns. Voltage impulses with two different rise rates of 300 V/ns and 500 V/ns were generated by charging the DBD reactor to peak voltages of 12 kV and 20 kV, respectively. The voltage across the reactor was measured by a Tektronix P6015A high-voltage probe, and the current through the reactor was measured by an FCT from Bergoz. A Hamamatsu photomultiplier (H10721-01) was employed to detect the emitted light when discharges occurred. The voltage, current and emitted light signals were recorded by a LeCroy oscilloscope (Waverunner 610Zi). The specification of these measurement devices can be found in Chapter 3.

7.3.2 Reduced Electric Field Measurement

The voltage waveforms and corresponding PMT signals from discharges under both rise rates are shown in Fig. 7-4. The voltage and PMT signal were configured to arrive at the oscilloscope at the same time before the experiment. Therefore, the discharge onset voltage can be determined, corresponding to the onset of the PMT signal. Twenty tests were carried out for each rise rate. The applied voltages when the discharges occurred are plotted in Fig. 7-5, which shows that the discharge onset voltages under both rise rates are inconsistent. This is due to the uncertainty of the statistical time lag associated with impulse breakdown of the gap [55]. The mean value of twenty tests under the rise rate of 300 V/ns was -10.46 kV, with standard deviation of 0.15 kV, while the mean value under the rise rate of 500 V/ns was -13.09 kV, with standard deviation of 0.13 kV. According to equation (7.2), the *E/N* inside the gap can be calculated, and the results are plotted in Fig. 7-6. The results show that voltage impulses with the rise rates of 300 V/ns and 500 V/ns provided *E/N* in the discharge gap with mean values of 546 Td and 683 Td, respectively. The reduced electric field was increased by 25% under the rise rate of 500 V/ns compared with the rise rate of 300 V/ns.

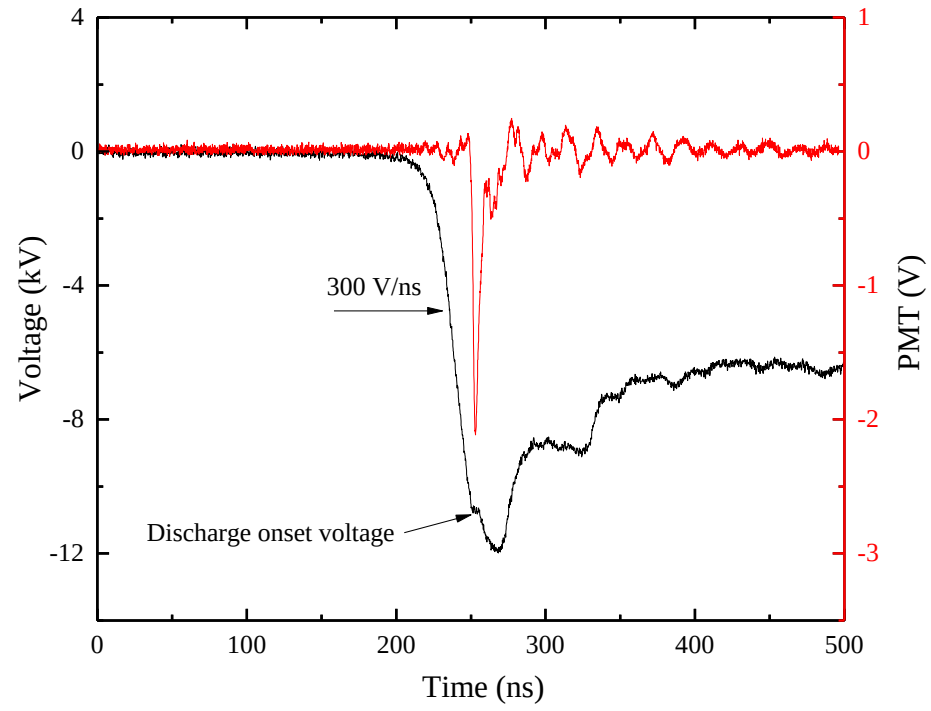

(a)

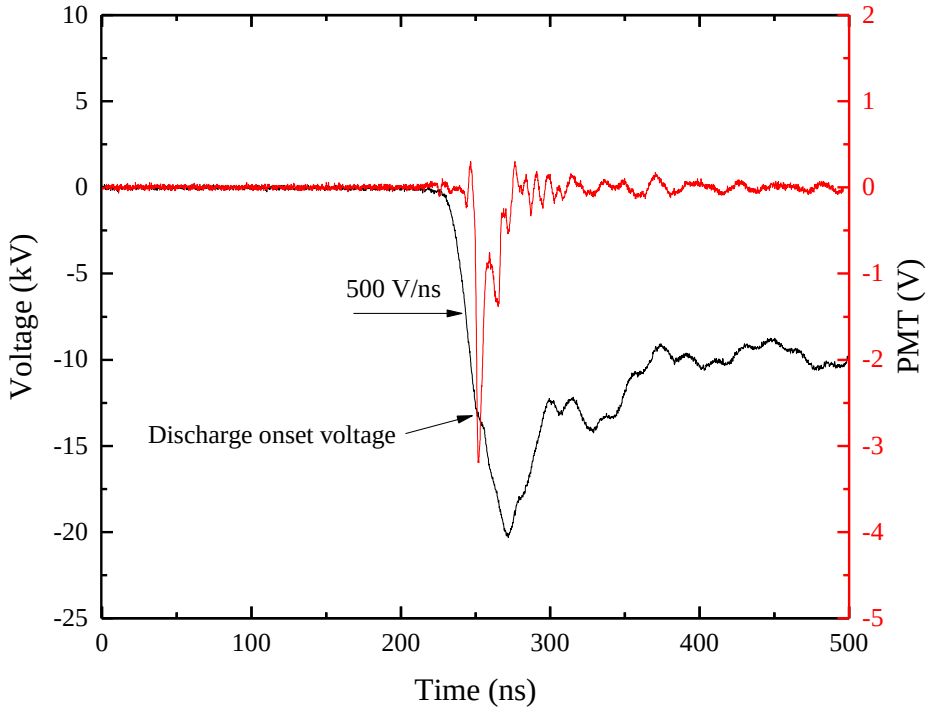

(b)

Fig. 7-4 Voltage impulses with (a) 300 V/ns and (b) 500 V/ns rise rates, and emitted light signal measured by PMT

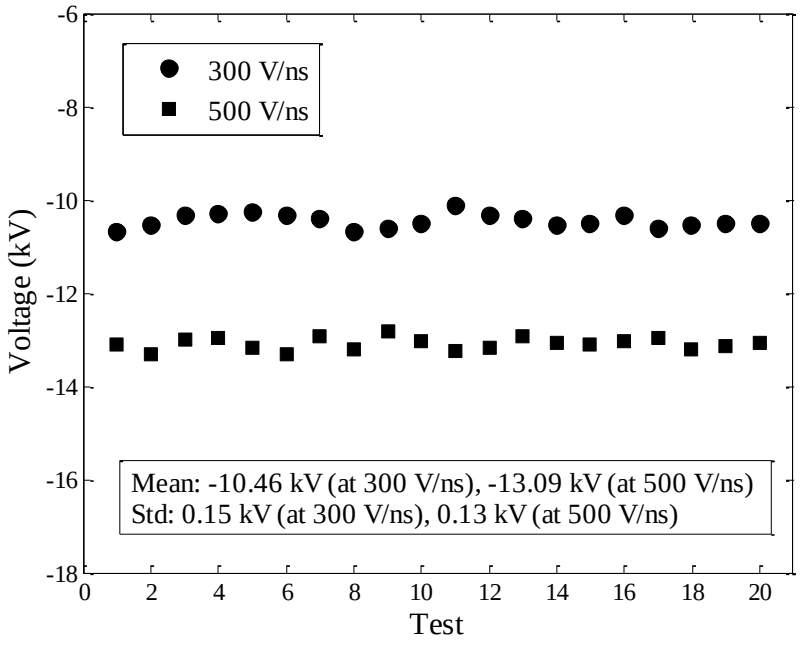

Fig. 7-5 Applied voltage when the discharges occur under both voltage impulses with different rise rate

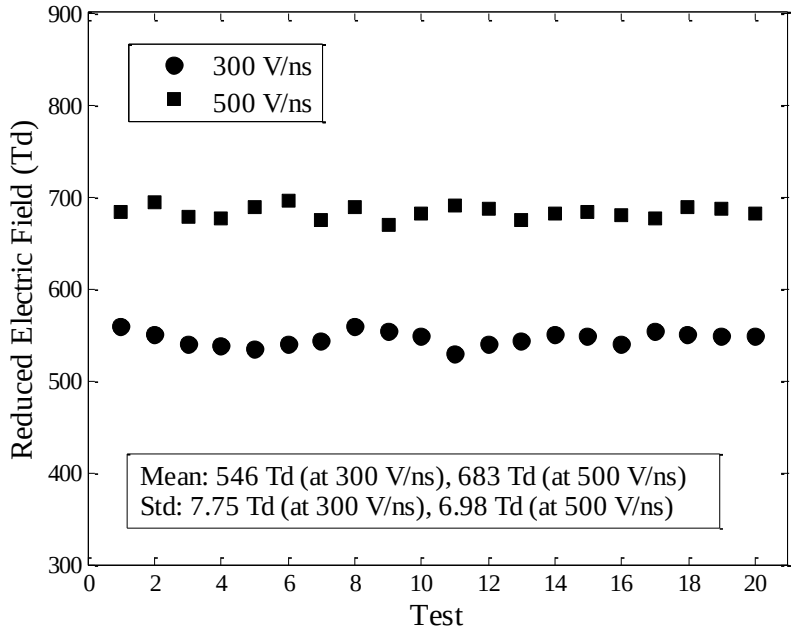

Fig. 7-6 Calculated reduced electric field under both voltage impulses with different rise rate

7.3.3 Discharge Current and Charge Transferred Measurement

Fig. 7-7 shows the voltage and current waveforms measured under different voltage rise rates when there was no occurrence of discharges. Since no discharge occurred in the gap, the DBD reactor was a purely capacitive load, and the current waveform displayed in Fig. 7-7 was a purely capacitive current, $I_{c,a}(t)$, under both voltage rise rates without discharge ignition.

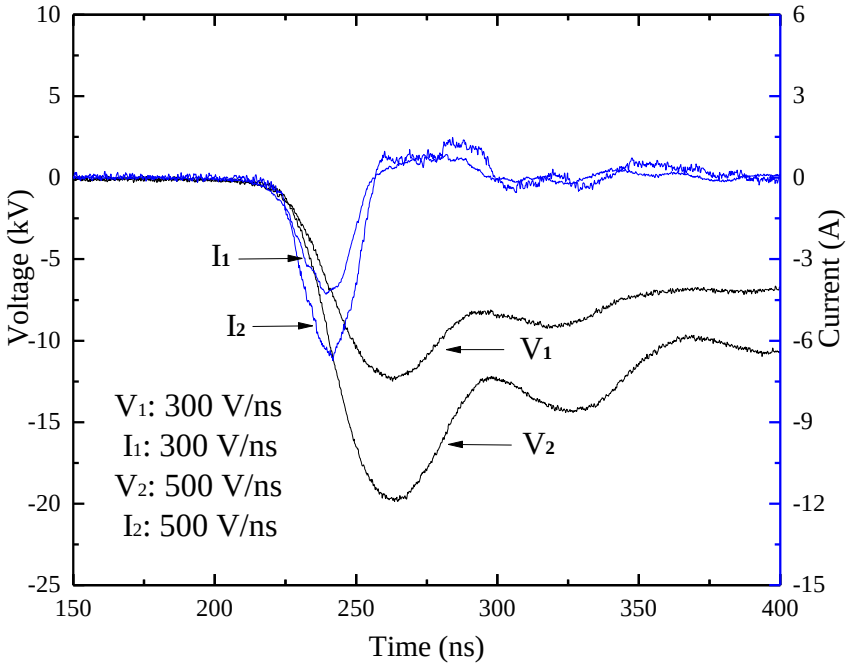

Fig. 7-7 Applied voltage and current through the DBD reactor when there is no discharge event

Fig. 7-8 shows the waveforms measured when discharges occurred. It is shown that the current increased sharply when the discharges occurred. This results from the contribution from the motion of charged particles in the discharge gap to the total current measured in the external circuit, represented as $I_{f,a}(t)$. From the DBD electrical model derived in Chapter 4, the total current $I_t(t)$ measured in the external circuit can be expressed as below:

$$\begin{aligned} I_t(\mathrm{t}) &= \frac{C_g C_d}{C_g + C_d} \cdot \frac{dV_a(\mathrm{t})}{dt} + \frac{I_f}{1 + C_g / C_d} \\ &= I_{c,a}(t) + I_{f,a}(t) \end{aligned} \tag{7.3}$$

I_f can be calculated from equation (7.3) as below:

$$I_f(t) = (I_t(t) - I_{c,a}(t)) \cdot (1 + C_g / C_d) \tag{7.4}$$

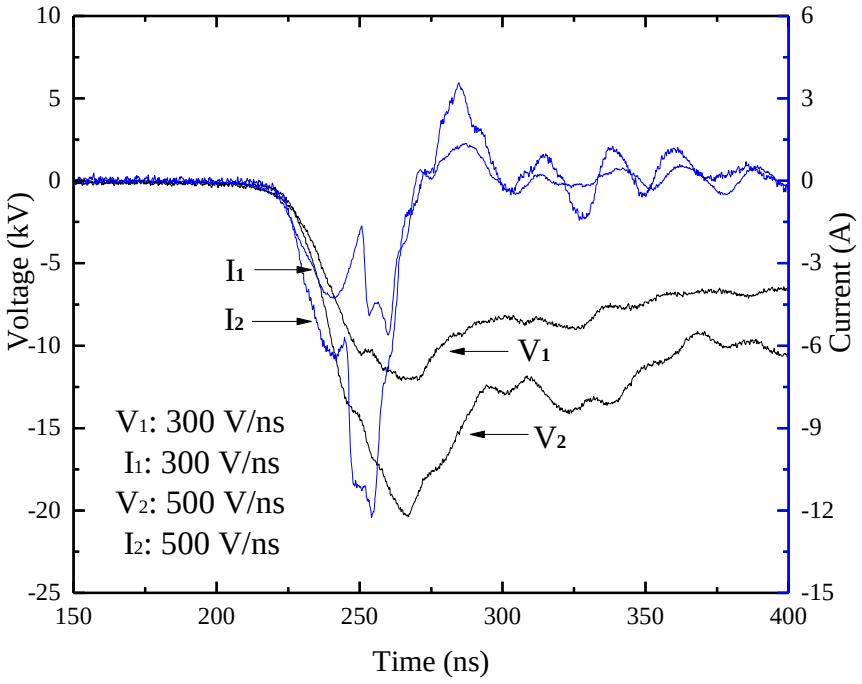

Fig. 7-8 Applied voltage and current through the DBD reactor when discharge event occurs

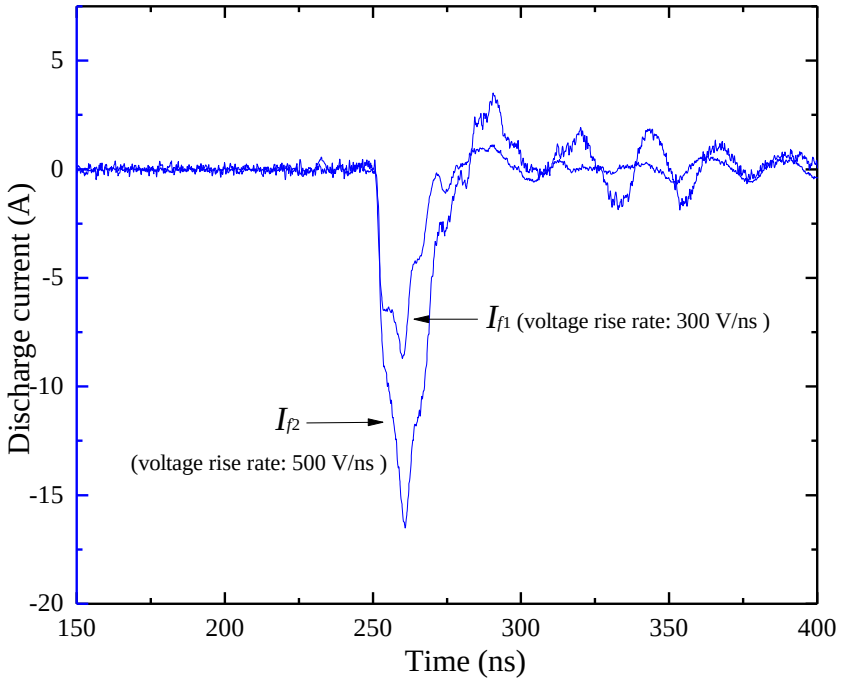

Fig. 7-9 Discharge current inside the discharge gap under the voltage rise rates of 300 V/ns and 500 V/ns respectively

The discharge currents inside the gap, I_f, were calculated, as plotted in Fig. 7-9. Integrating the discharge current pulse (from 250 ns to 280 ns), the charge transferred from twenty tests can be calculated, and this data is plotted in Fig. 7-10. The results show that the mean charge transferred under voltage rise rate of 500 V/ns was ~213 nC, 2.1 times higher than the ~101 nC transferred under the voltage rise rate of 300 V/ns. It can be explained that faster voltage rise rate provides higher *E/N*, hence more high energy electrons were generated, corresponding to the higher impulsive current shown in Fig. 7-9. Higher impulsive current provides higher electron density which promotes the formation of oxygen atoms.

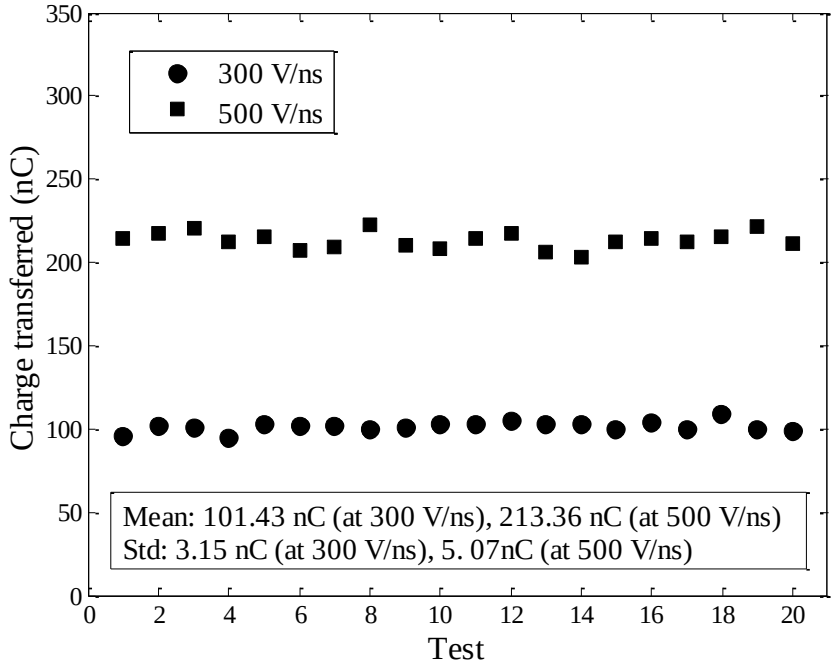

Fig. 7-10 Charge transferred inside the gap under both voltage rise rates

7.4 Ozone Generation by Using Pulsed DBDs

7.4.1 Test Cell

In order to investigate the ozone generation performance under pulsed dielectric barrier discharges, a new cylindrical DBD reactor (Type-D), integrated with the circulating cooling-water system, was designed and developed. The construction of this new reactor is shown in Fig. 7-11.

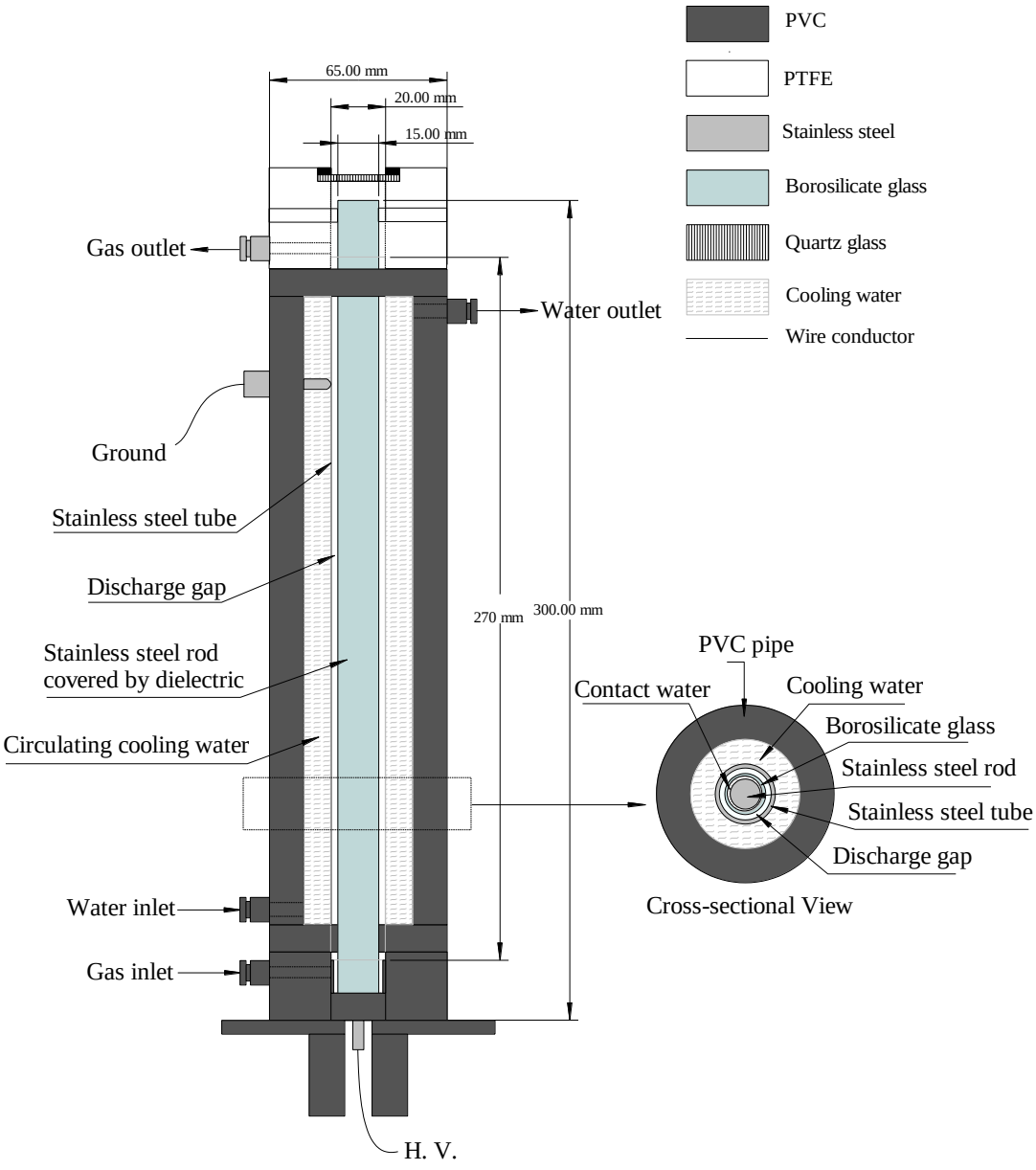

Fig. 7-11 Schematic diagram of Type-D cylindrical DBD reactor

Consisting of a single glass tube, the Type-D reactor has a lower capacitance than the Type-C reactor, which is beneficial for the generation of a fast rising impulse. The rate-of-rise of the impulse voltage generated in this part of the work was 120 V/ns, and the ozone generation performance under this energization mode was compared with a slow rising (2 V/ns) sinusoidal voltage with the frequency of 25 kHz.

The Type-D DBD reactor was developed to investigate pulsed dielectric barrier discharges. This reactor has a cylindrical electrode topology. The 270 mm long outer stainless steel tube serves as a grounding electrode, the temperature of which was kept at 15 °C by circulating water. The inner electrode was a stainless steel rod surrounded by water with a conductivity of 60 μS/cm, inside a borosilicate glass tube with wall thickness of 1.2 mm (thickness of water layer was 0.3 mm). The discharge gap length in this reactor was 0.4 mm. A quartz window was placed parallel to the cross section of the discharge space, through which the emitted light from discharges could be detected. The equivalent capacitances of the dielectric barrier and gap in this reactor were calculated based on equation (6.3), and their values are as below:

$$C_d = 0.40 \text{ nF} \tag{7.5}$$

$$C_g = 0.29 \text{ nF} \tag{7.6}$$

7.4.2 Experimental Procedure

A. Gas conditions

In this experiment, the gas flow rate was kept at 0.2 L/min, and the gas was maintained at atmospheric pressure. Ozone concentration was monitored using an IN-USA Mini-HiCon Ozone Analyzer. A schematic diagram of the gas handling system can be found in Fig 3-1 in Chapter 3.

B. Power supply and electrical measurement system

The electrical circuits of the power supplies employed in this work are shown in Fig. 7-12. In the pulsed power supply, the pulsed voltage was generated by charging a capacitor of 1 nF, fed by a 20 kV, 10 mA high voltage DC power supply via a 1 MΩ charging resistor. A 220 Ω resistor was connected in parallel with the ozone reactor for charging and discharging the capacitive load, and this resistance determines the length of the pulsed voltage across the

reactor. The pulse length is defined as the full-width at half maximum (FWHM) of the pulsed voltage. In this work, a negative pulsed voltage with FWHM of 500 ns was achieved. A three-electrode spark-gap switch, triggered by a trigger generator (SAMTECH TG-01) was used in the experiment to provide a repetition rate of 200 pps for ozone production. In the 25 kHz AC power supply a thyristor controlled frequency inverter was stepped up by a high frequency transformer and connected to the ozone reactor with a series-compensated resonant inductor of 60 mH. The average power output of this inverter was linearly regulated using pulse density modulation (PDM). The PDM was set to be 5% in this work.

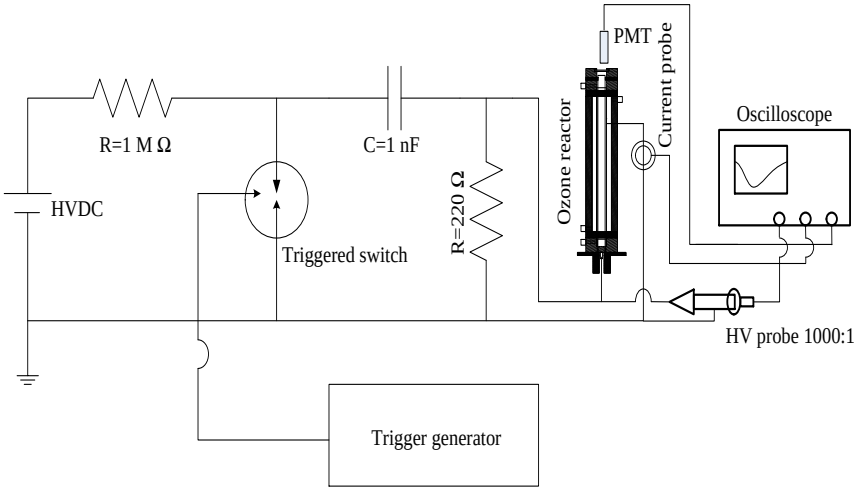

(a)

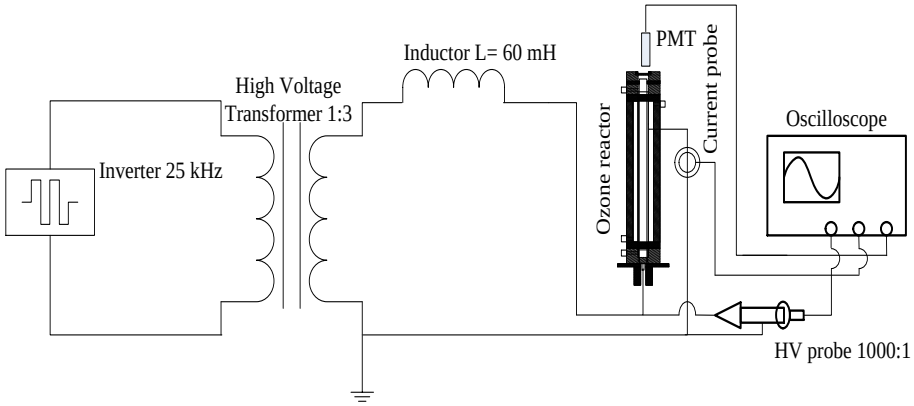

(b)

Fig. 7-12 Schematic diagram of electrical circuits of (a) pulsed power supply and (b) 25 kHz AC power supply

The voltage across the reactor was measured by a Tektronix P6015A high voltage probe and the discharge current was measured by a Pearson current probe (model 6585). A Hamamatsu photomultiplier (Model H10721-01) was also employed to detect the light emitted from discharges. The voltage, current and emitted light signal were recorded by a LeCroy oscilloscope (Waverunner 104 Xi, 1 GHz, 5 GS/s). The discharge energy was determined by the integration of the instantaneous product of the digitized voltage and current signals from the oscilloscope. The specific power in this work is defined as the ratio of discharge power to gas flow rate, with units of J/L.

7.4.3 DBD Modes under Pulsed Power and AC

The DBD mode under pulsed power and sine wave AC power supplies were studied by measurement of the voltage across the reactor, the discharge current in the external circuit, and the emitted light signal from the discharges. Fig. 7-13 and Fig. 7-14 show the voltage, current waveform and emitted light signals from discharges under pulsed power and sine wave AC power supplies, respectively.

Under pulsed operation (Fig. 7-13), the peak voltage applied was 18 kV. The current waveform had a peak value of 75 A. Compared with the current waveforms under AC operation, which had an impulsive current component superimposed onto the displacement current, the current measured under pulsed operation did not show an impulsive component. This is probably due to the fact that the magnitude of the impulsive component is much smaller compared with the displacement current component, so it cannot be distinguished.

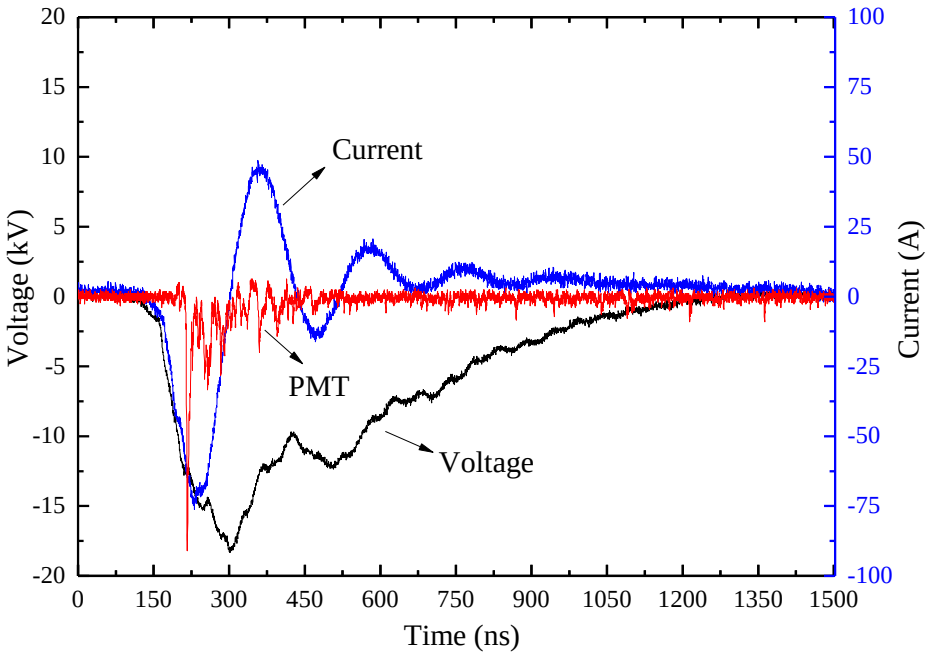

Fig. 7-13 Voltage, current and emitted light signal from discharges energised by pulsed power supply

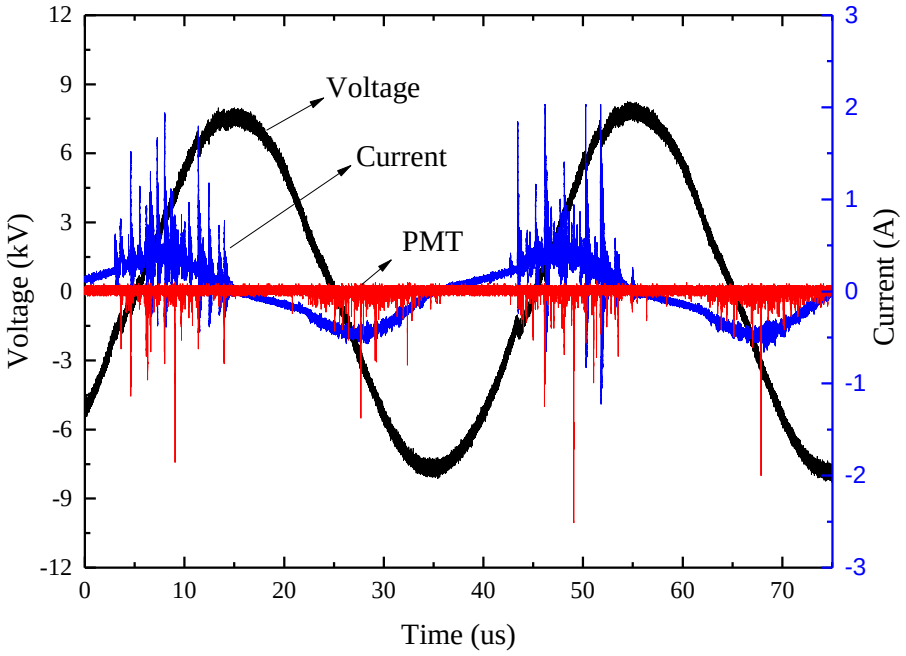

Fig. 7-14 Voltage, current and emitted light signal from discharges energised by sine wave AC power supply

From the emitted light signals, it can be seen that the first streamer discharge under pulsed energisation occurred when the voltage reached 11 kV. After reaching this breakdown onset voltage (11 kV), many emitted light pulses were detected, all with a smaller magnitude than the initial peak. These emitted light signals represented the filamentary discharges under pulsed energisation [98]. It is interesting to note that there were still emitted light signals detected even after the peak voltage under pulsed energisation. This was different from AC energisation, where the discharges stopped when the voltage reached its peak value. Also, under AC energisation, the discharges started at a lower voltage value. From Fig. 7-14, it is evident that positive discharges started from -1.2 kV, and negative discharges started from 1.4 kV. This is due to local electrical field enhancement, caused by the surface charges accumulated on the dielectric from the previous discharge. From Fig. 7-14, it can be observed that the impulsive currents were significantly lower during the negative voltage half-cycle as compared with those during the positive voltage half-cycle. This was expected because it was due to different discharge modes on different voltage half-cycles which were discussed before.

7.4.4 Comparison of Ozone Generation Performance

Fig. 7-15 and Fig. 7-16 show the ozone concentration and discharge power under pulsed and AC energisation. It can be seen that both the ozone concentration and discharge power increased almost linearly with the applied voltage. Four ozone concentrations of 18.4 g/Nm^3, 34.8 g/Nm^3, 38.1 g/Nm^3 and 52.5 g/Nm^3 were achieved under pulsed energization, and four similar ozone concentrations of 21.4 g/Nm^3, 33.8 g/Nm^3, 43.4 g/Nm^3 and 51.4 g/Nm^3 were achieved under 25 kHz AC energisation.

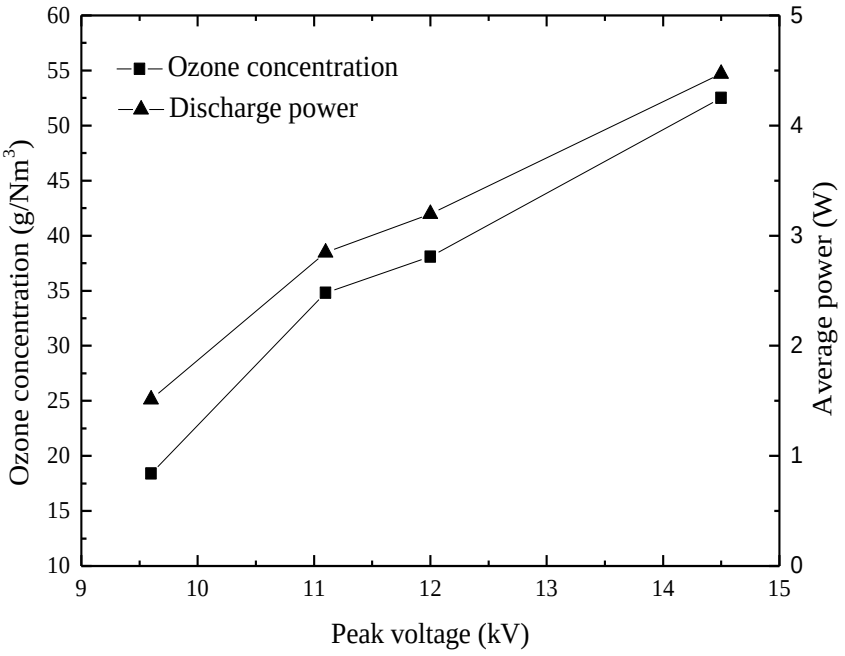

Fig. 7-15 Ozone concentration and discharge power at different peak voltage under pulsed energization

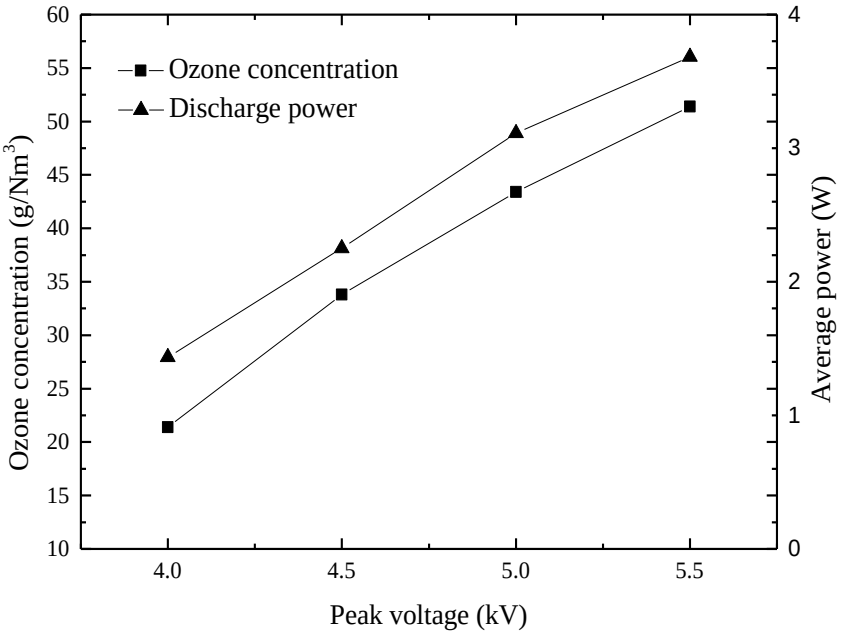

Fig. 7-16 Ozone concentration and discharge power at different peak voltage under AC energisation

Fig. 7-17 shows curves of ozone concentration versus specific power under both energisation regimes.

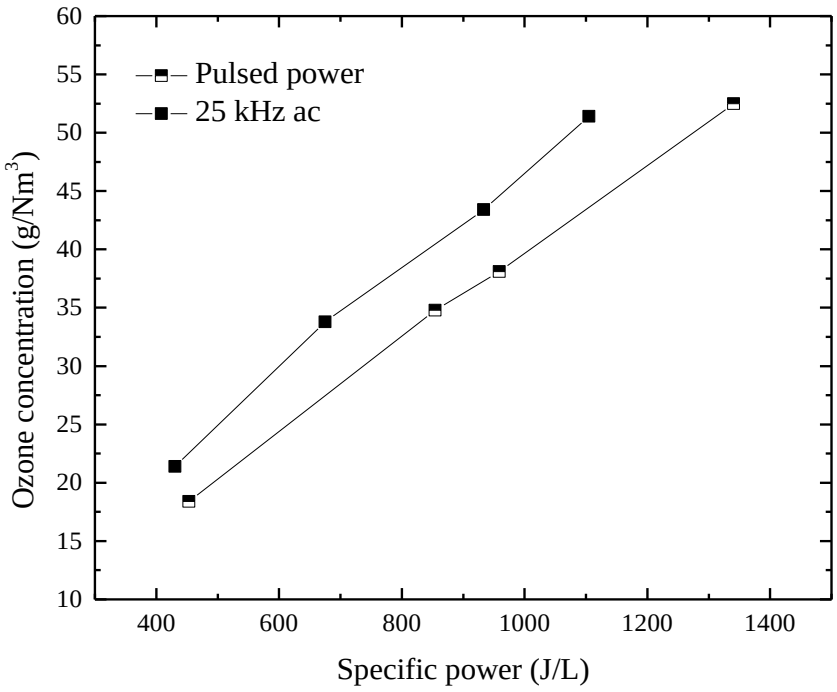

Fig. 7-17 Ozone concentration as a function of specific power under pulsed and AC energization

It can be seen that the ozone performance in both cases demonstrated a similar trend. At the same specific power, the AC energisation regime provided higher ozone concentration than pulsed energisation. From Fig. 7-17, at the specific power of 959 J/L under pulsed energisation, the ozone concentration was 38.1 g/Nm^3, while at the specific power of 933.45 J/L under AC energisation, the ozone concentration was 43.4 g/Nm^3. In the literature, Namihira *et al*. achieved 30 g/Nm^3 at the specific power of 1000 J/L using pulsed corona discharge in a spiral cylinder electrode configuration [126]. Nakai *et al*. reported 20 g/Nm^3 at specific input energy of 600 J/L under AC high voltage in a parallel plane type DBD ozonizer [92].

Fig. 7-18 shows the ozone generation efficiency achieved as a function of ozone concentration:

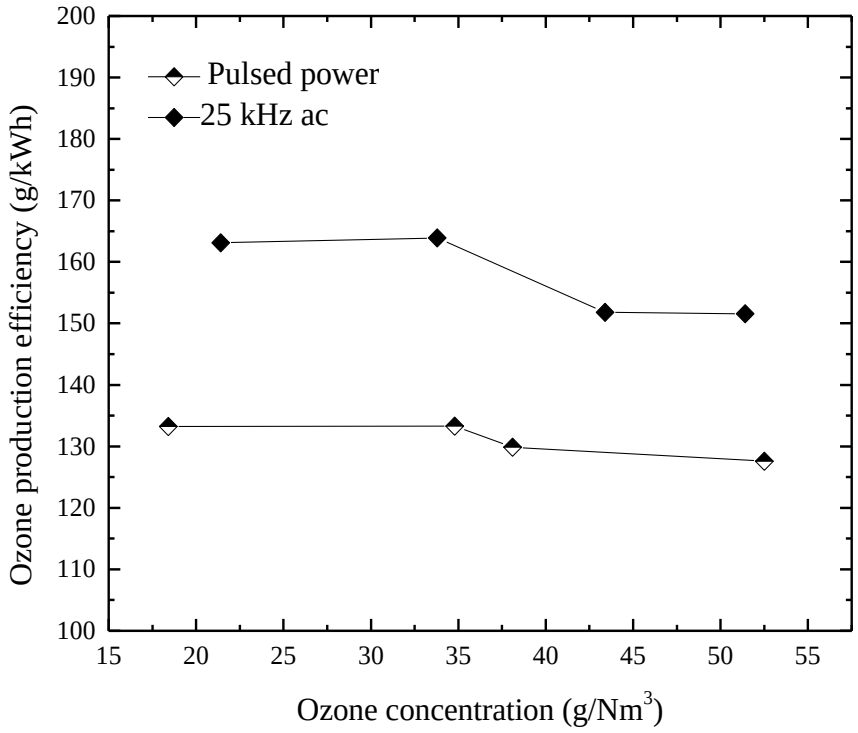

Fig. 7-18 Ozone production efficiency as a function of ozone concentration under pulsed and ac energisation

The ozone generation efficiencies are relatively consistent in the investigated range, with a small drop towards higher concentrations under both energisation regimes. The figure shows that 25 kHz AC energisation resulted in more efficient ozone production than impulsive energisation. At the concentration of 33.8 g/Nm^3, the ozone generation efficiency was 163 g/Nm^3 under continuous AC, compared to 133.3 g/Nm^3 at 34.8 g/Nm^3 under the pulsed power regime, 18% lower. In the literature, Namihira *et al.* attained an ozone production efficiency of 100 g/kWh at 30 g/Nm^3 [126]. Nakai *et al.* found that the ozone yield was 125 g/Nm^3 at about 20 g/Nm^3 [92]. The ozone generation efficiency achieved in this present work is higher than the above literature results.

There are two factors that account for the lower ozone generation efficiency under the impulsive energisation mode as compared with the 25 kHz AC energization mode in this work. One of the factors is the long tail of the impulse voltages, which results in power

losses due to the motion of ions. The other factor is that, in the AC energisation mode, the next discharge phase when the polarity of the voltage changed took advantage of the accumulated charges on the dielectric surface from the preceding discharge phase; the impulsive energisation mode in this work was unipolar, and so the accumulated charges on the dielectric surface from the preceding discharge phase act to prevent, rather than facilitate, the occurrence of subsequent discharges.

7.5 Conclusion

Pulsed power technology for ozone generation was reviewed and experimentally investigated in this chapter. Pulsed dielectric barrier discharges have been investigated by some researchers, but the literature work on its application to ozone generation is very limited. The effects of the impulse voltage rise rate on oxygen-fed DBDs were investigated in this chapter. Higher *E/N* of 683 Td was achieved under the faster voltage rise rate of 500 V/ns, as compared with the *E/N* of 546 Td achieved under the rise rate of 300 V/ns. The *E/N* values achieved under both voltage rise rates are much higher than the breakdown *E/N* value for oxygen, which is ~180 Td [143]. Effective ionisation of oxygen molecules was provided under these significant *E/N* values. The charge transferred under the higher rise rate was found to increase by 2.1 times compared with the lower rise rate. The DBD modes and ozone generation performances under a fast rising impulse and a slow rising AC sinusoidal voltage were compared in this work. Filamentary discharges mode has been observed for both pulsed and 25 kHz AC energisation regimes in oxygen. Ozone concentration was found to increase with applied voltage for both energisation regimes. Continuous AC energisation resulted in 18% more efficient ozone production as compared with pulsed energisation. The results suggest that a bipolar impulse voltage with a shorter tail may provide more efficient pulsed dielectric barrier discharges for ozone generation. However, it is worth noting that pulsed power has limitations for application in large-scale industrial ozone generation, as large ozone reactors have high capacitance, which will limit the rise rate of the pulsed voltage and, therefore, pulse durations of the order of ns cannot be practically achieved. In addition, the matching between the short pulse generator and the ozone reactor is an issue. A matching resistor has to be connected in parallel with the ozone reactor and most of the power delivered from the pulse generator will be consumed by this matching resistor, rendering the power supply inefficient.

8 CONCLUSIONS AND FUTURE WORK

8.1 Conclusions

Ozone is a strong and environmentally-friendly oxidant, and it has wide applications in industry. This thesis has focused on oxygen-fed dielectric barrier discharges for ozone generation. The aim of this thesis was to develop a narrow gap (<1 mm) DBD reactor for ozone generation, and to optimize the generated micro-discharges to increase the ozone generation efficiency. During the course of this research project, four DBD reactors, including plate configuration and cylindrical configuration, were designed and developed. Three types of DBD energisation mode, including 50 Hz AC, high-frequency (kHz) AC, and impulse voltage, were employed for ozone generation. Electrical and optical diagnostics techniques were applied to investigate the electric characteristics of micro-discharges in DBDs. Two ozone monitors with different measurement ranges were used to measure the ozone concentration in the experiments.

Initially, a background study was conducted, encompassing ozone properties, ozone applications and ozone generation mechanisms. The chemical kinetics of ozone generation was studied, followed by analysis of the physical processes of ozone generation in gas discharges. Oxygen dissociation is the first step of ozone generation in gas discharges. Increasing the proportion of electrons used to dissociate oxygen molecules and decreasing the proportion of electrons used to dissociate ozone is the key to improve the ozone generation efficiency from the view of physical process. Based on cross section data of electron collisions with oxygen and ozone, it was calculated that electrons with energy from 20 eV to 30 eV provide the maximum cross section value of oxygen dissociation, and electrons with energy from 1.06 eV to 3 eV provide the maximum cross section value of ozone dissociation. Therefore, it is important to increase the proportion of high energy electrons, and simultaneously reduce the proportion of low energy electrons, which provide no contribution to ozone generation, but do generate heat and cause ozone decomposition. The reduced electric field, *E/N*, is the key parameter to adjust the mean energy of the electrons in the micro-discharges in DBDs. From the literature, 100 Td to 300 Td is the optimum range of *E/N* for ozone generation. From the chemical kinetics of ozone generation, the most important parameter is the concentration of oxygen atoms; 10^{-4} is the optimum relative atomic oxygen concentration, and when this concentration is higher than 10^{-4}, the

ozone decomposition rate will increase. The effects of temperature and humidity on ozone generation have been reviewed. Preventing the temperature from increasing and maintaining, the dew point of the feed gas equal or below -40° are very important for ozone generation. Following the theoretical analysis of the ozone generation process, the historical development of industrial ozone generators was summarised. From the literature, it was found that there was very limited experimental data available on high concentration (>100 g/Nm^3) ozone generation. Therefore, undertaking a detailed study of high concentration ozone was one of the objectives of this research.

The experimental part of this research project started with an investigation of the electrical characteristics of DBDs. A sealed, plate type DBD reactor (Type-A) was designed and developed, which was fed with dried oxygen gas with a dew point of −40 °C. Continuous sinusoidal AC voltage was applied to energise the DBDs and the voltage, current and emitted light signals were measured to study the electrical characteristics of DBDs. The discharge impulsive current measured in the external circuit showed filamentary mode and it was found to conform to a Gaussian distribution. The voltage across the discharge gap was found to be constant during the discharge period of DBDs and its value was equal to the breakdown voltage of the gap, conforming to Paschen's law. The transferred charge and the charge accumulated on the surface of the dielectric were quantitatively analysed based on the Lissajous figure. It was found that the charge accumulated on the surface of the dielectric was different from the charge induced in the external circuit. The amount of the charge induced in the external circuit was determined by the total amount of accumulated charge on the surface of the dielectric and the ratio of the glass barrier capacitance to the discharge gap capacitance. However, the total charge transfer during a discharge period (half voltage cycle) was found to be the same, which was verified in this work. An equivalent circuit model of DBDs was established and the magnitude of the filamentary current in the discharge gap was derived by measuring the impulsive current and the transient voltage change of the DBD reactor in the external circuit. Following the single filamentary current measurement, the effects of the applied voltage amplitude and the energisation frequency on the discharge characteristics were studied. It was found that the applied voltage required to ignite a discharge decreased linearly with the increasing peak applied voltage, which was related to the amount of accumulated charge on the surface of the dielectric. The discharge was ignited at lower external voltages when the internal opposite electrical field was raised. DBDs energized by 5 kHz and 100 Hz sinusoidal voltages were compared in the last part of this

investigation, and it was found that the characteristics and the distribution of filamentary current was the same under both energisation frequencies.

In the next phase of this research project, another plate type DBD reactor (Type-B) with larger discharge volume was designed and developed to investigate the behaviour of pulsed micro-discharges and the ozone generation performance in DBDs under different experimental conditions. The effects of gas pressure, discharge gap length and applied voltage were studied. In order to simultaneously investigate the effects of different experimental conditions on pulsed micro-discharges and the ozone generation performance, a transient AC voltage with 200 cycles at the frequency of 5 kHz was used to energize the DBDs, and the transient concentration of ozone produced was recorded. A LabVIEW program was written to acquire the ozone concentration data from the ozone monitor in real time, through a RS232 cable. For the filamentary current measurement, four key parameters of a single current pulse inside the discharge gap were achieved: the amplitude of the current pulse, the duration of the current pulse, the transferred charge of the current pulse, and the micro-discharge energy consumed by a single current pulse. These parameters of filamentary currents were resolved using Matlab, and their distributions at different pressures and discharge gap lengths were plotted and studied. Before investigating the effects of gap length and gas pressure on the filamentary current features, the polarity effect of the filamentary current was observed in the experiments, which showed that the negative discharge current was twice higher than the positive discharge current. Also, it was found that the amplitude of the filamentary current was about four times higher than that of the external pulsed current.

Based on the filamentary current distributions under different gap lengths and gas pressures, it was found that the mean values of the filamentary current amplitude, the transferred charge and micro-discharge energy all increased as either the gap length or gas pressure were increased. The filamentary current pulse duration increased with an increase of gap length, but was not affected by the change of the gas pressure. The ozone generation efficiency was found to increase with an increase of gap lengths and pressure. The maximum ozone generation efficiency in this part of the work was 217 g/kWh, achieved with a gap length of 0.5 mm, 2.0 bar absolute pressure, and an applied voltage of 5.5 kV. It was considered that the *E/N* in the discharge gap was changed when the gap length and gas pressures were changed, which affected the ozone generation efficiency. Therefore, the *E/N* values at different gap lengths and different pressures were calculated. The results showed that increasing the discharge gap lengths from 0.2 mm to 0.6 mm led to a decrease of the *E/N* from 185 Td to 130 Td, while increase of the pressure from 1 bar to 2 bar resulted in a slight

decrease of the E/N from 136 Td to 126 Td. By plotting the ozone generation efficiency versus *E/N*, it was found that the maximum ozone generation efficiency obtained was at 126 Td, and the efficiency decreased with an increase of the *E/N*. The results in this part of the work have provided further understanding of the filamentary current of DBDs and the effects of *E/N* on the ozone generation efficiency. In addition, experiments were also carried out to investigate the filamentary current under different applied voltages from 3.5 kV to 5.5 kV. The mean values of the four key parameters of the filamentary current were almost the same for different applied voltages, but the number of filamentary current pulses was different, as expected. The ozone generation efficiency was found to decrease as the applied voltage was increased, which was considered to be due to the temperature increase at higher applied voltages.

Following the investigation of the characteristics of the micro-discharge current and ozone generation efficiency in DBDs energized by a transient voltage, the ozone concentration versus specific power and the ozone generation efficiency versus ozone concentration based on DBDs were researched by using a continuous AC power supply. Two types (plate and cylindrical) of DBD reactors were used in this part of work. The plate type reactor (Type-B) was employed for a parametric study, as it offered the advantage of ready adjustment of the discharge gap length. A cylindrical reactor was designed and developed because it was easier to integrate a water cooling system in this configuration compared with the plate configuration. At the end of this part, the ozone generation efficiencies of these two reactors with different configurations were compared and discussed.

The effects of gas flow rate, gas pressure, applied voltage, power frequency and discharge gap length on the ozone concentration and generation efficiency were investigated based on the plate type reactor (Type-B). It was found that the ozone concentration decreased linearly from 87.7 g/Nm^3 to 60.5 g/Nm^3 with an increase of the gas flow rate from 0.4 L/min to 1 L/min, while the ozone generation efficiency increased from 57.9 g/kWh to 100.5 g/kWh, respectively. It was considered that shorter gas residence time in the discharge gap resulted in higher ozone generation efficiency, but lower ozone concentration. For the change of the applied voltage, the ozone concentration increased by 50% with an increase of the amplitude of the applied voltage from 3.5 kV to 6 kV, but the ozone generation efficiency decreased by 53%. The drop of the ozone generation efficiency with an increase of the applied voltage in this part of work was attributed to higher temperature inside the discharge gap under the higher voltage, which increased the ozone decomposition rate. As both the applied voltage and flow rate can change the ozone concentration, it was in the interest of this work to

investigate the most efficient manner to increase ozone concentration. Two experiments were carried out to investigate this topic. The first was conducted by varying the discharge power at a constant gas flow rate (0.5 L/min), and the second was conducted by varying the gas flow rate at a constant discharge power (34 W). It was found that, with the same specific energy, the ozone concentration was slightly higher when the flow rate was kept constant. In this part of the work, it was observed that the ozone concentration under both cases both tended to saturate at ~87 g/Nm^3 when the specific energy reached a level of 5 kJ/L. The effect of the gas pressure on the ozone performance in this part of the work was studied by comparing the typical curve of the ozone generation efficiency versus the ozone concentration. It was found that the ozone generation was more efficient at 2 bar absolute than at 1 bar absolute. At the same ozone concentration of ~67 g/Nm^3, the ozone generation efficiency at 2 bar absolute was about twice than that at 1 bar absolute, but the difference gradually decreased with increasing ozone concentration. Following the effect of pressure, the effect of gap length on the ozone generation was researched. The results showed that the ozone generation efficiency decreased with increasing ozone concentration for all tested discharge gap lengths, but the ozone generation efficiency increased with an increase of the gap length at a constant ozone concentration.

Further research on the ozone generation performance under a continuous AC power supply was carried out by using a cylindrical reactor (Type-C), integrated with a water cooling system. During the experiment, the cooling water surrounding the dielectric barrier was maintained at 15 °C. For the discharge current measurement, it was found that there was no filamentary current in the positive half voltage cycle. To verify this finding, a PMT was used to detect the light emission signals from the discharge gap. It was observed that the light emission signals were detected in both half voltage cycles, therefore it was concluded that the discharges in the positive half voltage cycle showed homogenous mode, in which no filamentary current was detected in the external circuit, but numerous short light emission signals were detected. Following a detailed analysis of the discharge current, the ozone generation concentration and generation efficiency using this reactor were discussed. Comparing the ozone concentrations and ozone generation efficiencies with the Type-B reactor, the Type-C reactor provided a better performance. Without a cooling system, the ozone concentration tended to be saturated at ~90 g/Nm^3 when the specific energy increased to be 4 kJ/L with the Type-B reactor, while the ozone concentration kept increasing at the same range of specific energy with the Type-A reactor. From curves of ozone generation efficiency versus ozone concentration, it was found that, with a cooling system integrated,

the ozone generation was greatly improved. The ozone generation efficiency with the Type-C reactor was 20% higher than with the Type-B reactor, when the ozone concentration was ~60 g/Nm^3. When the ozone concentration increased to 90 g/Nm^3, the ozone generation efficiency with a cooling system was still as high as 150 g/kWh, but the ozone generation efficiency without a cooling system dropped to 62 g/kWh.

The effect of energisation frequency on the ozone generation efficiency was studied. Three AC power supplies with three different energisation frequencies, 50 Hz, 2.6 kHz and 20 kHz, were used to generate ozone and the ozone performances at these frequencies were compared. For 50 Hz with a peak voltage of 6 kV, the highest ozone concentration was 21 g/Nm^3 with an ozone generation efficiency of 192 g/kWh. For 2.6 kHz and 20 kHz with the same peak voltage of 6 kV, the highest ozone concentrations were 250 g/Nm^3 and 271 g/Nm^3, respectively. The highest ozone generation efficiencies at 2.6 kHz and 20 kHz were 101.9 g/kWh and 99 g/kWh, respectively. It was concluded that high energisation frequency resulted in higher discharge power, which led to higher ozone concentration, but the ozone generation efficiency was not improved by increasing the energisation frequency. The micro-discharge characteristics under the three different energisation frequencies were compared by measuring their filamentary currents and emitted light signals upon discharge. No significant difference was found in their impulsive current features. It was considered that the micro-discharges in DBDs were independent of the AC energization frequency because during the short period of the micro-discharge, of the order of ns, the micro-discharge was mainly affected by the surface charge accumulated on the dielectric barrier. However, higher energisation frequency (kHz regimes) does have advantages for the production of high concentrations of ozone. Compared to a 50 Hz power supply, using a kHz power supply can reduce the size of the ozone generator, and also reduced the applied voltage to generate the same amount of ozone. In this research work, an inverter-based high frequency power supply also provided more flexible control of the ozone concentration, by adjusting the voltage or frequency. A series resonant circuit was employed to generate the kHz sinusoidal voltage waveform in this work, which provided reactive power compensation and improved the power supply efficiency.

As it was considered that the AC energisation frequency had no effect on the generated micro-discharges because of the slowly-rising AC voltage, it was in the interest of this research to investigate the electrical characteristics of micro-discharges and ozone generation under a fast-rising pulsed voltage. Therefore, in the final stage of this research project, an investigation of pulsed dielectric barrier discharges for ozone generation was carried out.

The experiments undertaken in this section were divided into two parts. The first part was to investigate the effects of rise rate of voltage impulses on DBDs. Two types of voltage impulse, with rise rates of 300 V/ns and 500 V/ns, were applied to the Type-D DBD reactor. The Type-D reactor had a cylindrical configuration, consisting of a single discharge tube with a water cooling system. Compared with the Type-C reactor consisting three discharge tubes, the Type-D reactor had three times lower capacitance, which was beneficial to achieve a fast rise rate of the voltage across the reactor. Because of the different rise rates of the applied voltage, it was felt that the breakdown electric field inside the discharge gap would be different, which would affect the micro-discharge characteristics such as the magnitude of the discharge current and the charge transfer. Therefore, the reduced electric fields under the two different voltage impulse rates were measured and compared. It was observed that the reduced electric field was improved by 25% under the rise rate of 500 V/ns compared with the rise rate of 300 V/ns. In addition, the discharge current inside the discharge gap was measured under both types of voltage impulse, and the charge transfers were calculated. It was found that the mean charge transferred under the voltage rise rate of 500 V/ns was ~213 nC, 2.1 times higher than the ~101 nC transferred under the voltage rise rate of 300 V/ns. It was concluded that the voltage with a faster rise rate increased the reduced electric field in the discharge gap and increased the charge transfer in the micro-discharge. In the next part, an experiment was carried out to investigate the ozone generation using pulsed dielectric barrier discharges. At the specific power of 959 J/L under pulsed energization, the ozone concentration of 38.1 g/Nm^3 was measured. For comparison, a similar specific power of 933 J/L under AC energization was generated and the ozone concentration of 43.4 g/Nm^3 was measured, which was slightly higher than that under pulsed energisation. It was noteworthy that both ozone concentrations were higher than the ozone concentration achieved at the same specific power. The ozone generation efficiency under pulsed energization was found to be 18% lower than that under the AC continuous power at the same ozone concentration of ~34 g/Nm^3. It is considered that one of the reasons for the lower efficiency under the pulsed energisation was attributed to the long tail of the impulse voltage, which led to energy loss to ions. In addition, one important finding in this part of the work was that, under the pulsed energisation, micro-discharges in DBDs did not stop at the peak voltage, but stopped at some point when the voltage decayed, which was different from the case of AC energization.

Throughout this thesis, the research work has been focused on dielectric barrier discharges for ozone generation. The electrical characteristics of DBDs have been experimentally

studied. The effects of the physical parameters and electric parameters of DBDs on ozone concentration and generation efficiency have been investigated. The important findings and considerations in this thesis can be summarised as follows:

- To increase the ozone concentration and the ozone generation efficiency in DBDs, the key is to take away the heat generated from the discharge as quickly as possible.
- The ozone generation efficiency reduced when the ozone concentration increased. It is not possible to achieve a high concentration of ozone and high ozone generation efficiency simultaneously.
- The maximum ozone concentration produced in this work was 271 g/Nm^3, which is higher than the ozone concentrations from the literature. The ozone generation efficiency in this research work is also promising. At the typical industrial ozone concentration of 150 g/Nm^3 for waste water treatment, the ozone generation efficiency in this research work was ~8.2 kWh/kg which was ~20% higher than the typical ozone generation efficiency from the literature work.
- Pulsed DBDs have been found to be no more efficient than continuous AC DBDs in this work, which may be due to the long tail of the voltage impulse. In terms of the power supply efficiency, the inverter-based series resonant circuit is the most efficient power supply in this work, which can provided kHz energisation frequency and reactive compensation.

Concluding, this thesis has achieved a desired ozone generation efficiency and ozone concentration based on DBDs. The research work in this thesis fills the gap of the investigation of high concentration ozone based on DBDs in the literature, and can provide a reference for the design of industrial high concentration ozone generators.

8.2 Future Work

This research has investigated DBDs for ozone generation in terms of the electrical characteristics of DBDs and the ozone generation mechanisms. In order to increase the ozone generation efficiency and ozone concentration, there are some aspects of the research that can be investigated further.

As stated throughout the thesis, ozone generation is very sensitive to temperature. Therefore, monitoring the gas temperature inside the discharge gap during the ozone generation would provide interesting future work. A non-contact infrared thermometer can be applied to provide real-time monitoring of the temperature inside the discharge gap. In Chapter 6, the ozone concentration and ozone generation efficiency were plotted for different specific energies. Future work can be carried out to measure the temperature in the discharge gap at different specific energies. Measures can be taken to maintain the gas temperature at a constant value for a range of specific energies, and to compare the ozone generation efficiency under these conditions, which will verify if the decrease of the ozone generation efficiency at higher specific energy is due to the increase of the ozone concentration or the increase of the temperature. In terms of the water cooling system employed with cylindrical ozone reactors, future work can be conducted to design a new ozone reactor with cooling water surrounding both electrodes, rather than only one electrode. A feedback signal of the gas temperature inside the discharge gap could be sent back to the main control system to adjust the temperature of the circulating cooling water automatically, in order to maintain a constant temperature inside the discharge gap.

In addition, from the chemical kinetics of ozone generation, it is known that the atomic oxygen concentration is an important parameter for ozone generation. Therefore, future work can be carried out to measure the atomic oxygen concentration in DBDs. Optical emission spectroscopy will be required to investigate the oxygen plasma in DBDs. The relationship of the atomic oxygen concentration with the ozone generation efficiency can be studied experimentally. Optimization of the atomic oxygen concentration by adjusting the discharge parameters will be required to increase the ozone generation efficiency. At the same time, future work can also be carried out to investigate the electron energy distribution function in the DBDs, by modelling or practical measurement. The mean energy of electrons and the atomic oxygen concentration are both important parameters that determine the ozone generation efficiency.

In Chapter 7 of this thesis, pulsed DBDs for the ozone generation were investigated. Compared with the continuous AC power supply, the pulsed DBD was less efficient for ozone generation. The reason has been considered to be related to the long tail of the voltage impulse. Therefore, future work can also be focused on using a transmission-line based pulse-forming network to generate fast-rising, short-duration impulses for the ozone generation. An investigation of the effect of pulse length on the ozone generation efficiency can be done in the future work. In addition, DBDs generated using bipolar short pulses may be a promising method to generate ozone, because it can take advantage of the accumulated charges on the dielectric surface from the preceding discharge phase, similar to the mechanism in DBDs driven by AC sources. The investigation of ozone generation by using a bipolar short pulse can also be conducted in the future work.

Finally, recycling oxygen from an ozone generator is also a promising method that could be developed in future research. In traditional ozone generators, the oxygen in the output gas is usually wasted. If this oxygen gas could be separated from the ozone and recycled back into the ozone generator, the ozone generation efficiency would be improved by efficient use of the oxygen gas. It has been indicated that high concentration spun membranes are capable of achieving a degree of separation for the O_2/O_3 system [144]. Future work could focus on researching methods to separate the oxygen from the ozone.

In conclusion, the future work proposed here is focused on increasing the ozone generation efficiency based on DBDs by improving the discharge heat dissipation system, improving the diagnostic methods, using a shorter impulse voltage or a bipolar short pulse. Also, recycling oxygen gas from the ozone generator is proposed to improve the efficiency of gas usage. These ideas can contribute to the development of a modern ozone generator with high generation efficiency in industry.

9 REFERENCE

[1] U. Kogelschatz, B. Eliasson, and M. Hirth, "Ozone generation from oxygen and air: discharge physics and reaction mechanisms," *Ozone Science & Engineering*, vol. 10, pp. 367-378, 1988.

[2] W. Siemens, *Poggendorfs Ann. Phys. Chem.*, vol. 102, pp. 66-122, 1857.

[3] E. Diaper, "Practical aspects of water and wastewater treatment by ozone," *Ozone in Water and Wastewater Treatment*, pp. 145-179, 1972.

[4] D. Moras, P. Uhlig, J. F. Petitimbert, C. Hemery, and L. Ayad, "High concentration ozone generation," presented at the Proceeding of 11th Ozone World Congress, San Francisco, 1993.

[5] H. V. Lang, P. E. Erni, and P. A. Liechti, "Advanced ozone generation technology to solve the oxidation problems of today," presented at the Proc. 11th Ozone World Congress, San Francisco, 1993.

[6] U. Kogelschatz, "Silent discharges and their applications," in *10th International Conference on Gas Discharges and Their Applications*, Swansen, pp. 970-980, 1992.

[7] S. Yagi and M. Tanaka, "Mechanism of ozone generation in air-fed ozonisers," *J. Phys. D: Appl. Phys.*, vol. 20, pp. 1421-37, 1979.

[8] B. Eliasson, M. Hirth and U. Kogelschatz, "Ozone formation in dielectric barrier discharges in oxygen," pp. 339-344, 1985.

[9] U. Kogelschatz, B. Eliasson, and W. Egli, "From ozone generators to television screens: history and future potential of dielectric-barrier discharges," *Pure Appl. Chem.*, vol. 71, pp. 1819-1828, 1999.

[10] I. D. Chalmers, L. Zanella, S. J. MacGregor, and I. A. Wray, "Ozone generation by pulsed corona discharge in a wire cylinder arrangement," in *IEE Colloquium on Electro-Technologies for Waste Processing and Purification*, pp. 6/1-6/4, 1994.

[11] D. Braun, U. kuchler, and G. Pietsch, "Microdischarges in air-fed ozonizers," *Journal of Physics D: Applied Physics*, vol. 24, p. 564, 1991.

[12] N. Takamura, T. Matsumoto, D. Wang, T. Namihira, and H. Akiyama, "Ozone generation using positive- and negative-nano-seconds pulsed discharges," in *IEEE International Pulsed Power Conference (PPC)*, pp. 1300-1303, 2011.

[13] U. Kogelschatz, B. Eliasson, and W. Egli, "Dielectric-barrier discharges. Principle and applications," *Journal de Physique IV (Colloque)*, vol. 7, pp. 47-66, 1997.

[14] B. Eliasson, M. Hirth, and U. Kogelschatz, "Ozone synthesis from oxygen in dielectric barrier discharges," *Journal of Physics D: Applied Physics*, vol. 20, pp. 1421-1437, 1987.

[15] J. Kitayama and M. Kuzumoto, "Theoretical and experimental study on ozone generation characteristics of an oxygen-fed ozone generator in silent discharge," *Journal of Physics D: Applied Physics*, vol. 30, p. 2453, 1997.

[16] U. Kogelschatz, "Dielectric-Barrier Discharges: Their History, Discharge Physics, and Industrial Applications," *Plasma Chemistry and Plasma Processing*, vol. 23, pp. 1-46, 2003.

[17] C. F. Schonbein, *Comptes rendus Hebd. Seances Acad. Sci*, vol. 10:706, 1840.

[18] R.G. Rice and A.Netzer, "Handbook of Ozone Technology and Applications," vol. 1, 1982.

[19] D. R. Lide, *Physical Constants of Organic Compounds, 2005.*

[20] B. Ballantine, T. Morris, and P. Turner, *General and applied toxicology*, adbridged edition ed.: The MacMillan Press Ltd., 1995.

[21] F. L. Evans, *Ozone in water and wastewater treatment*, First ed.: Ann Arbor Science Publishers Inc, 1972.

[22] A. L. Lister and G. J. V. D. Kraak, "Endocrine disruption: why is it so complicated ?," *Water Qual. Res. J. Canada*, vol. 36, pp. 175-190, 2001.

[23] D. W. Kolpin, E. T. Furlong, M. T. Meyer, E. M. Thurman, S. D. Zaugg, L. B. Barber, and H. T. Buxton, "Pharmaceuticals, hormones and other organic wastewater contaminants in US streams, 1999-2000: a national reconnaissance.," *Environ. Sci. Technol. ,* vol. 36, pp. 1202-1211, 2002.

[24] G.-G. Ying, R. S. Kookana, A. Kumar, and M. Mortimer, "Occurrence and implications of estrogens and xenoestrogens in sewage effluents and receiving waters from South East Queensland," *Sci. Total Environ.,* vol. 407, pp. 5147-5155, 2009.

[25] J. Lee, H. Park, and J. Yoon, "Ozonation characteristics of bisphenol A in water," *Environ. Technol.,* vol. 24, pp. 241-248, 2003.

[26] S. Baig, G. Hansmann, and B. Paolini, "Ozone oxidation of oestrogenic active substances in wastewater in drinking water," *Water Sci. Technol.,* vol. 58(2), pp. 451-458, 2008.

[27] F. J. Rivas, A. Encinas, B. Acedo, and F. J. Beltran, "Mineralization of bisphenol A by advanced oxidation processes," *J. Chem. Technol. Biotechnol.,* vol. 84, pp. 589-594, 2009.

[28] T. Garoma, S. A. Matsumoto, Y. Wu, and R. Klinger, "Removal of bisphenol A and its reaction-intermediates from aqueous solution by ozonation," *Ozone Science and Engineering*, vol. 32, pp. 338-343, 2010.

[29] M. Umar, F. Roddick, L. Fan, and H. A. Aziz, "Application of ozone for the removal of bisphenol A from water and wastewater - A review," *Chemosphere*, vol. 90, pp. 2197-2207, 2013.

[30] M. Deborde, S. Rabouan, P. Mazellier, J.-P. Duguet, and B. Legube, "Oxydation of bisphenol A by ozone in aqueous solution," *Water Research*, vol. 42, pp. 4299-4308, 2008.

[31] BOC Process Gas Solutions, "Low temperature oxidation system demonstration at RSR Quemetco, Inc. City of Industry, California, Final report," 2001.

[32] J.-C. Hostachy, A. Metais, E. Germer, and V. Baratharaj, "Pulp bleaching with ozone industrial achievements & perspectives."

[33] WEDECO, "Ozone in the pulp & paper industry," 2012.

[34] F. Archibald and L. Roy-Arcand, "The use of ozone to decolorize residual direct paper dyes in kraft paper machine whitewater," *Ozone Science & Engineering,* vol. 19, pp. 549-565, 1997.

[35] WHO., *Monographs on the evaluation of carinogenic risks to humans* vol. 52. Geneva, 1990.

[36] Q. Han, H. Wang, W. Dong, T. Liu, and Y. Yin, "Formation and inhibition of bromate during ferrate(VI) – Ozone oxidation process," *Separation and Purification Technology,* vol. 118, pp. 653-658, 2013.

[37] A. Fridman and L. A. Kennedy, *Plasma Physics and Engineering*. United States: Taylor and Francis Group, 2011.

[38] C. J. Hochanadel, J. A. Ghormley, and J. W. Boyle, "Vibrationally excited ozone in the pulse radiolysis and flash photolysis of oxygen," *J. Chem. Phys.* , vol. 48, pp. 2416-2420, 1968.

[39] J. E. Ramirez, R. K. Bera, and R. J. Hanrahan, "Formation of ground state ozone on pulse radiolysis of oxygen," *Radiation Physics and Chemistry (1977),* vol. 23, pp. 685-689, 1984.

[40] B. Eliasson and U. Kogelschatz, "Modeling and applications of silent discharge plasmas," *IEEE Transactions on Plasma Science,* vol. 19, pp. 309-323, 1991.

[41] B. Eliasson and U. Kogelschatz, "Electron impact dissociation in oxygen," *Journal of Physics B: Atomic and Molecular Physics,* vol. 19, p. 1241, 1986.

[42] D. R. Lide, *CRC Handbook of Chemistry and Physics*. Boca Raton, FL: CRC Press,, 2005.

[43] A. Fridman, *Plasma Chemistry*. New York: Cambridge University Press, 2008.

[44] P. C. Cosby, "Electron impact dissociation of oxygen," *J. Chem. Phys.*, vol. 98, 1993.

[45] A. Michael, R. A. Knut, B. P. Duska, S. Momir, J. M. Nigel, and A. D. Julia, "Production of vibrationally autodetaching in low-energy electron impact on ozone," *Journal of Physics B: Atomic, Molecular and Optical Physics,* vol. 29, 1996.

[46] S. A. Rangwala, S. V. K. Kumar, E. Krishnakumar, and N. J. Mason, "Cross sections for the dissociative electron attachment to ozone," *Journal of Physics B: Atomic, Molecular and Optical Physics,* vol. 32, p. 3795, 1999.

[47] B. Eliasson and U. Kogelschatz, "Brown Boveri Research Report No KLR," 1986.

[48] G. J. M. Hagelaar and L. C. Pitchford, "Solving the Boltzmann equation to obtain electron transport coefficients and rate coefficients for fluid models," *Plasma Sources Science and Technology,* vol. 14, pp. 722-733, 2005.

[49] S. Jodzis and J. Petryk, "Gas Temperature in an Ozonizer. The Computer Modeling of an Actual Discharge System," *IEEE Transactions on Plasma Science,* vol. 39, pp. 2020-2021, 2011.

[50] S. Jodzis, "Temperature effects under ozone synthesis process conditions," *The European Physical Journal Applied Physics,* vol. 61, p. 24319, 2013.

[51] Rideal, "E. K. Ozone," Constable & Co., Ltd., London, 1920.

[52] W. S. Sease, "Supplementary Material, Short Course on Ozone Technology," The Center For Professional Advancement, Somerville, NJ, 1975.

[53] S. D. Razumovsky and G. E. Zaikov, *Ozone and its reactions with organic compounds*. Moscow, 1974.

[54] Y. P. Raizer, *Gas Discharges Physics: 2.3. Electron Energy*: Springer-Verlag, 1991.

[55] E. Kuffel, W. S. Zaengl, and J. Kuffel, *High Voltage Engineering: Fundamentals*: Newnes, 2000.

[56] A. Fridman, A Chirokov and A Gutsol, "Non-thermal atmospheric pressure discharges," *Journal of Physics D: Applied Physics,* vol. 38, p. R1, 2005.

[57] L. B. Loeb, *Basic Processes of Gaseous Electronics*. Berkeley, CA: University of California Press, 1960.

[58] H. Raether, *Electron Avalanches and Breakdown in Gases*. London: Butterworth, 1964.

[59] J. M. Meek and J. D. Craggs, *Electrical Breakdown of Gases*. New York: Wiley, 1978.

[60] A. Schutze, J. Y. Jeong, S. E. Babayan, P. Jaeyoung, G. S. Selwyn, and R. F. Hicks, "The atmospheric-pressure plasma jet: a review and comparison to other plasma sources," *IEEE Transactions on Plasma Science,* vol. 26, pp. 1685-1694, 1998.

[61] B. Eliasson and U. Kogelschatz, "Nonequilibrium volume plasma chemical processing," *IEEE Transactions on Plasma Science,* vol. 19, pp. 1063-1077, 1991.

[62] *Encyclopedia Britannica,* 9th ed. vol. XVIII (ORN-PHT). New York: Charles Scribner's Sons, 1885.

[63] V. F. Kozhinov, *Equipment for the Ozonation of Water*. Moscow: Publishing House on the literature of Construction, 1968.

[64] B. Eliasson and U. Kogelschatz, "Ozone generation with narrow–band UV radiation," *Ozone: Science & Engineering,* vol. 13, pp. 365-373, 1991.

[65] J. D. Seader and C. W. Tobias, *Ind. Eng. Chem. ,* vol. 9, pp. 2207-2211, 1952.

[66] D. P. Semchenko, E. T. Lyubushkina, and V. Lyubushkin, *Elektro-khimiya,* vol. 11, p. 1744, 1973.

[67] H. P. Fritz, J. Thanos, D. W. Wabner, and Z. Naturforsch, pp. 1617-1627, 1979.

[68] P. C. Foller and C. W. Tobias, "The Effect of Electrolyte Anion Adsorption on Current Efficiencies for the Evolution of Ozone," *J. Phys. Chem.,* vol. 85, p. 3238, 1981.

[69] U. Kogelschatz, "Fundamentals and applications of dielectric-barrier discharges," 2000.

[70] U. Kogelschatz, "Advanced ozone generation," *Process Technologies for Water Treatment,* pp. 87-120, 1988.

[71] U. Kogelschatz, "Filamentary, patterned, and diffuse barrier discharges," *IEEE Transactions on Plasma Science,* vol. 30, pp. 1400-1408, 2002.

[72] H. E. Wagner, R. Brandenburg, K. V. Kozlov, A. Sonnenfeld, P. Michel, and J. F. Behnke, "The barrier discharge: basic properties and applications to surface treatment," *Vacuum,* vol. 71, pp. 417-436, 2003.

[73] K. Buss, *Arch. Elektrotech,* vol. 26, 1932.

[74] T. C. Manley, "The electric characteristics of the ozonator discharge," *Trans. Electrochem. Soc.84*, pp. 83-96, 1943.

[75] A. Chirokov, A. Gutsol, A. Fridman, K. D. Sieber, J. M. Grace, and K. S. Robinson, "Analysis of two-dimensional microdischarge distribution in dielectric-barrier discharges," *Plasma Sources Science and Technology*, vol. 13, pp. 623-635, 2004.

[76] M. Kettlitz, H. Höft, T. Hoder, S. Reuter, K. D. Weltmann, and R. Brandenburg, "On the spatio-temporal development of pulsed barrier discharges: influence of duty cycle variation," *Journal of Physics D: Applied Physics*, vol. 45, p. 245201, 2012.

[77] M. Heise, T. Lierfeld, O. Franken, and W. Neff, "Single filament charge transfer and UV-emission properties of a cascaded dielectric barrier discharge (CDBD) set-up," *Plasma Sources Science and Technology*, vol. 13, pp. 351-358, 2004.

[78] T. Murata, M. Tatukawa, Y. Okita and K. Yasuoka, "Polarity Effect of Silent Discharge," *Ozone Science & Engineering*, vol. 17, pp. 575-586, 1995.

[79] J. Drimal, K. V. Kozlov, V. I. Gibalov, and V. G. Samoylovich, "On value of transferred charge in silent discharge under atmospheric pressure," *Czech. J. Phys. B 38*, pp. 159-165, 1988.

[80] J. Drimal, V. I. Gibalov, and V. G. Samoylovich, "The magnitude of the transfered charge in dielectric barrier discharges in oxygen," *Czech. J. Phys. B* vol. 37, pp. 1248-1255, 1987.

[81] A. S. Chiper, V. Aniţa, C. Agheorghiesei, V. Pohoaţa, M. Aniţa, and G. Popa, "Spectroscopic Diagnostics for a DBD Plasma in He/Air and He/N2 Gas Mixtures," *Plasma Processes and Polymers*, vol. 1, pp. 57-62, 2004.

[82] N. Naudé, J. P. Cambronne, N. Gherardi, and F. Massines, "Electrical model and analysis of the transition from an atmospheric pressure Townsend discharge to a filamentary discharge," *Journal of Physics D: Applied Physics*, vol. 38, p. 530, 2005.

[83] Shuhai Liu and M. Neiger, "Electrical modelling of homogeneous dielectric barrier discharges under an arbitrary excitation voltage," *J. Phys. D: Appl. Phys.*, vol. 36, pp. 3144-3150, 2003.

[84] S. Kanazawa, M. Kogoma, T. Moriwaki, and S. Okazaki, "Stable glow plasma at atmospheric pressure," *J. Phys. D: Appl. Phys.*, vol. 21, pp. 838-840, 1988.

[85] S. Okazaki, M. Kogomat, M. Uehara, and Y. Kimura, "Appearance of stable glow discharge in air, oxygen and introgen at apgusing a 50 Hz source," *J. Phys. D: Appl. Phys.*, vol. 26, pp. 889-892, 1993.

[86] J. Tepper and M. Lindmayer, "Investigations on two Different Kinds of Homogeneous Barrier Discharges at Atmospheric Pressure," presented at the HAKONE VII International Symposium on High Pressure, Low Temperature Plasma Chemistry, Greifswald, Germany, 2000.

[87] K. V. Kozlov, H. E. Wagner, R. Brandenburg, and P. Michel, "Spatio-temporally resolved spectroscopic diagnostics of the barrier discharge in air at atmospheric pressure," *Journal of Physics D: Applied Physics*, vol. 34, p. 3164, 2001.

[88] R. Jozef and M. S. Daniel, "The transition from a filamentary dielectric barrier discharge to a diffuse barrier discharge in air at atmospheric pressure," *Journal of Physics D: Applied Physics*, vol. 38, pp. 547-554, 2005.

[89] G. J. Pietsch and V. I. Gibalov, "Dielectric barrier discharges and ozone synthesis," *Pure & Appl. Chem.*, vol. 70, pp. 1169-1174, 1998.

[90] M. Kogoma and S. Okazaki, "Raising of ozone formation efficiency in a homogeneous glow discharge plasma at atmospheric pressure," *J. Phys. D: Appl. Phys.*, vol. 27, pp. 1985-1987, 1994.

[91] Z. Buntat, I. R. Smith, and N. A. M. Razali, "Generation of a Homogeneous Glow Discharge: A Comparative Study between the Use of Fine Wire Mesh and Perforated Aluminium Electrodes," *Applied Physics Research*, vol. 3, 2011.

[92] Y. Nakai, A. Takashi, N. Osawa, Y. Yoshioka and R. Hanaoka, "Comparison of Ozone Generation Characteristics by Filamentary Discharge Mode and Townsend Discharge Mode of Dielectric Barrier Discharge in Oxygen," *Journal of Chemistry & Chemical Engineering*, vol. 5, p. 1107, 2011.

[93] S. Wang, M. Ischibashi, Y. Feng, M. Nakaoka, and Y. Konishi, "Series-compensated inductor type resonant inverter using pulse density modulation scheme for efficient ozonizer," presented at the Proceedings of international conference on power electronics and drive systems, Singapore, 1997.

[94] J. M. Alonso, J. Garcia, A. J. Calleja, J. Ribas, and J. Cardesin, "Analysis, design, and experimentation of a high-voltage power supply for ozone generation based on current-fed parallel-resonant push-pull inverter," *IEEE Transactions. on Industry applications*, vol. 41, pp. 1364-1372, 2005.

[95] M. Facta, Z. Salam, A. Jusoh, and Z. B. Buntat, "Improvement in ozone generation with low voltage high frequncy power converters," presented at the 2nd IEEE International Conference on Power and Energy, Johor Baharu, Malaysia, 2008.

[96] V. Kinnares and P. Hothongkham, "Circuit Analysis and Modeling of a Phase-Shifted Pulsewidth modulation Full-Bridge-Inverter-Fed Ozone Generator With Constant Applied Electrode Voltage," *IEEE Transactions on Power Electronics,*, vol. 25, pp. 1739-1752, 2010.

[97] C. Heuser and G. Pietsch, "Comparison of gas dicharges forms producing ozone generation," presented at the Proc. 5th Int. Symp. on Plasma Chemistry, Edinburgh, UK, 1981.

[98] Shuhai Liu and N. Manfred, "Excitation of dielectric barrier discharges by unipolar submicrosecond square pulses," *Journal of Physics D: Applied Physics*, vol. 34, pp. 1632-1638, 2001.

[99] N. Mericam-Bourdet, M. J. Kirkpatrick, F. Tuvache, D. Frochot, and E. Odic, "Effect of voltage waveform on dielectric barrier discharge ozone production efficiency," *The European Physical Journal - Applied Physics*, vol. 57, 2012.

[100] I. D. Chalmers, L. Zanella, and S. J. MacGregor, "Ozone synthesis in oxygen in a dielectric barrier free configuration," in *IEEE International Pulsed Power Conference, Digest of Technical Papers.*, , pp. 1249-1254 vol.2, 1995.

[101] W. J. M. Samaranayake, T. Namihira, S. Katsuki, Y. Miyahara, T. Sakugawa, R. Hackam, and H. Akiyama, "Pulsed power production of ozone using nonthermal gas discharges," *IEEE Electrical Insulation Magazine*, vol. 17, pp. 17-25, 2001.

[102] Z. Buntat, J. E. Harry, and I. R. Smith, "Application of dimensional analysis to ozone production by pulsed streamer discharge in oxygen," *Journal of Physics D: Applied Physics*, vol. 36, p. 1553, 2003.

[103] W. J. M. Samaranayake, Y. Miyahara, T. Namihira, S. Katsuki, T.Sakugawa, R. Hackam, and H. Akiyama, "Pulsed streamer discharge characteristics of ozone production in dry air," *IEEE Transactions on Dielectrics and Electrical Insulaiton* vol. 7, pp. 254-260, 2000.

[104] W. J. M. Samaranayake, Y. Miyahara, T. Namihira, S. Katsuki, R. Hackam, and H. Akiyama, "Ozone production using pulsed dielectric barrier discharge in oxygen," *IEEE Transactions on Dielectrics and Electrical Insulation* vol. 7, pp. 849-854, 2000.

[105] W. J. M. Samaranayake, Y. Miyahara, T. Namihira, S. Katsuki, R. Hackam, and H. Akiyama, "Ozone production using cylindrical reactors with and without solid dielectrics layers in dry air," presented at the Conference on Electrical Insulation and Dielectric Pheomena, 1999.

[106] I. D. Chalmers and L. Zanella, "Wire/cylinder device with space charge distortion: ozone production," in *IEE Colloquium on Field Modelling: Applications to High Voltage Power Apparatus*, 1996, pp. 8/1-8/3.

[107] H. Tamaribuchi, D. Wang, T. Namihira, S. Katsuki, and H. Akiyama, "Effect of pulse width on generation of ozone by pulsed streamer discharge," in *IEEE International Pulsed Power Conference,* pp. 407-410, 2007.

[108] F. Fukawa, N. Shimomura, T. Yano, S. Yamanaka, K. Teranishi, and H. Akiyama, "Application of nanosecond pulsed power to ozone production by streamer corona," *IEEE Transactions on Plasma Science*, vol. 36, pp. 2592-2597, 2008.

[109] F. T. Ulaby, *Electromagnetics for Engineers*. United States of America: Tom Robbins, 2005.

[110] M. Holub, "On the measurement of plasma power in atmospheric pressure DBD plasma reactors," *International Journal of Applied Electromagnetics and Mechanics*, vol. 39, pp. 81-87, 2012.

[111] Matlab: The MathWorks, Inc.

[112] Origin. Northampton, Massachusetts, USA.: OriginLab.

[113] Z. Kregar, M. Biscan, S. Milosevic, and A. Vesel, "Monitoring oxygen plasma treatment of polyropylene with optical emission spectroscopy," *IEEE Transactions on Plasma Science*, vol. 39, pp. 1239-1256, 2011.

[114] *Photomultiplier tubes: basics and applications*: Hamamatsu photonics 2006.

[115] A. V. Pipa, J. Koskulics, R. Brandenburg, and T. Hoder, "The simplest equivalent circuit of a pulsed dielectric barrier discharge and the determination of the gas gap charge transfer," *Rev Sci Instrum*, vol. 83, p. 115112, Nov 2012.

[116] Z. Falkenstein and J. J. Coogan, "Microdischarge behaviour in the silent discharge of nitrogen - oxygen and water - air mixtures," *J. Phys. D: Appl. Phys. ,* vol. 30, pp. 817-825, 1997.

[117] P. Reichen, A. Sonnenfeld, and P. Rudolf von Rohr, "Influence of increased velocity on the statistical discharge characteristics of He and air barrier discharges," *Journal of Physics D: Applied Physics*, vol. 43, p. 025207, 2010.

[118] N. Jidenko, M. Petit, and J. P. Borra, "Electrical characterization of microdischarges produced by dielectric barrier discharge in dry air at atmospheric pressure," *Journal of Physics D: Applied Physics*, vol. 39, pp. 281-293, 2006.

[119] I. Radu, R. Bartnikas, and M. R. Wertheimer, "Diagnostics and modelling of noble gas atmospheric pressure dielectric barrier discharges in homogeneous or diverging electric fields," *Journal of Physics D: Applied Physics*, vol. 38, pp. 539-546, 2005.

[120] H. C. Kim, F. Iza, S. S. Yang, M. Radmilović-Radjenović, and J. K. Lee, "Particle and fluid simulations of low-temperature plasma discharges: benchmarks and kinetic effects," *Journal of Physics D: Applied Physics*, vol. 38, pp. R283-R301, 2005.

[121] H. W. BAE, I. C. SONG, S. W. HWANG, H.-J. LEE and H. J. LEE, "Effect of Gap Distance on the Characteristic of Atmospheric Pressure Micro Dielectric Barrier Discharges," *Journal of the Korean Physical Society*, vol. 59, p. 3453, 2011.

[122] R. G. Rice, D. M. Graham, W. H. Glaze, M. W. Pariza, G. W. Newell, J. W. Erdman, and J. F. Borzelleca, "Ozone preservation of foods and foodstuffs," in *Ozone World Congress*, Kyoto, Japan, pp. B2-6-5, 1997.

[123] O. Motret, C. Hibert, M. Nikravech, I. Gaurand, R. Viladrosa, and J. M. Pouvesle, "The dependence of ozone generation efficiency on parameter adjustment in a triggered dielectric barrier discharge," *Ozone Science & Engineering*, vol. 20, pp. 51-66, 1998.

[124] Y.-M. Sung and T. Sakoda, "Optimum conditions for ozone formation in a micro dielectric barrier discharge," *Surface and Coatings Technology*, vol. 197, pp. 148-153, 2005.

[125] M. B. Chang and S.-J. Wu, "Experimental study on ozone synthesis via dielectric barrier discharges," *Ozone Science & Engineering*, vol. 19, pp. 241-254, 1996.

[126] T. Namihira, K. Shinozaki, S. Katsuki, R. Hackam, H. Akiyama, and T. Sakugawa, "Characteristics of ozonizer using pulsed power," in *IEEE Pulsed Power & Plasma Science Conference*, pp. 1090-1093, 2001.

[127] C. Monge, R. Peyrous, and B. Held, "Optimization of a corona wire-to-cylinder ozone generator. Comparison with economical criteria. part I: Oxygen.," *Ozone Science & Engineering*, vol. 19, pp. 533-547, 1997.

[128] P. Tegeder, P. A. Kendall, M. Penno, N. J. Mason, and E. Illenberger, "Electron stimulated desorption of O– and O2– from condensed ozone: possible implications for the heterogeneous photochemistry of stratospheric O3," *Physical Chemistry Chemical Physics*, vol. 3, pp. 2625-2629, 2001.

[129] C. W. Isobel, M. G. John, J. M. Nigel, and M. George, "Dissociative electron attachment (DEA) in ozone 0 - 10 eV," *Journal of Physics B: Atomic, Molecular and Optical Physics*, vol. 29, pp. 4749-4759, 1996.

[130] W. J. M. Samaranayake, Y. Miyahara, T. Namihira, S. Katsuki, R. Hackam, and H. Akiyama, "Ozone Production Using Pulsed Dielectric Barrier Discharge in Oxygen," *IEEE Transactions on Dielectrics and Electrical Insulation*, vol. 7, pp. 849-854, 2000.

[131] A. Starke, *Z. Elektrochem*, vol. 29, 1923.

[132] L. B. Loeb, *Fundamental Processes of Electrical Discharge in Gases*. New York: John Wiley & Sons, Inc, 1939.

[133] Y. L. M. Creyghton, E. M. V. Veldhuizen, and W. R. Rutgers, "Electrical and optical study of pulsed positive corona," *Non-thermal plasma techniques for pollution control*, pp. 205-230, 1993.

[134] J. Mankowski and M. Kristiansen, "A review of short pulse generator technology," *IEEE Trans. Plasma Science,* vol. 28, pp. 102-108, 2000.

[135] M. Maclean, L. E. Murdoch, M. N. Lani, S. J. MacGregor, J. G. Anderson, and G. A. Woolsey, "Photoinactivation and Photoreactivation Responses," presented at the *IEEE International power modulators and high-voltage conference,* Las Vegas, NE, 2008.

[136] T. Wang, S. J. MacGregor, J. G. Anderson, and G. A. Woolsey, "Pulsed ultra-violet inactivation spectrum of Escherichia coli," *Water Research,* vol. 39, pp. 2921-2925, 2005.

[137] M. Blajan, A. Umeda, S. Muramatsu, and K. Shimizu, "Emission Spectroscopy of Pulsed Powered Microplasma for Surface Treatment of PEN Film," *IEEE Transactions on Industry Applications,* vol. 47, pp. 1100-1108, 2011.

[138] D. M. Barrett, B. D. Cockreham, A. J. Dragt, F. E. White, E. L. Neau, K. W. Reed, and H. C. lves, "A pulse power modulator system for commercial high-power ion beam surface treatment applications," presented at *the 12th IEEE International pulsed power conference,* Monterey, CA, USA, 1999.

[139] E. Spahn and G. Buderer, "A flexible pulse power supply for EM- and ETC-launchers," in *12th IEEE International Pulsed Power Conference, Digest of Technical Papers,* pp. 1353-1356 vol.2, 1999.

[140] T. H. G. G. Weise, S. Wisken, and A. Berg, "Setup and performance of a capacitive 300 kJ pulsed power supply system for ETC-gun investigations," in *11th IEEE International Pulsed Power Conference, Digest of Technical Papers,* pp. 250-255 vol.1, 1997.

[141] Z. Buntat and I. R. Smith, "Ozone Generation by Pulsed Streamer Discharge in Air," *Applied Physics Research,* vol. 1, pp. 2-10, 2009.

[142] P. Bletzinger and B. N. Ganguly, "The effect of displacement current on fast-pulsed dielectric barrier discharges," *Journal of Physics D: Applied Physics,* vol. 36, p. 1550, 2003.

[143] D. T. Blair and H. W. Whittington, "Ionization and breakdown in oxygen," *Journal of Physics D: Applied Physics,* vol. 8, p. 405, 1975.

[144] C. A. Jones, S. A. Gordeyev, and S. J. Shilton, "Poly(vinyl chloride) (PVC) hollow fibre membranes for gas separation," *Polymer,* vol. 52, pp. 901-903, 2011.

10 LIST OF PUBLICATIONS

G. M. Huang, Y. J. Zhou, T. Wang, I. V. Timoshkin, M. P. Wilson, S. J. MacGregor and M. J. Given, "Statistical analysis of pulsed micro-discharges and ozone generation in dielectric barrier discharges", IEEE Transactions on Plasma Science, vol. 44, No. 10, 2016.

Y. J. Zhou, **G. M. Huang**, T. Wang, S. J. MacGregor, Q. C. Ren, M. P. Wilson and I. V. Timoshkin, "Optimization of ozone generation by investigation of filament current characteristics under dielectric barrier discharges", IEEE Transactions on Plasma Science, vol. 44, No. 10, 2016.

G. M. Huang, Y. J. Zhou, M. P. Wilson, T. Wang, I. V. Timoshkin, S. J. MacGregor and M. J. Given, "Investigation of pulsed micro-discharges and ozone production by dielectric barrier discharges", Proceedings of 2015 IEEE Pulsed Power Conference, Austin, TX, 2015.

G. M. Huang, T. Wang, I. V. Timoshkin, S. J. MacGregor, M. J. Given and M. P. Wilson, "Effects of rise rate of voltage impulses on oxygen-fed dielectric barrier discharge", Proceedings of the 20th International Conference on Gas Discharges and Their Applications, pp. 287-290, 2014.

G. M. Huang, T. Wang, I. V. Timoshkin, S. J. MacGregor, M. J. Given and M. P. Wilson, "A comparative study of ozone generation using pulsed and continuous AC dielectric barrier discharges", Proceedings of 19th IEEE International Pulsed Power & 40th Plasma Science Conference, San Francisco, CA, 2013.

G. M. Huang, T. Wang, I. V. Timoshkin, S. J. MacGregor, M. J. Given and M. P. Wilson, "Investigation of ozone generation using dielectric barrier discharges at 50 Hz, 2.6 kHz and 20 kHz", Proceedings of the 19th International Conference on Gas Discharges and Their Applications, pp. 650-653, Beijing, 2012.

T. Wang, Y. Y. Zhao, M. Maclean, S. J. MacGregor, **G. M. Huang**, M. P. Wilson, "Investigation of water treatment using dielectric barrier discharge", Proceedings of the 19th International Conference on Gas Discharges and Their Applications, pp. 654-657, Beijing, 2012.

11 APPENDIX A: Distribution of Filamentary Current Parameters over Different Gap Lengths

Presented herein are the distributions of different filamentary parameters over different gap lengths at the pressure of 1 bar absolute, as referenced in Section 5.3.2.

11.1 Distribution of Filamentary Current Amplitude over Different Gap Lengths

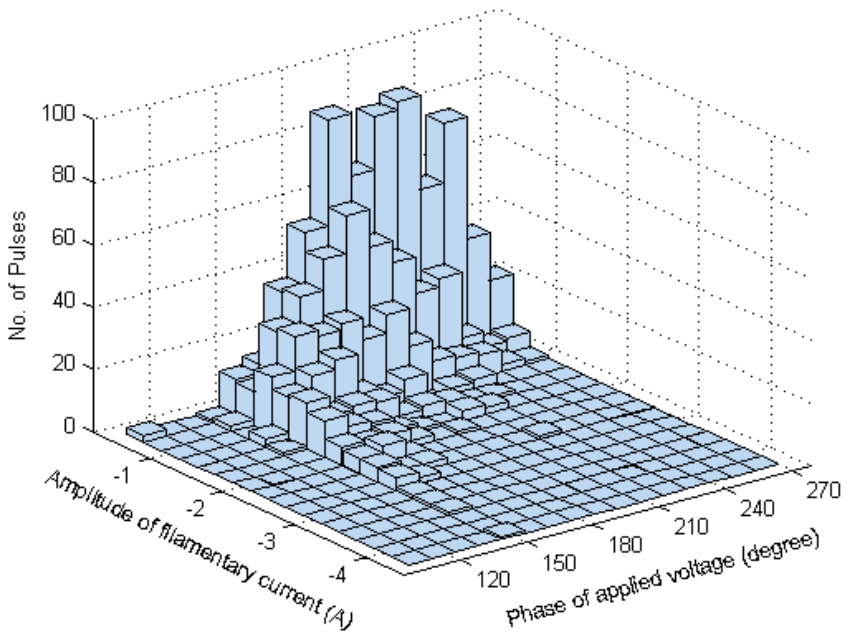

Fig. A- 1 Distribution of filamentary current amplitude for the gap length of 0.2 mm (at 1 bar absolute)

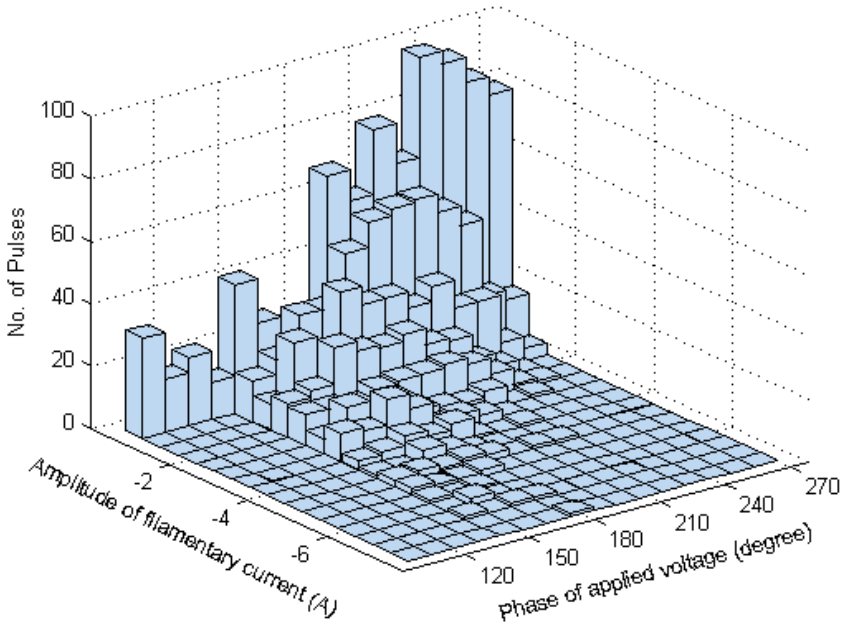

Fig. A- 2 Distribution of filamentary current amplitude for the gap length of 0.3 mm (at 1 bar absolute)

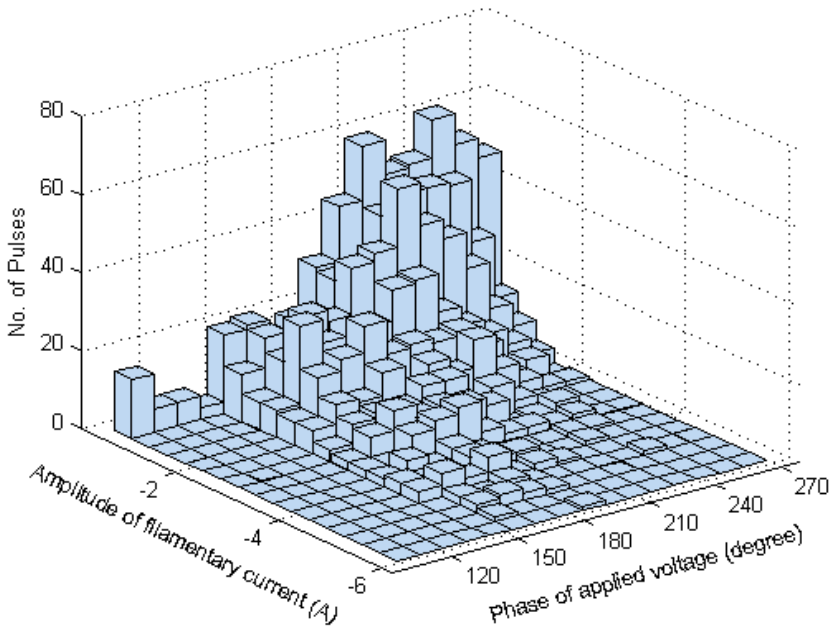

Fig. A- 3 Distribution of filamentary current amplitude for the gap length of 0.4 mm (at 1 bar absolute)

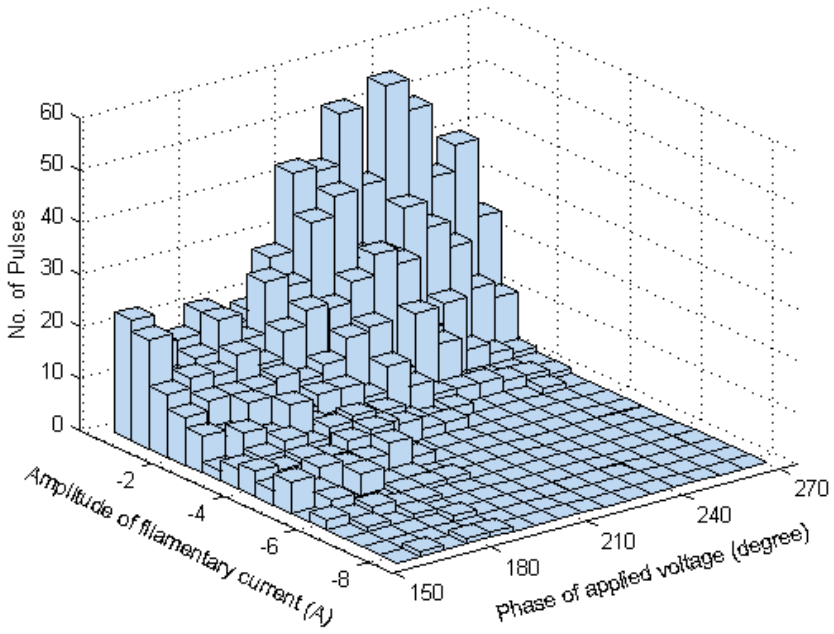

Fig. A- 4 Distribution of filamentary current amplitude for the gap length of 0.5 mm (at 1 bar absolute)

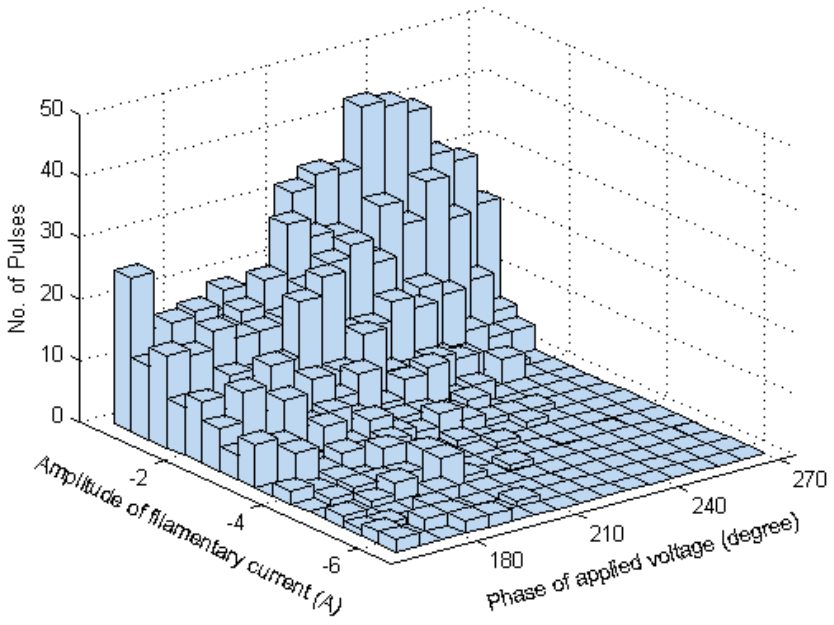

Fig. A- 5 Distribution of filamentary current amplitude for the gap length of 0.6 mm (at 1 bar absolute)

11.2 Distribution of Filamentary Current Duration over Different Gap Lengths

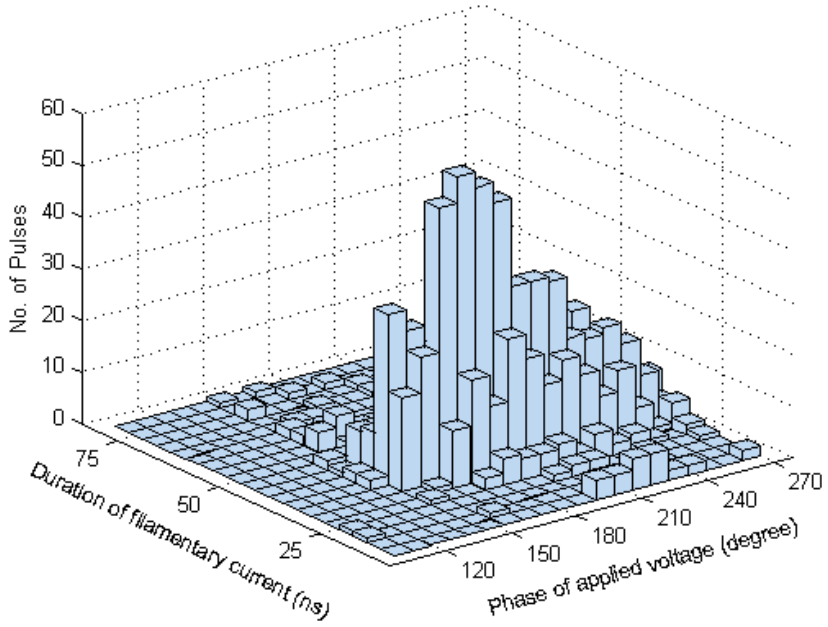

Fig. A- 6 Distribution of filamentary current duration for the gap length of 0.2 mm (at 1 bar absolute)

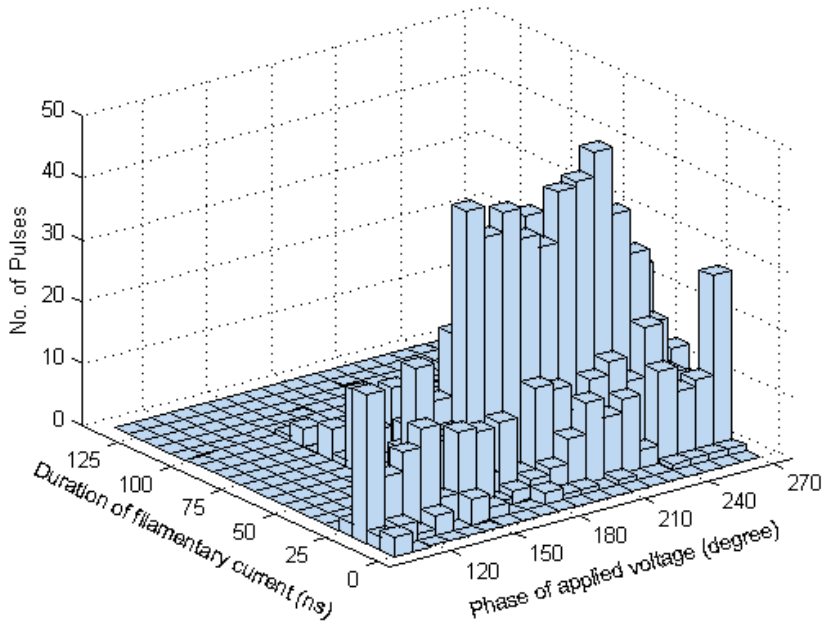

Fig. A- 7 Distribution of filamentary current duration for the gap length of 0.3 mm (at 1 bar absolute)

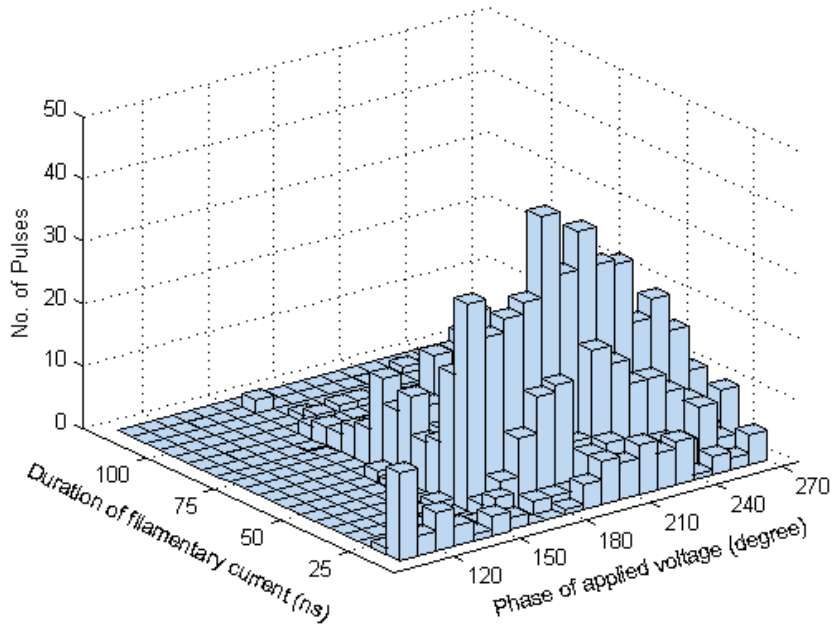

Fig. A- 8 Distribution of filamentary current duration for the gap length of 0.4 mm (at 1 bar absolute)

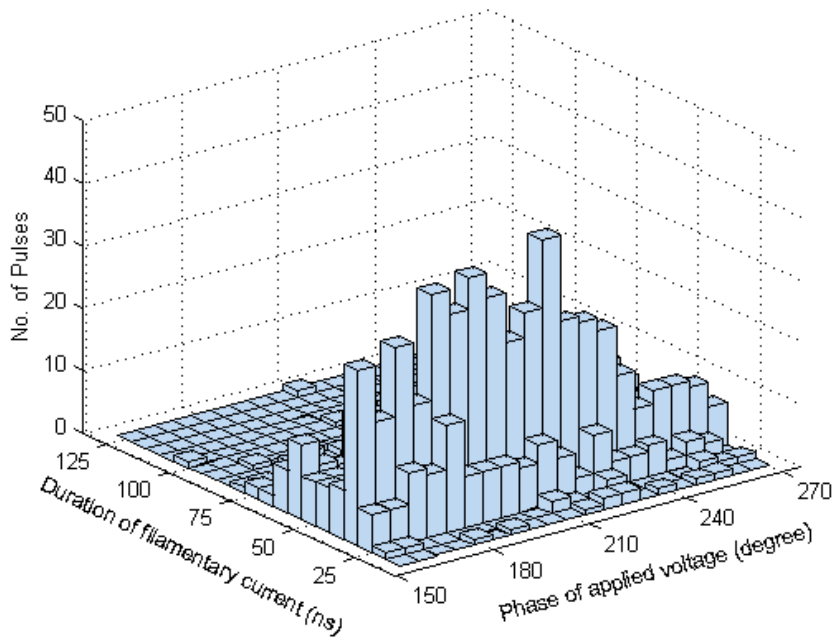

Fig. A- 9 Distribution of filamentary current duration for the gap length of 0.5 mm (at 1 bar absolute)

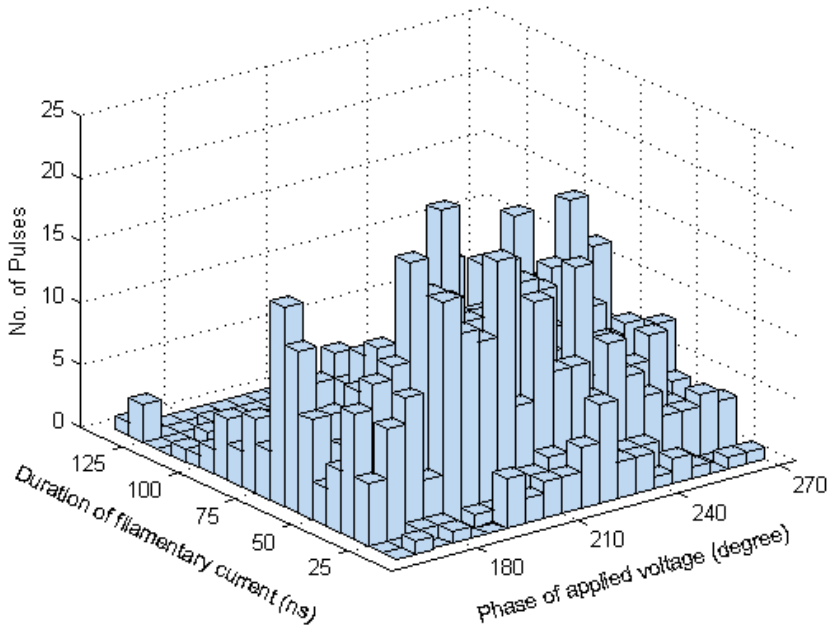

Fig. A- 10 Distribution of filamentary current duration for the gap length of 0.6 mm (at 1 bar absolute)

11.3 Distribution of Filamentary Transfer Charge over Different Gap Lengths

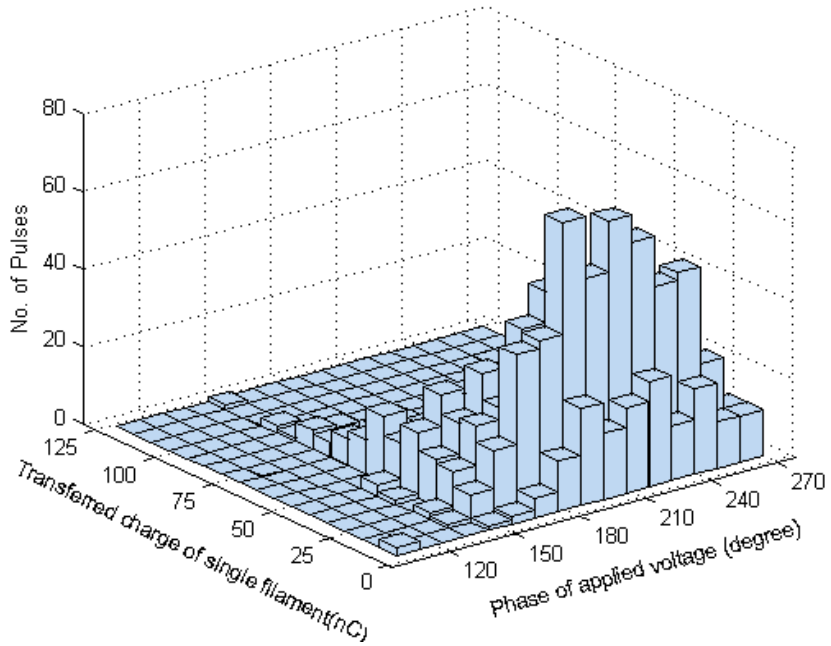

Fig. A- 11 Distribution of filamentary transfer charge for the gap length of 0.2 mm (at 1 bar absolute)

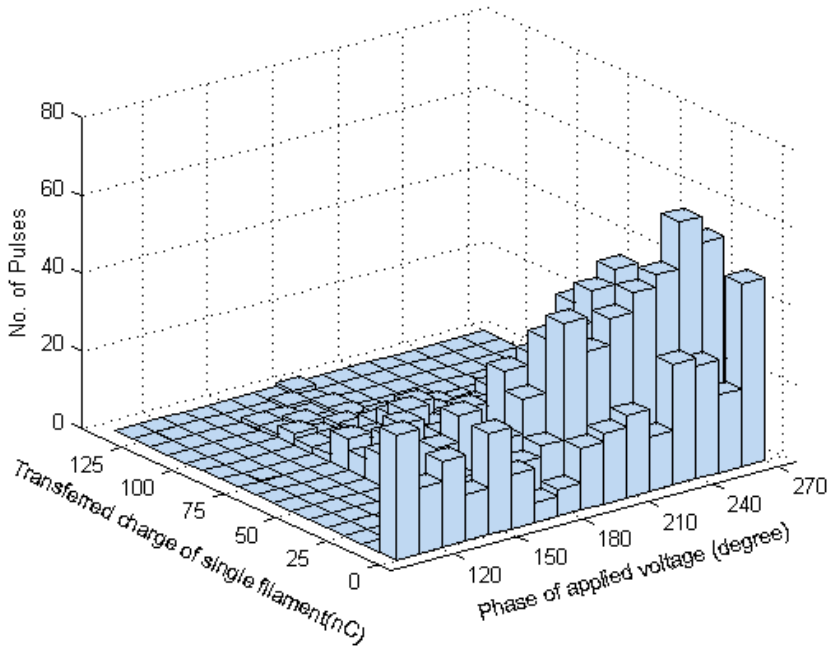

Fig. A- 12 Distribution of filamentary transfer charge for the gap length of 0.3 mm (at 1 bar absolute)

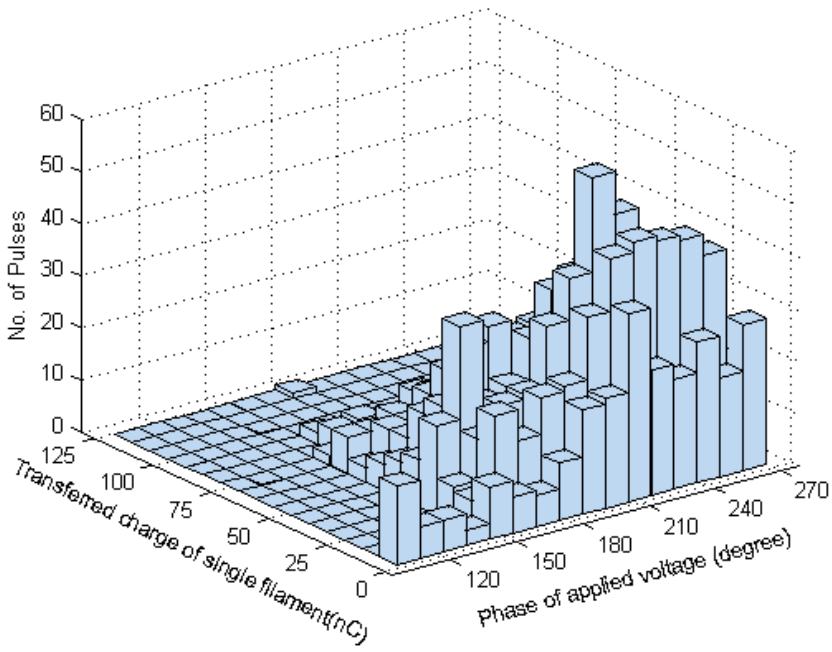

Fig. A- 13 Distribution of filamentary transfer charge for the gap length of 0.4 mm (at 1 bar absolute)

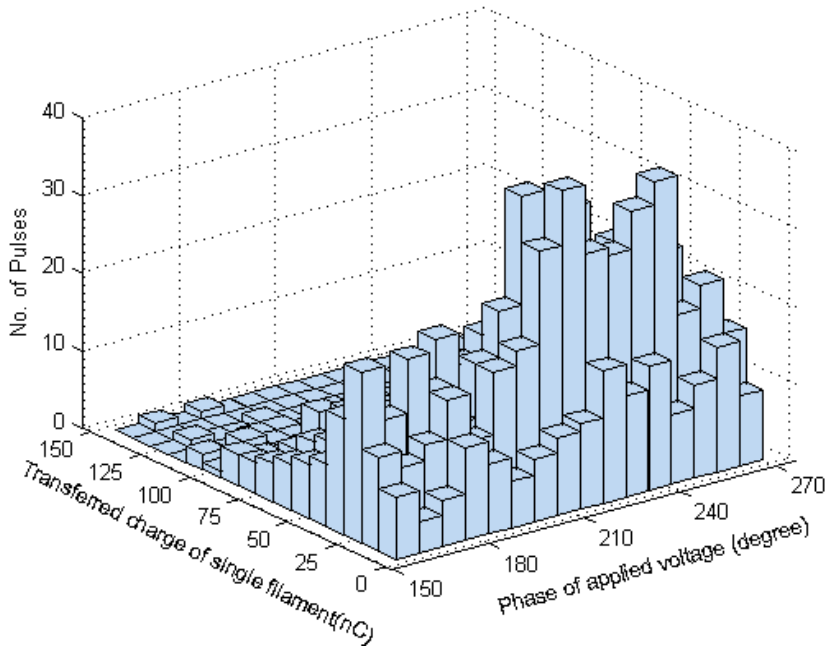

Fig. A- 14 Distribution of filamentary transfer charge for the gap length of 0.5 mm (at 1 bar absolute)

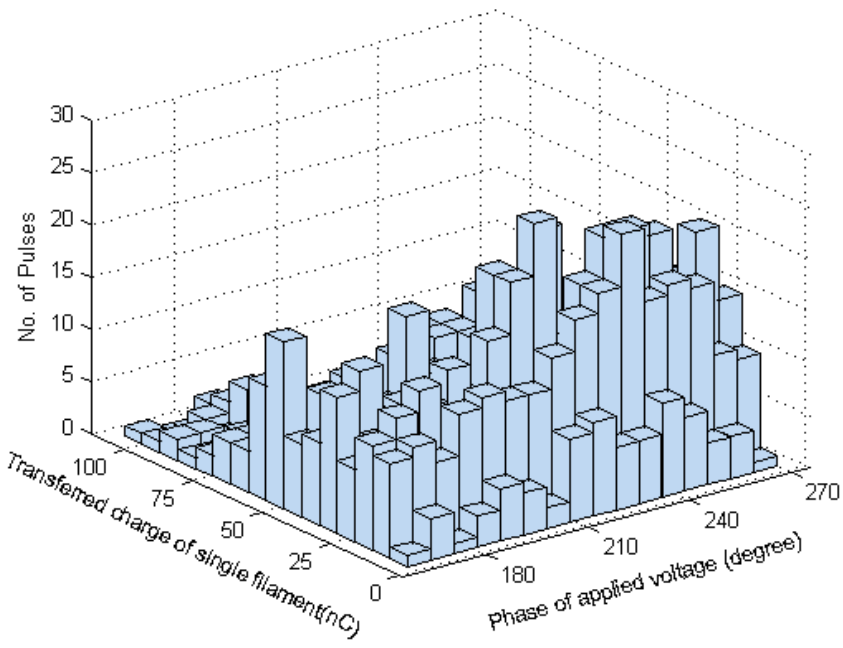

Fig. A- 15 Distribution of filamentary transfer charge for the gap length of 0.6 mm (at 1 bar absolute)

11.4 Distribution of Micro-discharge Energy over Different Gap Lengths

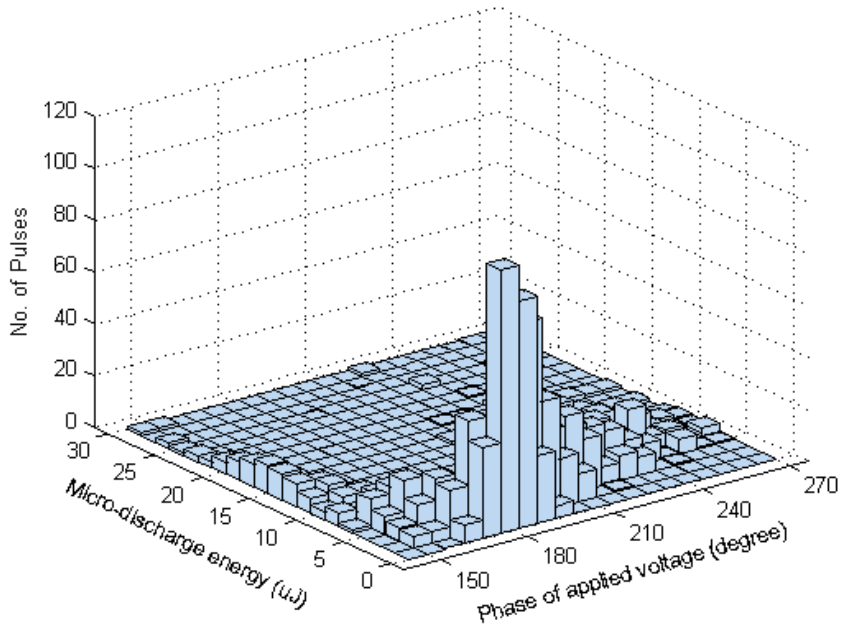

Fig. A- 16 Distribution of micro-discharge energy for the gap length of 0.2 mm (at 1 bar absolute)

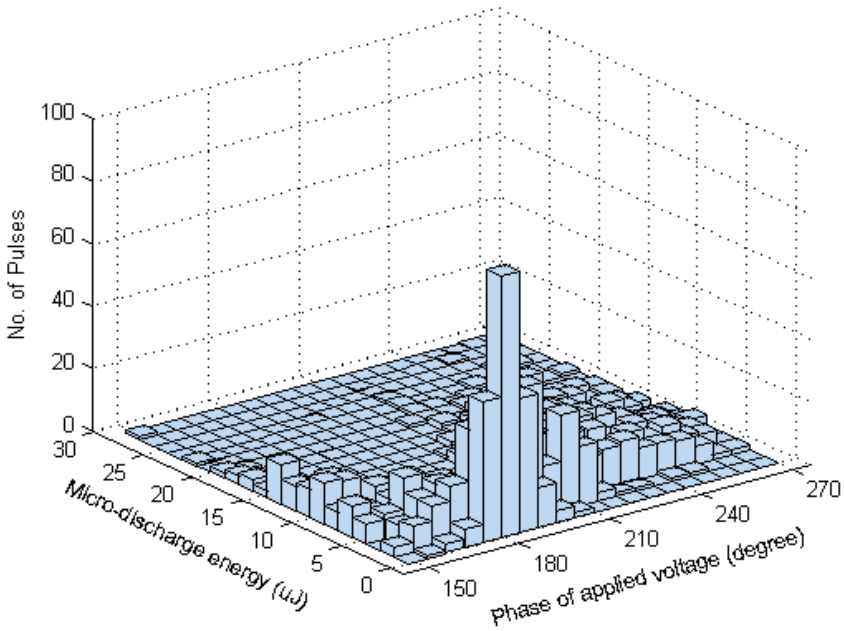

Fig. A- 17 Distribution of micro-discharge energy for the gap length of 0.3 mm (at 1 bar absolute)

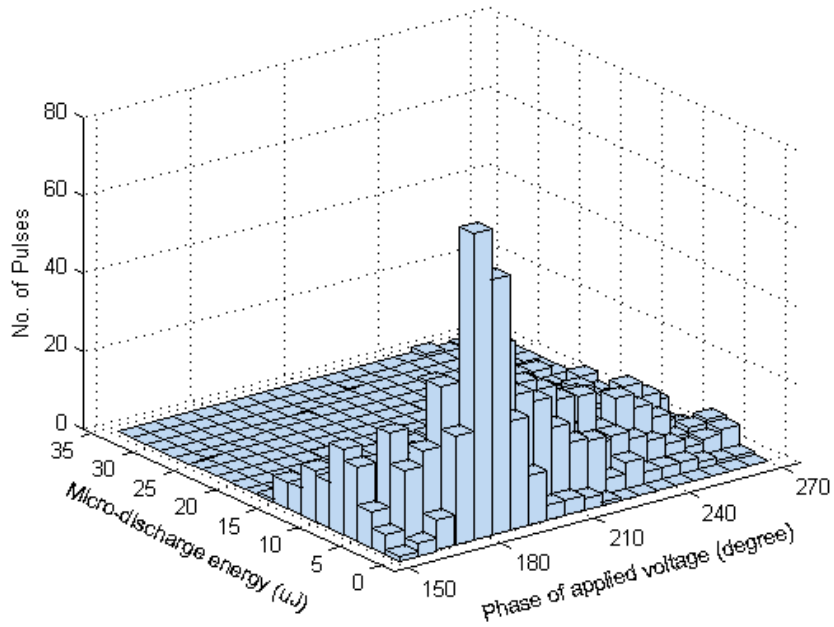

Fig. A- 18 Distribution of micro-discharge energy for the gap length of 0.4 mm (at 1 bar absolute)

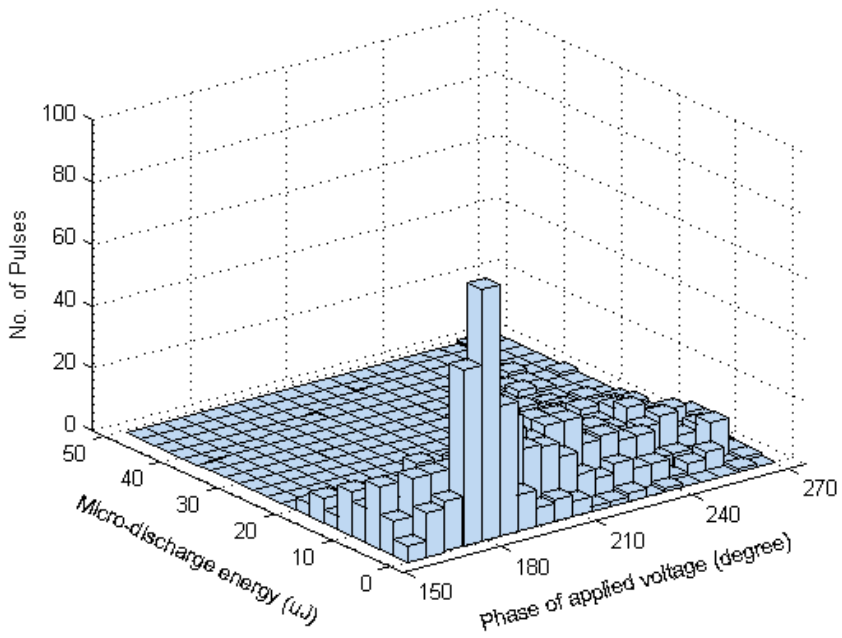

Fig. A- 19 Distribution of micro-discharge energy for the gap length of 0.5 mm (at 1 bar absolute)

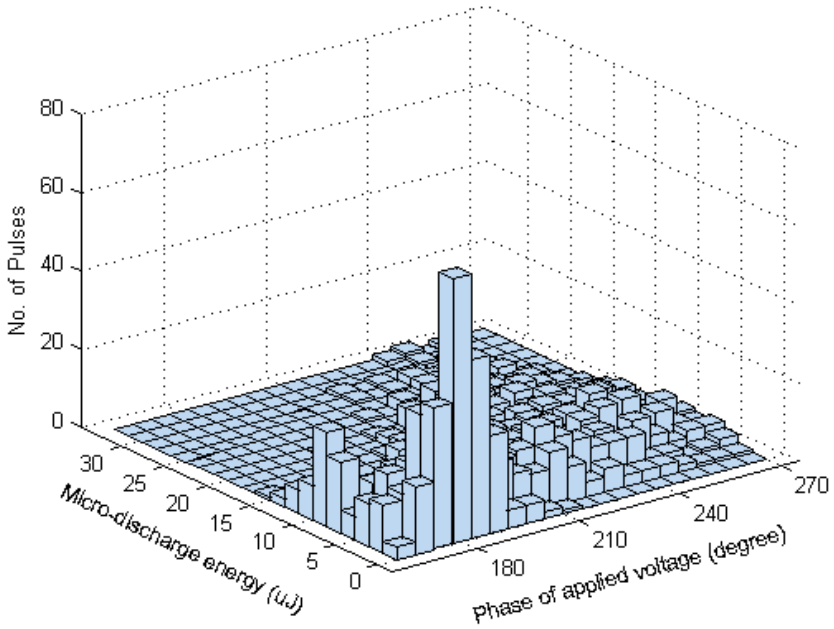

Fig. A-20 Distribution of micro-discharge energy for the gap length of 0.6 mm (at 1 bar absolute)

12 APPENDIX B: Distribution of Filamentary Current Parameters over Different Gas Pressures

Presented herein are the distributions of different filamentary parameters over different gas pressures at the discharge gap length of 0.5 mm, as referenced in Section 5.3.3.

12.1 Distribution of Filamentary Current Amplitude over Different Gas Pressures

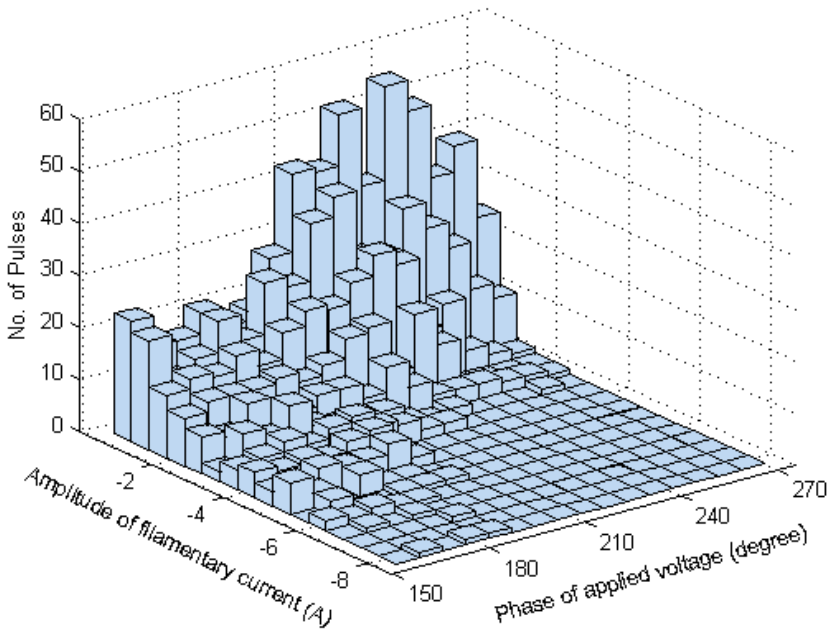

Fig.B-1 Distribution of filamentary current amplitude at the gas pressure of 1 bar absolute (at 0.5 mm gap length)

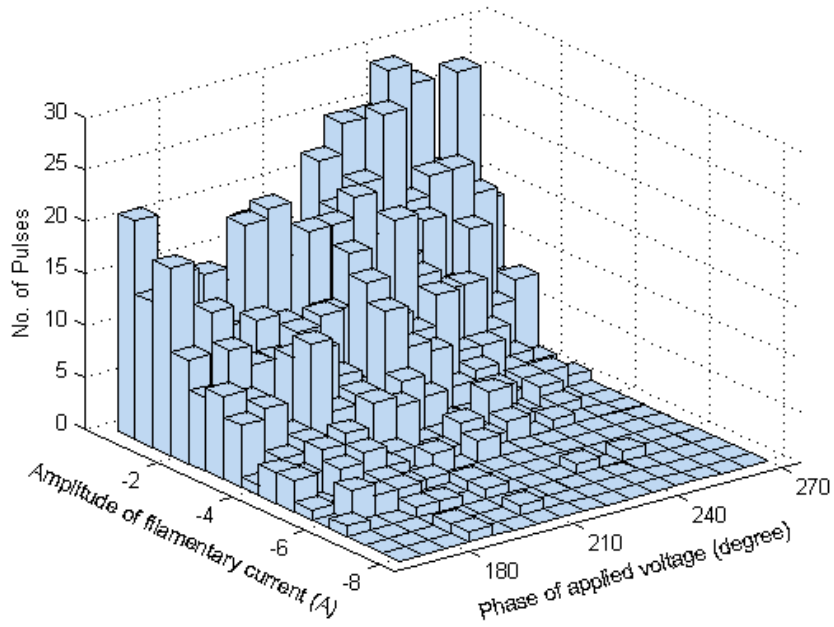

Fig.B-2 Distribution of filamentary current amplitude at the gas pressure of 1.2 bar absolute (at 0.5 mm gap length)

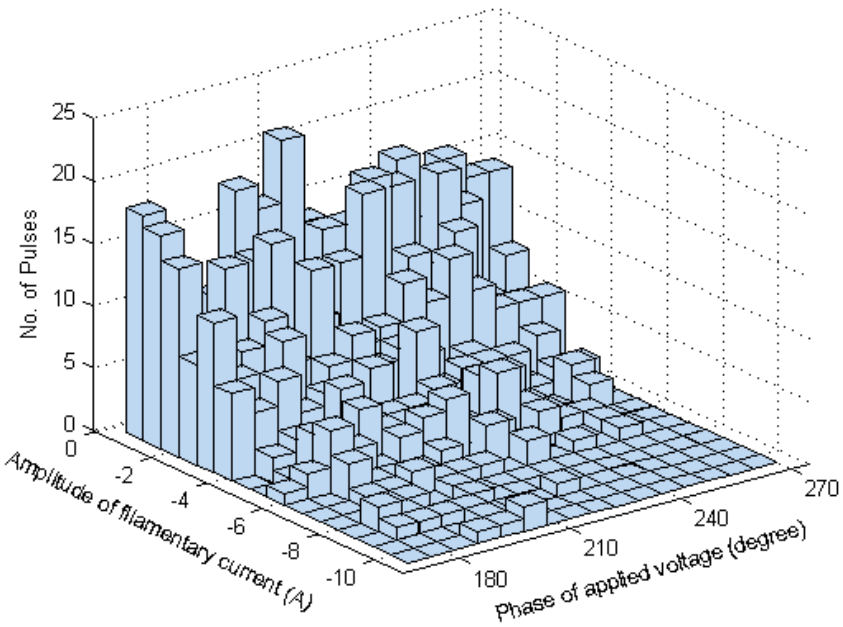

Fig.B-3 Distribution of filamentary current amplitude at the gas pressure of 1.4 bar absolute (at 0.5 mm gap length)

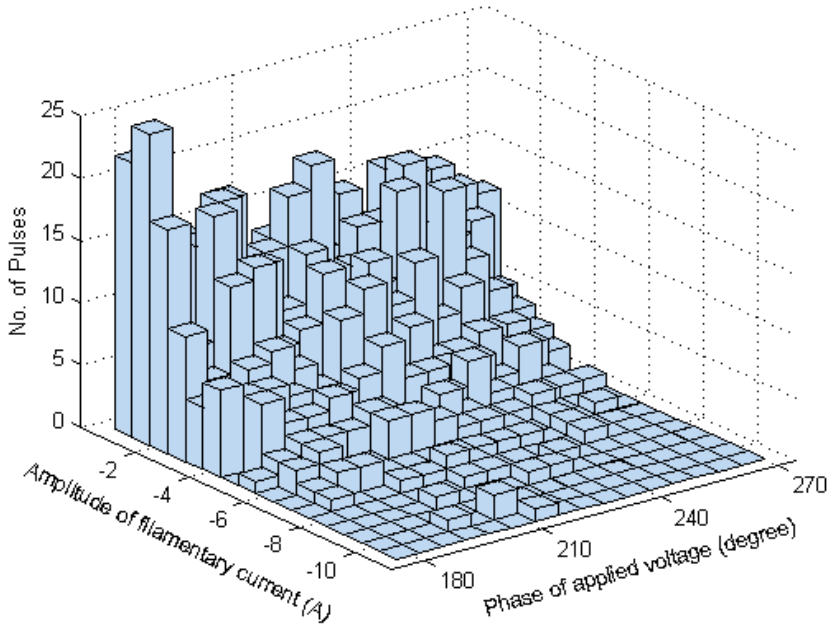

Fig.B-4 Distribution of filamentary current amplitude at the gas pressure of 1.6 bar absolute (at 0.5 mm gap length)

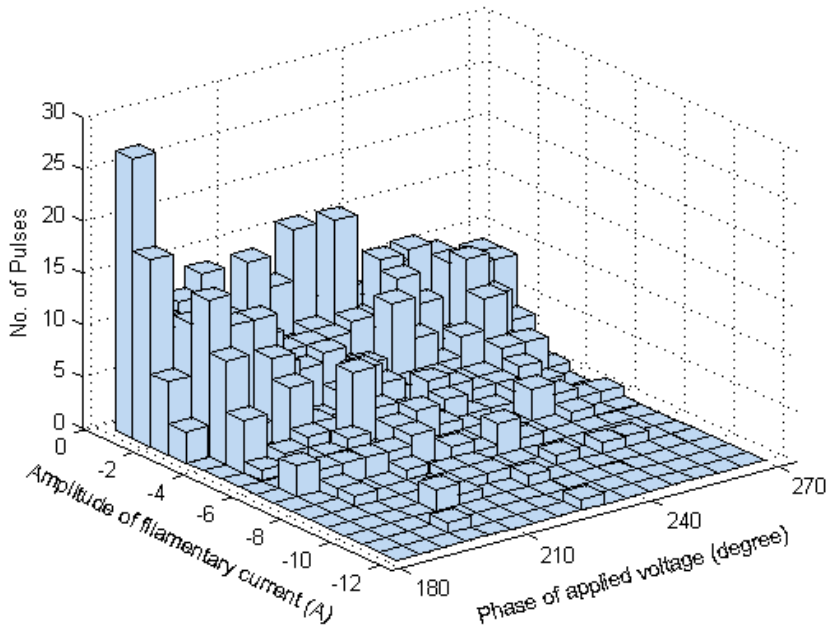

Fig.B-5 Distribution of filamentary current amplitude at the gas pressure of 1.8 bar absolute (at 0.5 mm gap length)

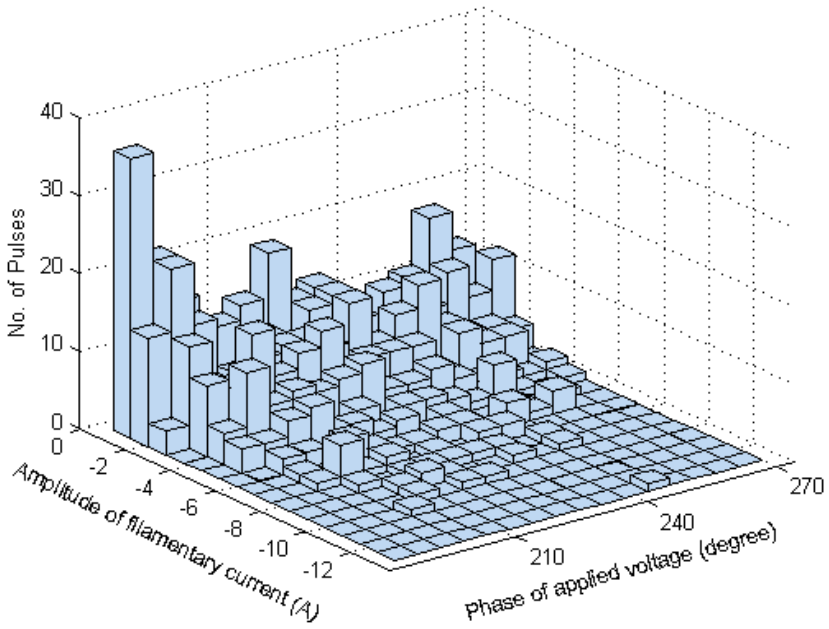

Fig.B-6 Distribution of filamentary current amplitude at the gas pressure of 2 bar absolute (at 0.5 mm gap length)

12.2 Distribution of Filamentary Current Duration over Different Gas Pressures

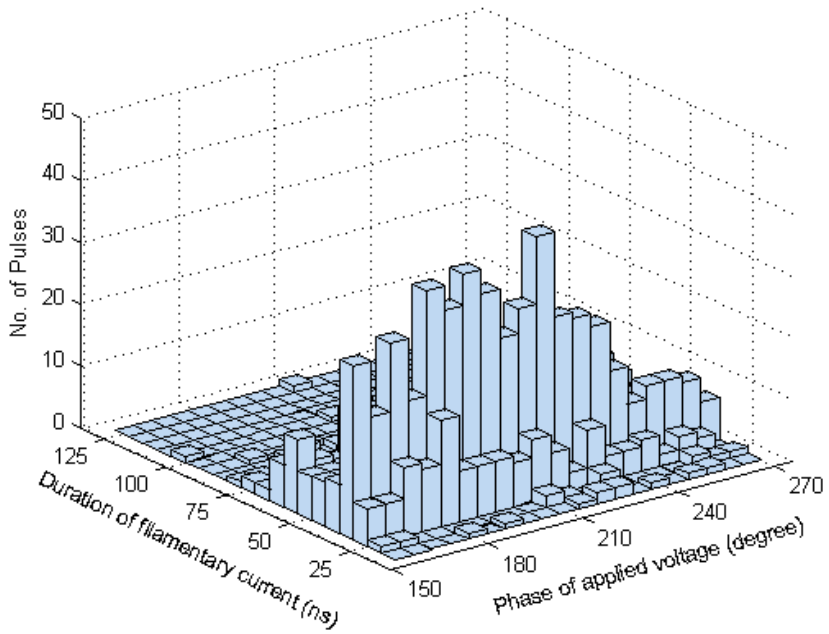

Fig.B-7 Distribution of filamentary current duration at the gas pressure of 1 bar absolute (at 0.5 mm gap length)

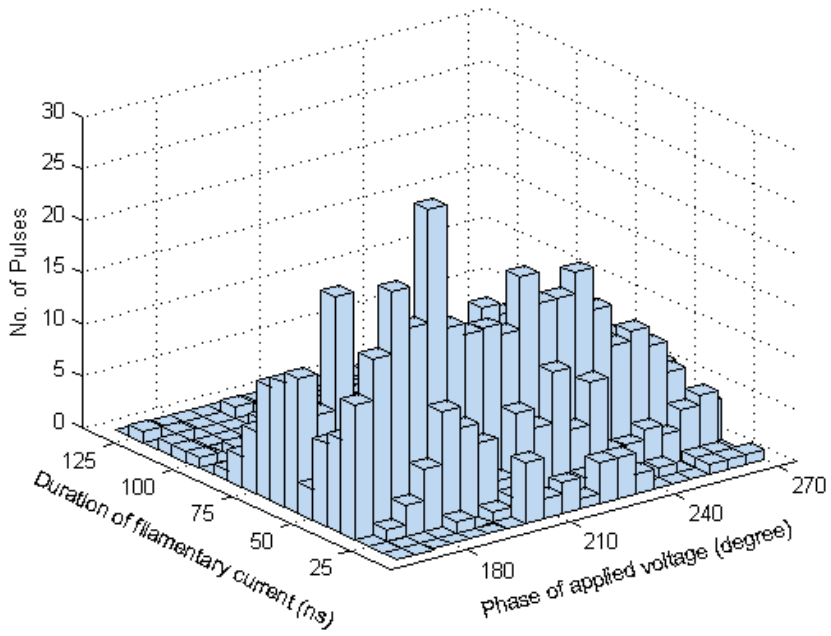

Fig.B-8 Distribution of filamentary current duration at the gas pressure of 1.2 bar absolute (at 0.5 mm gap length)

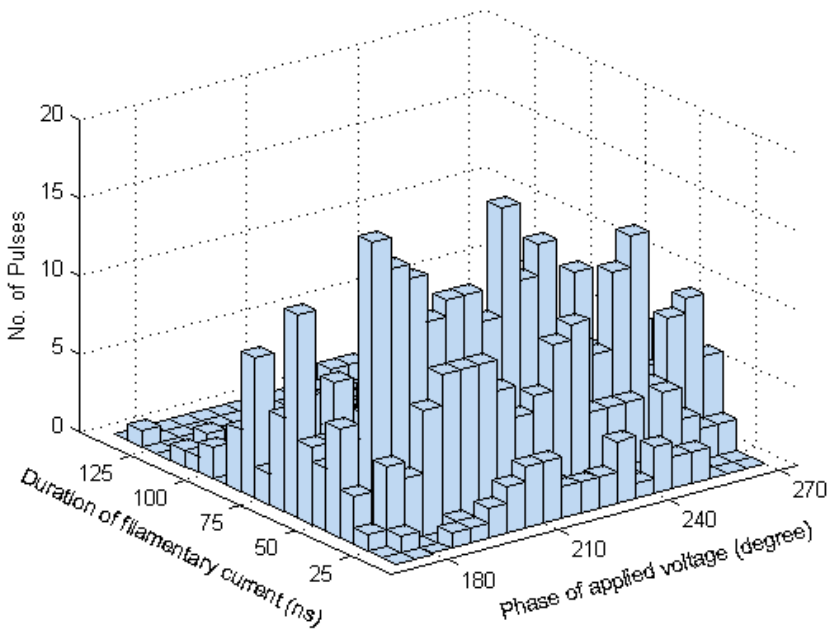

Fig.B-9 Distribution of filamentary current duration at the gas pressure of 1.4 bar absolute (at 0.5 mm gap length)

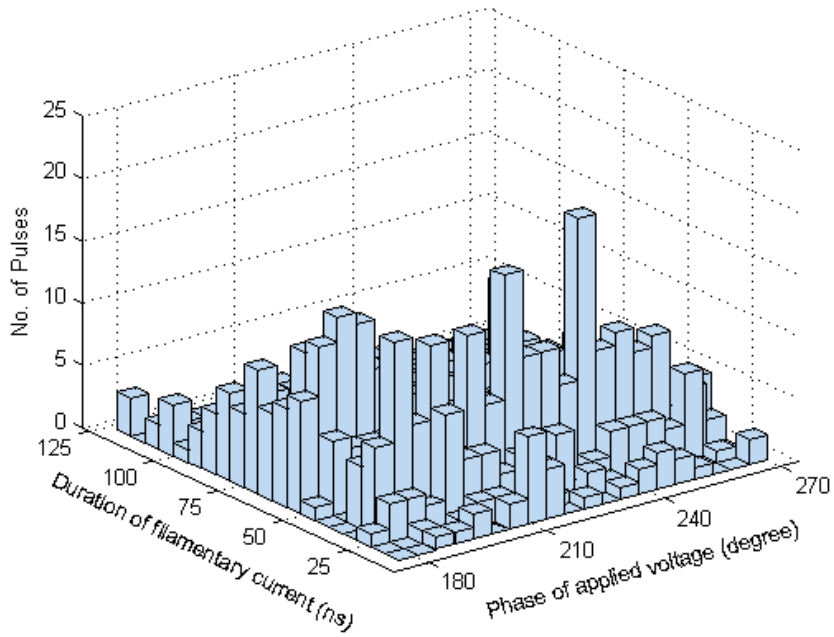

Fig.B-10 Distribution of filamentary current duration at the gas pressure of 1.6 bar absolute (at 0.5 mm gap length)

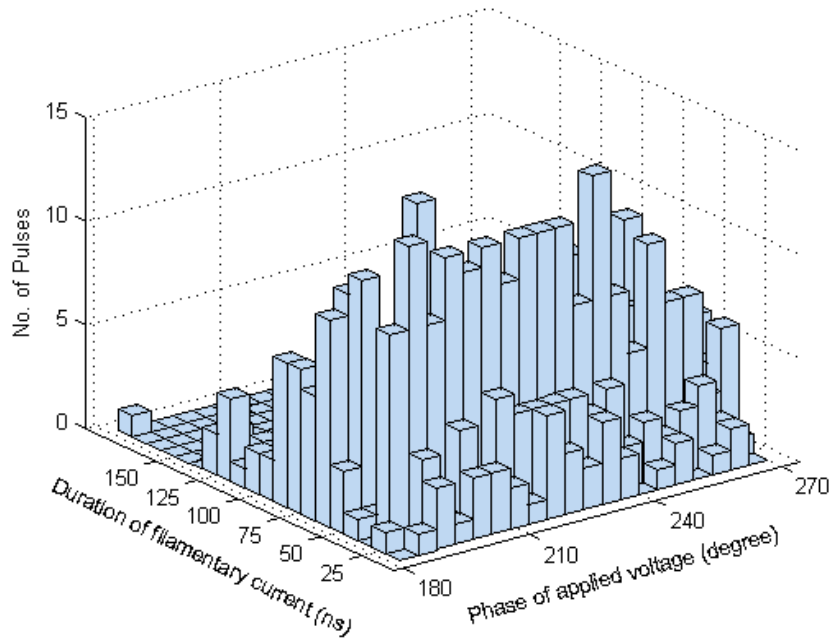

Fig.B-11 Distribution of filamentary current duration at the gas pressure of 1.8 bar absolute (at 0.5 mm gap length)

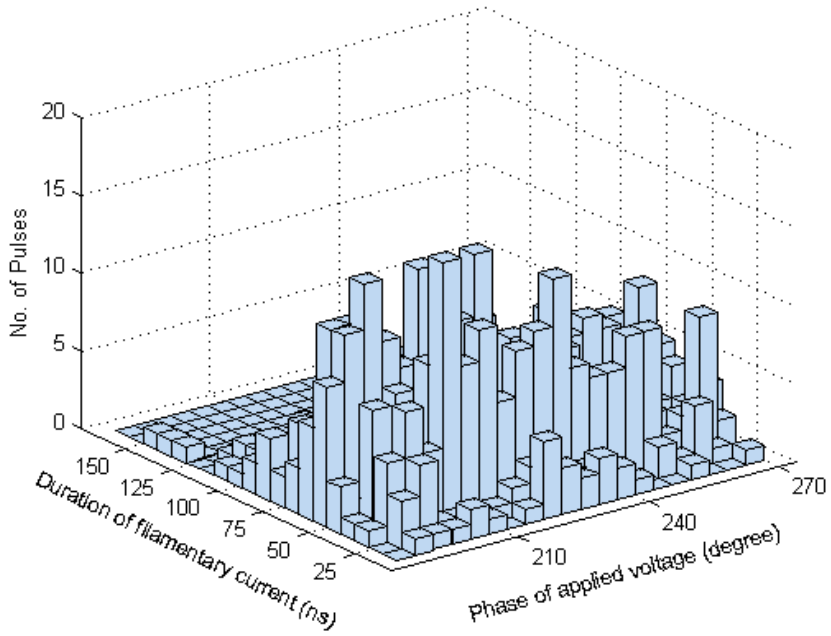

Fig.B-12 Distribution of filamentary current duration at the gas pressure of 2 bar absolute (at 0.5 mm gap length)

12.3 Distribution of Filamentary Transfer Charge over Different Gas Pressures

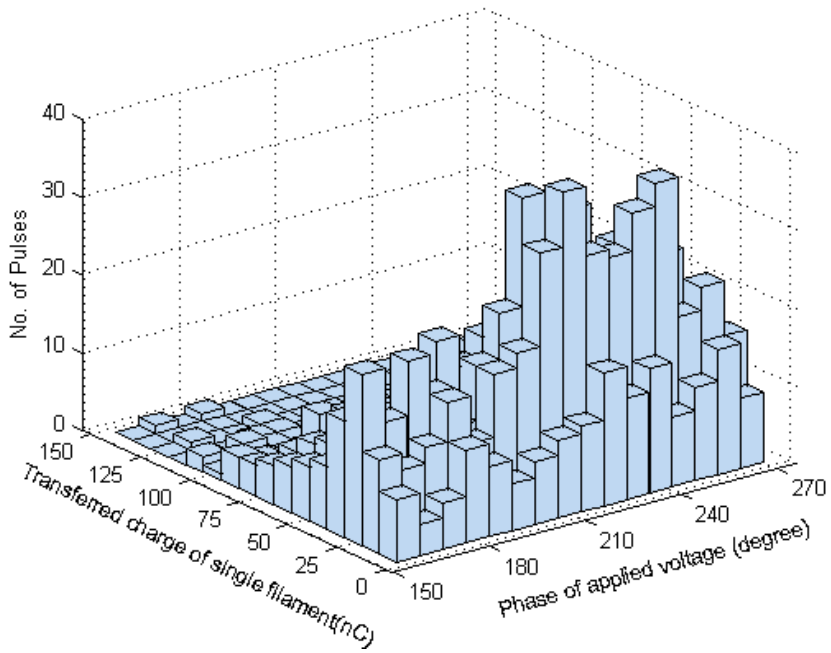

Fig.B-13 Distribution of filamentary transfer charge at the gas pressure of 1 bar absolute (at 0.5 mm gap length)

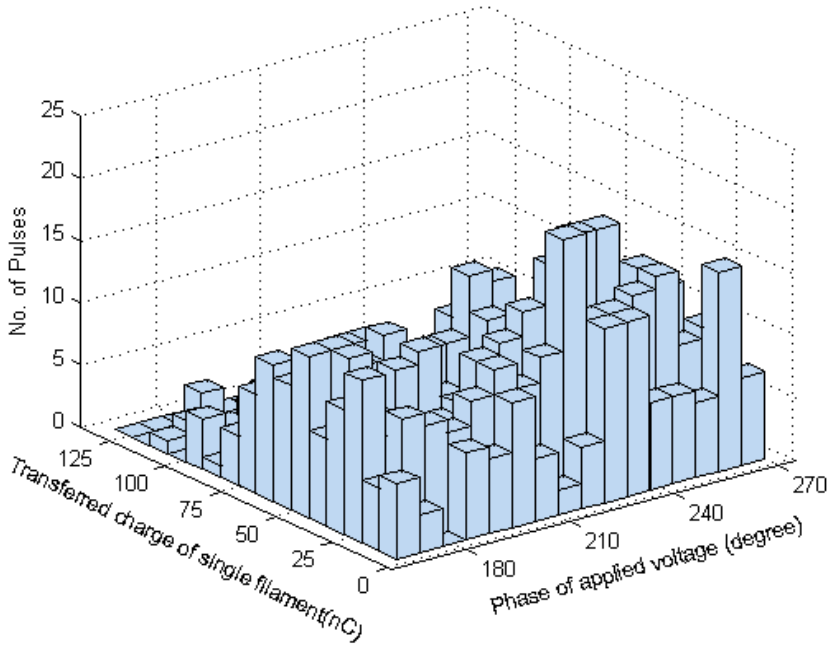

Fig.B-14 Distribution of filamentary transfer charge at the gas pressure of 1.2 bar absolute (at 0.5 mm gap length)

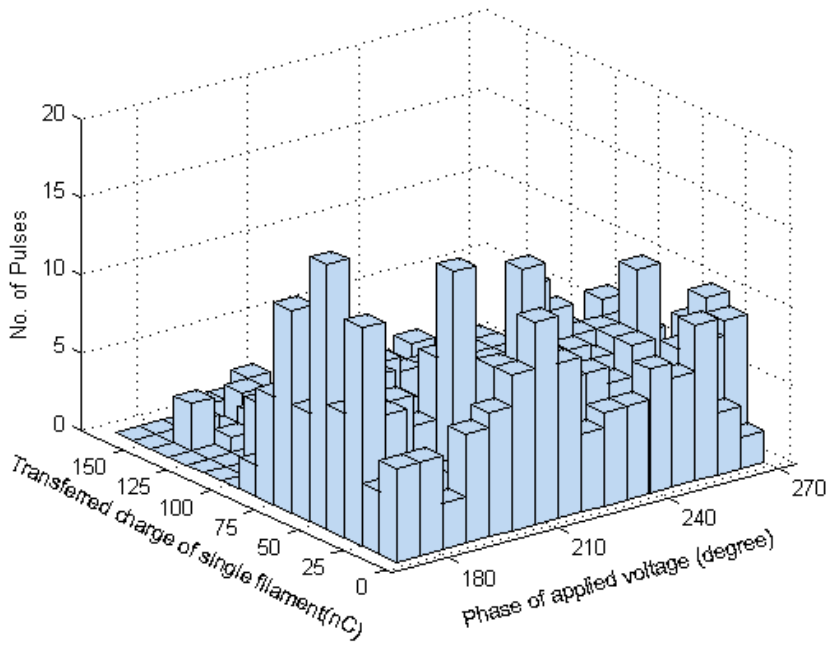

Fig.B-15 Distribution of filamentary transfer charge at the gas pressure of 1.4 bar absolute (at 0.5 mm gap length)

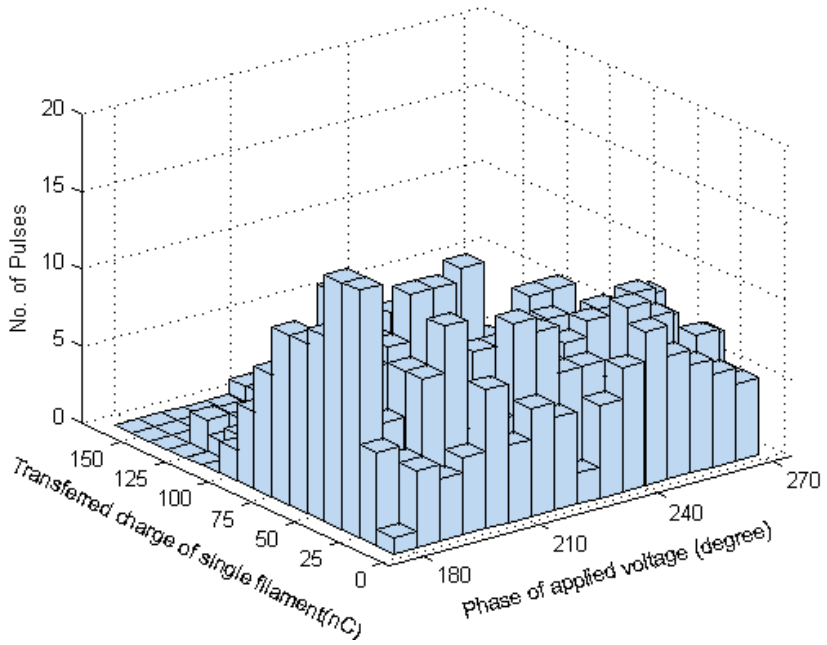

Fig.B-16 Distribution of filamentary transfer charge at the gas pressure of 1.6 bar absolute (at 0.5 mm gap length)

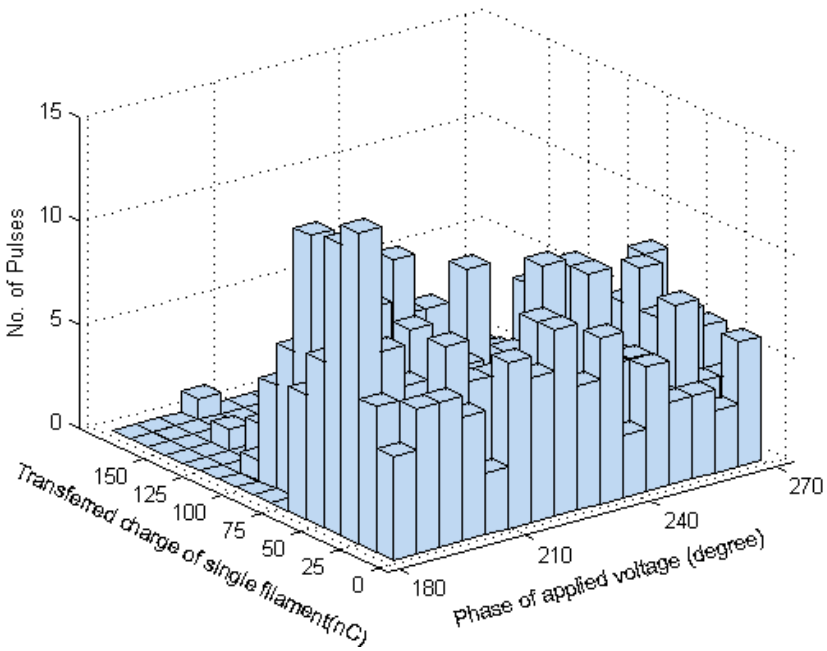

Fig.B-17 Distribution of filamentary transfer charge at the gas pressure of 1.8 bar absolute (at 0.5 mm gap length)

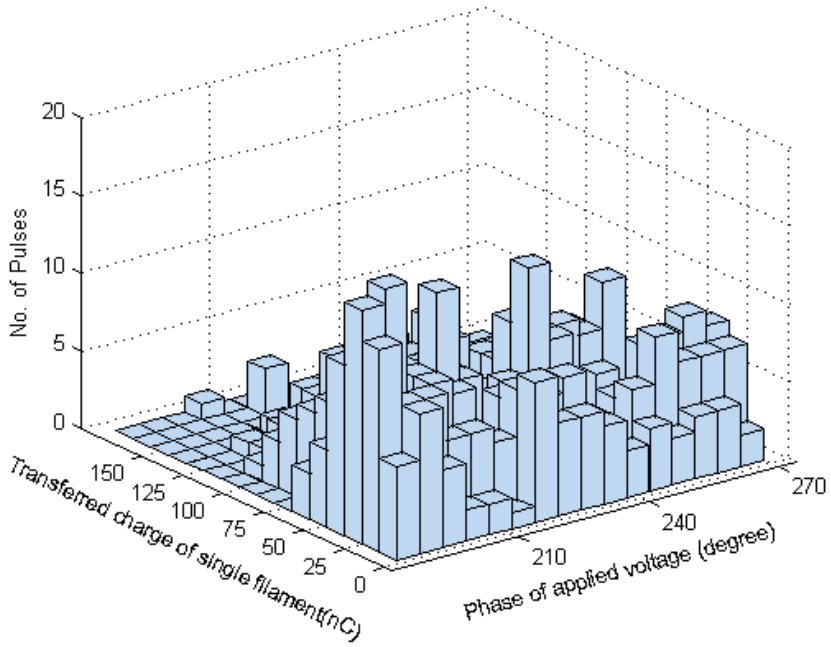

Fig.B-18 Distribution of filamentary transfer charge at the gas pressure of 2 bar absolute (at 0.5 mm gap length)

12.4 Distribution of Micro-discharge Energy over Different Gas Pressures

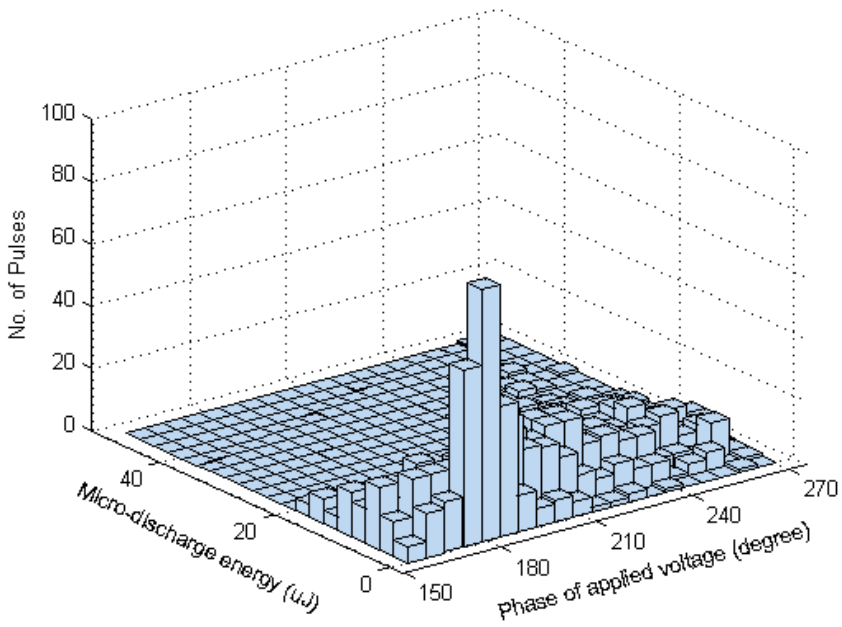

Fig.B-19 Distribution of micro-discharge at the gas pressure of 1 bar absolute (at 0.5 mm gap length)

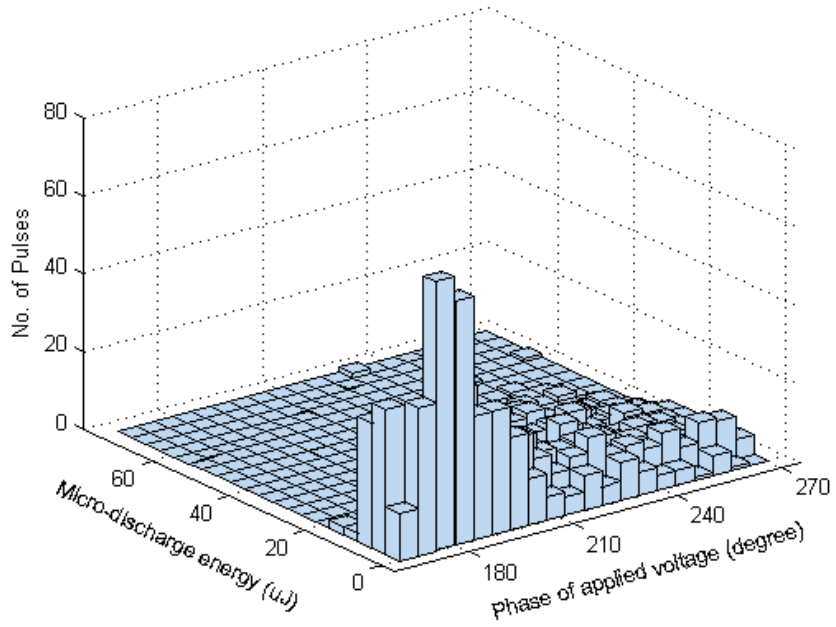

Fig.B-20 Distribution of micro-discharge at the gas pressure of 1.2 bar absolute (at 0.5 mm gap length)

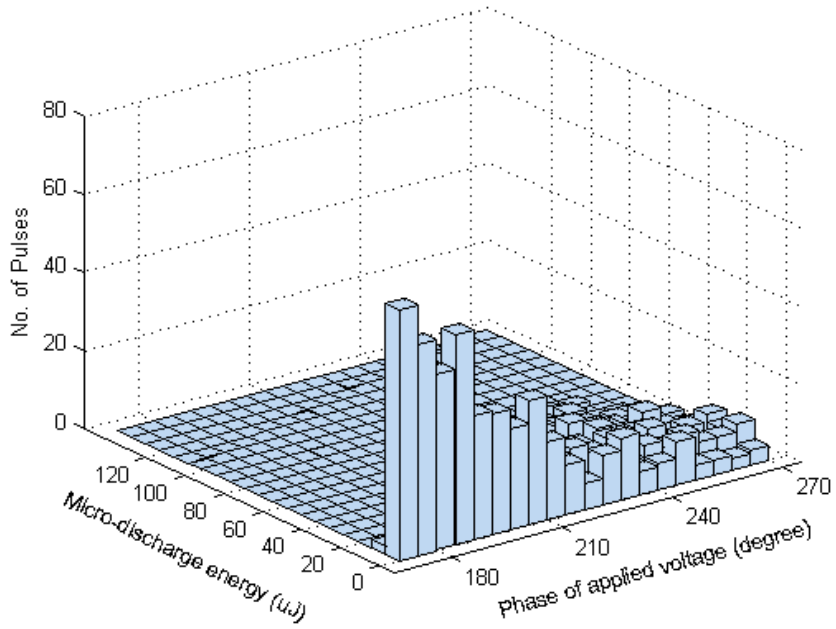

Fig.B-21 Distribution of micro-discharge at the gas pressure of 1.4 bar absolute (at 0.5 mm gap length)

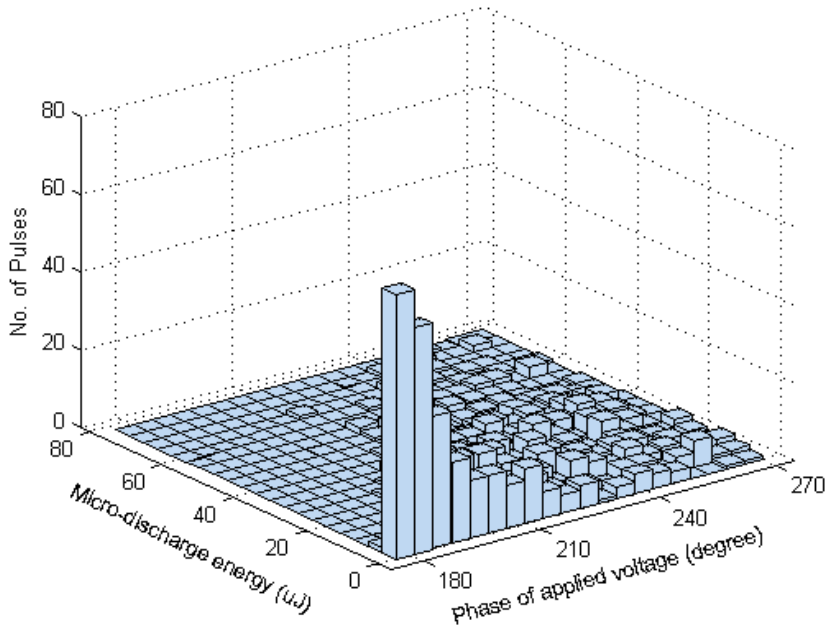

Fig.B-22 Distribution of micro-discharge at the gas pressure of 1.6 bar absolute (at 0.5 mm gap length)

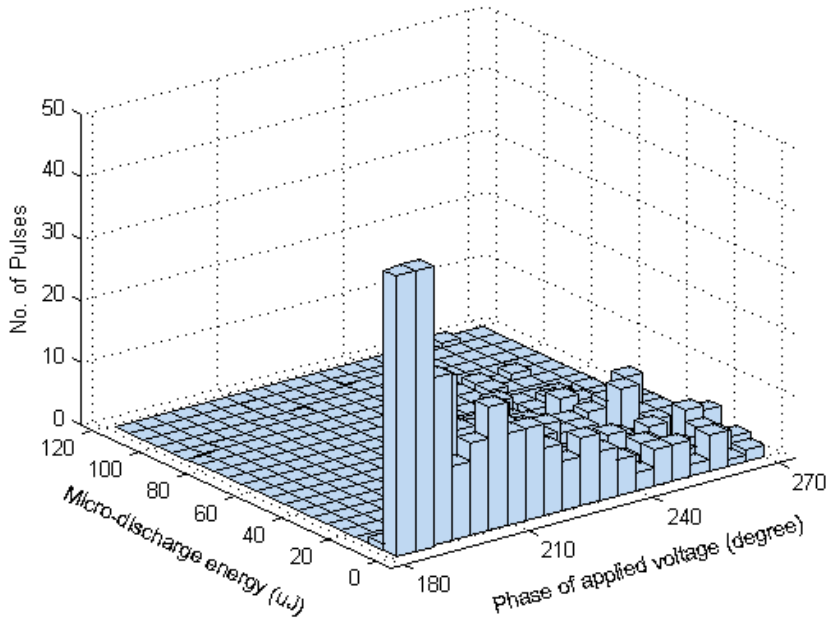

Fig.B-23 Distribution of micro-discharge at the gas pressure of 1.8 bar absolute (at 0.5 mm gap length)

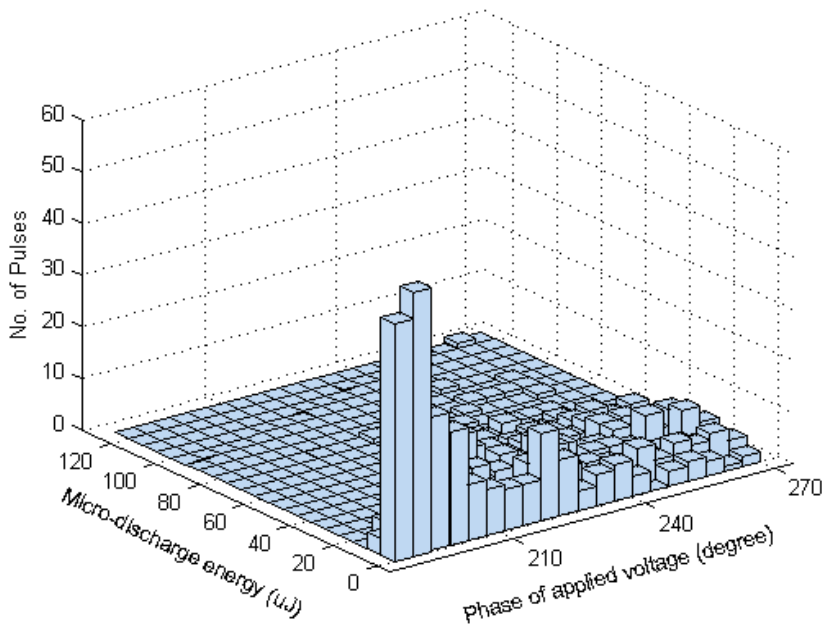

Fig.B-24 Distribution of micro-discharge at the gas pressure of 2 bar absolute (at 0.5 mm gap length)

13 APPENDIX C: Matlab Codes for Ozone Generation Efficiency Calculation

13.1 Discharge Power Calculation

```
% "Voltage" is the spreadsheet of one cycle voltage trace.
% "Current" is the spreadsheet of one cycle current trace.
% "dt" is the sampling period.
% "E" is the discharge energy under per cycle or per pulse of
voltage.
% "P" is the discharge power.

Voltage=csvread('Voltage.csv',5,0);
Current=csvread('Current.csv',5,0);
plot(Voltage(:,1),Voltage(:,2));
figure;
plot(Current(:,1),Current(:,2));
VI=Voltage(:,2).*Current(:,2);
dt=Voltage(3,1)-Voltage(2,1);
f=input('Enter the AC frequency or Pulse Repetition Rate:');
E=sum(VI)*dt;
P=f*E*dt;
```

13.2 Ozone Generation Efficiency Calculation Based on Steady Ozone Concentration

Presented herein are the codes used to calculation the ozone generation efficiency under the application of continuous AC power or pulsed power, as referenced to Section 3.7.2.

```
% "F" is the flow rate.
% "n1" is the number of moles of input oxygen.
% "m" is the mass of input oxygen per minute.
% "c" is the concentration of ozone produced.
% "n2" is the number of moles of ozone produced.
% "n3" is the number of moles of output oxygen.
% "x" is the weight concentration of ozone.
% "M" ozone produced per hour.
% "P" Power injected to the ozone reactor.
% "Spec" is the specific energy with the unit of J/L.
% "e" is the ozone generation efficiency with the unit of g/kWh.
% "24.465L/mole" is the molar volume of ideal gas at standard
condition.
% "22.414L/mol" is the molar volume of ideal gas at normal condition.

F=input('Enter the flow rate:');
n1=r./24.465;
m=n1.*31.9988;
c=input('Enter the ozone concentration:');
```

```
n2=c./47.9982;
n3=1000/22.414-n2;
x=c./(c+n3.*32);
M=m.*x.*60;
P=input('Enter the discharge power:');
Spec =P.*60./F;
e=M*1000./P;
```

13.3 Ozone Generation Efficiency Calculation Based on Transient Ozone Concentration Values

Presented herein are the codes used to calculation the ozone generation efficiency by using a transient AC power with 200 voltage cycles, as referenced to Section 3.7.3.

```
% "Time" is the sampling data of time.
% "Ozone" is the sampling data of ozone concentration with the unit
of PPM
% "E" is the discharge energy under per cycle
% "F" is the oxygen flow rate with the unit of L/min
% "O3" is the amount of ozone production
% "e" is the ozone generation efficiency with the unit of g/kWh.

Td=r=input('Enter the last point of time:');
x=0:0.01:Td;
yi=interp1(Time,Ozone,x);
yi=yi';
x=x';
plot(x,yi);
a=yi*2.144;
b=(1e6-yi)*1.429+yi*2.144;
c=a./b;
F=0.5;
Wt=F*31.9988/(24.465*60);
m0=c*Wt;
m=m0*0.01;
O3=sum(m);
e=3600000*O3/(200*E);
```